ISSN 2186-7968

ELPH ANNUAL REPORT

2015

TOHOKU UNIVERSITY

ELPH ANNUAL REPORT 2015

TOHOKU UNIVERSITY

Editor

HINODE, Fujio
MURAMATSU, Norihito
MUTO, Toshiya
TSUKADA, Kyo

Research Center for Electron Photon Science

Tohoku University

1-2-1 Mikamine, Taihaku, Sendai 982-0826

Japan

Phone: +81, 22-743-3400

Fax: +81, 22-743-3402

Web site: http://www.lns.tohoku.ac.jp/

982-0826　仙台市太白区三神峯1-2-1
東北大学電子光理学研究センター
電話　022-743-3400
Fax　022-743-3402

Preface

The ELPH Annual Report 2015 covers scientific and technical activities carried out at Research Center for Electron Photon Science (ELPH), Tohoku University in FY2015 (April, 2015 to March, 2016). ELPH has been a part of Joint Usage / Research Centers since FY2011. Joint Usage / Research Centers (JURC) system was engaged by the Ministry of Education, Culture, Sports, Science and Technology (MEXT) in FY2010 to encourage and promote collaborative research passing through the border of respective universities. Approximately 75 laboratories and research centers in national universities designated by the Minister of MEXT started their own activities under the program of JURC until FY2015 in which the term corresponds to the secondary stage of the six-year " Medium-term Goal and Plans " for national universities.

Because of the disaster of big Earthquake and Tsunami on March 11, 2011, an interim appraisal regarding JURC activity in 2012 for the ELPH was clearly poor, and it was not acceptable for us. However accelerator operation was back in the end of FY2013, and completed amount of Joint Usage of accelerators in ELPH was fully recovered in FY2014. Although we had embarrassed particularly by the steep rise of electricity price, we have performed exhaustive control of power consumption for every device equipped in accelerators and the facility utilities. In FY2015, the total machine operation time reached over 2000 hours and the total users participated to beam experiments was more than 1000 people. Consequently the JURC end-term evaluation for ELPH was, correctly, A. It means we should let us be substantial frame and pursuing interdisciplinary science for the next generation of Laboratory. We sincerely ask facility users and related scientific field communities for continuous supports and cooperation.

Director
Hiroyuki Hama

ELPH annual report, 2015

Contents

I. Papers

II. Status Report

I. Papers

(ELPH Experiment : #2761)

Development of a fast profile monitor with scintillating fiber hodoscopes for high-intensity photon beams

T. Ishikawa[1], Y. Honda[1], H. Kanda[2], S. Kido[1], Y. Matsumura[1], M. Miyabe[1],
H. Shimizu[1], A.O. Tokiyasu[1], Y. Tsuchikawa[1], and H. Yamazaki[1]

[1]*Research Center for Electron Photon Science (ELPH), Tohoku University, Sendai 982-0826, Japan*
[2]*Department of Physics, Tohoku University, Sendai 980-8578, Japan*

A fast beam-profile monitor has been developed for high-energy photon beamlines at the Research Center for Electron Photon Science, Tohoku University. The monitor consists of a trigger system for the photon identification and a tracker system for the position measurement. The position of the photon converted into an electron-positron pair in a 0.5 mm-thick aluminum plate is measured. The pair-production events are identified with a trigger plastic scintillator placed behind the plate. Charged particles produced upstream are rejected with a charge veto plastic scintillator placed in front of the plate. The position of the electron-positron pair is determined by two hodoscopes made of scintillating fibers with a cross section of 3×3 mm^2. The reconstruction of the incident position is made by a developed logic module with a field-programmable gate array, multi-purpose logic module MPLM4X. The dead time for processing an event is 35 ns, and a high data acquisition efficiency ($\sim$ 100%) can be achieved with this monitor for high-intensity photon beams in the normal operation corresponding to 20 MHz tagging signals.

§1. Introduction

Two high-energy tagged photon beamlines [1, 2] were constructed for meson photoproduction experiments [3] at the Research Center for Electron Photon Science (ELPH), Tohoku University. In both beamlines, bremsstrahlung photons are generated by inserting a thin carbon fiber into circulating electrons in the electron synchrotron [4]. The energy of the photon is determined by measuring the momentum of its corresponding post-bremsstrahlung electron [1, 2]. We have developed several versions of profile monitors giving a two dimensional intensity map of the photon beam for optimizing the photon beam direction.

Two types of the measurement of the photon beam profile have been made at ELPH. One is an analog-type measurement using a film or a charge-coupled device (CCD) video camera. A photon beam spot is taken with an instant film or a fluorescent screen together with a video camera. They are placed behind a thick metal plate, which is used as a radiator to produce secondary particles namely electron-positron pairs and associated X-rays. Although the analog-type measurements are simple, the linearity of the intensity map measured with a film or a video camera is not guaranteed due to reciprocity law failure characteristics or saturation effects. Therefore, alternative profile monitors with scintillating fiber (SciFi) hodoscopes have been developed [5–7].

§2. Profile monitors with scintillating fiber hodoscopes

All the monitors consist of a trigger system for the photon identification and a tracker system for the position measurement. The tracker system consists of two layers of SciFi hodoscopes. Each SciFi measures a cross section of 3×3 mm^2. The trigger system consists of a plastic scintillator (PS) for charge veto, an aluminum plate converter, one or two trigger PSs. Each of the charge and trigger PSs is connected to a photomultiplier tube, Hamamatsu Photonics H7195, for which power supply boosters are used to work for high-intensity photon beams. The trigger condition of the data acquisition is described as

$$[\overline{\text{charge PS}}] \otimes [\text{trigger PS}] \tag{1}$$

or

$$[\overline{\text{charge PS}}] \otimes [\text{trigger PS1}] \otimes [\text{trigger PS2}]. \tag{2}$$

The charge PS signal rejects the charged particles produced upstream. The discriminator thresholds for producing logic signals of the charge and trigger PSs are set to $0.5V_{\text{mip}}$ and $1.5V_{\text{mip}}$, respectively, where V_{mip} is the average pulse height of the minimum ionizing particles.

The thicknesses of PSs has been reduced from 5 to 1 mm and a trigger PS has been removed in the third generation monitor to be used for high-intensity photon beams. The charge PS with a size of 70×70 mm^2 was connected to a H7195 PMT. The trigger PS with a size of 55×55 mm^2 was connected to two H7195 PMTs arranged in an L-formation [6]. The uniform energy response of the charge and trigger PSs with respect to the incident position is important for minimizing the systematic uncertainty of the measured profile.

The uniformity maps were measured for the charge and trigger PSs at by using 460 MeV/c positron beam at ELPH [8]. Here, the aluminum plate for an e^+e^- converter was removed. The trigger condition of the uniformity map measurement was

$$[x \text{ SciFi OR}] \otimes [y \text{ SciFi OR}], \tag{3}$$

where x (y) SciFi OR denotes the logic OR of sixteen x (y) SciFi signals. The energy distributions of the charge and trigger PSs were obtained for 16 incident positions given by the responding x and y SciFis. The peak position corresponding to the minimum ionizing particles for each incident position was obtained by fitting the Moyal function [9] to the data. Fig. 1 shows the uniformity maps for the charge `Gv` and trigger `Gt1` and `Gt2` PS signals. Here, the signal for the central incident position was normalized to 1. The energy response was not uniform. An enhancement of the signal was observed at the PS side connected to a PMT, suggesting the size of the trigger PS was small. A signal drop was observed on the adjacent side connected to the other PMT, indicating that the L-type PMT connection was not appropriate. Therefore, we have replaced the trigger PS with a trigger PS with an area of

70 × 70 mm^2, and the scintillation light is collected only from one side. The details of the uniform map measurement is described elsewhere [10].

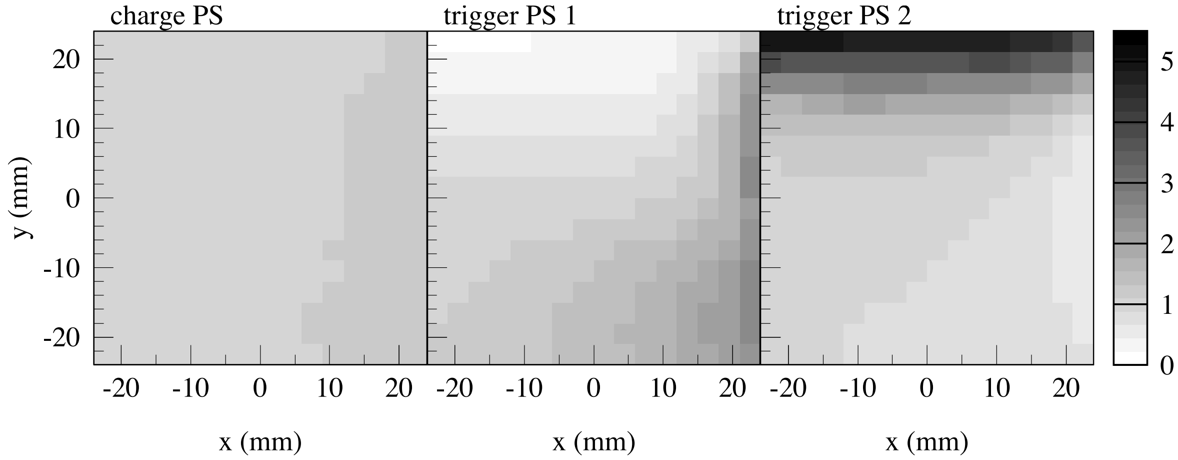

Fig.1. Uniformity maps for the charge and trigger PS signals. The trigger PS is connected to two H7195 PMTs arranged in an L-formation. The trigger PS 1 (2) signal is given by a PMT connected to the $+x$ ($+y$) side. The peak position of the pulse height distribution for minimum ionizing particles is obtained for each impact point and normalized to the signal in the central position. The gray scale is common to all the panels.

§3. Measured photon-beam profiles

A method for creating an intensity map of the photon beam in the fourth generation of the profile monitor is similar to the third generation. The newly developed NIM module, multi-purpose logic module MPLM4X [11] with a field-programmable gate array, Xilinx Spartan-6 [12], is used for the data acquisition of the profile monitor. The Data AcQuisition (DAQ) with MPLM4X for the profile monitor is programmed in VHDL using an integrated development environment Xilinx ISE WebPACK Ver. 14.7 [13]. The time jitter of the logic is made less than 5 ns by using edge-aligned signals with the 200 MHz clock. The functions of the profile monitor are as follows:

1. the incident position is determined with respect to the trigger signal,
2. the number of counts for all the positions are stored,
3. the counting process can be gated,
4. the incident position can be determined in coincidence with the photon-tagging signal, and
5. The data acquisition can be controlled with an RS-232C communication.

Since the MPLM4X logic module can accept and produce the NIM logic signals, additional level converters are prepared between NIM and RS-232 logic signals.

The number of hit SciFis is required to be one for each layer when the incident position is determined. Here, both charged particles converted from the photon beam are expected to come to the same SciFi region. One of them may, however, escape the active area of the SciFi hodoscopes due to the multiple scattering, complete energy loss, or other effects. In this case measured intensity map may be distorted. Since the distortion mainly comes from the low-energy electrons or positrons converted from the untagged photon, the intensity map for the tagged photon beam is note deteriorated, which is estimated by a Monte Carlo simulation based on GEANT4 [14]. The details of the simulation results are described elsewhere [10].

To estimate the number of coincidence signals with respect to the photon tagging signals, a sideband background-subtraction method is utilized. The background timing of the tagging signal is 165 ns (33 clock cycles) delayed with respect to the prompt timing. The harmonic number of the BST ring is 83 and the radio frequency is 500.14 MHz [4], which gives approximately 165.95 ns as a revolution period. Fig. 2 shows the typical beam profile in coincidence with the 81st photon-tagging channel at the circulating electron energy of 1.3 GeV. The details of the DAQ for the photon monitor are described elsewhere [15, 16].

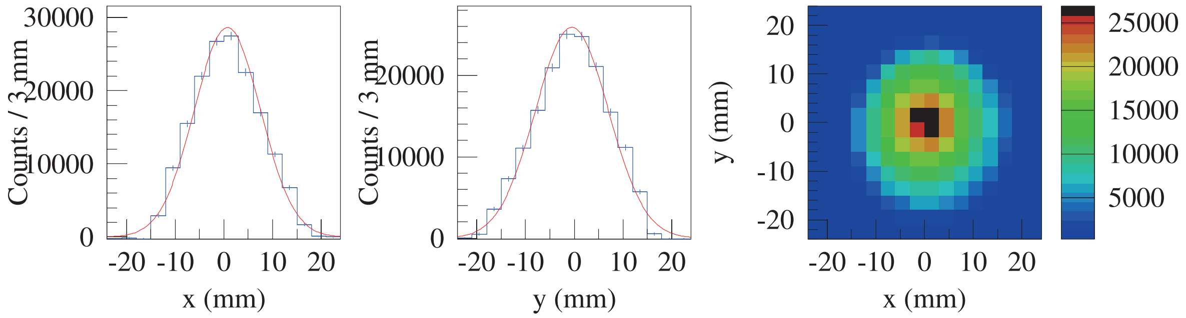

Fig.2. Typical beam profile in coincidence with the 81st photon-tagging channel at a circulating electron energy of 1.3 GeV. The left and central panels show the x and y distributions, and the right panel shows the two-dimensional profile. The curves in the left and central panels show the fitted Gaussian functions.

The photon beam profiles were measured for different intensities and different photon energies. The measured values for the mean and width in x and y distributions are the same for different conditions. The variations of the mean and width in a spill was also measured. The photon beam spot moving in the $+x$ to $-x$ direction with respect to the radiator motion from $-x$ to $+x$ was observed. This is because the horizontal position deviation from the center gives a negative momentum vector p_x/p deviation for the electrons coming to the radiator position in the BST ring [4]. The spot moved by approximately 3 mm in x with respect to the elapsed time in a spill. The details of the various photon-beam profiles measured are discussed elsewhere [7, 16].

§4. Summary

We have developed a fast profile monitor for high-intensity bremsstrahlung photon beams at ELPH. The positions of photons producing electron-positron pairs at the converter are determined by the developed logic module, MPLM4X, with an FPGA chip, Spartan-6. No intensity and tagging energy dependences were observed in the measured beam profile.

Acknowledgments

The authors wish to thank the ELPH accelerator staff for providing the primary electron beam in the stable condition. This work was supported in part by Grants-in-Aid for Scientific Research (A) (24244022), and for Scientific Research (C) (26400287).

References

[1] H. Yamazaki *et al.*: Nuclear Instruments and Methods in Physics Research Section A **536**, 70 (2005).

[2] T. Ishikawa *et al.*: Nuclear Instruments and Methods in Physics Research Section A **622**, 1 (2010).

[3] T. Ishikawa *et al.*: Proceedings of the 10th International Workshop on the Physics of Excited Nucleons (NSTAR2015), JPS Conference Proceedings **10**, 031001 (2016);

T. Ishikawa *et al.*: Proceedings of the XV International Conference on Hadron Spectroscopy-Hadron 2013, PoS (Hadron 2013) 095;

T. Ishikawa *et al.*: Proceedings of the 20th International IUPAP Conference on Few-Body Problems in Physics, Few Body Systems **54**, 1047 (2013);

T. Ishikawa *et al.*: Research Report of LNS, Tohoku University, **42&43**, 1 (2011).

[4] F. Hinode *et al.*: Proceedings of 2005 Particle Accelerator Conference, 2458 (2005);

F. Hinode *et al.*: Proceedings of 11th International Conference on Synchrotron Radiation Instrumentation (SRI2012), Journal of Physics: Conference Series **425**, 072011 (2013).

[5] M. Nanao, T. Ishikawa, and H. Shimizu, Research Report of LNS, Tohoku University, **36**, 56 (2003).

[6] H. Fujimura *et al.*: Research Report of LNS, Tohoku University, **42&43**, 56 (2011).

[7] T. Ishikawa *et al.*: Nuclear Instruments and Methods in Physics Research Section A **811**, 124 (2016).

[8] T. Ishikawa *et al.*: Nuclear Instruments and Methods in Physics Research Section A **694**, 348 (2012).

[9] J.E. Moyal, Philosophical Magazine 46 (1955) 263;

M.D. Marucho, C.A. Garcia Canal, H. Fanchiotti, International Journal of Modern Physics C 17 (2006) 1461.

[10] Y. Tsuchikawa, S. Kido, and T. Ishikawa: Internal GeV-γ analysis note HD No. **384**$\boldsymbol{\mathcal{T}}$ (2015).

[11] ELPH annual report 2011–2013, Tohoku University, 194 (2014);

I. Nagasawa and T. Ishikawa: Internal GeV-γ analysis note HD No. **380**$\boldsymbol{\mathcal{C}}$ (2015).

[12] Spartan-6 website: ⟨http://www.xilinx.com/products/silicon-devices/fpga/spartan-6.html⟩.

[13] ISE WebPACK website: ⟨http://www.xilinx.com/products/design-tools/ise-design-suite/ise-webpack.html⟩.

[14] S. Agostinelli, et al., Nuclear Instruments and Methods in Physics Research Section A 506 (2003) 250-303;

J. Allison, et al., IEEE Trans. on Nucl. Sci. 53 (2006) 270-278;

Geant4 website ⟨http://geant4.cern.ch/⟩.

[15] T. Ishikawa: Internal GeV-γ analysis note HD No. **386$\mathcal{T}$** (2015).

[16] Y. Matsumura and T. Ishikawa: Internal GeV-γ analysis note HD No. **391$\mathcal{T}$** (2015).

(ELPH Experiment : #2803, #2844)

Upgrade plan of the FOREST experiments at ELPH

T. Ishikawa[1], H. Fujioka[2], Y. Honda[1], Y. Inoue[1], K. Itahashi[3], H. Kanda[4],
H. Kawai[5], Y. Matsumura[1], K. Maeda[4], M. Miyabe[1], N. Muramatsu[1],
H. Ohnishi[3], K. Ozawa[6], M. Sasagawa[1], H. Shimizu[1], K. Shiraishi[1],
M. Tabata[5], A.O. Tokiyasu[1], and Y. Tsuchikawa[1]

[1]*Research Center for Electron Photon Science (ELPH), Tohoku University, Sendai 982-0826, Japan*
[2]*Department of Physics, Kyoto University, Kyoto 606-8502, Japan*
[3]*Nishina Center, RIKEN, Wako 351-0198, Japan*
[4]*Department of Physics, Tohoku University, Sendai 980-8578, Japan*
[5]*Department of Physics, Chiba University, Chiba 263-8522, Japan*
[6]*Institute of Particle and Nuclear Studies, High Energy Accelerator Research Organization (KEK), Tsukuba 305-0801, Japan*

The next generation FOREST experiments are planed to reveal the non-perturbative QCD phenomena. The main objective of the first experiment is to determine the η-n scattering length using the $\gamma d \to p\eta n$ reaction. The photon beam with energies around 950 MeV can give the recoilless condition of η mesons by detecting the protons at 0°. The effects of the the η-neutron final-state interaction must be enhanced due to the small relative momentum between an η meson and a residual neutron. We place a bending magnet, which has been transported from KEK, behind FOREST to measure the forward emitted protons. The similar experimental setup can perform an experiment to search for η-mesic nuclei, which are good probes to explore the properties of a nucleon resonance $N(1535)S_{11}$ in the nuclear medium. It should be noted that the resonance is speculated to be the chiral partner of the nucleon. In this report, the planned FOREST experiment is presented.

§1. Introduction

The hadron-hadron interaction is a subject of great interest in the non-perturbative quantum chromodynamics (QCD) domain. QCD is the fundamental theory of the strong interaction, and the hadron-hadron interaction is described in principle by quark and gluon dynamics. Owing to the large running QCD coupling constant, little is known for the QCD solution at low energies, where hadrons as color-neutral objects play an important role in effective theories or models.

Among the two-body dynamincs of the meson-nucleon systems, the interaction between the η meson and the nucleon (N) is not well determined although it has been found to be attractive [1]. Neither direct η-n scattering experiments using η beams nor X-ray measurements from η-mesic atoms can be performed because the η meson is neutral and unstable. The η-N scattering length $a_{\eta N}$ has been extracted using coupled-channel analyses [2–5] from the differential and total cross sections for the

$\pi N \to \eta N$ and $\gamma N \to \eta N$ reactions together with the $\pi N \to \pi N$ scattering and $\gamma N \to \pi N$ photoproduction reactions. Although the imaginary part of $a_{\eta N}$ is found to be ~ 0.26 fm for different analyses, its real part is scattered in a wide range from 0.4 to 1.1 fm. Another analysis of the $np \to \eta d$ process with a three-body treatment of the final state [6, 7] gives 0.4–0.6 fm for the real part of $a_{\eta N}$. Although a new analysis using $\pi^+ d \to \eta pp$ reaction is proposed [8], the corresponding experiment has not been carried out at this moment. It should be noted that the existence of the exotic η-mesic nuclei can highly depend on the value of the real part of $a_{\eta N}$ [9]. The numerical values obtained so far for $a_{\eta N}$ are summarized in Ref. [10]. We plan to conduct a new η photoproduction experiment [11] for the determination of the η-n low-energy scattering parameters at ELPH, Tohoku University.

The modification of hadrons (a decrease of mass, a broadening of the width, and so on) in the nuclear medium is another issue of the next generation FOREST experiments. Since the nucleon resonance $N(1535)S_{11}$ is speculated to be the chiral partner of the nucleon, the nucleon $N(938)P_{11}$ and $N(1535)S_{11}$ become a degenerate state when chiral symmetry is restored. Even in a nucleus, the masses and difference of them are expected to decrease due to the partial restoration of the symmetry. The cross sections of η photoproduction from C and Cu were measured at $E_\gamma = 600$–1100 MeV to investigate the behavior of the S_{11} resonance in a nucleus [12]. The angular and momentum distributions of η mesons are in quantitative agreement with the Quantum Molecular Dynamics (QMD) model calculations in a wide range. An enhancement from the calculation is observed only in the ratio of the total cross sections $\sigma_{\mathrm{Cu}}/\sigma_{\mathrm{C}}$ near the threshold as shown in Fig. 2 of Ref. [12], which can be explained by a simple toy model that takes into account the mass decrease of S_{11} and the change of the ηN phase volume. Other effects can also explain this enhancement, however. Thus, we plan to search for η-nucleus bound/resonance states to discuss in-medium properties of S_{11} more clearly.

An η-mesic nucleus was predicted by Haider and Liu [9, 13], and systematically studied by Chiang, Oset and Liu [14]. No clear conclusion for η-nucleus bound state has been obtained in spite of some experimental efforts [15] for investigating the η-N interaction in detail. The η mesons in the nuclear medium are expressed by mixing of the η meson and the S_{11}-particle and P_{11}-hole excitation states [16]. The particle-hole mode is 50 MeV higher than the mesonic one, and the level crossing of these modes are expected due to the degeneracy of S_{11} and P_{11} in the nuclear medium. The level crossing gives both the bound and resonance states of the η-nucleus system. Therefore, not only η-nucleus bound states but also resonance ones are affected by the in-medium properties of S_{11}. The expected energy spectra for the η-nucleus system obtained by the $\gamma A \to p\eta(A-1)$ reaction are calculated with/without the level crossing in Ref. [16]. The experimentally obtained spectrum is important for understanding the in-medium properties of S_{11} although it does not have a prominent peak. The signal of the level crossing in a nucleus is expected to give some structure in the resonance region.

§2. Upgrade experiments

To determine the η-n low-energy scattering parameters or to search for η-mesic nucleus states, we plan to carry out the experiments by using the photon beam around 950 MeV [17, 18] which satisfies the recoilless condition of η mesons by detecting the protons at 0° [16]. The small relative momentum between an η meson and a residual neutron or nucleus makes the probability higher giving the η-n final-state interaction or forming the η-nucleus bound/resonance states, respectively. Fig. 1 shows the experimental setup of the next generation FOREST experiments. The details of the FOREST detector is described elsewhere [19]. The forward scattered proton is momentum-analyzed with a bending magnet (transported from the low energy ring of KEKB) behind FOREST. The trajectory is planned to be measured with two planar drift chambers, and the time of flight will be measured with plastic scintillator hodoscopes . The additional e/π and π/K separations are made using SF5 lead glass and aerogel Cherenkov counters, respectively.

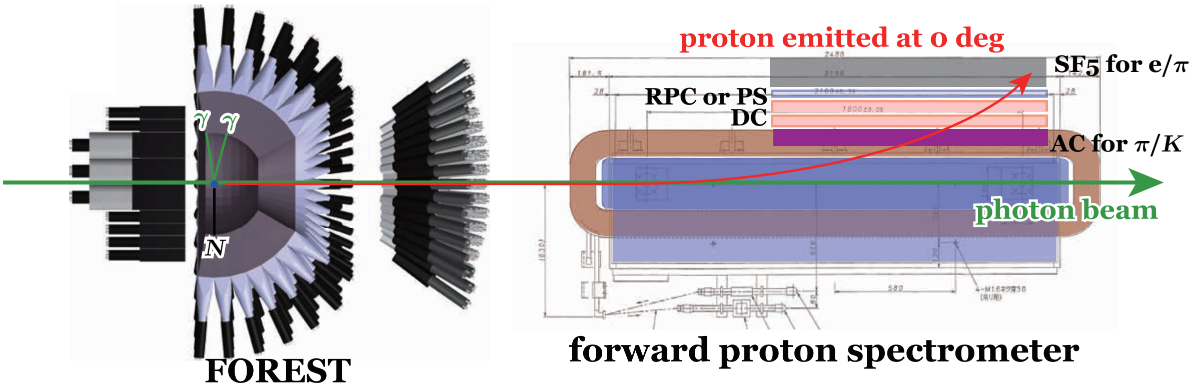

Fig.1. Experimental setup of the next generation FOREST experiments. The momentum and time of flight of the proton scattered at 0° are measured through a bending magnet. The forward emitted proton is momentum-analyzed with a bending magnet behind FOREST. The trajectory is measured with two planar drift chambers, and the time of flight is measured with plastic scintillator hodoscopes. The additional e/π and π/K separations are made using SF5 lead glass and aerogel Cherenkov counters, respectively.

2.1 Determination of the η-n scatering length

The planned FOREST experiment has an ideal condition to determine the η-n scattering parameters since it gives a small relative momentum between η and n and large relative momenta between η and p and between n and p. Only the η-n final-state interaction affect the yield of the reaction. Fig. 2 shows the diagram of the $\gamma d \to p\eta n$ reaction for determining the η-n scattering length. The advantages in the kinematics of the new FOREST experiment for the $a_{\eta n}$ determination are confirmed by Nakamura and Kamano [20] using the direct coupled channel (DCC) model [21].

To check the feasibility of the experiment, the relative momentum distribution without any final-state interaction is estimated. Fig. 3 shows the relative momentum distribution between an η meson and a neutron for the $\gamma d \to p\eta n$ reaction. Events having the small η-n relative momentum are enhanced by detecting the forward emitted protons with the spectrometer. An additional enhancement $|1/a_{\eta n} - ik|^{-2}$ is expected owing to the final-state interaction between the η meson and the neutron.

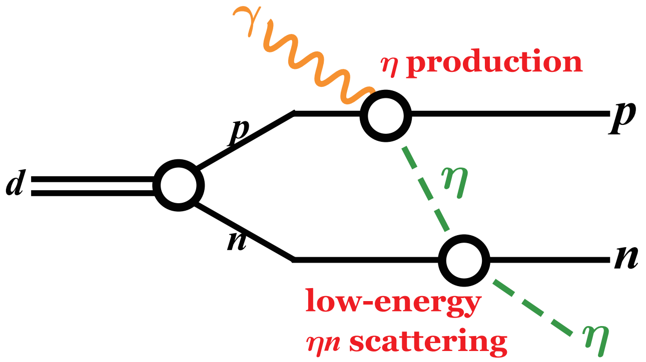

Fig.2. Diagrams for the $\gamma d \rightarrow p\eta n$ reaction. The reaction is a good probe to determine ηn scattering length since the relative momentum between η and n is small and the depicted diagram becomes dominant when the proton is measured at 0°.

2.2 Search for η-mesic nuclei

The experiment to search for η-mesic nuclei will be made in the similar experimental setup to that for determining the η-n scattering length. In addition to the forward proton measurement, we will detect a back-to-back $\pi^0 N$ or ηN pair with the FOREST detector to suppress background processes. It should be noted that the $\pi^0 N$ or ηN invariant mass gives information on the S_{11} mass in a nucleus. Since the gap of the bending magnet is 110 mm, the polar angle up to 0.6° is covered by the bending magnet. Assuming the 20 mm thick carbon target with a density of 1.5 g/cm^3, an eighty-day measurement gives approximately 100 events in a 10 MeV bin for the differential cross section of 100 nb/sr·MeV. The expected missing mass resolution is 3.8–6.1 MeV according to the assumed time resolution of the proton detecting hodoscopes 0.05–0.10 ns since the photon beam tagging resolution is 0.5–2.5 MeV. The photoproduction experiment for η-mesic nucleus search is complementary to the planned experiments at J-PARC using the (π^-, n) reaction [22].

§3. Other subjects

The subjects of the next generation FOREST experiments were discussed held from 23rd to 24th May, 2016 [23]. The following is the list for other subjects to be studied in the next generation FOREST experiments with a deuterium target:

1. determination of the Λ-n scattering length using the $\gamma d \rightarrow K^+ \Lambda n$ events,
2. investigation of the $N\Delta$ and $\Delta\Delta$ dibaryon states using the $\gamma d \rightarrow \pi^- X$ events, and
3. investigation of the ηpp states using the $\gamma d \rightarrow \pi^- X$ events.

There exist many physics subjects to be studied in the next FOREST experiments.

§4. Summary

The next generation FOREST experiments are planed to reveal the non-perturbative QCD phenomena. The main subject of the first experiment is to determine the η-n scattering length $a_{\eta n}$ using the $\gamma d \rightarrow p\eta n$ reaction. The 950 MeV photon beam and proton detection at 0° give the recoilless condition of

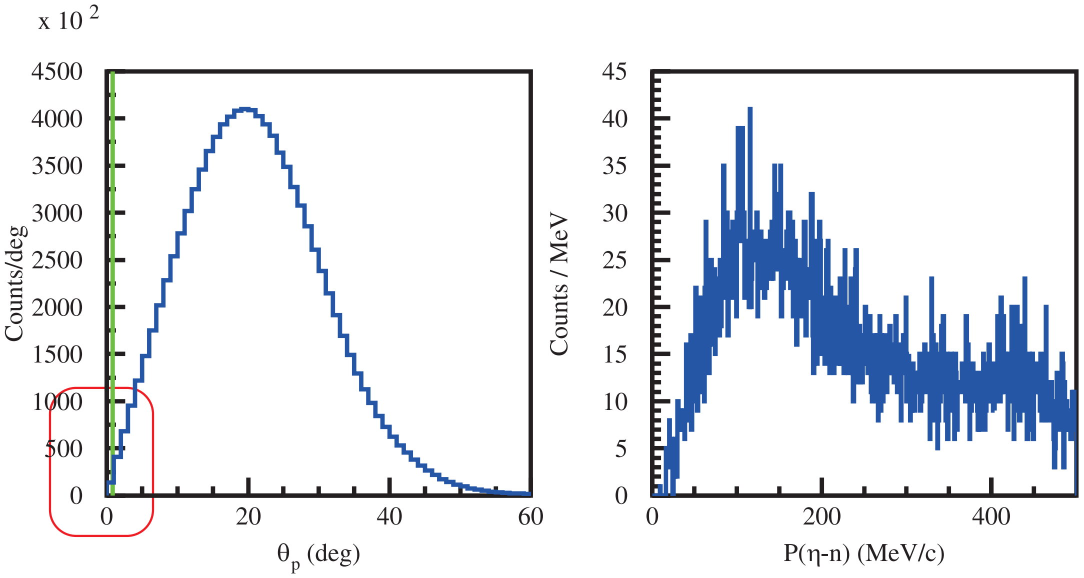

Fig.3. Relative momentum distribution between an η meson and a neutron for the $\gamma d \to p\eta n$ reaction. The number of counts are given for the 90 days in the same condition as the FOREST2009D experiment. The left panel shows the distribution for all the events, and the right shows the distribution for the events in which the proton is measured with the detectors behind the spectrometer.

η mesons. The η-neutron final-state interaction can be studied thanks to the small relative momentum between the η meson and the neutron. The detection of the forward emitted proton is essential for this study. We place a bending magnet behind FOREST to measure the forward emitted protons. We can perform an experiment to search for η-mesic nuclei in the similar experimental setup. The η-mesic nuclei good probes to explore the properties of a nucleon resonance $N(1535)S_{11}$, which is speculated to be the chiral partner of the nucleon, in the nuclear medium. We have many physics subjects to be studied in the next FOREST experiments.

Acknowledgments

This work was supported in part by Grants-in-Aid for Scientific Research (A) (24244022), and for Scientific Research (C) (26400287).

References

[1] Q. Haider, L. C. Liu: Physical Review C **66**, 045208 (2002).

[2] M. Batinić, I. Šlaus, A. Švarc, B.M.K. Nefkens, Physical Review C **51** (1995) 2310;
M. Batinić, I. Dadíc, I. Šlaus, A. Švarc, B.M.K. Nefkens, T.-S.H. Lee, Physica Scripta **58** (1998) 15.

[3] A.M. Green, S. Wycech, Physical Review C **55** (1997) R2167;
A.M. Green, S. Wycech, Physical Review C **60** (1999) 035208.

[4] A. Sibirtsev, S. Schneider, Ch. Elster, J. Haidenbauer, S. Krewald, J. Speth, Physical Review C **65** (2002) 044007.

[5] A.M. Gasparian, J. Haidenbauer, C. Hanhart, Physical Review C **68** (2003) 045207.

[6] H. Garcilazo, M.T. Peña, The European Physical Journal A **38** (2008) 209.

[7] H. Calén et al., Physical Review Letters **79** (1997) 2642;
H. Calén et al., Physical Review Letters **80** (1998) 2069.

[8] H. Fujioka, Acta Physica Polonica B 41 (2010) 2261;
H. Garcilazo, M.T. Peña, Physics Letters B 696 (2011) 386.

[9] Q. Haider, L.C. Liu, Physics Letters B **172** (1986) 257.

[10] Q. Haider and L.C. Liu, International Journal of Modern Physics E 24 (2015) 1530009

[11] T. Ishikawa, et al., ELPH-2803 letter of intent (2014);
T. Ishikawa, et al., ELPH-2844 experiment (2016).

[12] T. Kinoshita *et al.*: Phys. Lett. B **639**, 429 (2006).

[13] Q. Haider and L. C. Liu: Physical Review C **34**, 1845 (1986).

[14] H. C. Chiang, E. Oset, and L. C. Liu, Physical Review C **44**, 738 (1991).

[15] R.E. Chrien *et al.*: Physical Review Letters **60**, 2595 (1988);
M. Pfeiffer *et al.*: Physical Review Letters **92**, 252001 (2004).

[16] H. Nagahiro, D. Jido, S. Hirenzaki: Nuclear Physics A **761**, 92 (2005);
D. Jido *et al.*: Nuclear Physics A **811**, 158 (2008).

[17] T. Ishikawa, et al., Nuclear Instruments and Methods in Physics Research Section A **622**, 1 (2010).

[18] T. Ishikawa, et al., Nuclear Instruments and Methods in Physics Research Section A **811**, 124 (2016).

[19] T. Ishikawa *et al.*: Nuclear Instruments and Methods in Physics Research Section A (2016), `http://dx.doi.org/10.1016/j.nima.2016.06.054`;
T. Ishikawa, et al., Proceedings of the 10th International Workshop on the Physics of Excited Nucleons (NSTAR2015), JPS Conference Proceedings **10**, 031001 (2016);
T. Ishikawa, Proceedings of the XV International Conference on Hadron Spectroscopy-Hadron 2013, PoS (Hadron 2013) 095;
T. Ishikawa, et al., Proceedings of the 20th International IUPAP Conference on Few-Body Problems in Physics, Few Body Systems **54**, 1047 (2013).

[20] S.X. Nakamura and H. Kamano: private communication.

[21] H. Kamano *et al.*: Physical Review C **88**, 035209 (2013).

[22] K. Itahashi *et al.*: Letter of Intent for J-PARC ⟨`http://www.j-parc.jp/NuclPart/pac/0707/pdf/LoI-itahashi.pdf`⟩.

[23] FOREST workshop: ⟨`http://www.lns.tohoku.ac.jp/~hadron/mbr/ishikawa/forest16.php`⟩.

(ELPH Experiment : #2808)

A beam test of a charge-to-time converting leading-edge discriminator for plastic-scintillator signals

T. Ishikawa[1], Y. Honda[1], Y. Inoue[1], H. Kanda[2], S. Kido[1], Y. Matsumura[1],
M. Miyabe[1], H. Shimizu[1], K. Shiraishi[1], A.O. Tokiyasu[1], Y. Tsuchikawa[1],
and H. Yamazaki[1]

[1]*Research Center for Electron Photon Science (ELPH), Tohoku University, Sendai 982-0826, Japan*
[2]*Department of Physics, Tohoku University, Sendai 980-8578, Japan*

A charge-integrating analog-to-digital converter (ADC) is too expensive only for monitoring of the gain and applying a pulse-height time-walk correction since it requires a long delay cable for each channel. Recently, a multi-hit time-to-digital converter (TDC) module is available such as CAEN V1190 and V1290, which can digitize both the timings of the leading and trailing edges of signals. We have developed a charge-to-time converting (QTC) leading-edge discriminator for plastic-scintillator signals in cooperation with Fuji Diamond International Co. Ltd. (FDI). A test of a prototype 1CH QTC discriminator, FDI 1370, is reported in the previous annual report [1]. In this report, a beam test of a manufactured 16CH QTC discriminator, FDI GeVγ-1370, is presented.

§1. Introduction

To use a charge-integrating analog-to-digital converter (ADC or QDC), each analog signal should be delayed with a long coaxial cable so that the analog signal starts after the gate signal opens. The number of channels to be measured in nuclear physics experiments is increasing, and the trigger logic becomes more complicated and requires a longer delay for each analog signal. Nowadays, we can easily use multi-hit TDC modules, which can record both the leading and trailing edges of logic signals, such as CAEN V1190 and V1290. A charge-to-time converting (QTC) leading-edge discriminator, which outputs the logic signal with a width giving the charge integration of an input signal, can remove QDC modules. We have developed QTC discriminator for fast plastic-scintillator signals to monitor the gain and to obtain the pulse-height time-walk corrected timing. A test of a prototype 1CH QTC discriminator, Fuji Diamond International Co. Ltd. (FDI) 1370, is reported in the previous annual report. Here, a beam test of a manufactured 16CH QTC discriminator, FDI GeVγ-1370, is presented.

§2. Experimental setup

The time resolution was measured for a plastic scintillator (PS) (ELJEN Technology EJ-212) with a size of 20 mm (W) × 30 mm (H) × 30 mm (T) at the electron beamline for testing detectors [2, 3] at the Research Center for Electron Photon Science (ELPH), Tohoku University. The PS was connected to two photo-multiplier tubes (PMTs), Hamamatsu Photonics H6410. The PS was located at 5.9 m downstream of the center of $\mathcal{R}$TAGX to reduce the effect of its fringing field. In front of the PS, two scintillating fibers (SciFis) with a cross-section of 3×3 mm^2 were placed in a plus form to determine the impact position of the electrons. The distance between the SciFis and PS was approximately 55 mm. Each SciFi was connected to a PMT, Hamamatsu Photonics R4125G. Figure 1 shows the experimental setup for the time resolution measurement.

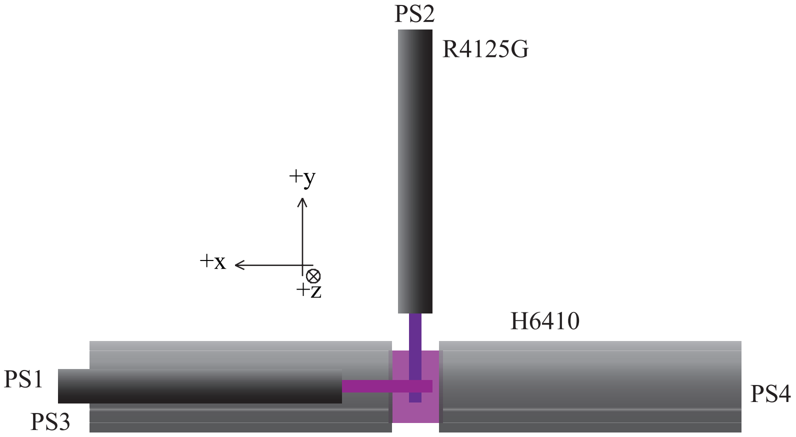

Fig.1. Experimental setup. The upstream two SciFis are used to determine the incident position of the electron beam. The downstream PS measures 20, 30, and 30 mm in width, height, and thickness, respectively. The connected PSs are R4125Gs and H6410 for two SciFis and PS, respectively.

An output analog signal from each PMT was delivered to the VME based data acquisition (DAQ) system located in the GeV-γ counting room through a 50 m 3D-FB coaxial cabel. Each signal was divided into two, and one was input to a charge-integrating ADC module, REPIC RPV-171, through a 200 ns cable delay. The other was input to a QTC discriminator after the attenuation (0–14 dB). The NIM output of the QTC discriminator was input to a multi-hit TDC module, CANE V1290N. The 1/83 prescaled RF signal (500.14 MHz) was also input to V1290N. Figure 2 shows the circuit diagram for the time resolution measurement. The trigger of DAQ was a logic OR between a coincidence signal of the two SciFi signals and 100 Hz clock signal, and was made by an FPGA-based logic module, MPLM4X [4, 5]. The gate width for RPV-171 was 100 ns, and readout from the RPV-171 and V1290 was made 10 μs after the trigger formation.

The measurement was carried out from 14 to 15 in May 2015. After the adjustment of the attenuation factors and supplied voltages and so on, three runs (`run00078`, `00080`, and `00081`) were acquired. The numbers of events collected were 199999, 107187, and 94859, and those of the clock-triggered events were 169979, 92399, and 82255 for `run00078`, `00080`, and `00081`, respectively. The $\mathcal{R}$TAGX current is set to 375 A corresponding the electron momentum of 707 MeV/c. The 200-μm thick W converter was used for producing the electron beam. The singles rates for the upstream and downstream SciFis were 0.4 and 1.7 kHz, and those for the PS signals were 2.8 and 2.8 kHz. The rate was 130 Hz for the coincidence signals of the two SciFis.

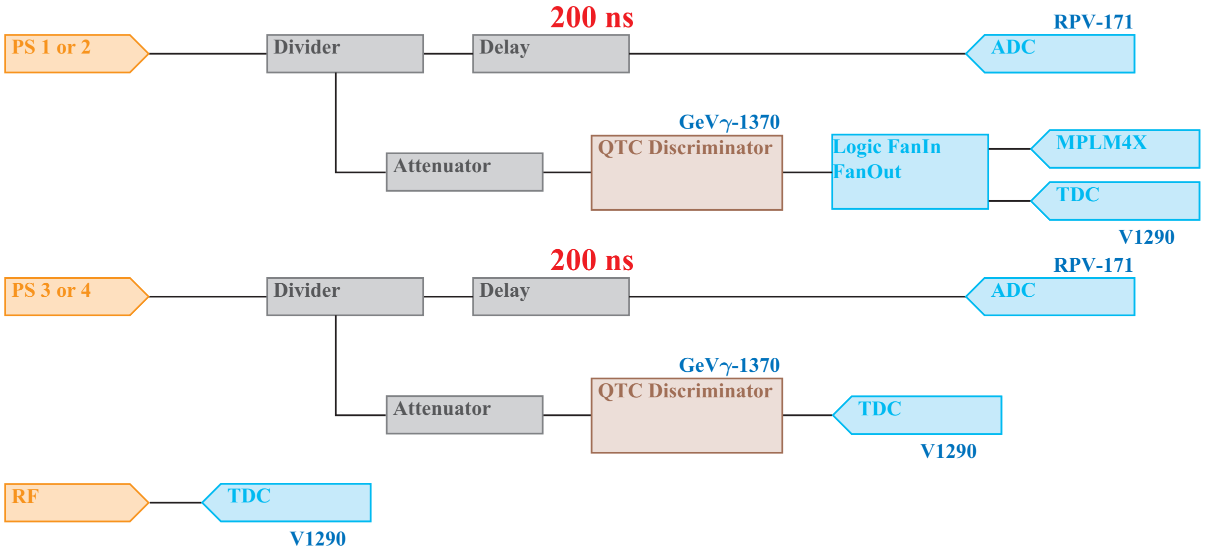

Fig.2. Circuit diagram for the time resolution measurement. Each signal is divided into two, and one is input to an RPV-171 ADC module through a 200 ns cable delay. The other is input to a QTC discriminator after the attenuation. The NIM output of the QTC discriminator is input to a V1290N multi-hit TDC module. The 1/83 prescaled RF signal (500.14 MHz) is also input to V1290N. The trigger of DAQ is handled with the MPLM4X logic module.

§3. Time resolution

The pedestal of each signal is described in subsection 3.1. The measured charge integration is discussed in subsection 3.2, here the correlation between the charge integration and QTC output width is given. The measured timings corrected by the charge integration and QTC output width are presented in subsections 3.3 and 3.4, respectively. Finally, the time fluctuation of the delivered RF signal is discussed in subsection 3.5.

3.1 Pedestal

The pedestal distribution corresponding to the zero energy distribution was estimated for each channel for each run by selecting the events in which any TDC values were recorded for two SciFi and two PS signals. Figure 3 shows the typical pedestal distributions for 4 signals. The width of the upstream SciFi signal was very broad. A horizontally placed R1425G PMT was often affected by a noise probably due to the fringing field of the $\mathcal{R}$TAGX magnet.

The centroid and width of the pedestal distribution for each channel for each run were given by the average and standard deviation of the distribution. The evaluation of the average and standard deviation was made in the range $[\mu - 10 \text{ channel}, \mu + 10 \text{ channel})$ five times, and the final values were used. Figure 4 shows the centroid and width as a function of the run number for each signal. The centroids and widths for all the signals were stable during all the measurements.

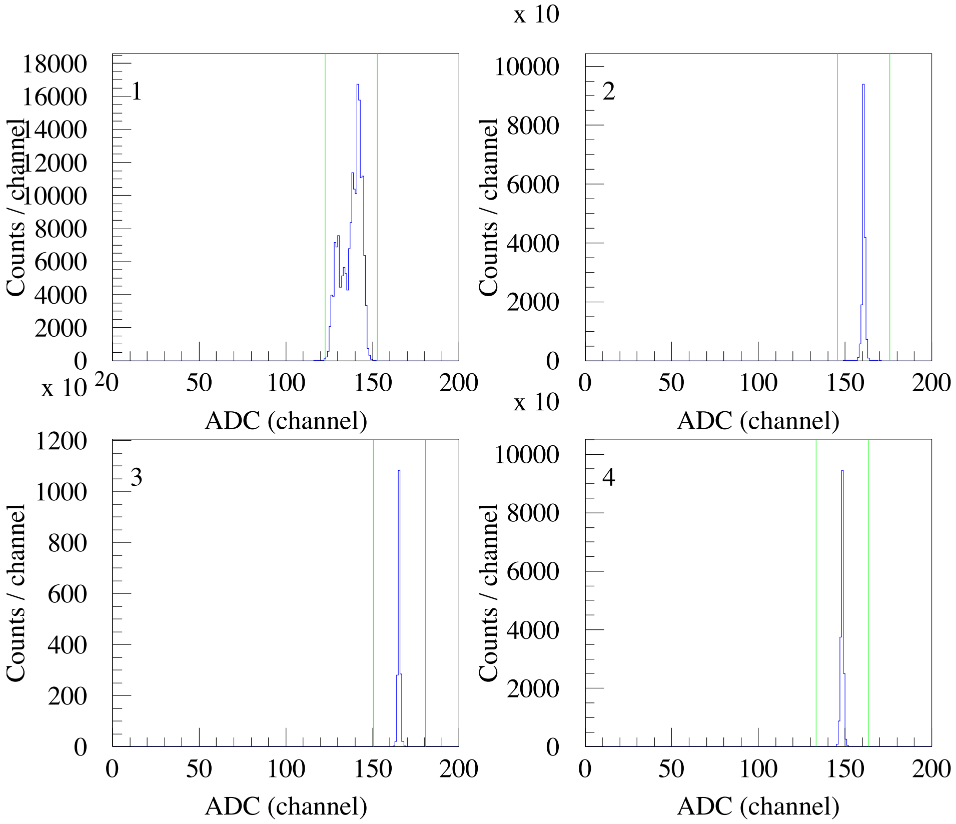

Fig.3. Typical pedestal distributions for 4 signals (`run00078`). The signal is described in each panel, PS 1 and 2 denote the two SciFi signals, and PS 3 and 4 denote the two PS signals. The vertical lines show the boundaries for evaluating the centroids and widths.

3.2 Charge integration and QTC output width

The charge integration Q_i for i-th channel was determined by an equation:

$$Q_i = \alpha_Q \left(A_i - \mu_i \right), \tag{1}$$

where μ_i stands for the centroid of the corresponding pedestal distribution. The $\alpha_Q = 0.25$ pC/channel (catalog value) is the channel-to-charge converting coefficient. The events were selected in which both the leading- and trailing edge TDC values were recorded for two SciFi and two PS signals. Figure 5 shows the measured charge distributions for 4 signals. Together with the measured charge distributions for all the events, those are shown for the events in which the corresponding leading-edge TDC value is recorded, and for the events in which all the leading-edge values are recorded in the four signals. Except for the charge distribution for the upstream SciFi signal, the charge distributions have a peak at 0 for the events n which the corresponding leading-edge TDC value is recorded. This suggests that the discriminator threshold is too low to exclude the dark current events. Anyway the penetration condition is clearly obtained by selecting the events in which all the leading-edge values are recorded in the four signals.

Next, the correlation between the measured charge integration and QTC output width was investigated for each channel. Here, the events were selected in which all the leading- and trailing-edge values

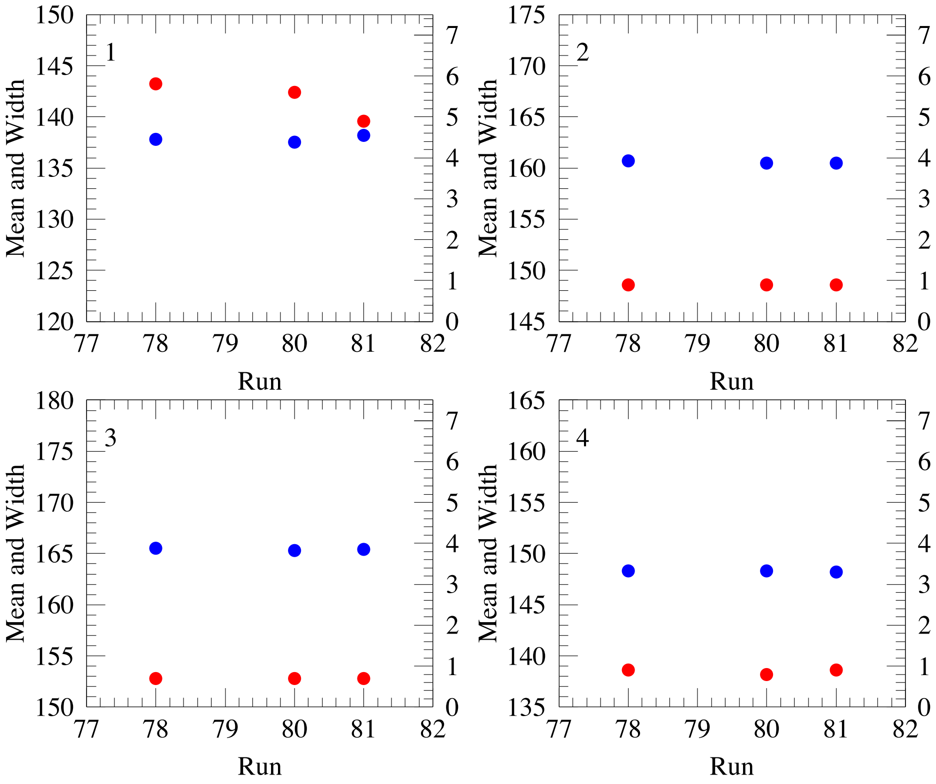

Fig.4. Centroid and width as a function of the run number for each signal. The signal is described in each panel, PS 1 and 2 denote the two SciFi signals, and PS 3 and 4 denote the two PS signals. The blue and red markers represent the centroid and width referring the left and right axes, respectively.

are recorded in the four signals. Figure 6 shows the correlations for 4 signals between the measured charge integration and QTC output width. The measured TDC value was corrected according to its least significant 10 bits (V1290N S/N 247) [6]. The output width was given by the difference of the TDC values corresponding to the leading- and trailing-edges. To avoid the bit rotation effects, the negative difference was corrected by adding 2 × 1024 × 1024 channels. The coefficient 24.4138 ps/channel was multiplied to the width to convert the channel to time taking into account the fact that the interval of the 1/83 prescaled 500.14 MHz RF signal was 6797.531 channels, which is discussed below in subsection 3.5). Two SciFi signals have a good linearity between the charge integration and QTC output width in the whole region. While the two PS signals lose a linearity when the input charge to the QTC discriminator exceeds 20 pC, here it should be noted that the attenuation factor for two PS signals were 14 and 9dB. The output width was shorter than expected in such case. The correlation as shown in Fig,ure 6 was assumed to be expressed as

$$W_i = f_i^W(Q_i) = a_Q Q_i + b_Q Q_i^2 \tag{2}$$

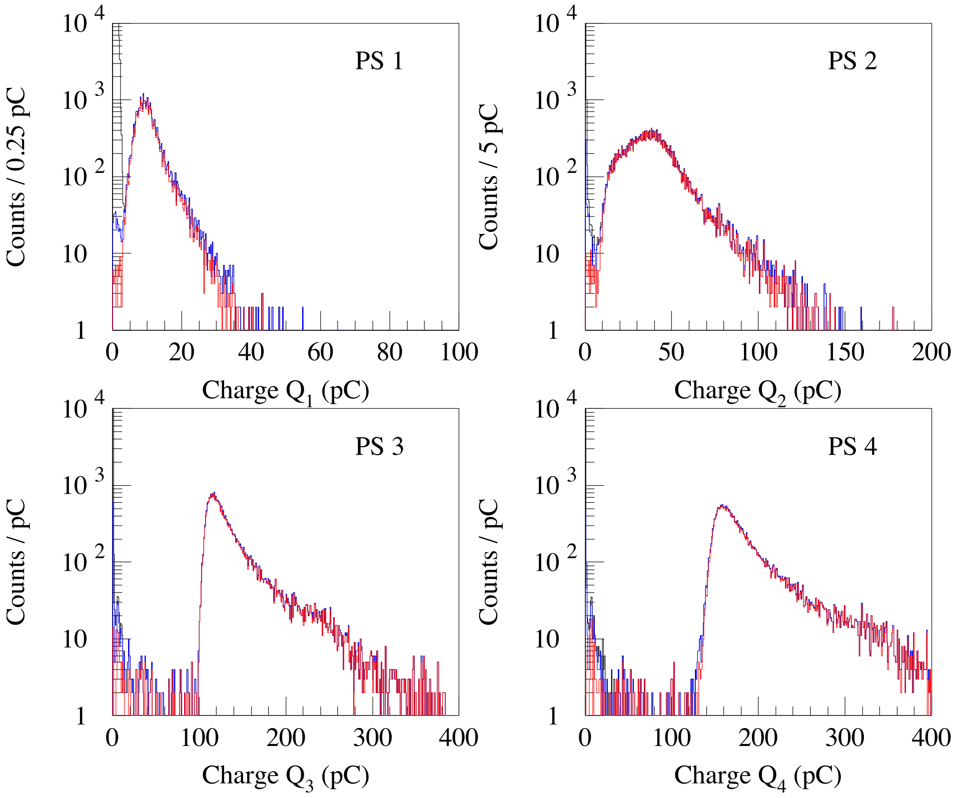

Fig.5. Measured charge distributions for 4 singlas (`run00078`). The signal is described in each panel, PS 1 and 2 denote the two SciFi signals, and PS 3 and 4 denote the two PS signals. The black, blue, and red histograms represent the charge distributions for all the events, for the events in which the corresponding leading-edge TDC value is recorded, and for the events in which all the leading-edge values are recorded in the four signals, respectively.

where W_i stands for the QTC output width and Q_i denotes the charge integration for each channel. The obtained parameters a_Q and b_Q by fitting the equation (2) to the data were

$$(a_Q, b_Q) = \begin{cases} \left(17.902(0)\ \mathrm{ns/pC}, -0.021880(29)\ \mathrm{ns/pC^2}\right) & \text{for SciFi 1,} \\ \left(4.689(0)\ \mathrm{ns/pC}, -0.000782(2)\ \mathrm{ns/pC^2}\right) & \text{for SciFi 2,} \\ \left(3.740(0)\ \mathrm{ns/pC}, -0.002418(0)\ \mathrm{ns/pC^2}\right) & \text{for PS 1, and} \\ \left(2.151(0)\ \mathrm{ns/pC}, -0.000620(0)\ \mathrm{ns/pC^2}\right) & \text{for PS 2.} \end{cases} \tag{3}$$

Here, the fitting procedure was made run by run for each channel, and the parameter was obtained by averaging the fitting parameters for different runs.

The fluctuation of the QTC output width for each channel was estimated. Here, the residual of the width δW was given as a difference between the measured width and evaluated width from the charge integration:

$$\delta W = W_i - f_i^W(Q_i) \tag{4}$$

assuming the equations (2) and (3). The widths of the residuals are broad for two SciFi signals, and those are narrow for two PS signals. The centroid μ_W and width σ_W were obtained by fitting the Gaussian function to each residual distribution. The fitting procedure was repeated five times in the

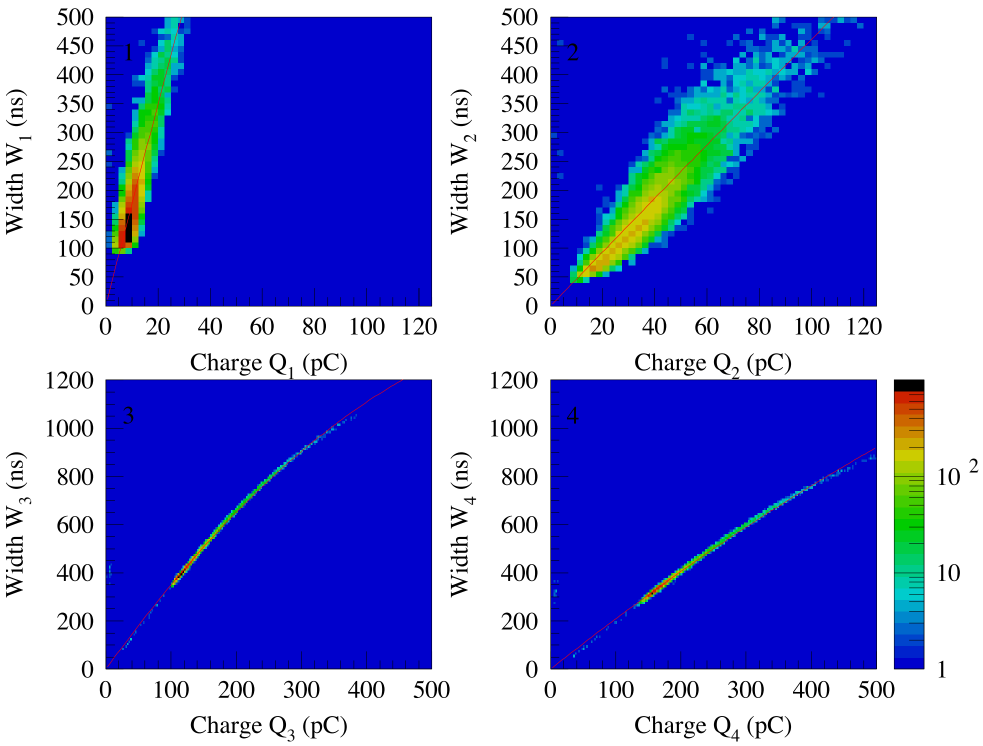

Fig.6. Correlations between the charge integration and QTC output width for 4 signals (`run00078`). The signal is described in each panel, PS 1 and 2 denote the two SciFi signals, and PS 3 and 4 denote the two PS signals. The red curves show the fitted functions expressed in Eq. (2).

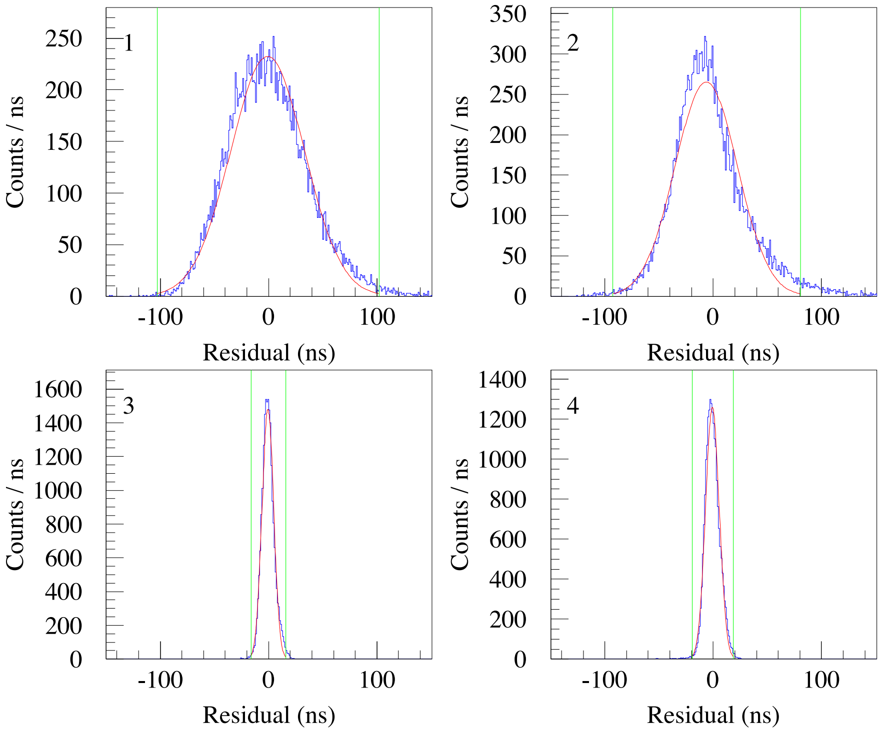

Fig.7. Fluctuations of the QTC output width for 4 signals (`run00078`). The signal is described in each panel, PS 1 and 2 denote the two SciFi signals, and PS 3 and 4 denote the two PS signals. The red curve shows the fitted Gaussian in each panel. The vertical green lines show the boundaries for the fitting regions.

range $[\mu_W - 2\sigma_W, \mu_W + 2\sigma_W)$, and the final values were adopted. Table 1 summarizes the centroid μ_W and width σ_W for each signal for each run.

Table 1. Centroid μ_W and width σ_W for each signal for each run by fitting a Gaussian function to the residual distribution for the QTC output width.

鏡緒申鏡緒申	PS 3		PS 4		PS 3		PS 4	
	μ_W (ns)	σ_W (ns)	μ_W (ns)	σ_W (ns)	μ_W (ns)	σ_W (ns)	μ_W (ns)	σ_W (ns)
`00078`	$-0.9(2)$	$34.0(1)$	$-6.4(2)$	$28.8(2)$	$-0.6(0)$	$5.3(0)$	$-0.7(0)$	$6.3(0)$
`00080`	$+0.6(3)$	$33.9(2)$	$-5.6(3)$	$28.6(2)$	$-0.7(0)$	$5.3(0)$	$-0.6(0)$	$6.3(0)$
`00081`	$+0.0(3)$	$32.5(2)$	$-5.6(3)$	$28.7(3)$	$-0.7(0)$	$5.2(0)$	$+0.1(0)$	$6.3(0)$

3.3 Measured timing corrected by the charge integration

The QTC discriminator is a kind of leading-edge discriminators. The leading-edge timing is delayed from the actual response timing according to the pulse-height of the input signal. The large pulse is likely to respond earlier because the time interval is shorter between the response and exceeding over the threshold. This effect is often called pulse-height time-walk (PHTW). Here, the PHTW-corrected timing is discussed using the charge integration. As same as subsection 3.2, the events were selected in which both the leading- and trailing edge TDC values were recorded for two SciFi and two PS signals.

At the first stage, the time difference of two PS responses was estimated without any PHTW correction. Figure 8 shows the time difference of two PS responses. The PHTW effect is more or less canceled in the time difference of two PS responses since the charge integration in a PS signal is larger when that in the other PS becomes is large. The width of the time difference σ_t is as small as 78 ± 1 ps (`run00078`), 77 ± 1 ps (`run00080`), and 77 ± 1 ps (`run00081`) even when the timing is evaluated without any PHTW correction. Here, σ_ts was given by fitting a Gaussian function to the time difference distribution in the range $[\mu_t - 2\sigma_t, \mu + 2\sigma_t)$ where μ_t denotes the centroid of the distribution. The fitting procedure was repeated five times, and the final values were adopted. The μ_ts obtained wer 904 ± 1 ps for all the runs.

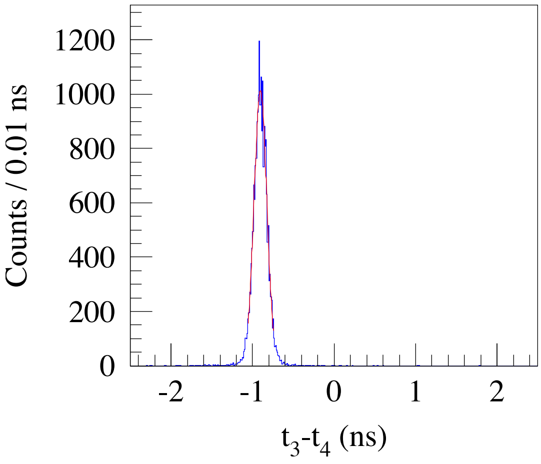

Fig.8. Time difference of two PS responses (`run00078`). Here, the timing is given without any PHTW correction. The red curve shows the fitted Gaussian function.

To get the PHTW behavior for the two PS signals, the time interval was investigated between a PS timing and an average timing of two latest RF signals. The average timing of two latest RF signals was calculated in the following way:

1. the time interval of the 1/83 prescaled RF signal was determined,
2. the first 1/83 prescaled RF signal timing was calculated using time interval (bit rotation was correctly taken into account),
3. the average of all the first 1/83 prescaled RF signal timings determined in 2 was determined (standard RF timing), and
4. the time interval between the standard RF signal and the average of two PS response timings was determined in a unit of half period of the RF signal.

Figure 9 shows the correlation between the response timing of a PS signal and the charge integration. Here, the response timing is given in the elapsed time from the average timing of two latest RF signals, and the response timing is given without any PHTW correction. Two loci are observed because the average of the two PS signal timings are not correctly determined.

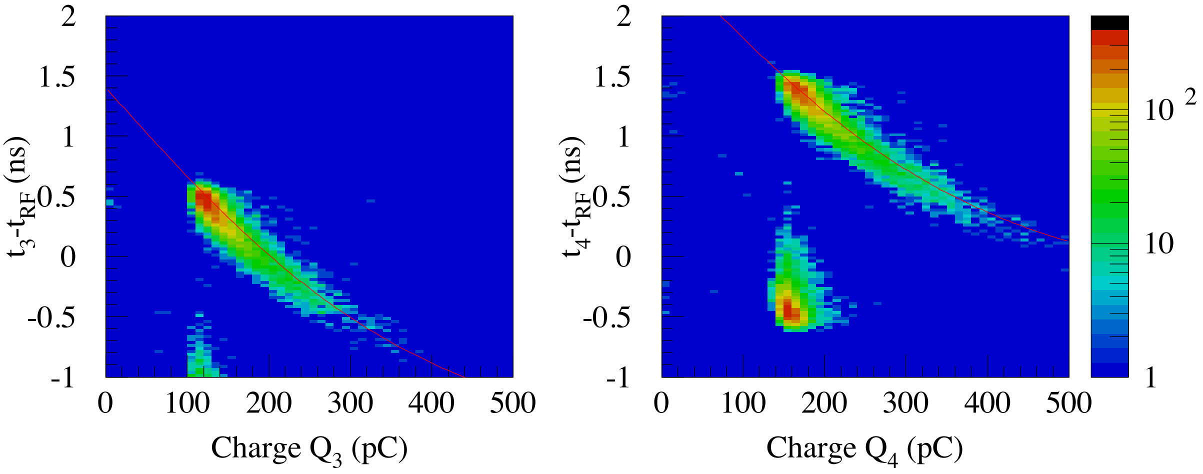

Fig.9. Correlation between the response timing of a PS signal and the charge integration (`run00078`). The left panel shows that for the first PS signal (PS3), and the right shows that for the second PS signal (PS4). Here, the response timing is given in the elapsed time from the average timing of two latest RF signals, and the response timing is given without any PHTW correction. The data are compared with the equation (5) with parameters (6).

The PHTW function is assumed to be expressed by a function of the charge integration Q_i

$$t_i - t_{\mathrm{RF}} = f^i_{\mathrm{PHTW}}(Q_i) = t^i_0 - \alpha_i \tanh\left(\beta_i Q_i\right), \tag{5}$$

where $t_i - t_{\mathrm{RF}}$ denotes the response timing (the elapsed time from the average timing of two latest RF signals). The initial parameters were determined by hand:

$$(t^i_0, \alpha_i, \beta_i) = \begin{cases} (1.4\ \mathrm{ns}, 3.0\ \mathrm{ns}, 0.0025\ \mathrm{pC}^{-1})\ \text{for PS3, and} \\ (2.5\ \mathrm{ns}, 2.8\ \mathrm{ns}, 0.0025\ \mathrm{pC}^{-1})\ \text{for PS4.} \end{cases} \tag{6}$$

The PHTW functions were also superimposed in Figure 9. It should be noted that the first and second

PS signals are described as PS3 and PS4 in all the figures. In the next step, the measured timing t_i was given using a PHTW correction:

$$t_i \leftarrow t_i - f^i_{\mathrm{PHTW}}(Q_i). \tag{7}$$

The elapsed time from the average timing of two latest RF signals was estimated again, the latest RF signal timings were obtained using the average of the PHTW corrected timings for the two PS signals. Figure 10 shows the re-estimated correlation between the response timing of a PS signal and the charge integration. Only a locus is observed because the average of the two PS signal timings is correctly determined. By fitting a function expressed in Eq. (5) to the data, the following parameters were obtained:

$$(t^i_0, \alpha_i, \beta_i) = \begin{cases} (1.577 \pm 0.042\ \mathrm{ns}, 2.741 \pm 0.066\ \mathrm{ns}, 0.00324 \pm 0.00016\ \mathrm{pC}^{-1}) \text{ for PS3, and} \\ (2.681 \pm 0.051\ \mathrm{ns}, 3.128 \pm 0.059\ \mathrm{ns}, 0.00249 \pm 0.00011\ \mathrm{pC}^{-1}) \text{ for PS4.} \end{cases} \tag{8}$$

Here, the parameters are obtained by averaging those for the three runs.

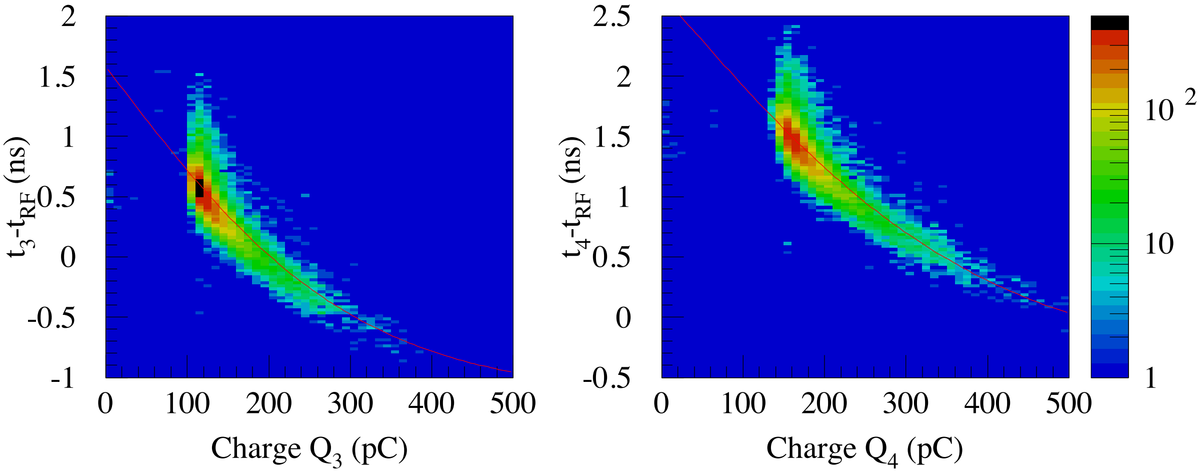

Fig.10. Re-estimated correlation between the response timing of a PS signal and the charge integration (`run00078`). The left panel shows that for the first PS signal (PS3), and the right shows that for the second PS signal (PS4). Here, the response timing is given in the elapsed time from the average timing of two latest RF signals, and the response timing is given without any PHTW correction. The data are compared with the equation (5) with parameters (8).

The initial PHTW functions may not well reproduce the average of the latest two RF timings. Thus, the elapsed time from the average timing of two latest RF signals was re-calculated using parameter expressed in Eq. (8), and the response timing was given without any PHTW correction. Figure 11 shows the second re-estimated correlation between the response timing of a PS signal and the charge integration. By fitting a function expressed in Eq. (5) to the data, the following parameters were obtained:

$$(t^i_0, \alpha_i, \beta_i) = \begin{cases} (1.842 \pm 0.067\ \mathrm{ns}, 2.644 \pm 0.052\ \mathrm{ns}, 0.00446 \pm 0.00026\ \mathrm{pC}^{-1}) \text{ for PS3, and} \\ (2.911 \pm 0.062\ \mathrm{ns}, 3.036 \pm 0.052\ \mathrm{ns}, 0.00314 \pm 0.00015\ \mathrm{pC}^{-1}) \text{ for PS4.} \end{cases} \tag{9}$$

Here, the parameters are also obtained by averaging those for the three runs.

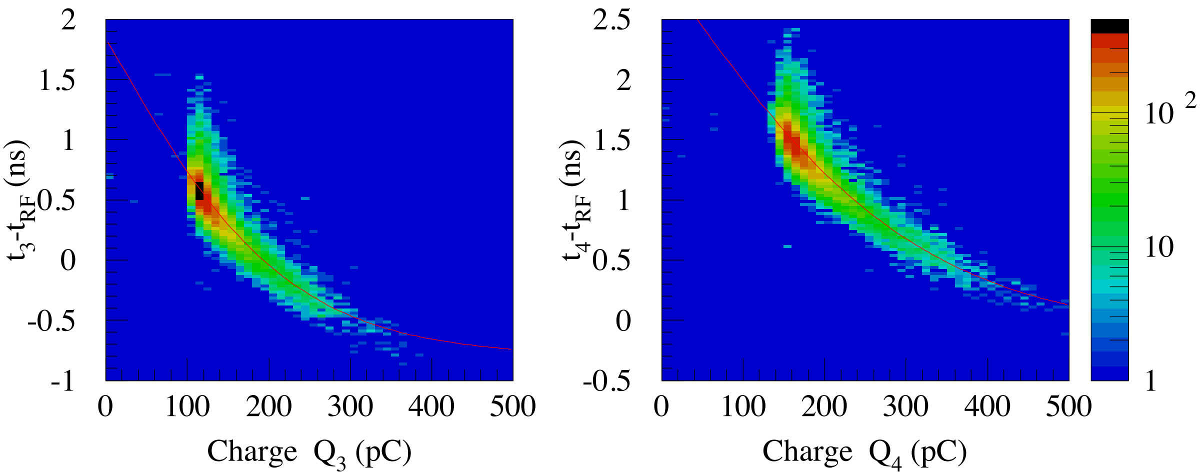

Fig.11. Second re-estimated correlation between the response timing of a PS signal and the charge integration (`run00078`). The left panel shows that for the first PS signal (PS3), and the right shows that for the second PS signal (PS4). Here, the response timing is given in the elapsed time from the average timing of two latest RF signals, and the response timing is given without any PHTW correction. The data are compared with the equation (5) with parameters (9).

The PHTW-corrected timings were obtained using the final parameters expressed in Eq. (9), and the time difference distribution between the PHTW-corrected PS3 and PS4 timings were estimated. Figure 12 shows the time difference distribution between the PHTW-corrected PS3 and PS4 timings. The centroid μ_t^{34} and width σ_t^{34} were obtained fitting a Gaussian function to the distribution in the range $[\mu_t^{34} - 2\sigma_t^{34}, \mu_t^{34} + 2\sigma_t^{34})$. The fitting procedure was repeated five times, and the final values were adopted. The parameters obtained were

$$(\mu_t^{34}, \sigma_t^{34}) = \begin{cases} (-2.4 \pm 0.5, 60.3 \pm 0.5) \text{ ps for } \texttt{run00078}, \\ (-1.1 \pm 0.7, 59.8 \pm 0.7) \text{ ps for } \texttt{run00080}, \text{ and} \\ (+3.0 \pm 0.7, 58.7 \pm 0.7) \text{ ps for } \texttt{run00081}. \end{cases} \tag{10}$$

The centroid is approximately 0 for all the runs, and the average width was 59.8 ± 0.3 ps. If the time resolutions are common for the PS3 and PS4 signals, the time resolution is thought to be 42.3 ps.

Next, the elapsed time distribution of the PS 3 (PS 4) signal from the lated RF signal. Here, the response timing of the PS 3 (PS 4) signal is given using the PHTW correction with the parameters expressed in Eq. (9), Figure 13 shows the elapsed time distribution of the PS 3 (PS 4) signal from the lated RF signal. The centroid μ_t^3 (μ_t^4) and width σ_t^3 (σ_t^4) were determined by fitting a Gaussian function to the distribution. The fitting process was repeated five times in the range $[\mu_t^3 - 2\sigma_t^3, \mu_t^3 + 2\sigma_t^3)$ and $[\mu_t^4 - 2\sigma_t^4, \mu_t^4 + 2\sigma_t^4)$, and we adopted the final values. The obtained parameters μ_t^3, σ_t^3, μ_t^4, and σ_t^4 were

$$(\mu_t^3, \sigma_t^3, \mu_t^4, \sigma_t^4) = \begin{cases} (-23.3 \pm 0.8, 99.7 \pm 0.8, -21.9 \pm 0.9, 106.4 \pm 0.9) \text{ ps for } \texttt{run00078}, \\ (-25.3 \pm 1.2, 101.1 \pm 1.2, -25.4 \pm 1.3, 106.5 \pm 1.3) \text{ ps for } \texttt{run00080}, \text{ and} \\ (-22.6 \pm 1.3, 99.8 \pm 1.3, -26.4 \pm 1.4, 103.6 \pm 1.4) \text{ ps for } \texttt{run00081}. \end{cases} \tag{11}$$

The average values of μ_t^3 and μ_t^4 were -23.6 ± 0.6 and -23.8 ± 0.7 ps, respectively. The average values of σ_t^3 and σ_t^4 were 100.1 ± 0.6 and 105.8 ± 0.7 ps, respectively. When the time resolution for the delivered

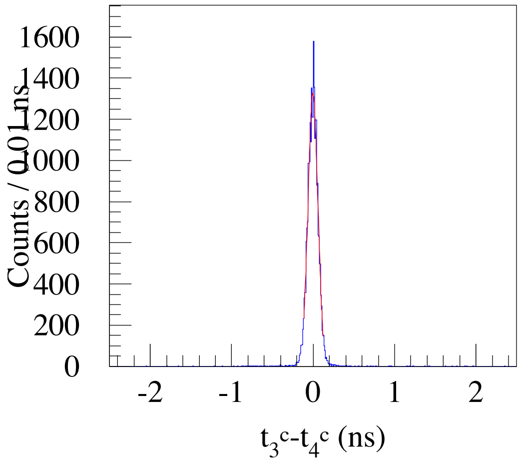

Fig.12. Time difference distribution between the PHTW-corrected PS3 and PS4 timings (`run00078`). The PHTW-corrected timings are obtained using the parameters in Eq. (9).

RF signal is extremely high, the obtained widths σ_t^3 and σ_t^4 are much larger than the approximate time resolution 42.3 ps for PS 3 and PS 4. This inconsistent time resolutions will be discussed below in subsection 3.5.

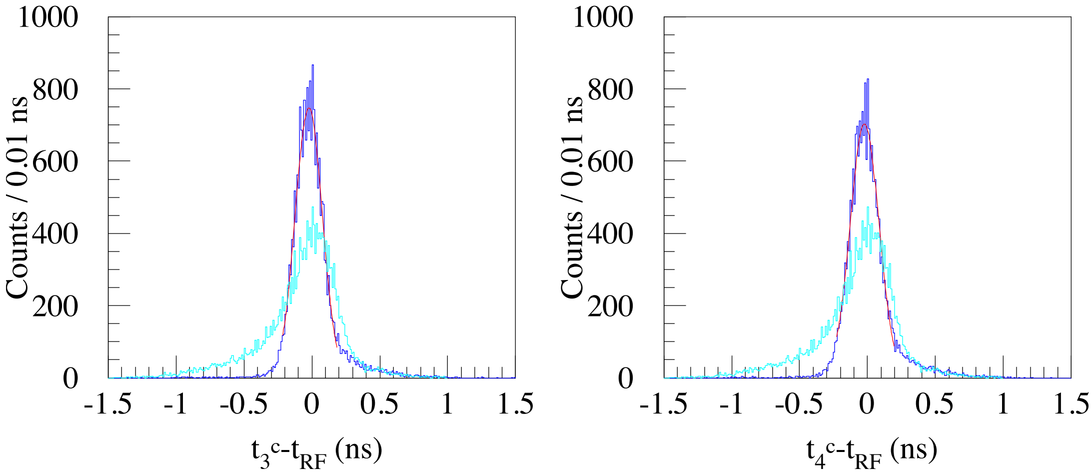

Fig.13. Elapsed time distributions of the PS 3 (left) and PS 4 (right) signal from the lated RF signal (`run00078`). The PHTW-corrected timings with the parameters (9) are used for the response timings of the PS 3 and PS 4 signals. The elapsed time distributions without any PHTW correction are also plotted in cyan.

3.4 Measured timing corrected by the QTC output width

The PHTW-corrected timing using the charge integration is discussed in subsection 3.3. Here, the PHTW-corrected timing using the QTC output width is discussed in this subsection. At first, the average PHTW-corrected timing of the PS 3 and PS 4 signals are estimated with the parameters expressed in Eq. (9), and the correlation between the response timing of a PS signal and the QTC output width is investigated. Figure 14 shows the correlation between the response timing of a PS signal and the QTC output width. Here, the response timing is given as the elapsed time from the average timing of two latest RF signals estimated without any PHTW correction. To give the PHTW equation as a function of the QTC output width W_i, the PHTW function is assumed to be expressed sa

$$t_i - t_{\mathrm{RF}} = f^i_{\mathrm{PHTW}}(W_i) = t^i_0 - \alpha_i \tanh\left(\beta_i f^Q_i(W_i)\right) \tag{12}$$

where $t_i - t_{\mathrm{RF}}$ denotes the elapsed time from the average timing of two latest RF signals. By fitting a function expressed in Eq. (12) to the data, the following parameters were obtained:

$$(t^i_0, \alpha_i, \beta_i) = \begin{cases} (1.796 \pm 0.062\ \mathrm{ns}, 2.597 \pm 0.081\ \mathrm{ns}, 0.00866 \pm 0.00063\ \mathrm{ns}^{-1}) \text{ for PS3, and} \\ (3.013 \pm 0.066\ \mathrm{ns}, 2.960 \pm 0.057\ \mathrm{ns}, 0.00702 \pm 0.00040\ \mathrm{ns}^{-1}) \text{ for PS4.} \end{cases} \tag{13}$$

Here, the parameters are also obtained by averaging those for the three runs.

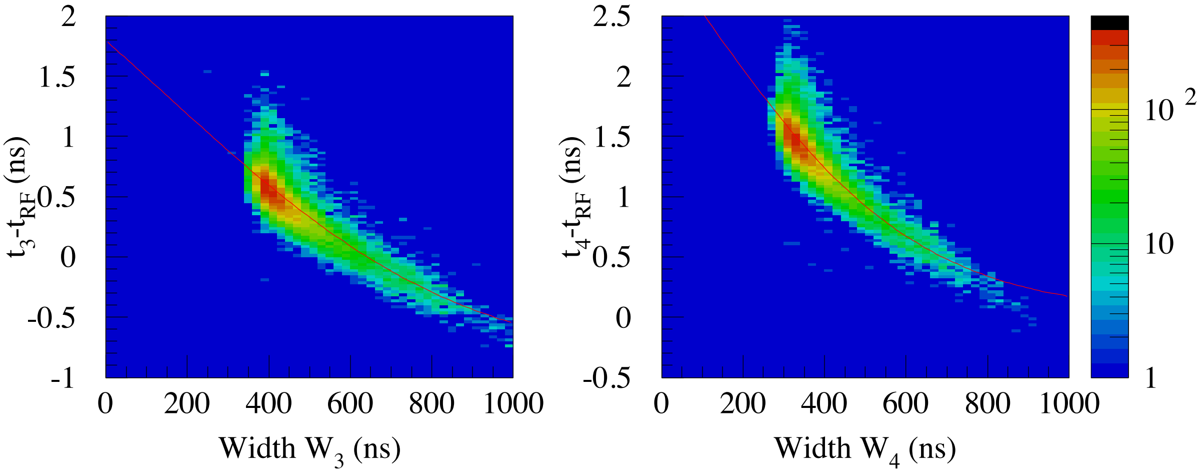

Fig.14. Correlation between the response timing of a PS signal and the QTC output width (`run00078`). Here, the response timing is given as the elapsed time from the average timing of two latest RF signals estimated without any PHTW correction. The red curves show the fitted functions (12). The equation (5) with the parameters (9) is used for the determination of the latest two RF signal timings.

The PHTW-corrected timings were obtained using the final parameters expressed in Eq. (13), and the time difference distribution between the PHTW-corrected PS3 and PS4 timings were estimated. Figure 15 shows the time difference distribution between the PHTW-corrected PS3 and PS4 timings. The centroid μ^{34}_t and width σ^{34}_t were obtained fitting a Gaussian function to the distribution in the range $[\mu^{34}_t - 2\sigma^{34}_t, \mu^{34}_t + 2\sigma^{34}_t)$. The fitting procedure was repeated five times, and the final values were adopted. The parameters obtained were

$$(\mu^{34}_t, \sigma^{34}_t) = \begin{cases} (-6.1 \pm 0.5, 63.6 \pm 0.5)\ \mathrm{ps\ for\ \texttt{run00078}}, \\ (-5.6 \pm 0.7, 63.7 \pm 0.5)\ \mathrm{ps\ for\ \texttt{run00080}},\ \text{and} \\ (-3.9 \pm 0.8, 63.1 \pm 0.7)\ \mathrm{ps\ for\ \texttt{run00081}}. \end{cases} \tag{14}$$

The centroid is approximately 0 for all the runs, and the average width was 63.5 ± 0.3 ps which is a little bit poorer than the obtained value 59.8 ± 0.3 ps in subsection 3.3.

Next, the elapsed time distribution of the PS 3 (PS 4) signal from the lated RF signal. Here, the response timing of the PS 3 (PS 4) signal is given using the PHTW correction with the parameters

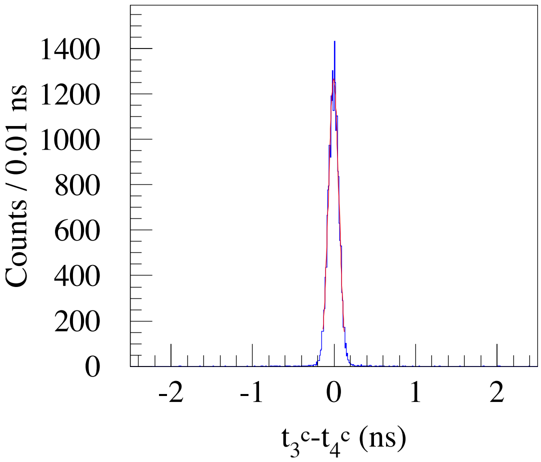

Fig.15. Time difference distribution between the two PS signals (`run00078`). The response timings are calculated by applying the PHTW correction with Eq. (5) with the parameters expressed in Eq. (13).

expressed in Eq. (13), Figure 16 shows the elapsed time distribution of the PS 3 (PS 4) signal from the lated RF signal. The centroid μ_t^3 (μ_t^4) and width σ_t^3 (σ_t^4) were determined by fitting a Gaussian function to the distribution. The fitting process was repeated five times in the range $[\mu_t^3 - 2\sigma_t^3, \mu_t^3 + 2\sigma_t^3)$ and $[\mu_t^4 - 2\sigma_t^4, \mu_t^4 + 2\sigma_t^4)$, and we adopted the final values. The obtained parameters μ_t^3, σ_t^3, μ_t^4, and σ_t^4 were

$$(\mu_t^3, \sigma_t^3, \mu_t^4, \sigma_t^4) = \begin{cases} (-35.2 \pm 0.8, 100.4 \pm 0.8, -30.1 \pm 0.9, 107.7 \pm 0.9) \text{ ps for } \texttt{run00078}, \\ (-38.1 \pm 1.2, 101.9 \pm 1.2, -33.9 \pm 1.3, 107.8 \pm 1.3) \text{ ps for } \texttt{run00080}, \text{ and} \\ (-34.6 \pm 1.3, 100.3 \pm 1.3, -32.7 \pm 1.4, 106.9 \pm 1.4) \text{ ps for } \texttt{run00081}. \end{cases} \quad (15)$$

The average values of μ_t^3 and μ_t^4 were -35.8 ± 0.6 and -31.6 ± 0.7 ps, respectively. The average values of σ_t^3 and σ_t^4 were 100.7 ± 0.6 and 107.6 ± 0.7 ps, respectively. The deviation the centroid from 0 is a little bit larger than that in subsection 3.3, suggesting that the fitting function (12) with the measured QTC output widths is not wors than the function (5) with the measured charge integrations. The obtained values of 100.7 ± 0.6 and 107.6 ± 0.7 ps for σ_t^3 and σ_t^4, however, are consistent with the values 100.1 ± 0.6 and 105.8 ± 0.7 ps obtained in subsection 3.3. This suggests that the QTC output width can be used for the pulse-height time-walk correction instead of the charge integration.

3.5 Delivered RF signals

The PHTW-corrected timings given by the charge integrations are used in this subsection since they are little bit better than those given by the QTC output widths. The time resolution between the PS 3 and PS 4 response timings is 59.8 ± 0.3 ps, that between the PS 3 and the latest RF signals is 101.6 ± 0.6 ps, and that between the PS 4 and the latest RF signals is 105.8 ± 0.7 ps. The time resolution σ_t^{34} between the PS 3 and PS 4 response timings are expressed by the intrinsic time resolutions for PS 3 σ_3 and PS4 σ_4:

$$\left(\sigma_t^{34}\right)^2 = \sigma_3^2 + \sigma_4^2. \quad (16)$$

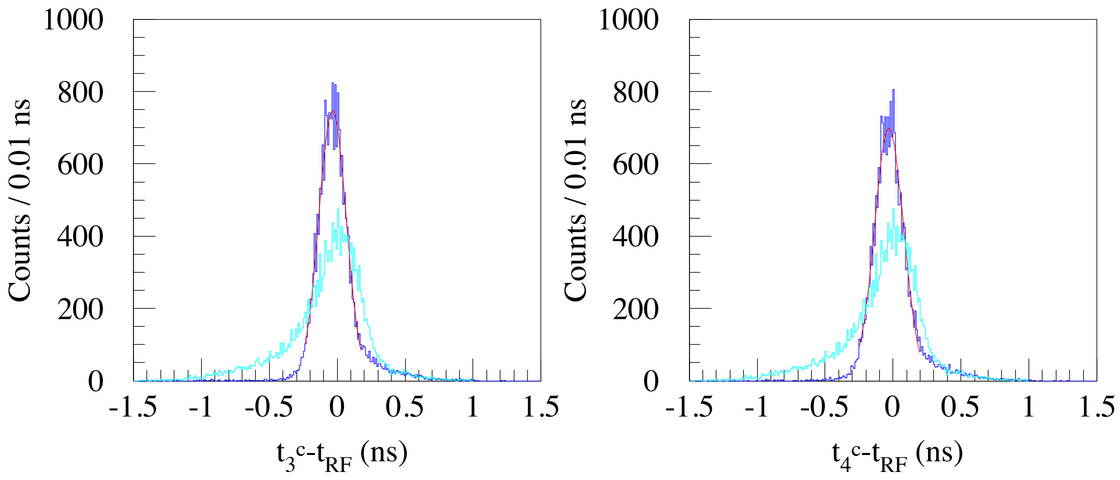

Fig.16. Elapsed time distributions of the PS 3 (left) and PS 4 (right) signal from the lated RF signal (`run00078`). The PHTW-corrected timings with the parameters (13) are used for the response timings of the PS 3 and PS 4 signals. The elapsed time distributions without any PHTW correction are also plotted in cyan.

The time resolution σ_t^3 between between the PS 3 and the latest RF signals is assumed using the intrinsic RF time resolution σ_{RF} as

$$\left(\sigma_t^3\right)^2 = \sigma_3^2 + \sigma_{\mathrm{RF}}^2, \text{ and} \tag{17}$$

the time resolution σ_t^4 between between the PS 4 and the latest RF signals is also assumed as

$$\left(\sigma_t^4\right)^2 = \sigma_4^2 + \sigma_{\mathrm{RF}}^2. \tag{18}$$

By solving the simultaneous three equations, the intrinsic time resolutions are obtained as

$$(\sigma_3, \sigma_4, \sigma_{\mathrm{RF}}) = (36.8, 47.2, 94.7) \text{ ps}. \tag{19}$$

Let consider the elapsed time of the average PHTW-corrected timing between PS3 and PS4 from the latest RF signal. The width of the elapsed time distribution σ_t^{ave} is expressed by

$$(\sigma_t^{\mathrm{ave}})^2 = \frac{1}{4}\left(\sigma_3^2 + \sigma_4^2\right) + \sigma_{\mathrm{RF}}^2, \tag{20}$$

and $\sigma_t^{\mathrm{ave}} = 99.3$ ps is expected. To confirm this, the elapsed time distribution of the average PHTW-corrected timing between PS3 and PS4 from the latest RF signal has been estimated using the parameters expressed in Eq. (9). Figure 17 shows the elapsed time distribution of the average PHTW-corrected timing between PS3 and PS4 from the latest RF signal. The centroid μ_t^{ave} and width σ_t^{ave} are determined by fitting a Gaussian function to the distribution in the range $[\mu_t^{\mathrm{ave}} - 2\sigma_t^{\mathrm{ave}}, \mu_t^{\mathrm{ave}} + 2\sigma_t^{\mathrm{ave}})$. The fitting procedure has been repeated five times, and we have adopted the final values. The parameters μ_t^{ave} and σ_t^{ave} obtained are

$$(\mu_t^{\mathrm{ave}}, \sigma_t^{\mathrm{ave}}) = \begin{cases} (-23.8 \pm 0.8, 97.0 \pm 0.8) \text{ ps for } \texttt{run00078}, \\ (-25.4 \pm 1.2, 98.1 \pm 1.2) \text{ ps for } \texttt{run00080}, \text{ and} \\ (-25.0 \pm 1.2, 96.0 \pm 1.2) \text{ ps for } \texttt{run00081}. \end{cases} \tag{21}$$

The average width is 97.0 ± 0.6 ps, and is consistent with the expected value 99.3 ps. When the obtained value of 97.0 ± 0.6 ps is treated as a measured one, and the intrinsic time resolutions are estimated again from the four measured widths:

$$(\sigma_3, \sigma_4, \sigma_{\rm RF}) = (37.2 \pm 1.3, 46.8 \pm 1.0, 93.7 \pm 0.4)\ \text{ps}. \tag{22}$$

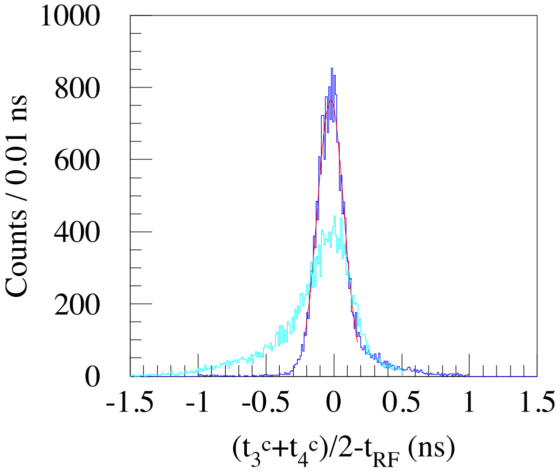

Fig.17. Elapsed time distribution of the average PHTW-corrected timing between PS3 and PS4 from the latest RF signal. The red curve shows the fitted Gaussian function. The elapsed time distribution of the average timing between PS3 and PS4 without any PHTW correction from the latest RF signal is also plotted in cyan.

The reason why the intrinsic time resolution for the RF signal is poor as 93.7 ± 0.4 ps is investigated. The 1/83 prescaled RF signal was recorded 37–38 times event by event. The average μ_{83} and standard deviation σ_{83} of the time interval was calculated for every event. Figure 18 shows the average μ_{83} and standard deviation σ_{83} of the time interval of the 1/83 prescaled RF signal. The centroid and width are given fitting a Gaussian function to the distributions. The fitting procedure is made fiver times in the range $[\mu - 3\sigma, \mu + 3\sigma)$, and we have adopted the final values. The centroid of the μ_{83} distribution is 6797.531 ± 0.000 channel, and its width is 0.036 ± 0.000 channel for `run00078`. The centroid of the σ_{83} distribution is 1.162 ± 0.001channel, and its width is 0.157 ± 0.001 channel. The errors of the centroids and widths in `run00080` and `00081` are larger than those in `run0078`, but the parameters in `run00080` and `00081` are consistent with those in `run0078`. Because the time interval 6797.531 ± 0.000 channel corresponds to the time $83 \times (500.14\ \text{MHz})^{-1}$, the time-to-channel coefficient is found to be 24.414 ps/channel for the TDC values in the V1290N used. The fluctuation of μ_{83} is 0.036 channel, and σ_{84} is 1.162 ± 0.157 channel. The time resolution for the measurement of the delivered RF timings is from 1 to 2 channels. Since the RF timings are recorded 37–38 times for each event, the precision of the standard RF timing determination is thought to be 0.17–0.35 channels corresponding to 4–8 ps.

The time resolution for the delivered RF signal is 4–8 ps, thus the obtained value $\sigma_{\rm RF} = 93.7$ ps is thought to be the bunch length including the timing fluctuation in the Booster STorage (BST) ring [7]. The equilibrium bunch length σ_t at high energies is expressed by

$$\sigma_t = \frac{\alpha_p}{2\pi f_s} \frac{\sigma_E}{E} = 91.7\ \text{ps}, \tag{23}$$

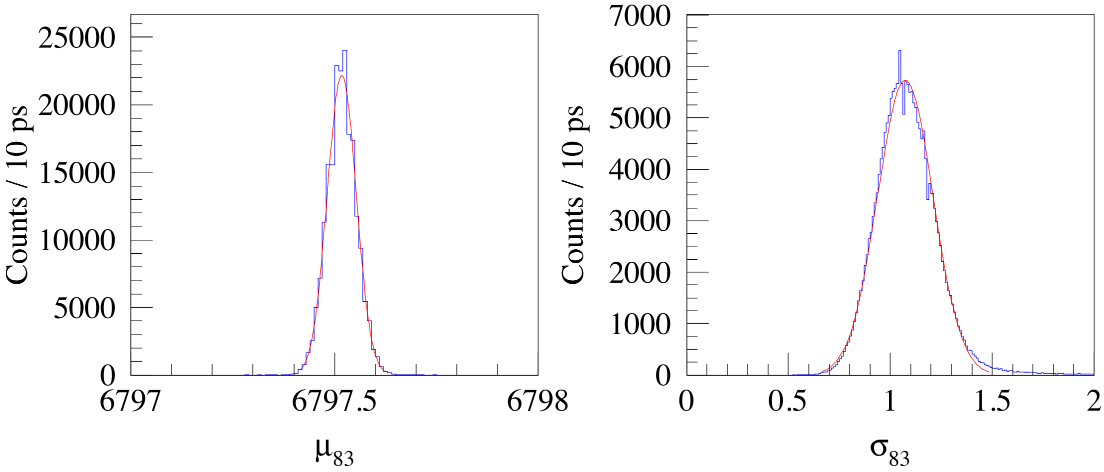

Fig.18. The average μ_{83} and standard deviation σ_{83} distributions for the time interval of the 1/83 prescaled RF signal. The red curves show the fitted Gaussian functions.

where $\alpha_p = 0.0486$ stands for the momentum compaction factor, $f_s = 53$ kHz denotes the synchrotron frequency, and $\sigma_E/E = 6.28 \times 10^{-4}$ is equilibrium energy spread [8]. The obtained value of $\sigma_{\mathrm{RF}} = 93.7 \pm 0.4$ ps is consistent with the expected bunch length of 91.7 ps.

§4. Summary

The performance of the developed QTC discriminator has been investigated measuring the time resolution of the 30-mm-thick plastic scintillator in response to the 707 MeV/c electron beam at ELPH. The timings are determined by applying pulse-height time-walk correction. The time resolutions agree well between when we used the correction functions as a function of the charge Q_i and when we used those as a function of the QTC output width W_i. This suggests that the developed QTC discriminator works well for applying the pulse-height time-walk correction in the timing measurement. The bunch length including the timing fluctuation in the Booster STorage ring is found to be 93.7 ± 0.4 ps. It is difficult to use the RF signal as a start timing of the time of flight measurement in the present condition.

Acknowledgments

The authors would like to thank the ELPH accelerator staff for providing the stable primary electron beam. They deeply appreciate Y. Takeda and T. Takeda (Fuji Diamond International Co. Ltd.) for their cooperation of the development and manufacture of the QTC discriminator modules. This work was supported in part by Grants-in-Aid for Scientific Research (A) (24244022), and for Scientific Research (C) (26400287).

References

[1] T. Ishikawa: ELPH Annual Report 2014, Tohoku University, 113 (2015).

[2] T. Ishikawa *et al.*: Research Report of LNS, Tohoku University, **40**, 6 (2007).

[3] T. Ishikawa *et al.*: Nuclear Instruments and Methods in Physics Research Section A **694**, 348 (2012).

[4] T. Ishikawa *et al.*: Nuclear Instruments and Methods in Physics Research Section A **811**, 124 (2016).

[5] I. Nagasawa and T. Ishikawa: Internal GeV-γ Analysis Note HD No. **380**$\mathcal{C}$, (2015).

[6] T. Ishikawa: Internal GeV-γ Analysis Note HD No. **379**$\mathcal{C}$, (2015).

[7] F. Hinode *et al.*: Proceedings of 11th International Conference on Synchrotron Radiation Instrumentation (SRI2012), Journal of Physics: Conference Series 425 (2013) 072011.

[8] F. Hinode and T. Muto: private communication.

(ELPH Experiment : #2809)

Development of a compact photon-beam profile monitor

S. Kido[1], T. Ishikawa[1], Y. Honda[1], H. Kanda[2], Y. Matsumura[1], M. Miyabe[1],
I. Nagasawa[1], H. Shimizu[1], and Y. Tsuchikawa[1]

[1]*Research Center for Electron Photon Science (ELPH), Tohoku University, Sendai 982-0826, Japan*
[2]*Department of Physics, Tohoku University, Sendai 980-8578, Japan*

§1. Introduction

We have been conducting the meson photoproduction experiments for baryon spectroscopy at the Research Center for Electron Photon Science (ELPH), Tohoku University [1]. The energy-tagged photon beams are used; an internal radiator produces a bremsstrahlung photon from the circulating electrons in a synchrotron called Booster STorage (BST) ring [2], and its energy is determined by measuring the corresponding electron with a tagging counter [3]. A photon beam-profile monitor is one of the important devices to adjust accelerator parameters.

We have developed several versions of photon beam-profile monitors at ELPH [4–6]. The fourth generation monitor can measure the intensity map with a dead time of 35 ns for the high-intensity photon beams corresponding to the circulating electron current of 20 mA in the BST ring. It can measure the (x, y) position by a 3 mm step, and it is enough resolving power for the photon beams since their widths are approximately 8 mm at the circulating electron energy of 1.3 GeV. We have satisfied the performance of the fourth generation monitor.

All the monitors constructed take a large volume for their readout systems:

1. detector itself measures a size of approximately 500 mm (W)×500 mm (H)×300 mm (T),
2. coaxial cables between the detector in the experimetal hall and the discriminator modules in the counting room,
3. discriminator modules,
4. an FPGA based logic module, and
5. high voltage (HV) supplier to operate photomultiplier tubes.

It is difficult to change the locations for measuring the photon beam-profile. Thus, we have started to develop a new monitor which can be used at different location in our facility and also in other facilities easily.

We have required the following conditions for the development of the new monitor:

1. detector itself is small,
2. cirucuit for creating an intensity map is implemented in a board and directly connected to the detector, and
3. HV supplier is included in the circuit.

And all the elements for the monitor except for a personal computer display an intensity map are planned to be placed in a box.

§2. Response of a metal-packaged PMT to the photon

So far, we have employed two layers of scintillating fiber (SciFi) hodoscopes for a tracker system. Each layer has 16 SciFi, and each of which measures a cross section of 3 × 3 mm^2. To determine the two-dimensional position, two layers are required in this manner. Thus, we consider a multi-anode metal-packaged photo-multiplier tube (PMT) as a tracker system. For example, a PMT, Hamamatsu Photonics H9500, is a candidate, which has 16 × 16 anodes and measures an effective area of approximately 50 × 50 mm^2. We have tested metal-packaged PMTs by using photon beams and positron beams at ELPH [7]. At first, the signal of a 4 × 4 multi-anode PMT, Hamamatsu Photonics H6568, in response to the photon beam is investigated by using a digital phosphor oscilloscope, Tektronics DPO-4104. Fig. 1 shows the waveform of the output signal of the H6568 PMT in response to the photon beam. The signals have a pulse height of 500–700 mV apparently, while the pulse height corresponding to the dark current is less than 100 mV in the same condition.

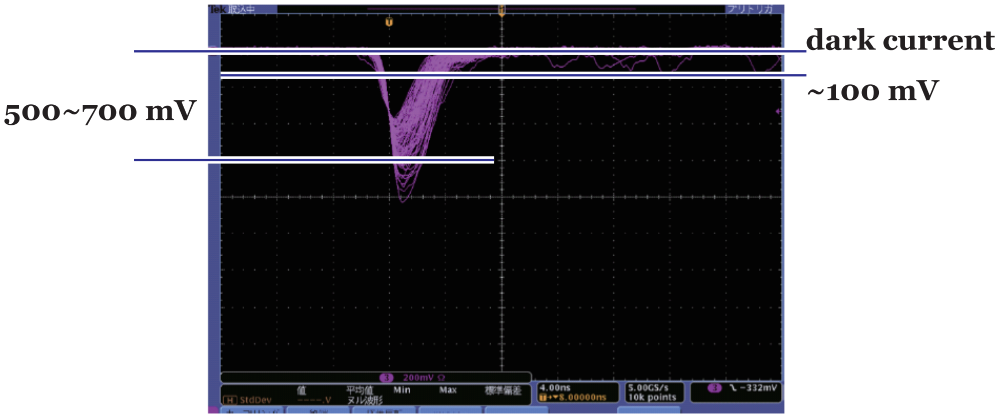

Fig.1. Waveform of the output signal of the H6568 PMT in response to the photon beam. The signals have a pulse height of 500–700 mV. The similar pulse-height is observed in other anodes. The pulse height corresponding to the dark current is less than 100 mV.

We have investigated the output signals of metal-packaged PMTs in response to the high energy positron beam. In this study, a single-anode metal-packaged PMT, Hamamatsu Photonics R8900U is used. Fig. 2 shows the experimental setup for investigating the response of a R8900U PMT for the high energy positron beams. Two layers of SciFi hodoscopes, which is the same as the tracker system for the previous photon beam-profile monitor, determine the incident position, and make a trigger for data acquisition. The SciFis are connected to H6558 PMTs. The penetration of the positron beam is confirmed with a PS with an area of 70 × 70 mm^2 with a thickness of 1 mm, which is the same as a trigger PS in the previous photon beam-profile monitor. The PS is connected to a 2-inch PMT, Hamamatsu Photonics H7195. The CAMAC-based data acquisition system is used. The energies of the output signals are measured with ADC modules, LeCroy 2249W and REPIC RPC-022, and the timings are measured with TDC modules, REPIC RPC-060.

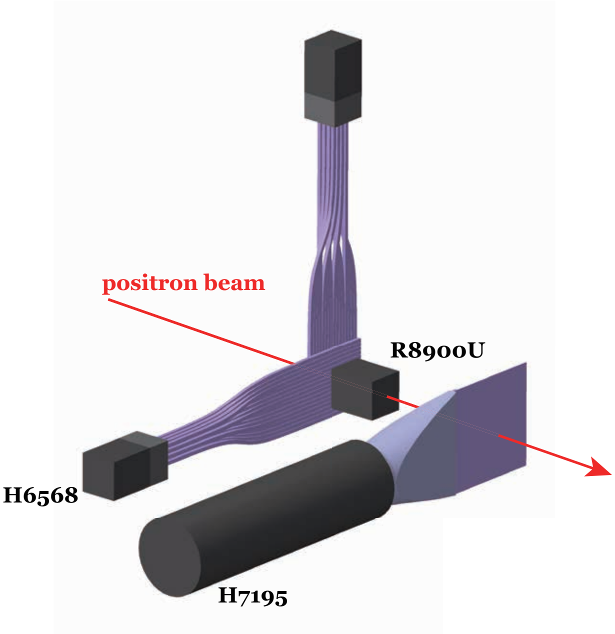

Fig.2. Experimental setup for investigating the response of a R8900U PMT for the high energy positron beams. The incident position is determined with two layers of SciFi hodoscopes, and the penetration of the positron beam is confirmed with a PS with an area of 70 × 70 mm^2 with a thickness of 1 mm. The SciFis are connected to H6558 PMTs, and the PS is connected to a 2-inch PMT, Hamamatsu Photonics H7195.

The efficiency of the R8900U PMT in response to the positron beam is estimated from the taken data. The positron beams are injected from the front, rear, and side faces. Fig, 3 shows the efficiency maps of the R8900U PMT in response to the positron beam. The efficiency is approximately 100% in the active area (23.5×23.5mm^2)of the R8900U PMT when the positron beam is injected from the front and rear faces. When the positron beam is injected from the side rear face, an enhancement of the efficiency is observed in two lines corresponding to the PMT window and first dynode. The obtained efficiency maps suggest that the secondary electrons produced at the PMT window and first dynode generate the output signals. The gain is thought to be higher for events in which the secondary electrons are produced at the PMT window, and the number of the seed electrons are larger than that corresponding to the dark current.

We have also investigated the output signals with several thicknesses of PSs connected to the R8900U in response to the positron beam. The thicknesses of PSs are 0, 0.5 and 3.0 mm, where 0 means that no PS is connected to the PMT. Fig. 4 shows the charge integration distributions for three thicknesses together with the distribution for the dark current. Each distribution is fitted with a Moyal function [8] to get the centroid (μ) and the width (σ) of the peak. The parameters (μ, σ) are $(6.3 \pm 0.7, 1.5 \pm 0.1)$, $(45.5 \pm 0.3, 6.6 \pm 0.4)$, and $(389.2 \pm 1.2, 34.2 \pm 2.1)$ pC for 0, 0.5 and 3.0-mm thicknesses. Some dark current events have the charge integration larger than 2 pC although it is basically

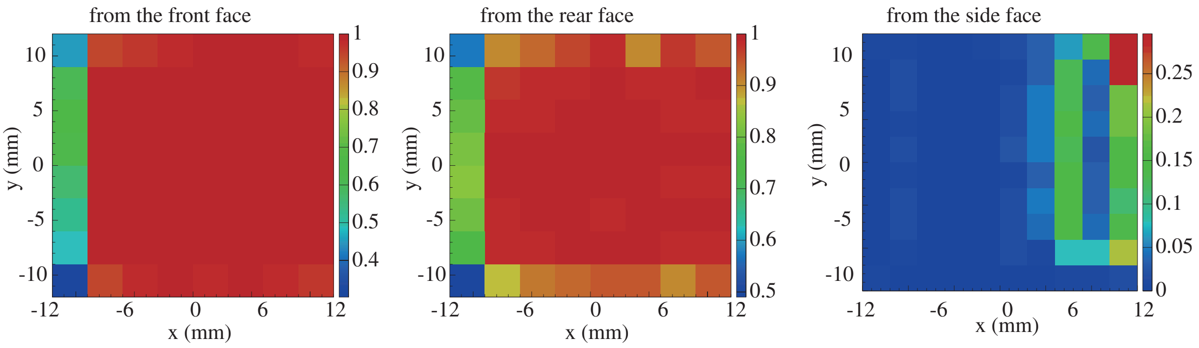

Fig.3. Efficiency maps of the R8900U PMT in response to the positron beam. The left, central, and right panels shows those the positron beams are injected from the front, read, and side faces, respectively.

much smaller than 2 pC. The separation power is not so high for a single positron penetration. The separation power becomes much better for a photon detection because we detect two minimum ionizing particles namely an electron and positron pair.

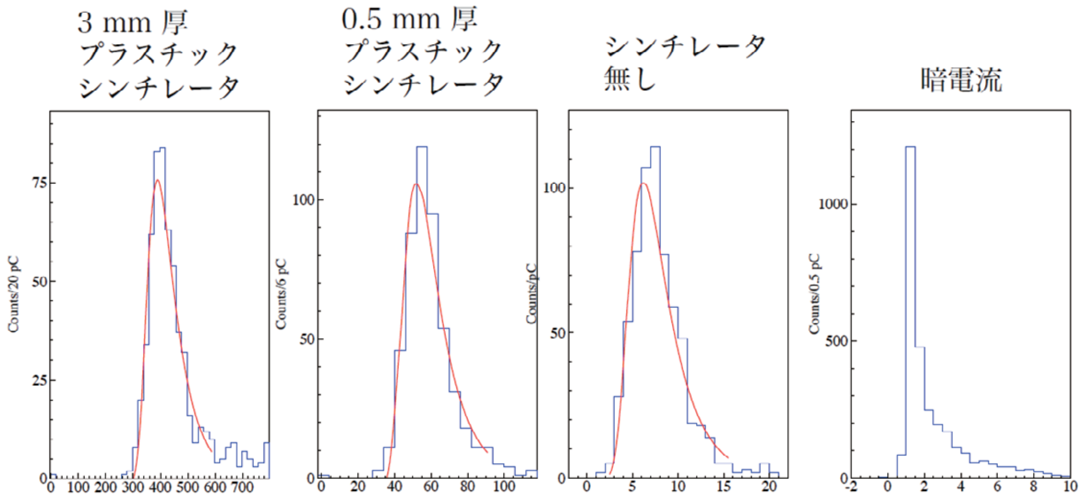

Fig.4. Charge integration distributions for 0, 0.5, and 3.0 thicknesses together with the distribution for the dark current. The left three panels show those for 3.0, 0.5, 0 mm thicknesses from the left side, and the right panel shows the distribution for the dark current.

§3. Test of a prototype beam-profile monitor

We have constructed a prototype beam-profile monitor consisting of a charge PS, 4 × 4 multi-anode H6568 PMT, and manufactured print-circuit-board including a Spartan-6 FPGA chip [9], 16 leading-edge discriminators, 2 constant-fraction discriminators, and a level converter for the RS-232C communication. The data acquisition with the board for the profile monitor is programmed in VHDL using an integrated development environment Xilinx ISE WebPACK Ver. 14.7 [10]. Fig, 5 shows the prototype print-circuit-board for the profile monitor and typical profile measure with it. The position is determined by the responding anodes in the H6568 PMT, and the charged particles produced upstream are rejected with the charge PS. The photon intensity in a unit area is measured for several anodes without using trigger PS, and the measured intensity is scattered from 0.5 to 2.0 even in the same position. This is because the signals of an anode includes those for the dark current and the measured intensity is affected by the dark current rate. The details of the analysis are described elsewhere [11].

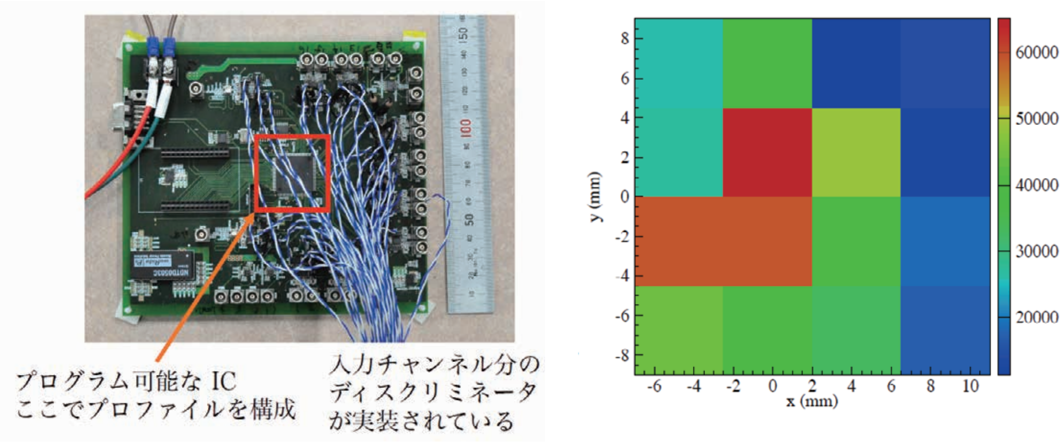

Fig.5. Prototype print-circuit-board for the profile monitor and typical profile measure with it. The H6568 PMT is used as a multi-anode PMT.

§4. Summary

We have been developing a new compact photon beam-profile monitor at ELPH. The positions of photons producing electron-positron pairs at the converter are determined with a multi-anode PMT. The secondary electrons produced by the electron-positron pairs are found to generate enough large signals in the PMT. The detector and circuit will be contained in a box, and we can use it anywhere we want.

Acknowledgments

The authors wish to thank the ELPH accelerator staff for providing the primary electron beam in the stable condition. This work was supported in part by Grants-in-Aid for Scientific Research (A) (24244022), and for Scientific Research (C) (26400287).

References

[1] T. Ishikawa *et al.*: Proceedings of the 10th International Workshop on the Physics of Excited Nucleons (NSTAR2015), JPS Conference Proceedings **10**, 031001 (2016);
T. Ishikawa *et al.*: Proceedings of the XV International Conference on Hadron Spectroscopy-Hadron 2013, PoS (Hadron 2013) 095;
T. Ishikawa *et al.*: Proceedings of the 20th International IUPAP Conference on Few-Body Problems in Physics, Few Body Systems **54**, 1047 (2013);
T. Ishikawa *et al.*: Research Report of LNS, Tohoku University, **42&43**, 1 (2011).

[2] F. Hinode *et al.*: Proceedings of 2005 Particle Accelerator Conference, 2458 (2005);
F. Hinode *et al.*: Proceedings of 11th International Conference on Synchrotron Radiation Instrumentation (SRI2012), Journal of Physics: Conference Series **425**, 072011 (2013).

[3] T. Ishikawa *et al.*: Nuclear Instruments and Methods in Physics Research Section A **622**, 1 (2010).

[4] M. Nanao, T. Ishikawa, and H. Shimizu, Research Report of LNS, Tohoku University, **36**, 56 (2003).

[5] H. Fujimura *et al.*: Research Report of LNS, Tohoku University, **42&43**, 56 (2011).

[6] T. Ishikawa *et al.*: Nuclear Instruments and Methods in Physics Research Section A **811**, 124 (2016).

[7] T. Ishikawa *et al.*: Nuclear Instruments and Methods in Physics Research Section A **694**, 348 (2012).

[8] J.E. Moyal, Philosophical Magazine 46 (1955) 263;
M.D. Marucho, C.A. Garcia Canal, H. Fanchiotti, International Journal of Modern Physics C 17 (2006) 1461.

[9] Spartan-6 website: ⟨http://www.xilinx.com/products/silicon-devices/fpga/spartan-6.html⟩.

[10] ISE WebPACK website: ⟨http://www.xilinx.com/products/design-tools/ise-design-suite/ise-webpack.html⟩.

[11] S. Kido, Mater thesis, Tohoku University, 2016.

(ELPH Experiment : #2812, #2813)

Development of the photon tagger for the NKS2 experiment

H. Kanda[1], K. Honda[1], T. Ishikawa[2], M. Kaneta[1], K. Maeda[1], M. Miyabe[2],
Y. Muroi[1], S. Nagao[1], S. N. Nakamura[1], A. Ninomiya[1], T. Nishizawa[1],
K. Ozeki[1], T. Sasaki[1], A. O. Tokiyasu[2], and Y. Toyama[1]

[1]*Graduate School of Science, Tohoku University, Sendai 980-8578, Japan*
[2]*Research Center for Electron Photon Science, Tohoku University, Sendai 982-0826, Japan*

We have been developing an internal photon tagger for the NKS2 experiment. It is composed of 40 counter units based on MPPCs. Assembling of the counter units and their arrangement on the counter base frame were completed. Their commissioning and test experiments with the electron beam was performed. After the completion of the basic development, we measured the eta meson photoproduction on the proton for the energy calibration of the tagger using the threshold energy of the eta meson. The analysis of the data is underway. We report the current status of the development of the photon tagger and the analysis for the energy calibration.

We have been developing an electron detector of the internal photon tagger as a recovery and an upgrade of the STB-Tagger [1] which was damaged by the Tohoku Earthquake on 11 March 2011. Bremsstrahlung photon beams are generated at a target called as the radiator inserted in the electron beam line of the electron booster and storage ring (BST ring) [2]. The movable target system is located at 300 mm upstream of the fourth bending magnet (BM4) of the accelerator. The electron detector is placed in the space between the pole and the yoke of BM4 and detects momentum analyzed electrons after the bremsstrahlung and thus define timing and energy of radiated photons. The newly developed electron detector consists of scintillation counters based on Multi-Pixel Photon Counters (MPPCs) supplied by Hamamatsu Photonics K. K. The read-out system for the timing counters (TagBs) consists of ordinary leading edge discriminators. A differential amplifier circuit was developed [3, 4], to reduce the pile-up of the MPPC signal with long tail and the dark counts of the parallel-connected MPPC array. The other read-out system for the position counters (TagFs) is EASIROC [5] based electronics [6] aiming at an easy operation of multi-channel counters. We designed an electron detector of the photon tagger composed of counter units each of which has four TagFs and one TagB. By a coincidence of a TagB and one of four TagFs belonging to one counter unit, a trajectory of an electron can be selected to reduce an electromagnetic background from electrons, positrons or gamma rays coming from other sources.

The alignment of the counter unit was determined using a GEANT4 based Monte Carlo simulation with a magnetic field of the BM4. Trajectories of electrons after the bremsstrahlung of 1.31 GeV electrons on the radiator was calculated and the injection angles, positions and energy deposits of the electrons on the scintillators of the counter units were simulated. We aligned the counter units with angles parallel to the electron trajectories and positions avoiding the interference between counter units. The calculated positions and some samples of the trajectories are shown in the magnified view of Fig. 1. The range of the tagged photon energy was estimated to be 0.78 to 1.27 GeV for the 1.3 GeV operation of the BST ring.

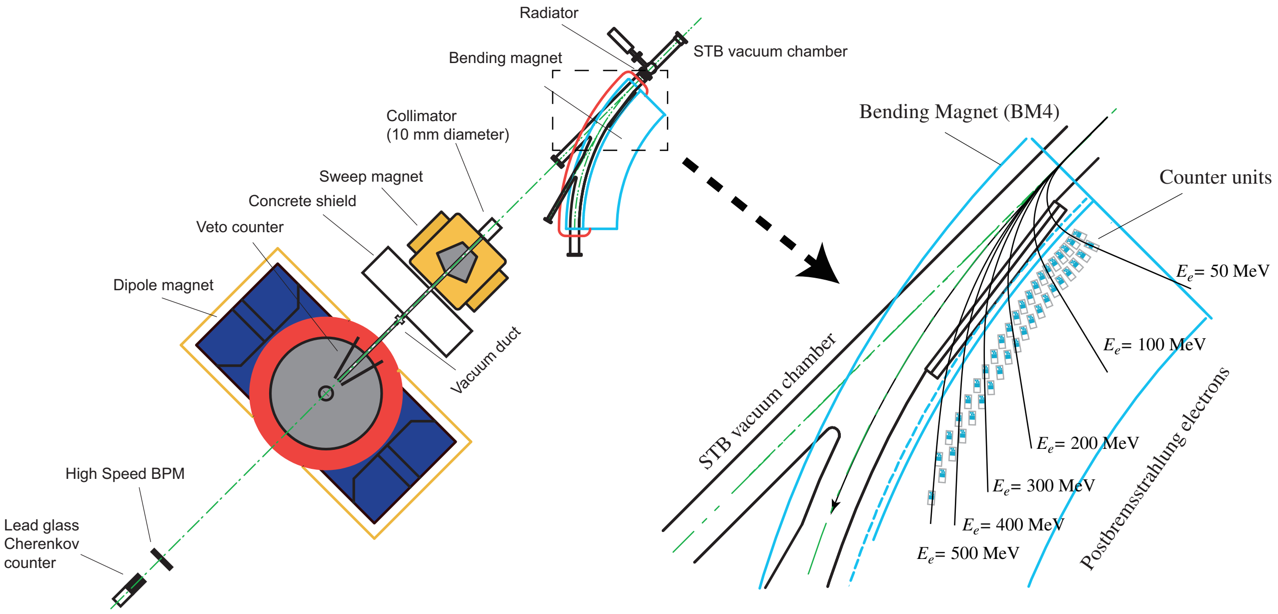

Fig.1. Schematic diagram of the setup along the photon beam line and the magnified view of the tagger.

The case for the electron detector was designed to have the following three functions: (f1) to align and fix the counter units on it; (f2) to hold connector changing circuit boards, cables for signals, bias power, and preamplifier power; and (f3) align the base itself to the magnet. Its shape had to fulfill the following requirements: (r1) compactness for the insertion through the limited space between the BM4 and a quadrapole magnet (QC2) just upstream of the BM4; (r2) sufficient length to fix all the counter units with the length of 1 m; and (r3) avoidance of the matters which affect the magnetic field of the BM4. The final design is shown in Fig. 2. We fixed a rail with a groove on the lower yoke of BM4 and set a pin which fits the groove to fix its motion along the rail for (f3). The frame itself has two levels of base plates. Top plate is used for (f1) and the bottom plate is used for (f2). The cables from the counter units to the connector changing boards are placed through small holes on the top plate. They are fixed with black silicone RTV to be light-tight. The frame was separated in two parts with lengths of 0.397 m for the upstream and 0.73 m for the downstream to fulfill two requirements (r1) and (r2) at the same time. They were connected with a detachable pin to allow a rotation around it. After the insertion in the BM4, the downstream part was puled to the upstream part with a wire for the tight connection between two parts. The frame was fixed to the BM4 with some jigs fixed on the side yoke. The plates and spacers between top and bottom plates were made of black MC nylon and all the matters of screws and pins were selected with small magnetism such as brass, titan, and thermal treated SUS304 for fulfilment of (r3). We assembled all the counter units and mounted them on the detector case (Fig. 3).

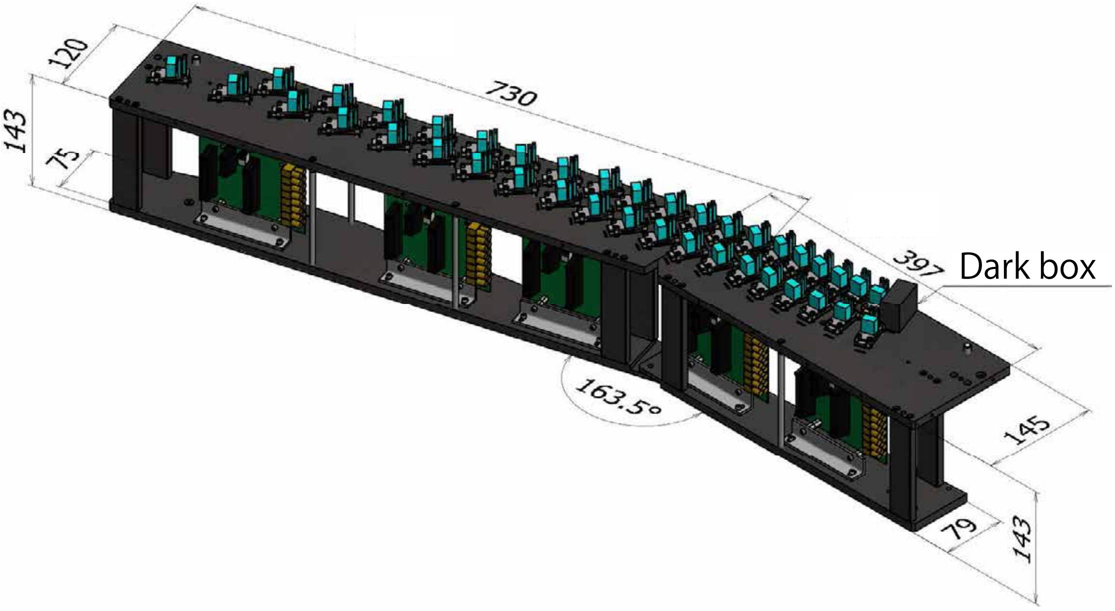

Fig.2. Schematic design of the detector case of the tagger.

Fig.3. Photograph of the detector case of the tagger with all the counter units mounted on it.

After the construction and the installation of the electron detector to the BM4, we tested its tagging efficiency and relative energy for each tagging counter using a lead glass Cherenkov detector (LG). Its experimental setup is shown in Fig. 1. The LG was placed at the most downstream part of the beam line and used for the measurement of the energy of photons with sufficient efficiency. The description of the LG is found elsewhere [7]. The ADC spectrum of the LG gated on the hit of each tagging counter was fitted with a Gaussian function to find the central value. These central values were normalized to the value for TagB1 and shown as a function of the TagB segment number in Fig. 4. There were slight discrepancy from the simulation. The data and simulation are currently being checked.

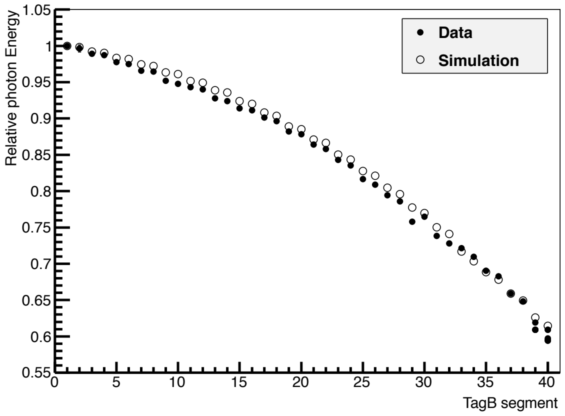

Fig.4. Relative tagged photon energy normalized to the photon energy corresponding to TagB1 shown as a function of the TagB segment number for the 1.3 GeV operation of the BST ring. Solid circles denote the measured data and open circles denote results of the Monte Carlo simulation. Energies for TagB39 and 40 were measured several times as the reference of the systematic error.

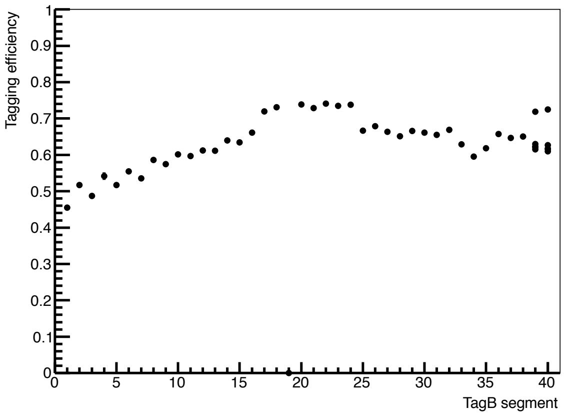

Fig.5. Tagging efficiency as a function of the TagB segment number for the 1.3 GeV operation of the BST ring. Efficiencies for TagB39 and 40 were measured several times as the reference of the systematic error.

The tagging efficiency ϵ_i for the i-th tagging counter was defined as

$$\epsilon_i = \frac{N_i^{\text{photon}}}{N_i^{\text{tag}}(ON) - N_i^{\text{tag}}(OFF)} \tag{1}$$

where N_i^{photon} is the number of photons detected with the LG in coincidence with the i-th tagging counter; $N_i^{\text{tag}}(ON)$, the number of the hits on the i-th tagging counter with the radiator interested to the electron beam; and $N_i^{\text{tag}}(OFF)$, the number of the hits on the i-th tagging counter without inserting the radiator. Number of photons were obtained by setting gates on the ADC values of the LG because the ADC spectrum had the broad tail in the lower energy region due to the secondary particles from a supporting rod and the wall of the vacuum chamber of the accelerator in the BM4. The tagging efficiency measured for the 1.3 GeV operation of the BST ring is shown in Fig. 5. It was sufficient for the experiment. We selected the single hit on the TagB in these analyses. The detailed analysis of TagBs and TagFs for the selection of the trajectory of the post-bremsstrahlung electrons is underway.

We performed an experiment for the calibration of the photon energy using η photoproduction on the proton taking advantage of the steep rise of the cross section from the threshold (0.7078 GeV). The electron energy of the BST was set as 0.900 GeV. The energy of the tagged photon beams was estimated to range from 0.533 GeV to 0.868 GeV with the simulation. TagB26 was estimated to correspond to the threshold energy of η photoproduction on the proton. The main decay modes of η are neutral modes such as $\eta \to 2\gamma(39.41\%)$ and $\eta \to 3\pi^0(32.68\%)$. We detected the recoil proton with the NKS2 to identify the η with the missing mass. Detailed setup of the detectors of the NKS2 is shown in Fig. 6. The inner hodoscope (IH) of the NKS2 does not cover the most forward angular region in order to reduce the matter along the beam line. For covering the proton emitted in the very forward angle at the threshold, we placed a counter with a 2.6 mm-thick scintillator (TC). It was treated as another segment of the IH in the analysis. The largest emission angle of the proton in the laboratory system was 31 degrees. The 4th segment of the IH covers the horizontal angle from 18 to 30 degrees. We set a multiplicity trigger only including the TC and the 1st to the 4th segments of the IH. The segments of the outer hodoscope (OH) required for the trigger were also limited to cover the emitted proton. The other segments of the IH and the OH were used for the detection of charged pions in the offline analysis. The request of the detection of a proton and no other charged particles was expected to efficiently reduce the largest background from $\gamma p \to \pi^+\pi^- p$. The momentum of the recoil proton ranged from 0.2 GeV/c to 0.8 GeV/c which were sufficiently in the momentum acceptance of the NKS2 for the proton.

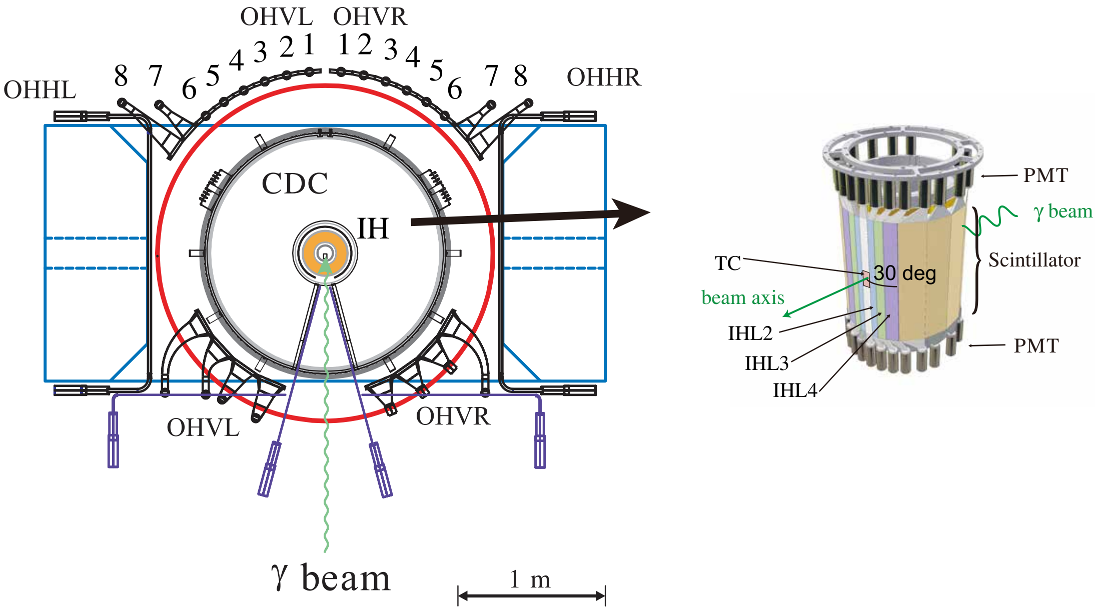

Fig.6. Setup of the detectors of the NKS2.

Total numbers of the tagger hits were 1.3×10^{11} for the hydrogen target runs, and 5.3×10^{10} for the empty target runs in the beam time. The empty target runs were used for the subtraction of the background emerging from the non-target region because we could not define the target region from the vertex reconstructed from the single proton measured in the forward angle. The numbers of recorded events were 1.4×10^{8} for the hydrogen target runs. By the simple estimation considering the η photoproduction cross section calculated with eta-MAID [8], a target density, a duty factor of the accelerator and efficiencies of the data acquisition, the tracking and the tagger, the estimated yield of η was estimated to be 80 for single TagB at the threshold region.

As the first step analysis, we only used the information of the hodoscopes. The segments of the IH used in the analysis were limited to TC and IHL2. The segments of the OH used were OHVL1, OHVL2, OHVL3, and OHVL4, considering the bending angle of the proton passing through both of the TC and the IHL2. The first ADC peak of the hodoscopes were assumed to correspond to the energy deposit of a minimum ionizing particle and used for the calibration of the energy deposit. The timing of the counters were calibrated using minimum ionizing particles and assuming their flight length as 1 m from the IH to the OH and their velocity as $\beta = 1$. Correlation between the velocity of the particle and its energy deposit of the OH was used for the particle identification (PID). The lowest momentum of the charged pion measured with the NKS2 was 0.1 GeV/c and its velocity was $\beta = 0.58$. The highest momentum of the proton in the η photoproduction in this energy region was 0.8 GeV/c and is velocity was $\beta = 0.65$. The graphical cut condition for the proton was defined as shown in Fig. 7 by considering the resolution of the velocity and energy deposit and for reducing distribution in the small energy deposit region.

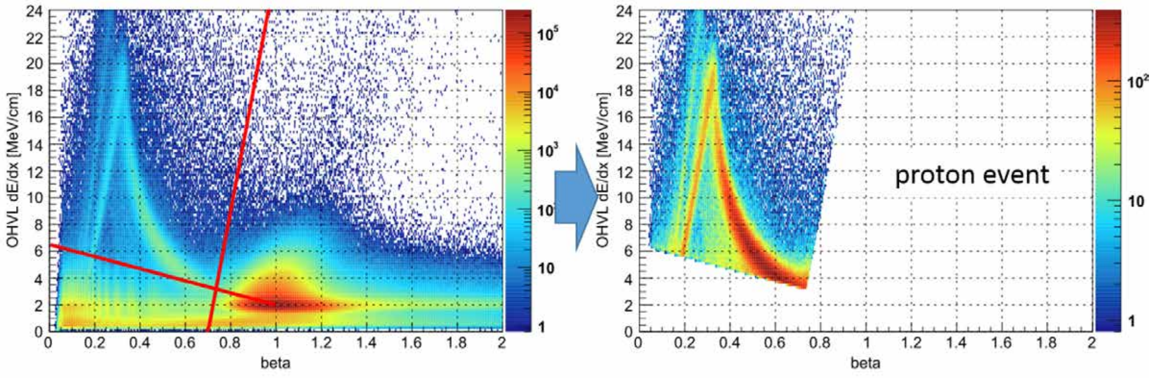

Fig.7. Correlation plot of dE/dx on OHVL counter vs. beta for the proton selection. Distribution for particles identified as the proton is shown in the right panel

The momentum distributions of the selected proton for the hydrogen target runs and the empty target runs normalized for the number of accepted trigger are shown in Fig. 8. Enhancement of the proton yield in the momentum range of 0.3 GeV/c to 0.6 GeV/c can be seen. The momentum corresponds to the recoil proton in the η photoproduction from its threshold to the photon energy of 0.74 GeV. For better selection of the proton and the kinematical selection with the missing mass, absolute momentum and the direction at the target region is indispensable. The calibration of the MWDCs and analysis with the tracking information is underway.

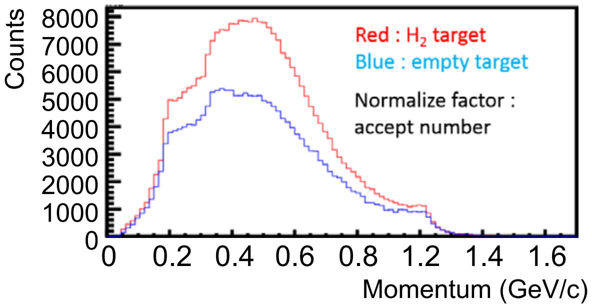

Fig.8. Momentum distribution of the proton for the hydrogen target runs (red curve) and for the empty target runs (blue curve).

In summary, the development of a new tagger for the NKS2 was coming to its final stage. The tagging efficiency and the relative photon energy were measured using the LG. The tagging efficiency was sufficiently high for the performance of the experiment for the 1.3 GeV operation of the BST ring. The discrepancy of the photon energy from the simulation is currently being checked. In the analysis of the η photoproduction on the proton for the energy calibration, a sign of the η production were seen in the momentum distribution of the proton. Detailed data analysis in underway.

We plan to perform the commissioning of the NKS2 with the Λ photoproduction on the deuteron in the photon energy region from 1 to 1.27 GeV in June 2016. It partly overlaps the energy range of our previous measurement of Λ photoproduction from 0.78 to 1.08 GeV [9] but exceeds it by 0.2 GeV. The obtained data will be used for checking of the consistency with the previous data but it will be a new data taking full advantage of the upgrade of the BST and the new tagger.

Acknowledgment

We would like to thank the administration and technical staff in ELPH and the faculty of science. This program was partly supported by Core-to-core program (21002), strategic young researcher overseas visits program for accelerating brain circulation (R2201), and KAKENHI Grant Number 23540334 by JSPS.

References

[1] H. Yamazaki *et al.*: Nucl. Instr. and Meth. in Phys. Res. A **536** (2005) 70.

[2] F. Hinode *et al.*: Proceedings of 11th International Conference on Synchrotron Radiation Instrumentation (SRI2012), Journal of Physics: Conference Series **425** (2013) 072011.

[3] T. Nishizawa *et al.*: IEEE trans. Nucl. Sci. **61** (2014) 1278.

[4] H. Kanda *et al.*: Conference Record, Nuclear Science Symposium and Medical Imaging Conference (NSS/MIC), 2013 IEEE.

[5] S. Callier *et al.*: Phys. Procedia **37** (2012) 1569.

[6] R. Honda *et al.*: PoS PhotoDet2012 (2012) 031.

[7] H. Kanda *et al.*: Research Report of Laboratory of Nuclear Science, Tohoku University **44** (2011).

[8] W.-T. Chiang, S.-N. Yang, L. Tiator, D. Drechsel: Nucl. Phys. A **700** (2002) 429.

[9] B. Beckford *et al.*: Prog. Theor. Exp. Phys. **2016** (2016) 063D01.

(ELPH Experiment : #2813, #2828)

新光子標識化装置 STB TaggerⅡs で使用する MWDC の性能評価

佐々木未来 [1], 本多 佑記 [2], 井上陽介 [2], 石川貴嗣 [2], 岩佐美和 [1], 叶内萌香 [1*], 木戸聡 [2],
松村裕二 [2], 三浦大輔 [1], 宮部学 [2], 村松憲仁 [2], 櫻井輝昴 [1], 笹川瑞樹 [2], 盛道太郎 [1],
関悠登 [1], 清水肇 [2], 田島靖久 [1], 高橋季己 [1], 時安敦史 [2], 土川雄介 [2†], 吉田浩司 [1]

[1] 山形大学理学部　(990-8560 山形県山形市 小白川町一丁目 4-12)
[2] 東北大学電子光理学研究センター（982-0826 仙台市太白区三神峯 1-2-1）

Performance test of MWDC for a photon tagging system STB TaggerⅡs

M. Sasaki[1], Y. Honda[2], Y. Inoue[2], T. Ishikawa[2], M. Iwasa[1], H. Kanauchi[1*],
S. Kido[2], Y. Matsumura[2], D. Miura[1], M. Miyabe[2], N. Muramatsu[2],
T. Sakurai[1], M. Sasagawa[2], M. Sei[1], Y. Seki[1], H. Shimizu[2], Y. Tajima[1],
T. Takahashi[1], A.O. Tokiyasu[2], Y. Tsuchikawa[2†], and H.Y. Yoshida[1]

[1] *Department of Physics, Yamagata University, Yamagata 990-8560*
[2] *Research Center for Electron Photon Science, Tohoku University, Sendai, 982-0826*

A new photon tagging system, which is STB TaggerⅡs, has been developed for the FOREST experiment. In order to measure the photon energy more precisely, the STB TaggerⅡs consists of the multi wire drift chamber (MWDC) and the hodoscope. A new MWDC is adopted as an electron tagging device to determine the trajectories of the recoil electrons from the target. And it was tested using positron beam at ELPH in November 2015. The measured efficiency was 99 % or higher and the position resolution 76 μm.

§１． 研究背景

現在 ELPH では、FOREST 実験のための新しい標識化装置 STB TaggerⅡs を開発している。FOREST 実験で使用する光子ビームは、BST リングの周回電子へカーボンファイバーを差し込むことによって起こる制動放射から作られている。制動放射により発生した光子のエネルギーは連続スペクトルを持つため、個々の光子ビームを特定し、エネルギーを決定する必要がある。その為の装置が標識化装置である。第１図に標識化装置の概要を示す。制動放射により光子を放出した反跳電子はエネルギーを失い、加速器の偏向電磁石により周回軌道よりも内側に曲げられる。標識化装置はこの反跳電子の軌道上に設置され反跳電子を検出する。反跳電子の検出は反跳電子と対をなす光子ビームを特定することができ、これを標識化と呼ぶ。反跳電子の電子のエネルギー $E_{e'}$ を測定することで、光子ビームのエネルギーを E_γ も求めることができ、周回電

---

[*] Present address : Department of Physics, Tohoku University, Sendai, 980-8578
[†] Present address : Department of Physics, Nagoya University, Nagoya, 464-8602

子のエネルギーを E_e とすると、

$$E_\gamma = E_e - E_{e'} \tag{1}$$

となる。

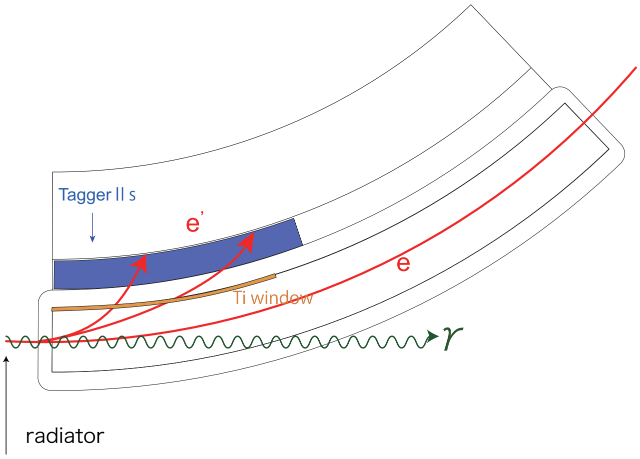

第 1 図　光子標識化概念図

反跳電子は周回する加速器のビームパイプから 50 μm 厚のチタン製のウィンドウを通過して STB TaggerIIs へ入射する。この際に、高エネルギー反跳電子はウィンドウのフレームにあたり低エネルギーの二次粒子を発生させる。現行の標識化装置である STB TaggerⅡ では、この二次粒子がバックグラウンドになることがわかっており、新しく製作する STB TaggerⅡs には反跳電子と二次粒子を区別するための 5° の角度分解能と、周回ビームのバンチを区別するための 200 ps 以下の時間分解能が要求される。これらの要求を満たすため、高角度分解能を持つ MWDC と、高い時間分解能を持つホドスコープの二つの機器から構成される。本レポートでは製作した STB TaggerⅡs の MWDC の性能評価試験を行った。

1.1 MWDC

STB TaggerⅡs で使用する MWDC について述べる。MWDC の仕様を第 1.1 表、写真を第??図に示す。フレームは設置場所である偏向電磁石の内壁に合わせた円弧上になっている。第 2 図に MWDC のセル構造を示す。赤い点はセンスワイヤー、青い点はポテンシャルワイヤーそして緑の点はスイープワイヤーの配置を表す。一つのセルはセンスワイヤーを中心に六角形にポテンシャルワイヤーが配置されている。センスワイヤーの間隔は 6 mm で、X プレーンのみの 3 層構造である。

第 1 表　MWDC 仕様

フレーム寸法	1000 mm × 136 mm
フレーム材質	アルミニウム
ワイヤー長	30 mm
ワイヤープレーン	X のみ
層数	3
チャンネル数	448
ワイヤー材質	金メッキタングステン
ポテンシャルワイヤー、スイープワイヤー径	50 μm
センスワイヤー径	20 μm

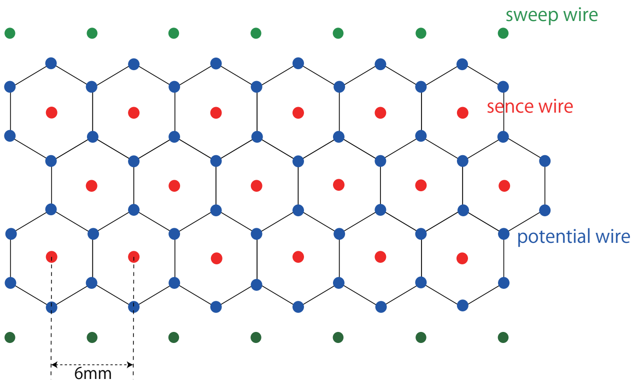

第 2 図　MWDC のセル配置。赤がセンスワイヤー、青がポテンシャルワイヤー、緑がスイープワイヤーを表す。

MWDC の信号の読み出しには林栄精器と KEK で開発された読み出しボード 64ch RAINER [1]を小型化した 32ch RAINER を使用する。RAINER はボード上で入力信号の ADC、TDC データの取得が可能で、処理されたデータは SiTCP を使って、イーサネット経由で PC へ読み出すことができる。第 3 図に示したように、RAINER の大きさは 120 mm × 100 mm で、MWDC に取り付けて偏向電磁石の内部 (120 mm × 350 mm) に挿入できるサイズに収めた。性能を第 2 表に示す。

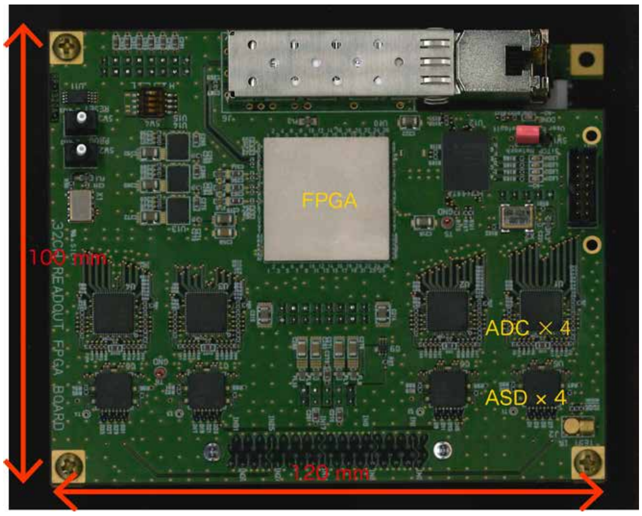

第 3 図　32ch RAINER

§2. 性能評価実験

第 4 図にビームテストのセットアップを示す。T0、T1、T2 はトリガーカウンターで、T0 は 50 mm × 50 mm × 10 mm、T1、T2 は 30 mm × 30 mm × 5 mm のプラスチックシンチレータで構成されている。また、T0 は両側、T1、T2 は片側に PMT を取り付けている。陽電子ビームは 100~900 MeV のエネルギーを使用した。また、入射角度に対する応答を測定するため、チェンバーは回転ステージに乗せ、回転させることによってビームを入射角度 0、30、45、60° で入射させた。今回の実験では、32ch RAINER は 2 枚使用し、中心部分の 64 チャンネルのみのデータを取得した。

第 2 表　RAINER 仕様 [2]、[3]

処理信号数	32 チャンネル
Amp Shaped Discrimenater	アナログゲイン -1.1 V/pC デジタルゲイン -15 V/pC タイムウォーク $<$ 500 ps
ADC	解像度 10 bit 取り込み周期 32 ns サンプリング周波数 31.25 MHz
TDC	解像度 1 nsec
データバッファ	8 μs リングバッファ

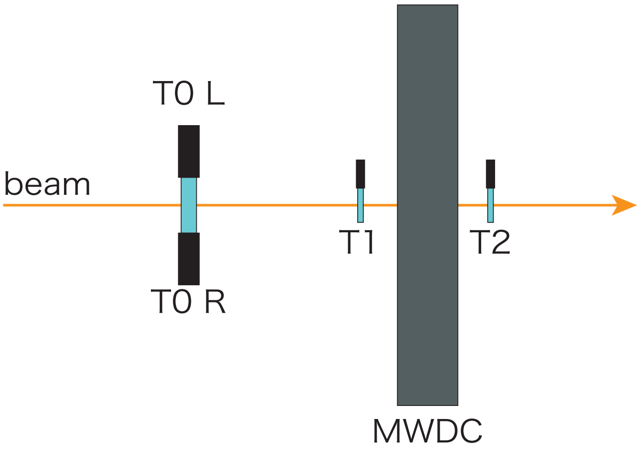

第 4 図　Set up of the beam test.

2.1　プラトーカーブ

MWDC に印加する電圧は、以下の式で定義した第 n 層の検出効率が 99 %以上になるように決定した。

$$\text{efficiency} = \frac{3\text{ 層すべてが hit したイベント数}}{\text{第 n 層以外の 2 層がヒットしたイベント数}} \tag{2}$$

スイープワイヤーにはポテンシャルワイヤーの 90 %の電圧を印加した。測定した検出効率と印加電圧の相関図を, 図 5 に示す。2 層目の検出効率が 1 、3 層目に比べて低いのはポテンシャルワイヤーとスイープワイヤーの電圧比が最適化されていないためと考えられる。印加電圧 2200 V 以上で検出効率 99 %以上を達成できることがわかるが、2200 V では放電の兆候が見られたため、印加電圧はポテンシャルワイヤー 2150 V、スイープワイヤー 1950 V に決定した。[4]

2.2　X-T 分布

垂直入射のデータから得られた時間の分布を第 6 図に示す。このような、TDC 分布からビームの通過位置を再構築する。各層のビームの通過位置 X_n' は、センスワイヤーの位置 X_0、ガス中の電子のドリフト速度 v_d と TDC 分布より得られるドリフト時間 t_n より,

$$X_n' = v_d \times t_n + X_{0n} \tag{3}$$

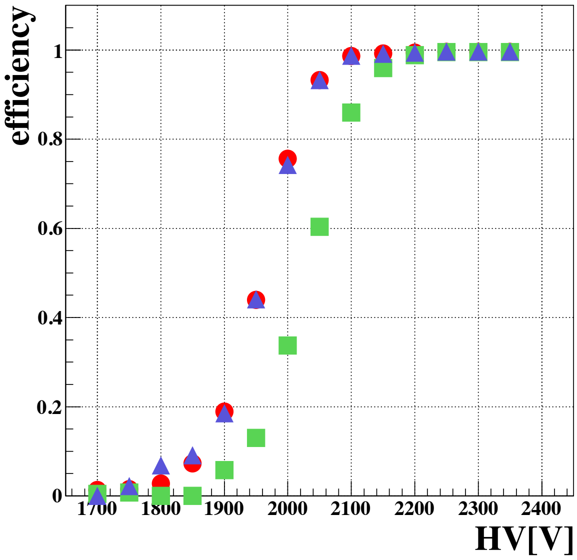

第 5 図　各層ごとのプラトーカーブのプロット。赤が 1 層目、緑が 2 層目、青が 3 層目の検出効率を表す。

で計算できる。式より得られた各層の X'_n とセンスワイヤーの Z 位置からビームの飛跡が直線であることを仮定してフィッティングし、新たな各層のビームの通過位置を X_n を算出する。フィッティングには図 7 に示すような入射座標を用いて行った。垂直入射を仮定しているので陽電子が通過した Z 座標にはセンスワイヤーの Z 座標と同じ値を用いた。

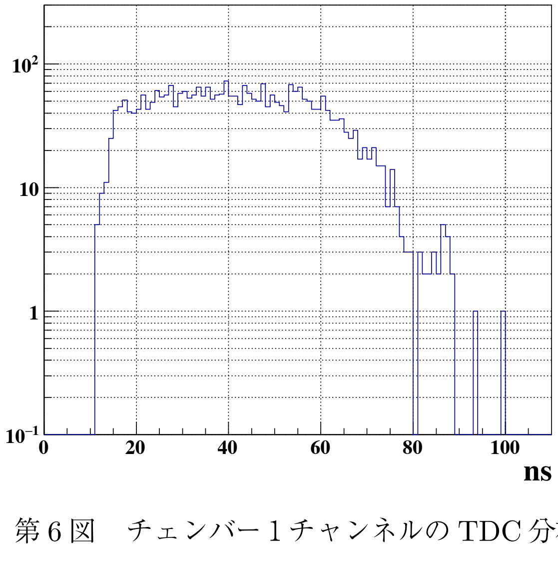

第 6 図　チェンバー 1 チャンネルの TDC 分布

式 3 より求めた X_n と，フィッティングにより求めた X'_n の残差分布を第 9 図に示す。この結果，得られた位置分解能は 76 μm となった [4]。

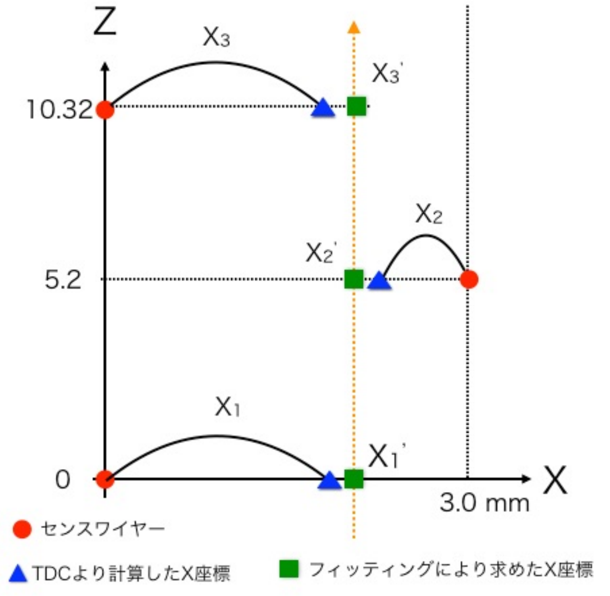

第７図　フィッティングに用いた入射位置の座標

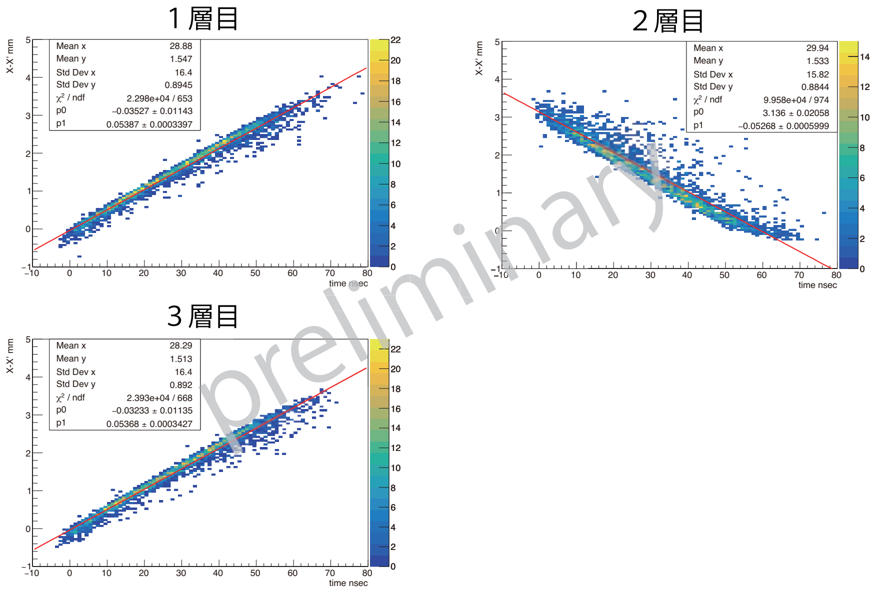

第８図　X-T プロット。図中の赤線はこの分布へ直線でフィッティングした結果である。

§3. まとめ

ELPH では FOREST 実験のための新しい標識化装置 STB TaggerⅡs を開発している。標識化装置は飛跡検出のための MWDC と、時間測定のためのプラスチックシンチレータから構成されている。本研究では 100 ～ 900 MeV/c の陽電子ビームを用いて MWDC の性能評価試験を行った。その結果 99 %以上の検出効率と、76 μm の位置分解能が得られた。今後、斜め入射の実験データを用いて角度分解能を見積もる予定である。

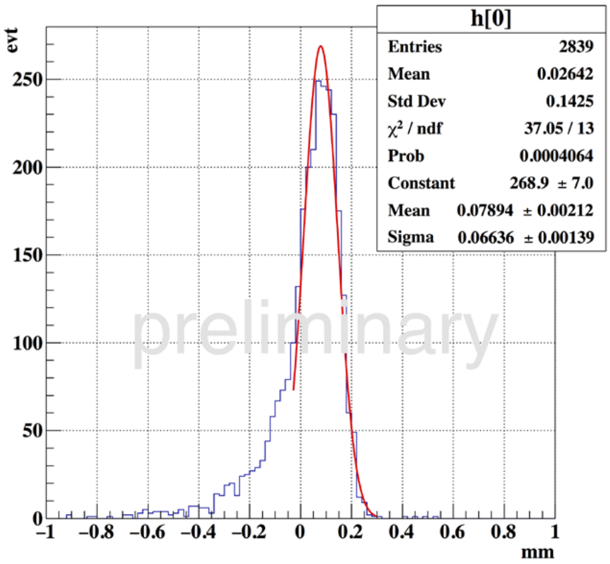

第 9 図　式 3 より求めた X_n とフィッティングにより求めた X'_n との残差分布

参考文献

[1] Readout electronics for the central drift chamber of the Belle II detector, Uchida, T., Ikeno, M., Iwasaki, Y., Saito, M., Shimazaki, S., Tanaka, M., Taniguchi, N., Uno, S., 2012 IEEE Nuclear Science Symposium Conference Record, pp. 694-698.

[2] 林栄精器株式会社：64ch READOUT BOARD スタートアップガイド Rev01 3

[3] 林栄精器株式会社：ASD IC 型式 JRK B ASD-CMOS カタログ

[4] 佐々木未来 他: GeV-γ ビームラインにおける新光子標識化装置の開発 V、日本物理学会第 71 回年次大会 (2016)

(ELPH Experiment : #2815)

Measurement of the electron beam size at the BM5 radiator in the BST ring

Y. Obara[1], H. Hama[2], F. Hinode[2], T. Ishikawa[2], H. Kanda[3], S. Kashiwagi[2],
M. Miyabe[2], T. Muto[2], K. Ozawa[4], H. Shimizu[2], and A.O. Tokiyasu[2]

[1]*Department of Physics, University of Tokyo, Tokyo 113-0033, Japan*
[2]*Research Center for Electron Photon Science, Tohoku University, Sendai 982-0826, Japan*
[3]*Department of Physics, Tohoku University, Sendai 980-8578, Japan*
[4]*Institute of Particle and Nuclear Studies (IPNS), High Energy Accelerator Research Organization (KEK), Tsukuba 305-0801, Japan*

§1. Introduction

Meson photoproduction experiments for baryon spectroscopy have been conducted at the Research Center for Electron Photon Science (ELPH), Tohoku University. In the experiments, we use the energy-tagged bremsstrahlung photon beams, which are generated by inserting a carbon fiber (radiator) into circulating electrons in a synchrotron called Booster STorage (BST) ring [1]. The BST ring is the upgraded synchrotron from the STretcher Booster (STB) ring [2], and the maximum energy has been increased from 1.2 to 1.3 GeV. It is important to measure the properites of the circulating electrons in the BST ring, which affects the properties of the photon beams. We have measured the electron beam size at the radiator point.

The horizontal beam size σ in a synchrotron is expressed by

$$\sigma = \sqrt{\beta\epsilon + \left(\eta \frac{dp}{p}\right)^2} \tag{1}$$

where β denotes one of the Twiss parameters α, β, and γ, η stands for the dispersion, and dp/p is the equibrium momentum spread. The lattice structure of the BST ring gives α, β, γ, η, and dp/p. Misalignment of the elements and poor degree of vaccum in the BST ring also affect these values. To reveal the properties of the circulating electrons, we have measured the horizontal beam size.

§2. Method

The electron beam intensity penetraring the radiator can be determined from the the photon intensity as a function of the elapsed time. The bremsstrahlung is generated by inserting a carbon fiber into the circulating electron beam. Figure 2 shows the schematic view of the radiator and its frame. To keep the photon intensity constant, this frame is moved by the stepping motor in the normal operation. An energy of a generated photon is tagged using STB-Tagger-II [3]. It is composed of 116 telescopes of upstream and downstream scintillating fibers, eight of which are directly connected to a multi-anode photomultiplier tube . Each telescope determines the trajectory of a recoil electron and gives its momentum and the corresponding generated photon as shown in Fig. 1. The details of STB-Tagger II are described elsewhere [3]. When the radiator is fixed at a position of x, a counting rate of a tagging channel is proportional to the number of circulating electrons passing through the radiator. The counting rate $N(t)$ as a function of the elapsed time t is given as

$$N(t) = N_0 \exp(-\alpha(x)t) \tag{2}$$

where N_0 is the counting rate at the time of $t = 0$ and $\alpha(x)$ denotes a decay constant at a fixed position of the radiator. Assuming that the electron beam profile in the BST ring does not depend on the circulating current, the decay constant $\alpha(x)$ is proportional to a fraction of electrons at a position x. Thus, the center position and width of the electron beam can be determined from the decay constant $\alpha(x)$ as a function of the radiator position x. We have determined the horizontal electron beam sizes at the radiator position for 1.3, 1.0 and 0.8 GeV modes.

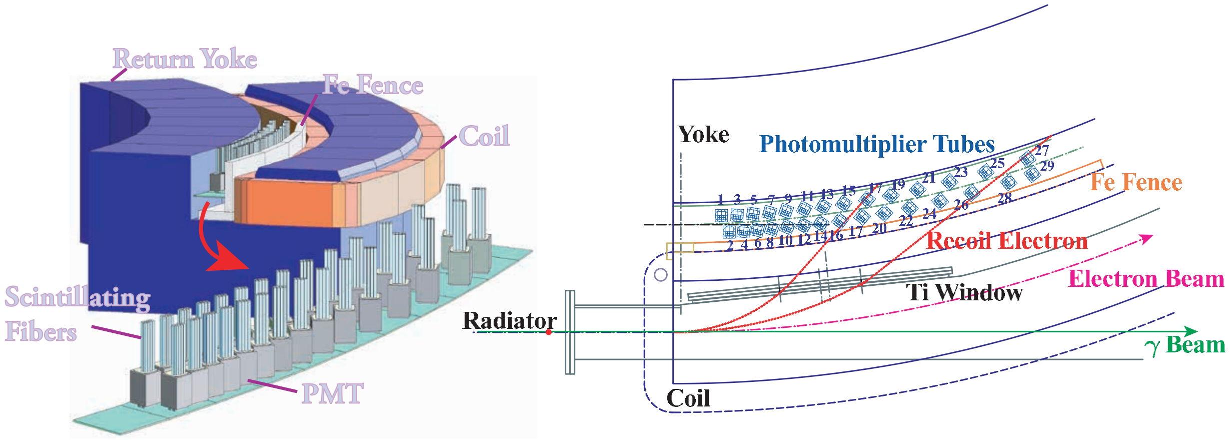

Fig.1. Schematic view of STB-Tagger II. The energy of a produced photon is determined measuring its corresponding recoil electron.

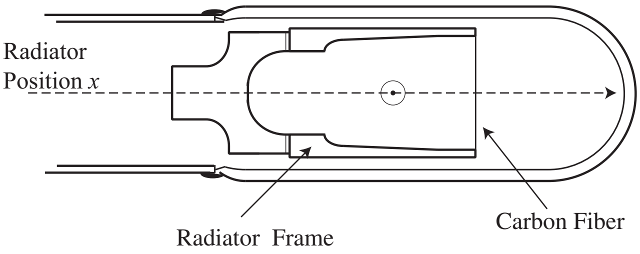

Fig.2. Schmeatic view of the radiator and its frame. The carbon fiber with a diameter of 11 um is fixed between two tips of a fork-like frame. The frame can be moved in a horizontal direction using a stepping motor.

§3. Readout

To give the photon intensity as a function of the elapsed time, the number of counts of the taggers in a definite period of time is measured. We measured a beam size once during the SCISSORS II experiments. In the previous measurement [4], we have measured counting rates in every 0.1 s (0.5 s) period for the E_e = 0.9 GeV (E_e = 1.2 GeV) mode. One of the tagging channels was measured using a CAMAC scaler in one measurement. Photon intensity near center of the beam could not be evaluated owing to counting loss by probleams of signal processing. To obtain the number of counts for several tagging channels without counting loss for a long time, we used a scaler circuit implemented in a general-purpose lgoic module called MPLM4X [5], which has a Xilinx Spartan-6 FPGA chip. We placed electric circuits nearby the tagging counter station in order to decrease the deterioration of the singals during the propagation. The counting rates of sixteen channels in the taggers were measured in order to check consistency of obtained center positions and widths of the electron beam. The number of data points in each side ($+x$ and $-x$) ranges from 10 to 20 in a 0.1 mm step. We measured the counting rates in one of the data points for a block RAM implemented in the FPGA of the MPLM4X. The block RAM has a depth of two minutes.

The scaler implemented in the FPGA was composed of the following functions:

1. MPLM4X_DCM2 converts an input clock of 10 MHz to a clock of 200 MHz and distributes other components,
2. EOS_RESET outputs a global reset signal until the READY state after power activation,
3. Scaler counts the number of hits of the taggers for 0,1 seconds,
4. Scaler_controller controls data which the ’Scaler’ component records,
5. the BRAM component gives a block RAM for describing the number of counts in 120 s, and
6. DAQ_Controller controls states of the constructed circuit in the measurement and data transmission between a PC using an RS-232C communication.

Figure 3 shows a block diagram of the components of the scaler.

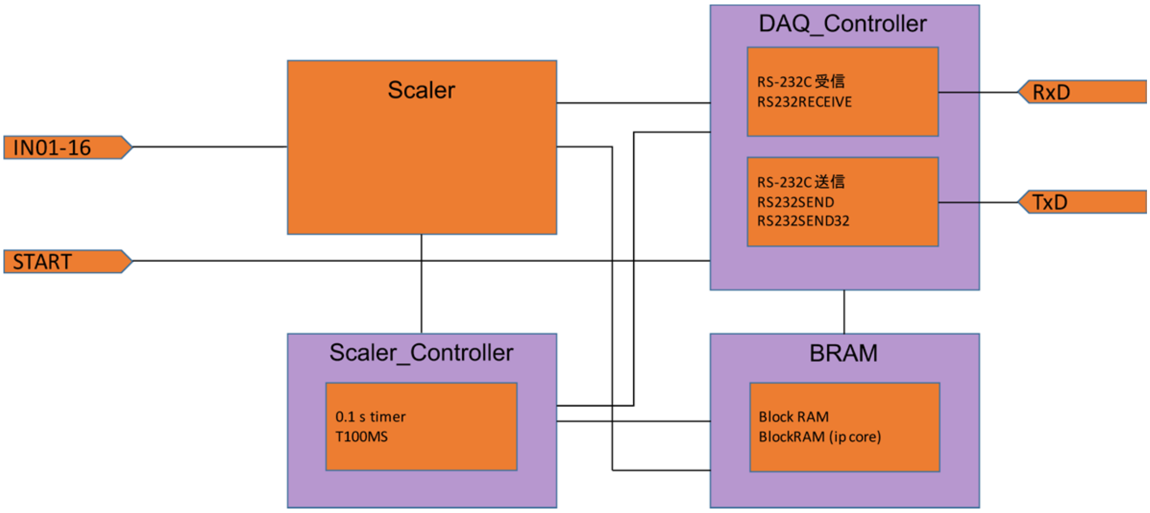

Fig.3. Block diagram of the scaler.

§4. Measurement of the electron beam profile

We have measured counting rates of the taggers after inserting the radiator in modes of E_e = 1.3, 1.0 and 0.8 GeV as shown in Fig. 4. The counting rate decays exponentially and the red lines are fitting curves expressed as

$$N(t) = \begin{cases} \exp(p_0 + p_1 t) & (\alpha(x) = |p_1|) \qquad (3) \\ \exp(p_0 + p_1 t) + \exp(p_2 + p_3 t) & (|p_1| > |p_3|,\ \alpha(x) = |p_3|) \qquad (4) \end{cases}$$

where p_0, p_1, p_2 and p_3 are fitting parameters and $\alpha(x)$ stands for a decay constant of the counting rates at the radiator's position of x. In case that the temporal changes explicitly have two different slopes between the former part and the latter part of time t, we used the fitting function given in Eq. (4).

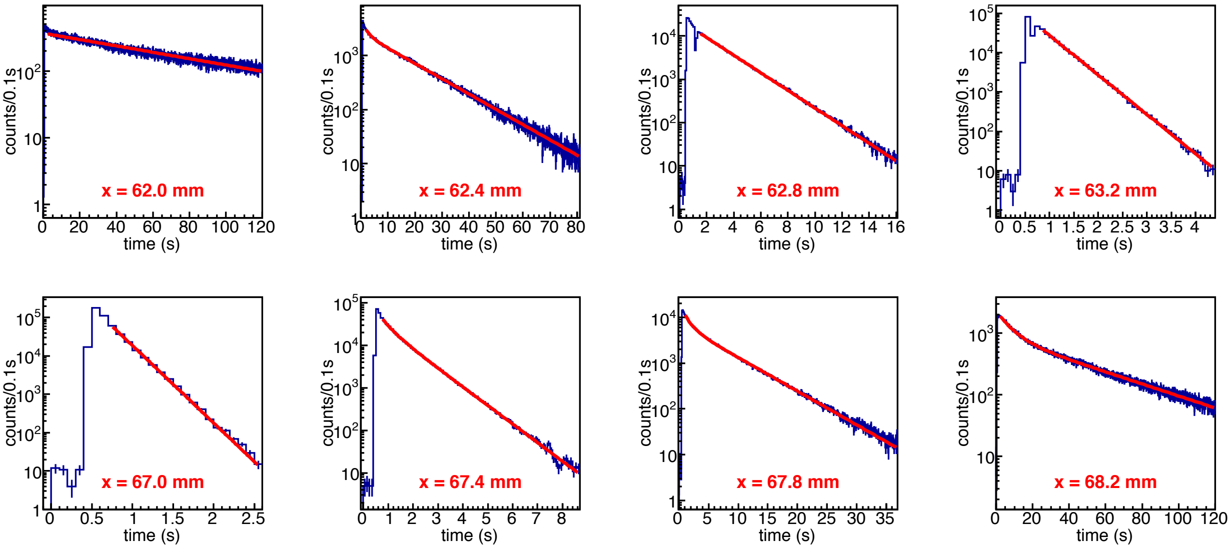

Fig.4. Tagging rates as a function of the elpased time after the radiator is inserted (first tagging channle, $E_e = 1.3$ GeV mode). The radiator position is described in each panel, and each red line shows the fitted function expressed in Eq. (3) or (4).

The decay constant $\alpha(x)$ were extracted by the fitting for measured points of the position x. Figure 5 shows results for all energy modes of E_e = 1.3, 1.0 and 0.8 GeV. We evaluated the center position and width of the circulating electrons by fitting with Gaussian function $g(x)$ given in the following equation

$$g(x) = C \exp\left(-\frac{(x-\mu_x)^2}{2\sigma_x^2}\right) \qquad (5)$$

where C denotes a scale parameter of the distribution, μ_x and σ_x are the position and width of the beam, respectively. Table 1 summarizes results of the measurement. The values in the table are the mean value of sixteen channels of the tagger. No dependence on the channels of the tagger is found and errors of the values are smaller than 10^{-3} mm. The width of the beam can be evaluated by Eq. (1) using parameters such as the Twiss parameter (β = 3.69 m) and parameters of the accelerator ($\epsilon = 1.38\times10^{-7}$ m, $\eta = 0.45$ m and $dp/p = 6.2\times10^{-4}$). The results of the calculation are also summarized in Table 1. Uncertanity of the calculation is approximately 10% due to accuracy of the parameters. The measured values are in agreement with the calculated values in the accuracy. The measured value in the

E_e = 0.8 GeV mode is slightly larger than the calculated value. This is because decreasing of emittance in vacuum has significant effect in lower energy of the electron beam.

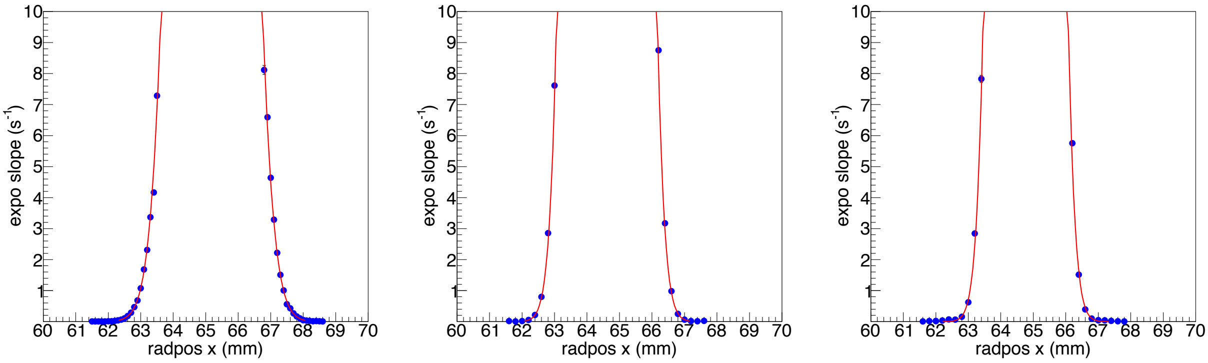

Fig.5. Decay constant $\alpha(x)$ as a function of the radiator position x. The left, central, and right panels show those for the 1.3 GeV, 1.0 GeV, and 0.8 GeV modes, respectively. The red curve in each panels shows the fitted function expressed in Eq. (5).

Table 1. Central position and width of the horizontal profile of the electron beam at the BM5 radiator position. The caluculated width is given using Eq (1) and the designed values for the Twiss and other parameters of the BST ring.

E_e (GeV)	center position (mm)	width (mm)	calculated width (mm)
1.3	65.19	0.73	0.77
1.0	64.61	0.57	0.59
0.8	64.77	0.51	0.47

§5. Summary

The horizontal electron beam size at the radiator point in the BST ring was measured for the first time. A scaler was implemented in the MPLM4X module in order to measure counting rates of the taggers. The beam sizes are 0.73, 0.57 and 0.51 mm for E_e = 1.3, 1.0 and 0.8 GeV, respectively. The measured widths of the beam are in agreement with the calculated widths in the 10% accuracy. Evaluation of the beam size by inserting a radiator is one of the important methods that we measure properties of an electron synchrotron. Measurement of a form of electron beams by a radiator is used as a monitor of circulating electrons in the synchrotron. We expect that the measured properties of electron beams feed back to operation of the accelerator and evaluation of properties of photon beams.

Acknowledgments

The authors wish to thank the ELPH accelerator staff for providing the electron beam in the stable condition. They also give I. Nagasawa their sincere gratitude for his technical support in the development of the MPLM4X module. This work was supported in part by Grant-in-Aid for Scientific Research (C) (26400287). One of the authors (Y. O.) would like to thank the Advanced Leading Graduate Course for Photon Science (ALPS) team at the University of Tokyo for giving a chance to participate this interesting measurement.

References

[1] F. Hinode *et al.*: Journal of Physics: Conference Series **425** (2013) 072011.

[2] F. Hinode *et al.*: Proceedings of 2005 Particle Accelerator Conference (2005) 2458.

[3] T. Ishikawa *et al.*: Nucl. Iintsrum. Meth. A **622**, (2010) 1.

[4] F. Miyahara: Internal GeV-γ Analysis Note, **33** (2007).

[5] I. Nagasawa and T. Ishikawa: Internal GeV-γ Analysis Note, **380C** (2015).

(ELPH Experiment : #2822)

Performance of Undoped CsI Crystal with Both-end Readout for the KOTO Experiment at J-PARC

H. Nanjo[1*], H. Haraguchi[2], M. Iwasa[3], H. Kanauchi[3†], S. Su[4], T. Sakurai[3],
M. Sasaki[3], Y. Sugiyama[2], Y. Tajima[3], M. Togawa[2], T. Yamanaka[2],
and H.Y. Yoshida[3]

[1]*Department of Physics, Kyoto University, Kyoto, 606-8502, Japan*
[2]*Department of Physics, Osaka University, Toyonaka, 560-0043, Japan*
[3]*Department of Physics, Yamagata University, Yamagata, 990-8560, Japan*
[4]*Department of Physics, University of Michigan,, Ann Arbor, MI 48109, USA*

Both-end readout of undoped CsI crystals was developed in order to distinguish gamma and neutron for the KOTO experiment at J-PARC. Gamma and neutron can be distinguished with the depth of hits in the crystal, since the radiation length of gamma is shorter than the interaction length of neutron. Photon sensors on both ends of the crystal provide information of the depth from the difference of their corresponding hit times. We report on the performance of the both-end readout using a positron beam, where a photomultiplier tube was used for one end, and multi-pixel photon counters for the other.

§1. Introduction

We are conducting the KOTO experiment [1] at J-PARC to search for the rare CP-violating decay, $K_L \to \pi^0\nu\overline{\nu}$. Its branching ratio, $\mathcal{B}(K_L \to \pi^0\nu\overline{\nu})$, is predicted to be 3×10^{-11} in the Standard Model (SM) with the theoretical uncertainty of ∼1% [2]. Such highly suppressed and well predicted process in the SM is suitable to explore new physics beyond the SM in higher energy scale. Some new physics models predict an-order-of-magnitude enhancement of the branching ratio for new physics in the energy scale 1-100 TeV [3–6]. The KOTO experiment searches for such new physics with a single event sensitivity close to the SM prediction.

The KOTO experiment identifies the decay $K_L \to \pi^0\nu\overline{\nu}$ by requiring only two gammas from a π^0 and nothing else. Figure 1 shows the KOTO detector, into which a narrow collimated K_L beam enters. The “CsI calorimeter” consists of 2716 undoped CsI crystals stacked inside a cylinder 2 m in diameter. The dimensions of the crystals are $2.5\times2.5\times50\,\mathrm{cm}^3$ for the inner region, and $5\times5\times50\,\mathrm{cm}^3$ for the outer region. The scintillation light is read out by a photomultiplier tube (PMT) attached on the downstream end of each crystal. The two gammas are detected with the CsI calorimeter, and the hit positions and energies are reconstructed from the clusters of their hit crystals. The decay vertex is reconstructed by assuming that the two gammas decayed from a π^0 on the beam axis. Neutral pions with larger

---

[*] Present address: Department of Physics, Osaka University, Toyonaka, 560-0043

[†] Present address: Department of Physics, Tohoku University, Sendai, 980-8578

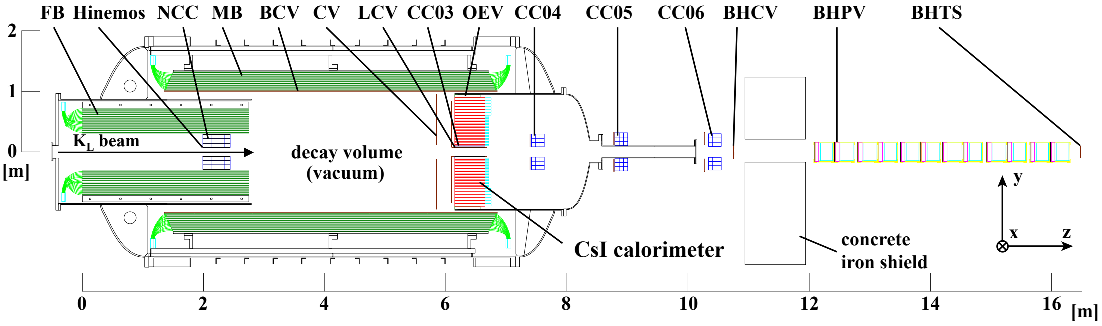

Fig.1. Cross-sectional view of the KOTO detector.

transverse momentum are selected in order to reject the decay $K_L \to 2\gamma$. The other detectors are used as veto detectors in order to ensure "nothing else", thus rejecting the other K_L decays that have charged particles or more than two gammas in the final state.

Neutrons also exist in the beam, and small fraction of neutrons remains in the beam halo escaping from the beam collimation. Neurons in the beam halo may hit the veto-detector components near the beam and generate a π^0 which decays into two gammas and mimics the signal. This type of background is suppressed by requiring the decay vertex to be away from detectors near the beam.

A neutron in the beam halo also can hit the CsI calorimeter directly and generate two clusters. One cluster is generated from a hadron shower by the incident neutron. The second cluster can be made from another neutron generated in the hadron shower which travels in the calorimeter by some distance from the first cluster. This two clusters will contribute to background, and this is the main background source in the KOTO physics analysis of the data taken in 2013. In the analysis, one event was observed with all the event selection at the sensitivity of 1.29×10^{-8} [7], The observed one event is consistent with the expected level of this background, which is still high even after cluster shape information (hit patterns of the crystals in a cluster) greatly reduces this background. We are further investigating reduction methods of this background using cluster shape information and waveform information from the PMT signals.

In addition to the analysis efforts, we are preparing to add a new hardware to reduce this background, new readout of the scintillation light on the upstream end of the crystal. The timing difference between the upstream and downstream readouts will provide the depth of the energy deposition in the crystal. With the depth, one can distinguish between gammas and neutrons because the gamma showers are localized in the upstream end whereas the location of neutron showers are distributed broadly due to the difference between the interaction length and radiation length of the crystal. the background by one order of magnitude at least. Combining the shower depth measurement with analysis cut improvements, reduction of the neutron-induced background by three orders of magnitude is expected, which is enough to reach the sensitivity close to the SM prediction.

§2. Upstream readout

The downstream readout with PMTs in the current KOTO experiment is unchanged in order to keep the calorimeter performance. For the upstream readout, a multi-pixel photon counter (MPPC) is planned, which is multi-pixel silicon avalanche photodiode operating in Geiger mode. It enables photon-counting capability with a typical gain of 10^6 at a relatively low operating voltage around 60 V. The MPPC, HAMAMATSU Photonics S13360-6050CS, was selected, which had the active area of $6 \times 6\,\mathrm{mm}^2$, the pixel size of $50 \times 50\,\mu\mathrm{m}^2$, and a silicone window. The window material, silicone, makes the MPPC sensitive to UV photons, which fits the scintillation spectrum of the the undoped CsI with the maximum scintillation yield at the wavelength of 310 nm. The features of the MPPC are as follows.

- Gain, typically 1.7×10^6
- Peak photon detection efficiency of 40% at the wavelength of 450 nm
- Sensitivity to UV photons, photon detection efficiency of 20% at the wavelength of 300 nm
- Small response to charged particles, single photon level.
- Low mass, 0.6 g for $6 \times 6\,\mathrm{mm}^2$ sensor
- Cost effectiveness

For the future upgrade of the calorimeter with the both-end readout, we will attach one MPPC to each $2.5 \times 2.5\,\mathrm{cm}^2$ crystal, and four MPPCs to each $5 \times 5\,\mathrm{cm}^2$ crystal. The total number of MPPCs needed will be 4096, but the number of readout channels can be reduced to be 256, since fine segmentation is not needed for the discrimination of neutron and gamma. The design will be achieved with a series connection of four MPPCs, and with an amplifier summing four such outputs.

§3. Performance test with positron beam

3.1 Motivation

In this test experiment, we tested the feasibility of measuring the shower depth with the both-end readout. The timing resolution is important, since the discrimination between neutron and gamma is based on the timing difference between the two readouts. This discrimination was applied after the signal event selection, requiring the energy of the cluster to be above 100 MeV. The corresponding photo-electron yield of the PMT was 900 with the typical light yield of 9 photo-electron/MeV. The expected light yield of the MPPC was 90 considering the smaller photon detection area of the MPPC.

3.2 Setup of both-end readout

We prepared an undoped CsI crystal with four MPPCs[‡] and a PMT[§] as shown in Fig. 2. The crystal was 50 cm long and $5 \times 5\,\mathrm{cm}^2$ in cross-section. The PMT was 65 mm in diameter with a quartz window. A UV transmitting filter[¶] was inserted in order to remove slow components of the scintillation light.

[‡] HAMAMATSU Photonics S13360-6050CS

[§] HAMAMATSU Photonics H6521

[¶] SIGMAKOKI UTVAF-50S-33U

Silicone optical joints[‖] were also inserted for the good optical contact[**]. Four MPPCs were soldered on a printed circuit board (PCB), and another silicone joint was also inserted between the MPPCs and the crystal.

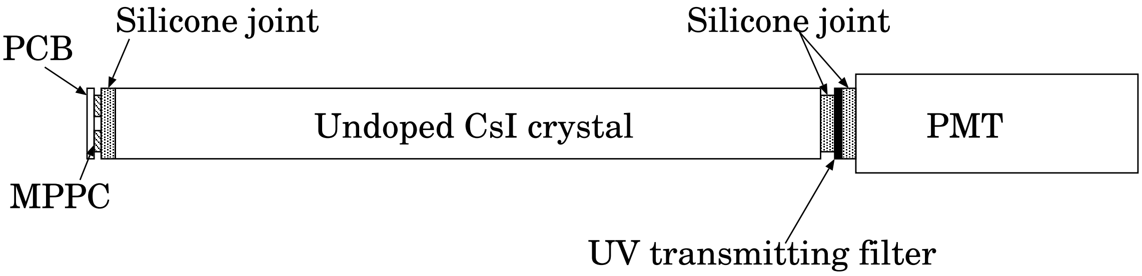

Fig.2. Setup of the both-end readout.

The four MPPCs were connected in series and bias voltage of 219 V was applied, which corresponded to the gain of 1.7×10^6 for each MPPC. The output was amplified by a factor of 5 using a commercial amplifier with the input impedance of 50 Ω.

To study the light propagation speed inside the crystal, we placed the crystal normal to the beam as shown in Fig. 3, and moved the crystal. Four trigger counters were prepared. The most upstream one defined the timing with a plastic scintillator 1 cm thick and 5 cm × 7 cm in cross-section. The other three counters defined the beam size with plastic scintillators 0.5 cm thick and $1 \times 1\,\mathrm{cm}^2$ in cross-section

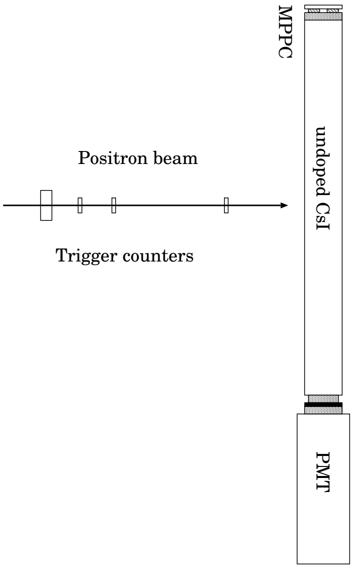

Fig.3. Setup perpendicular to beam.

To study the energy and the response timing for electromagnetic showers, the crystal was placed parallel to the beam as shown in Fig. 4,

---

[‖] MOMENTIVE TSE3032

[**] The PMT and MPPCs were pushed to the crystal with the spring force of 5.6 N.

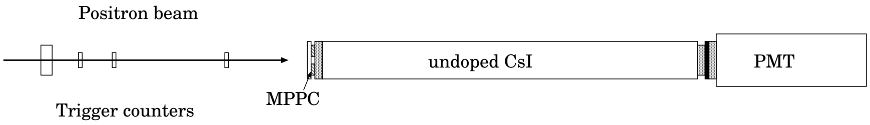

Fig.4. Setup parallel to beam.

3.3 Data acquisition and waveform

Data was taken with an oscilloscope. The trigger was issued by the coincidence of four trigger scintillators. The waveforms from the MPPC and the PMT on the crystal were recorded with the input impedance of 50 Ω, and with the time interval of 0.4 ns. The logic signal for the trigger was also recorded. The triggered waveforms were acquired through an Ethernet cable

The waveforms of the PMT and MPPC are shown in Fig. 5 and Fig. 6, respectively, which were collected in the perpendicular setup with 500 MeV/c positrons. The decay time of the PMT pulse was 22 ns, which corresponded to the decay time of the scintillation. The MPPC waveform can be fitted with convolution of two exponentials with the decay times of 22 ns and 61 ns. The former corresponded to the scintillation decay, and the latter corresponded to the response of the MPPC to a single photon.

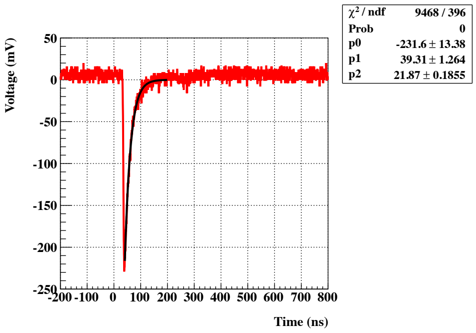

Fig.5. Waveform from PMT.

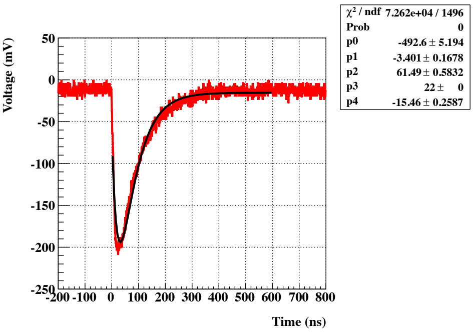

Fig.6. Waveform from MPPC.

The timing was decided from the obtained waveform using constant fraction timing at the half pulse height. The base line was decided with earlier samples. The highest sample was used to decide the peak height. The constant fraction timing was decided with the middle height between the base line and peak height. The energy deposition in the crystal was measured with the area between the base line and waveform.

3.4 Energy response and calibration

Energy response of the both-end readout was studied in the parallel setup with four momentum configurations of the positron beam, 200, 400, 600, and 800 MeV/c. The distributions of the energy deposition for the PMT readout are shown in Fig. 7, and those for the MPPC are shown in Fig. 8. Figure 9 shows the peak position as a function of the energy deposition in the crystal simulated with Geant4. Linearity of 3% is obtained for both readouts.

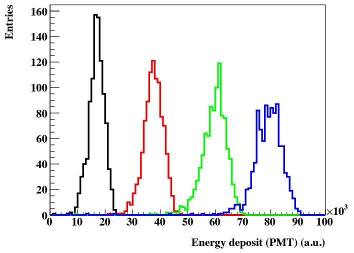

Fig.7. Distributions of the energy deposition with the PMT readout for the positron momentum 200 (black), 400 (red), 600 (green), and 800 (blue) MeV/c.

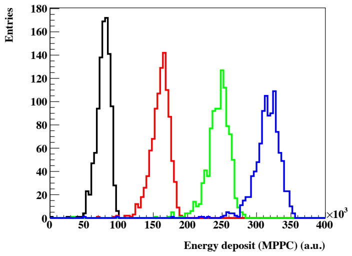

Fig.8. Distributions of the energy deposition with the MPPC readout for the positron momentum 200 (black), 400 (red), 600 (green), and 800 (blue)MeV/c.

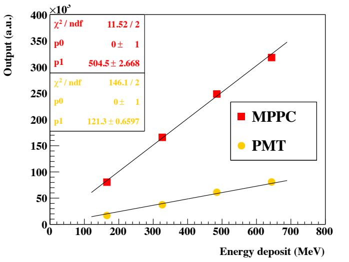

Fig.9. Peaks of measured energy deposition as a function of the energy deposition simulated with Geant4. Linear fits are also shown.

3.5 Propagation time and timing difference

The propagation time of the both-end readout was studied in the perpendicular setup by moving the incident position of the beam to -18, -9, 0, 9, and 18 cm, along the 50-cm long crystal, where 0 is at the middle of the crystal. The momentum of the positron beam was 500 MeV/c. Figure 10 †† shows the timing distributions for the PMT readout, and Fig. 11 shows those for the MPPC readout. The peak timings are plotted as a function of the beam position in Fig. 12. Linear relations were obtained and the propagation times were 10.7 ns/m and 8.0 ns/m for the PMT and MPPC readouts, respectively. This difference may be partially explained with the dispersion of the CsI. The MPPC without a UV-transmitting filter was sensitive to scintillation with the wavelength larger than 400 nm, whereas the PMT with the UV filter was only sensitive to the scintillation with the wavelength shorter than 400 nm. The refractive index of CsI is 2 for the wavelength of 300 nm, and 1.8 for 500 nm. This makes the propagation time with the MPPC readout shorter by 10%.

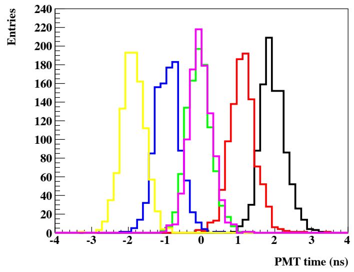

Fig.10. Timing distributions for the PMT readout for the beam positions, -18, -9, 0, 9, 18 cm.

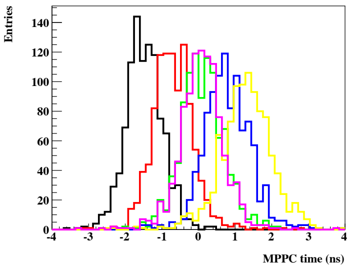

Fig.11. Timing distributions for the MPPC readout for the beam positions.

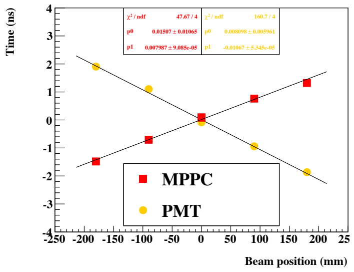

Fig.12. Peak times as a function of the beam incident position.

The distributions of the time difference between the PMT and MPPC readout are shown in Fig. 13. The peaks and resolutions in the distributions are shown as a function of the beam position in Fig. 14

[††] The measurements for the center position were performed twice, the first and the last measurement in this series of measurements, which shows the stability and reproducibility.

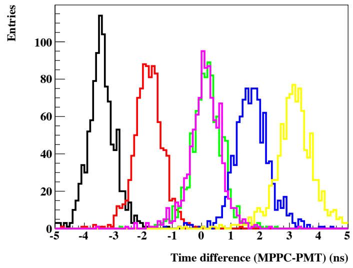

Fig.13. Distributions of the time difference in the both-end readout.

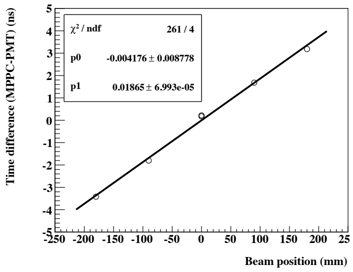

Fig.14. Peaks of the time difference as a function of the beam position.

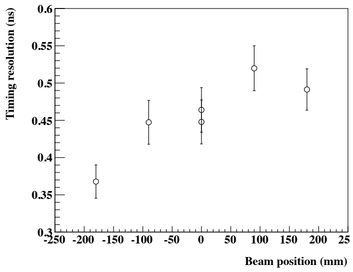

Fig.15. Resolutions of the time difference distribution as a function of the beam position.

and Fig. 15, respectively. The linear response can be used to evaluate the scintillation position in the crystal, and the timing resolution was less than 0.6 ns for the energy deposition of 110 MeV. The worse resolution in the downstream region (positive side in the position) is explained with smaller light yield measured in the MPPC readout for the region. The effective propagation time was 18.65 ns/m, which corresponded to 9.3 ns for the maximum time difference in the 50-cm long crystal. The timing resolution corresponds to the position resolution of 3.2 cm.

3.6 Timing difference for electromagnetic shower

The time difference of the both-end readout for the electromagnetic shower was studied in the parallel setup with the positron momentum of 200, 400, 600, and 800 MeV/c. Figure 16 shows the distributions of the time difference, which is interpreted that the position of the electromagnetic shower was reconstructed near the upstream end due to the short radiation length. The time difference of −3.2 ns corresponded to 79 mm (4.2 radiation length) deep from the upstream surface of the crystal. It is similar to the shower maximum position, 2.4-3.8 radiation lengths for the momentum range. The timing resolution less than 0.6 ns was achieved, which was better than our expectation 0.8 ns from the simulation study.

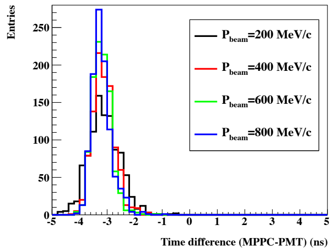

Fig.16. Distribution of the time difference in the parallel setup.

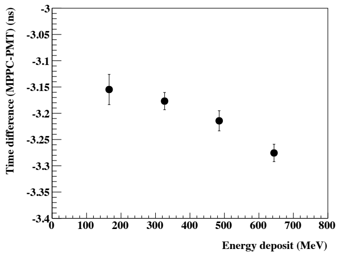

Fig.17. Peaks of the time difference as a function of the deposition energy in the crystal

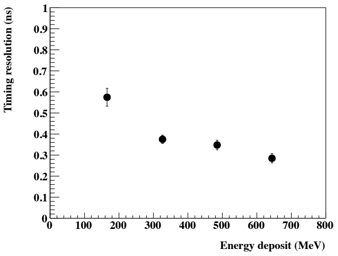

Fig.18. Width of the time difference as a function of the deposition energy in the crystal.

§4. Conclusion

We first demonstrated the performance of the both-end readout with a PMT and MPPC for the undoped CsI crystal. By using the timing difference of the both-end readout, the depth of the energy deposition in the crystal was obtained with the resolution better than 3.2 cm for the incident positron momentum larger than 200 MeV/c.

Acknowledgment

We would like to express our gratitude to the staff of the Research Center for Electron Photon Science. Part of this work is supported by JSPS/MEXT KAKENHI Grant Number 23224007.

References

[1] T. Yamanaka for the KOTO Collaboration, PTEP **2012**, 02B006 (2012).
[2] A. J. Buras, D. Buttazzo, J. Girrbach-Noe and R. Knegjens, JHEP **1511**, 033 (2015).
[3] A. Buras, PoS FWNP , 003 (2015).
[4] M. Blanke, A. J. Buras and S. Recksiegel, Eur. Phys. J. C **76**, no. 4, 182 (2016).
[5] M. Blanke, PoS KAON **13**, 010 (2013).
[6] M. Tanimoto and K. Yamamoto, PTEP **2015**, no. 5, 053B07 (2015).
[7] K. Shiomi for the KOTO Collaboration, Proceedings of the 8th International Workshop on the CKM Unitarity Triangle (CKM 2014), Vienna, Austria, September 8-12, 2014.

(ELPH Experiment : #2832)

Test of an X-ray flat panel sensor as a beam profile monitor

H. Kanda[1], K. Honda[1], T. Ishikawa[2], M. Kaneta[1], K. Maeda[1], M. Miyabe[2],
Y. Muroi[1], W. Nakai[3], S. N. Nakamura[1], A. Ninomiya[1], Y. Obara[3], K. Ozawa[4],
K. Ozeki[1], T. Sasaki[1], H. Shimizu[1], and A. O. Tokiyasu[2]

[1]*Graduate School of Science , Tohoku University, Sendai 980-8578, Japan*
[2]*Research Center for Electron Photon Science, Tohoku University, Sendai 982-0826, Japan*
[3]*Department of Physics, University of Tokyo, Tokyo 113-0033, Japan*
[4]*Institute of Particle and Nuclear Studies, High Energy Accelerator Research Organization*
(KEK), Tsukuba 305-0801, Japan

We have been developing a beam profile monitor for 1 GeV region gamma-ray beams using an X-ray flat panel sensor. It consists of a thin inorganic scintillator for X-rays and a CMOS area sensor. For obtaining the profile of the 1 GeV region gamma-ray beams, carriers induced by the passing of gamma-ray photons and $e^{\pm}$ converted from them are accumulated in its pixels. We tested its sensitivity and linearity to the gamma-ray photons with various types of converter plates. It was found to be dependent on the thickness of the converter in X_0. We also tested its accuracy by the x and y spreads of the profile of the gamma-ray beams and the positron beams. The gamma-ray beam profile was consistent with the one measured with a beam profile monitor consisting of scintillation fiber hodoscopes triggered in coincidence with a hit on a tagging counter corresponding to a 1 GeV photon. The positron beam profile was consistent with the one measured with a Gas Electron Multiplier tracker. From these results, sufficient sensitivity and accuracy were expected to the X-ray frat panel sensor for the use of the beam profile monitor.

Diagnosis of a beam is one of the matters of importance for defining and optimizing the experimental condition in beam experiments. 1 GeV region tagged photon beams are provided at The Research Center for Electron Photon Science (ELPH), Tohoku University. The beams are produced by bremsstrahlung of 1.3 GeV electrons on the carbon fiber target. Energy of emitted photon are tagged with tagging counters which measures the momentum analyzed electrons after the photon emission [1, 2]. Several kinds of beam profile monitor (BPMs) for 1 GeV region gamma-ray beams have been developed and in use at ELPH. They are used for monitoring and tuning the gamma-ray beams. One consists of plastic scintillator hodoscopes to detect the electron and positron converted from the photon (HSBPM) [3]. It is remote-controllable, real-time, and radiation-hard. However, it needs signal processing electronics and a data acquisition system which usually push up its price. The width of one segment of the hodoscopes was 3 mm. It is sufficient for finding the center of the beam. But it is not sufficient to inspect reason of deformation of a beam profile if it is deformed. The other one consists of a lead plate and an instant photographic film (Gamma Camera). It is compact and with good spatial resolution. However, it needs manual development process and its linearity is not guaranteed. A new kind of the BPM which combines compactness, spatial resolution and remote-controllability was waited for.

One of the candidates was an X-ray Flat Panel Sensor (XFPS). It is an area sensor widely used for the X-ray diffraction, the medical X-ray imaging, and the nondestructive testing [4]. It has advantages over other kinds of X-ray imaging devices as a following list:

over X-ray films better linearity, digital data acquisition and repetitive use

over Image intensifier cameras compactness and freedom from distortions

over Imaging plates instant imaging.

We adopted a Remote RadEye2 manufactured by Rad-icon Corporation [5] for the test. It consists of a thin inorganic scintillator, Kodak Min-R2190 [6, 7], for the absorption of X-ray photons and a CMOS area sensor for the detection of visible lights emitted from the scintillator (Fig. 1). Because the thickness of the scintillator is 47 μm and the base material of the CMOS sensor is a silicon, the sensitivity of the XFPS to the 1 GeV region gamma-ray was expected to be low. We added a converter plate to increase its sensitivity. The principle of gamma-ray detection is also demonstrated in Fig. 1. The converter absorbs the X-ray photons but converts the gamma-ray photons with sufficient energy to electrons and positrons which travel through the scintillator and the CMOS sensor for induction of the signal to the CMOS sensor.

The Remote RadEye2 consists of a compact sensor head and an electronic circuit box. The size of the sensor head is a $111.0 \times 77.5 \times 24$ mm^3 with a 49.3×49.2 mm^2 effective area. A DVI cable was used for the connection between the sensor head and the circuit box. It enables the freedom of the location of the sensor head. The electronics module is connected to a Windows PC for the data acquisition with a Gigabit Ethernet. Thus the remote monitoring of the beam profile is achieved. The characteristics of these BPMs are summarized in Table 1. The spatial resolution of the HSBPM in the table was estimated as an ideal resolution expected for 3 mm pitch pixel size. Its unit, lp/mm, means the number of pairs of black and white lines resolvable with 50% contrast. Another unit ppi is an abbreviation of pixels per inch. A BPM for the 1 GeV region gamma-ray beams with linearity, spatial resolution, and remote monitoring was expected with the XFPS.

Table 1. Comparison of the characteristics of the detectors for the beam profile monitoring.

	Gamma Camera (w/ Polaroid 53)	HSBPM	XFPS
Spatial resolution	12 – 14 lp/mm	0.16 lp/mm (8.5 ppi)	10 lp/mm (530 ppi) 3.5 lp/mm w/ Min-R2190
Fiducial size	131×106mm^2	48×48mm^2	49.3×49.2mm^2
Whole size	$200 \times 150 \times 30$ mm^3	$420 \times 420 \times 246$ mm^3	$111 \times 77.5 \times 24$ mm^3
Data	Photographic image	Counts of the $e^{\pm}$ hits on the scintillator	Pixel Brightness
Detector	Pb converter + AgBr	Al converter + Plastic Scintillator	Converter + Gd_2O_2S:Tb + CMOS image sensor
Remote monitoring	Not possible	Possible	Possible

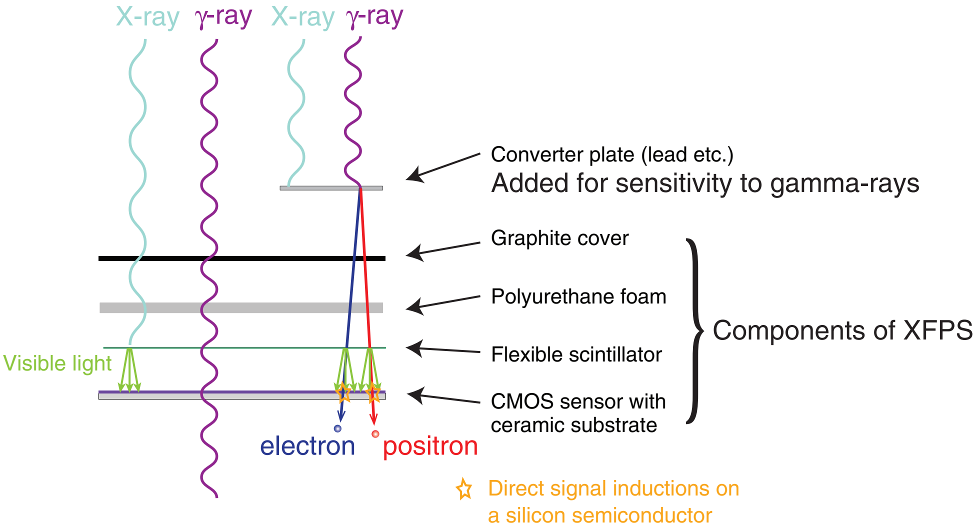

Fig.1. Schematic view of the cross sectional structure and the principle of gamma-ray detection of the RadEye2 sensor.

We tested the sensitivity of the XFPS with various converter plates. The materials and the thicknesses of the converter plates were 1 mm Al (0.011 X_0), 2 mm Al (0.022 X_0), 4 mm Al (0.045 X_0) 8 mm Al (0.090 X_0), 10 mm Al (0.11 X_0), 1 mm Cu (0.07 X_0), 2 mm Cu (0.14 X_0), 4 mm Cu (0.28 X_0), 0.5 mm Pb (0.089 X_0), 2 mm Pb (0.36 X_0), and 4 mm Pb (0.71 X_0). The tagged photon beam with intensity of approximately 2 MHz for the tagged region (60 MHz including the untagged region) were irradiated on the XFPS with the converter. The XFPS was placed 10 m downstream of the target for the bremsstrahlung. The accumulation time was set as 1 s. We obtained 5 images before the exposure as the background and 5 images during the exposure. The averaged background image was subtracted from the averaged beam image to obtain a image data for the beam profile. An example of the image obtained with a 4 mm Cu converter is shown in (Fig. 2(a). A region of interest (ROI) is shown as an black open box in Fig. 2(a). The brightnesses of the pixels in the ROI was averaged for the test of the sensitivity. The averaged brightness with a normalization to the number of irradiated photons is shown as a function of the material thickness(x) in a unit of X_0 in Fig. 2(b). It was well fitted with a function:

$$f(x) = C_1 N_{e^\pm}(x) + C_2 N_\gamma(x), \tag{1}$$

where $N_{e^\pm}(x) = 2\left(1 - \exp(-\frac{7}{9}x)\right)$ denotes the number of $e^\pm$ converted from the gamma-ray photon increasing with x and $N_\gamma(x) = \exp(-\frac{7}{9}x)$ denotes the number of the gamma-ray photon of the beam decreasing with x. The strong dependence on $N_{e^\pm}$ suggests the linearity of the brightness to the number of $e^\pm$. The intensity of the X-ray emission due to the ionization by the passage of $e^\pm$ was considered to correlate to $N_{e^\pm}$. But its contribution cannot be separated from this measurement. Monte Carlo study with a detailed electromagnetic interaction with the EGS5 [8] is currently underway.

We compared the profile of the 1 GeV region gamma-ray beams with the one measured with the HSBPM. The intensity of the gamma-ray beams was typically 10 MHz for the tagged region (300 MHz including the untagged region). The distance from the target for the bremsstrahlung was 20 m and thus

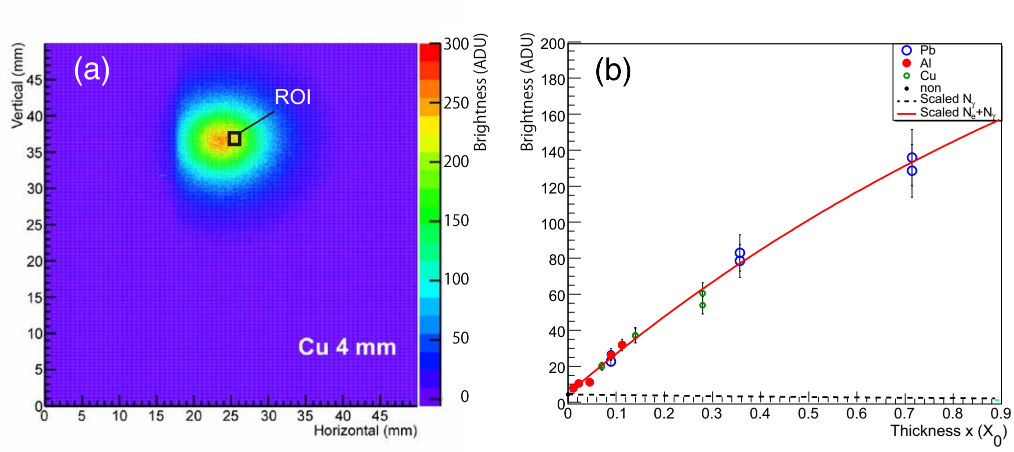

Fig.2. An example of the image data for a gamma-ray beam profile obtained with a 4 mm Cu converter plate (a). A region of interest for the test of sensitivity is shown as a black open box. The averaged brightnesses with Cu (small open circle), Al (closed circle), and Pb (open circle) converters and without any converter (small closed circle) are shown as a function of their thickness in X_0. The fitting function (solid curve) and its gamma-ray photon component (dotted curve) are drawn.

the flux density was almost similar to the previous test of sensitivity. Thus the accumulation time of 1 s was sufficient for obtaining the beam profile with the XFPS. We found that the HSBPM suffered the broad spread of multiple-scattered $e^{\pm}$ generated from the the low energy photons ($E_\gamma < 0.2$ GeV) by a Monte Carlo simulation. In order to reduce the broad spread, the HSBPM was triggered in coincidence with a tagging counter corresponding to $E_\gamma = 1$ GeV. The obtained profiles and their horizontal (x) and vertical (y) projections are shown in Fig. 3. These projections were fitted with a sum of two Gaussian functions. The spread was evaluated as the standard deviation (S) of the fitted function. It was obtained from the height (h_i), mean (m_i) and σ (σ_i) of i-th Gaussian function with a following formula:

$$M = \frac{\sum_{i=1}^{2} h_i m_i \sigma_i}{\sum_{i=1}^{2} h_i \sigma_i} \tag{2}$$

$$S = \sqrt{\frac{\sum_{i=1}^{2} h_i \sigma_i (\sigma_i^2 + (m_i - M)^2)}{\sum_{i=1}^{2} h_i \sigma_i}}. \tag{3}$$

The result of the fitting is summarized in Table 2. The x and y spreads of the positron beam profile obtained with the XFPS was consistent with the ones obtained with the HSBPM.

We also measured the profile of 400 MeV/c positron beam at the ELPH test beam line. A trigger counter, a Gas Electron Multiplier (GEM) tracker [9] and the XFPS was aligned on the positron beam line from the upstream. The distance between the GEM tracker and the XFPS was minimized as 50 mm to assure that x and y positions of a positron passing through the GEM tracker were the same

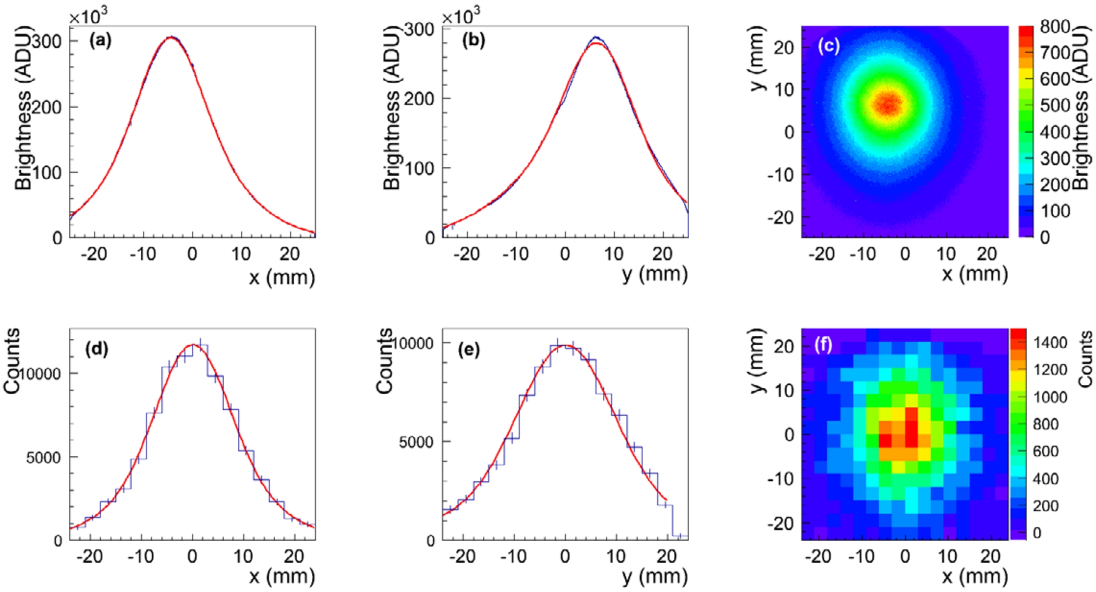

Fig.3. The gamma-ray beam profiles obtained with the X-ray flat panel sensor (c) and the HS-BPM (f). Panels (a), (b), (d), and (e) show x-projection of (c), y-projection of (c), x-projection of (f), and y-projection of (f), respectively. Each projection was fitted with a sum of two Gaussian functions.

Table 2. Summary of the x and y spreads of the 1 GeV region gamma-ray beams measured with the XFPS and the HSBPM.

	x spread (mm)	y spread (mm)
XFPS	9.5 ± 0.1	12.1 ± 0.2
HSBPM	9.6 ± 1.0	12 ± 1

as those passing through the XFPS. Strips with 350 μm pitch in x direction and 1400 μm pitch in y direction were used for the readout of the signal from the GEM tracker. Two dimensional position of a charged particle can be obtained using the GEM tracker with better than 100 μ m resolution in Gaussian σ for the x direction. It was thus expected to be the optimum position sensitive detector to test the resolution of the XFPS. The typical intensity of the positron was 4 kHz. We took typically 10 beam images with 1 s accumulation during the beam exposure period and 2 background images during the beam stop period. In total, 3000 beam images and 600 background images were obtained in 1.5 hours. The summed background was multiplied by approximately 5 and subtracted from the summed beam image. The hit positions on the GEM tracker were recorded at the same time. Because of the DAQ efficiency of the GEM tracker, approximately 50% of the positrons passing through the setup were recorded. The obtained profiles and their x and y projections are shown in Fig. 4. These projections were fitted with a Gaussian function for the evaluation of the spread of the beam. A fixed error was set to all the data points of x and y projections of the beam profile obtained with the XFPS. It was estimated with the fluctuation of the base line after the subtraction of the background. Statistic errors were set to all the data points of x and y projections of the beam profile obtained with the GEM tracker.

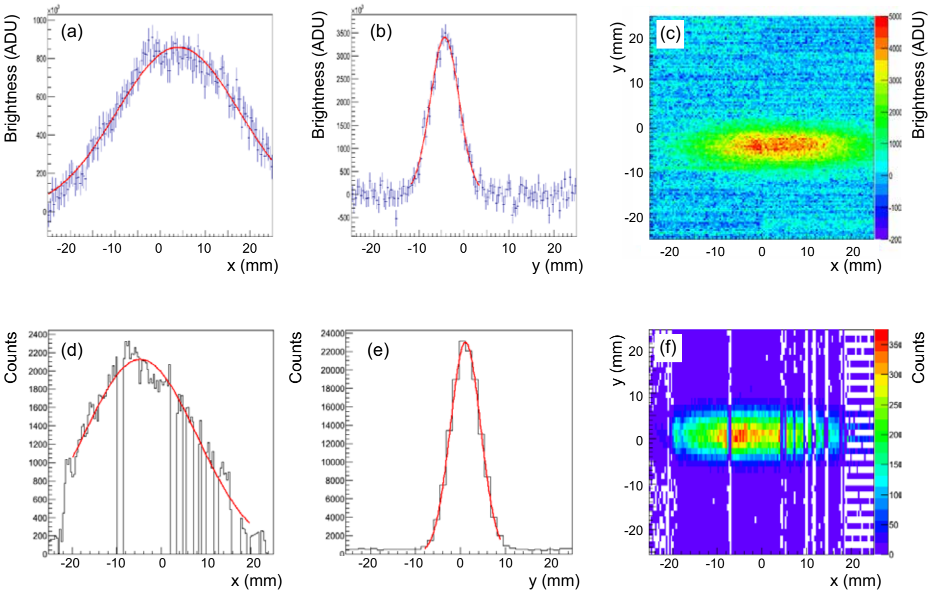

Fig.4. The profiles of a positron beam obtained with the X-ray flat panel sensor (c) and the GEM tracker (f). Panels (a), (b), (d), and (e) show x-projection of (c), y-projection of (c), x-projection of (f), and y-projection of (f), respectively. Each projection was fitted with a Gaussian function.

The Gaussian σs obtained by the fitting and their errors are summarized in Table 3. Because of the dead channels of the GEM tracker in x direction, the result of the fitting was varied with changing the region of interest for fitting. Thus the range of the σs was given in the table. The x and y spreads of the positron beam profile obtained with the XFPS was consistent with the ones obtained with the GEM tracker.

Table 3. Summary of the x and y spreads of the 400 MeV/c positron beam measured with the XFPS and the GEM tracker.

	x spread (mm)	y spread (mm)
XFPS	13.6 ± 0.2	3.2 ± 0.1
GEM tracker	$12.4 - 13.5$	3.36 ± 0.01

In summary, we tested the XFPS to be used as the beam profile monitor for 1 GeV region gamma-ray beams, regarding on the sensitivity and accuracy by comparing the output for various matter and thickness of converter plates using 1 GeV region gamma-ray beams. It was found to be dependent on the thickness of the converter in X_0 and linear to the number of passing $e^{\pm}$. The beam profile of the gamma-ray photons of a few tens of MHz were measured using a 1 mm thick lead plate with accumulation time of 1 s with sufficient sensitivity. The x and y spreads of obtained beam profile was consistent with the ones measured for 1 GeV gamma-ray beam with the HSBPM. The x and y spreads of the beam profile of the 400 MeV/c positron beam was consistent with the ones measured with the GEM tracker. It also suggests the sufficient linearity to the number of positron passing through the XFPS. It is the first application of the XFPS to the gamma-ray beam monitor. A software for easy image acquisition synchronized to the beam spill is currently developed. It will provide more efficient monitoring and tuning method for the gamma-ray beams.

Acknowledgment

We would like to thank the administration and technical staff in ELPH for their support.

References

[1] H. Yamazaki *et al.*: Nucl. Instr. and Meth. in Phys. Res. A **536** (2005) 70.

[2] T. Ishikawa *et al.*: Nucl. Instr. and Meth. in Phys. Res. A **622** (2010) 1.

[3] M. Nanao, T. Ishikawa, and H. Shimizu: Research Report of Laboratory of Nuclear Science, Tohoku University **36** (2003) 56.

[4] Hamamatsu Photonics K.K.: Opto-Semiconductor Handbook (2014).

[5] T. Graeve and G. P. Weckler, in Proc. SPIE Vol. **4320** (2001) 68.

[6] Michael Farrier, Thorsten Graeve Achterkirchen, Gene P. Weckler, and Alex Mrozack: IEEE trans. Elec. Dev. Vol. **56** (2009) 2623.

[7] Eastman Kodak Company: CAT No. **173 9473** (2006).

[8] H. Hirayama *et al.*: The EGS5 Code System, Stanford Linear Accelerator Center Report SLAC-R-730 (2005).

[9] K. Kanno *et al.*: Nucl. Instr. and Meth. in Phys. Res. A **819** (2016) 20.

(ELPH Experiment : #2835)

Performance Test of a Sampling Calorimeter for the SPring-8/LEPS2 experiment

A. O. Tokiyasu[1], M. Yosoi[2], H. Goto[2], Y. Yanai[2], and M. Miyabe[1]

[1]*Research Center for Electron Photon Science, Tohoku University, Sendai 982-0826*
[2]*Research Center for Nuclear Physics, Osaka University, Ibaraki 567-0047*

In the SPring-8/LEPS2 experiment, we will use a sampling calorimeter system to measure the energies of γ-rays from hadron decays. We performed a test experiment using a positron beam with the energy upto 650 MeV, and investigated the performance of the calorimeter. The energy resolution of the calorimeter was found to be 13% for 250-MeV positrons, and the time resolution was found to be 300 ps.

§1. Introduction

In the SPring-8/LEPS2 experiment, we will study hadron photo-production processes by using a high-intensity photon beam [1]. The photon beam will be produced by the backward Compton process, and tagged by the tagging counter at the energy ranging from 1.4 to 2.9 GeV. The beam will be injected to a liquid hydrogen or deuterium target, and exotic hadrons will be searched for. One of the physics motivations of the SPring-8/LEPS2 experiment is the study of $\Lambda(1405)$ structure [3]. $\Lambda(1405)$ can be treated as a composite of two dynamically-generated $\overline{K}N$ bound state and $\Sigma\pi$ resonance. $\Lambda(1405)$ is tagged in the Σ^0 and π^0 decay channel, and subsquently the Σ^0 and π^0 decay into $\Lambda\gamma$ and 2γ, respectively. The energy of γ-rays to be detected ranges from 10 to 400 MeV.

A new spectrometer system, which is under construction, will be used to detect the charged and non-charged particles. Figure 2 is a schematic view of the spectrometer. The γ-rays from the hadron decays are detected by a sampling calorimeter, called the Barrel-γ. Barrel-γ is the segmented sampling calorimenter system made up of 1 mm thick leads and 5 mm thick plastic-scintillator plates. Barrel-γ is originally developed for the BNL-E787 experiment to identify π^0. The configuration and the performance are reported elsewhere [2].

The acceptance and experimental resolution are estimated by a Monte-Carlo simulation. In the simulation, the detector responses like the energy resolution are implemented as input parameters. To improve the precision of the simulation study and check the experiment feasibility, we need to know the detecrtor responses as input parameters.

Therefore, we performed a test experiment to investigate the performance of Barrel-γ. Barrel-γ has already been installed in the spectrometer, then we used the BV-liner detector in the BNL-E949 experiment to investigate the performance. The configuration of the BV-liner is shown in Fig.3, which contains 13 layers of 5 mm thick plastic-scintillator and 12 laysers of 1 mm leads. The material of BV-liner is the same as the one of Barrel-γ. By testing the performance of BV-liner and comparing the

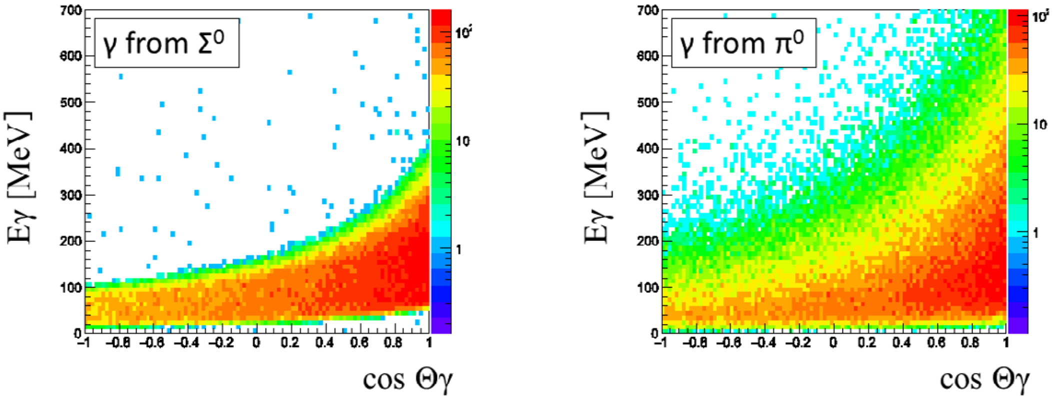

Fig.1. Correlation between the emitted angle and the energy in the laboratory system of γ from the $\Lambda(1405)$ decay. Left: γ from Σ^0 decay. Right: γ from π^0 decay.

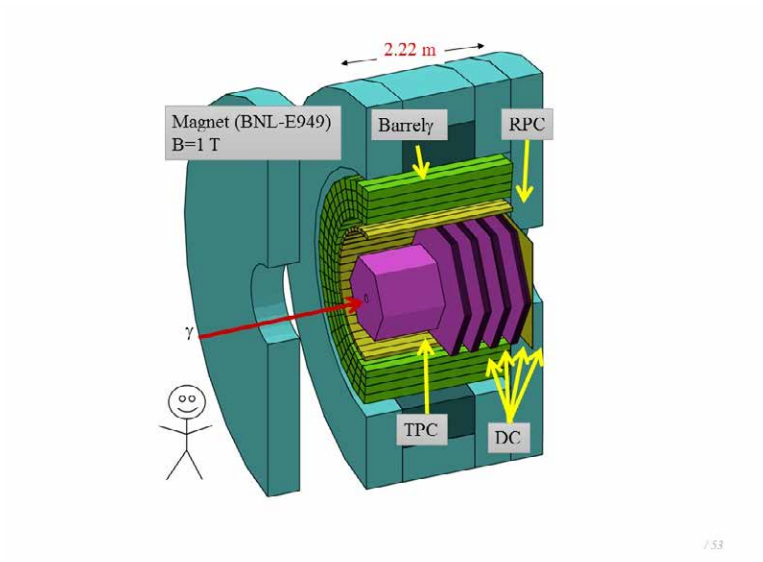

Fig.2. Schematic view of the LEPS2 spectrometer. Barrel-γ is shown as a green part in the figure.

experimental data with the simulation, we can extract the information of Barrel-γ.

We performed the test experiment at the positron beamline for testing detectors in the Research Center for Electron Photon Science, Tohoku University. Positron beam was exposed to the three BV-liner's with the different energy conditions. Energy resolution and timing resolution were measured for each BV-liner.

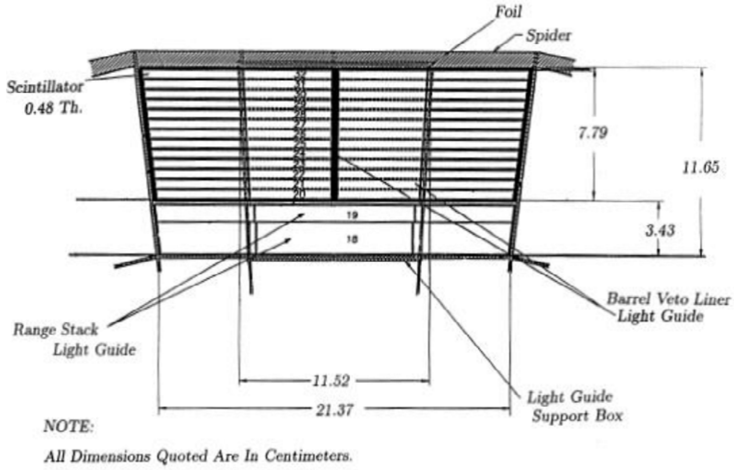

Fig.3. The cross section of the BV-liner. the unit in the figure is cm.

§2. Performance Test

2.1 Setup

The experimental setup is shown in Fig.4. Three BV-liners were installed perpendicularly along the positron beam axis. In front of the calorimeters, the defining counter T1 was installed. T1 is a 5-mm thick plastic-scintillator with the area of 10 x 10 mm^2, on both sides of which PMT's are attached to read out the light signal. T1 is installed in the center of the detectors and used to define the beam area in taking data.

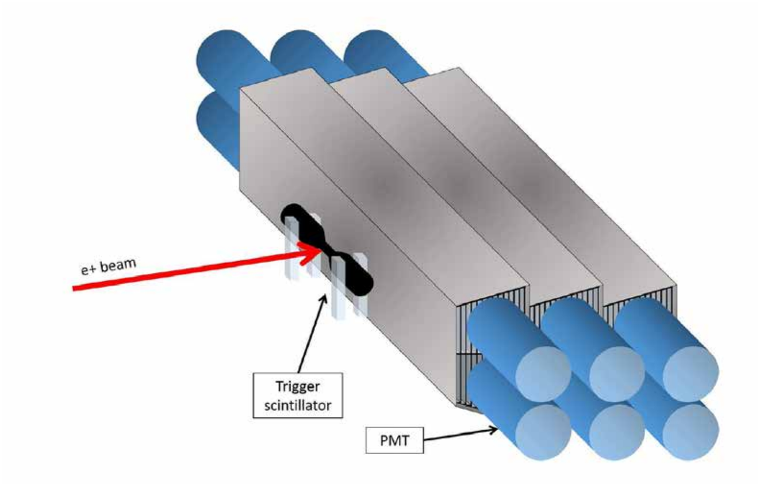

Fig.4. Setup of the test experiment. The positron beam was injeced from the left direction and hit T1 and three BV-liners.

The detector signals were degitized with NIM modules, and the trigger for the data taking was produced by the T1 signal. ADC(charge information of the signal) and TDC(timing information of the signal) were obtained with CAMAC system. The schematic diagram of the data taking system is shown in Fig.5.

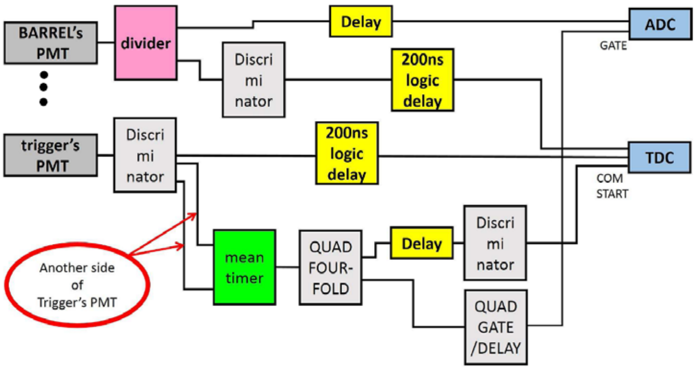

Fig.5. Data taking system of the experiment.

2.2 Experimental condition

The beam energy was varied by changing TAGX magnetic field [4]. We performed the experiment by using the beam with the energy of 50, 100, 150, 250, 350, 450, 500, 550 and 650 MeV. The beam energy spread is sufficiently smaller than the detector resolution.

In additon, the setup was tilted by the 16.5 degree to the beam axis, and the beam with the energy of 50, 150, 350 and 550 MeV was exposed to the detectors. For each condition, approximately 10^5 positrons were injected to the setup in total.

§3. Result

3.1 ADC spectrum

ADC historams for different beam energies were shown in Fig.6. In that figure, ADC values of three BV-liners were summed up. The detector gain was calibrated by using comic-ray run without beam. The MIP values were obtained by cosmic-ray run, and the relative gain of each detector was determined.

Each ADC histogram was fitted with a gaussian function. The fitting results were shown in Table.1. Here, the value σ/mean is corresponding to the energy resolution. The energy resolution measured was approximately 13% at 250 MeV. Mean values of ADC histograms with respect to varying beam energies are plotted in Fig.7. Fitting results with linear function are also shown in the same figure. The deviation from the linear fuction becomes large from 220 MeV because the leakage effect cannot be ignored when the beam energy becomes large. The linearity of the measured energy is introduced below 220 MeV.

3.2 Time resolution

Time resolution was also measured in the experiment. The mean value of both PMTs' TDC in each calorimeter is used to eliminate of position dependence of the timing. In addition, to correct the timing jittering effect of ADC, the slewing correction method was applied. Typical correlation plot of TDC and ADC is shown in Fig.8. The time resolution was determined to be approximately 300 ps. This value is corresponding to the position resolution of 5 cm.

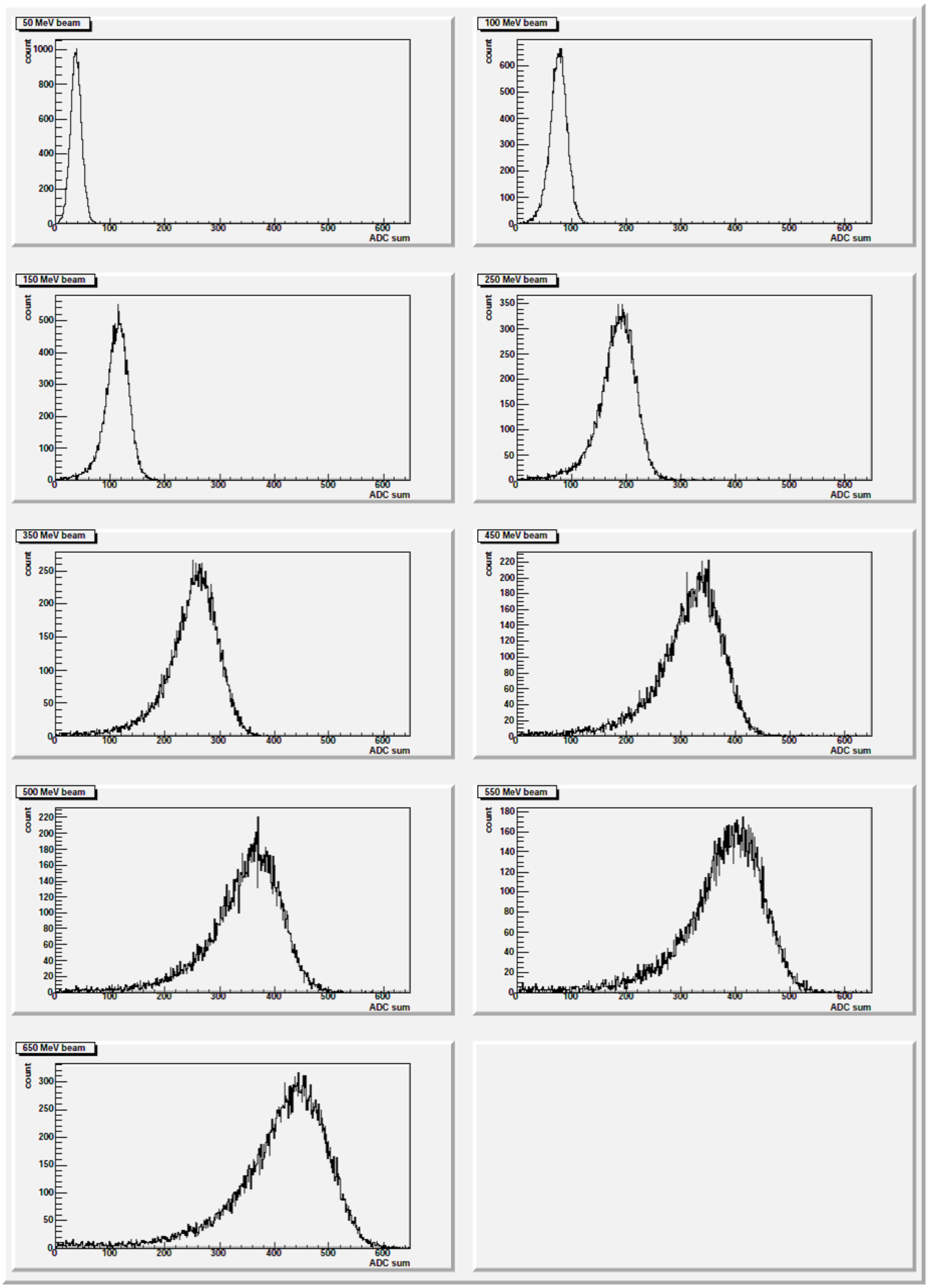

50 MeV beam

100 MeV beam

150 MeV beam

250 MeV beam

350 MeV beam

450 MeV beam

500 MeV beam

550 MeV beam

650 MeV beam

Fig.6. ADC histograms for different beam energies.

3.3 GEANT4 simulation

To understand the experimental result, a Monte-Carlo simulation based on GEANT4 was performed. In the simulation, the calorimeter geometry was implemetend, and the positron beam was

Table 1. The fitting results of the spectrum for each condition.

E[MeV]	Mean[ch]	Mean err[ch]	σ	σ err [ch]	σ/mean [%]
50	35.89	0.66	10.54	0.37	29.4
100	76.57	0.95	14.14	0.52	18.5
150	113.7	1.1	18.71	0.64	16.5
250	191.4	1.6	25.25	0.91	13.2
350	261.8	2.4	34.88	1.3	13.3
450	338.8	2.9	38.71	1.56	11.6
500	378.4	0.3	38.42	1.66	10.2
550	412.6	3.1	42.8	1.8	10.4
650	458.5	2.6	46.32	1.45	10.1

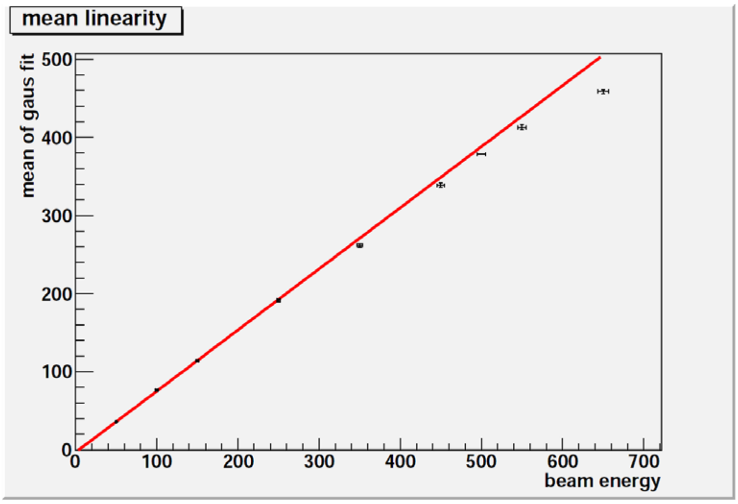

Fig.7. Mean Values of energy histogram with respect to beam energy.

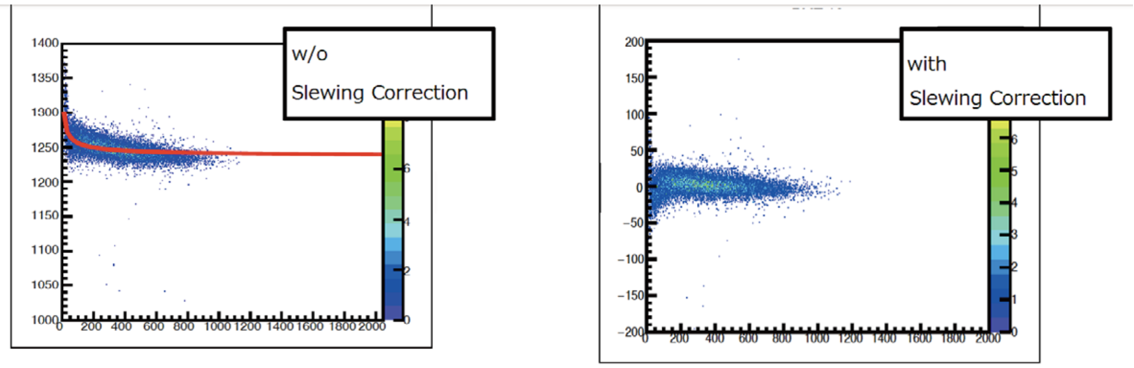

Fig.8. A correlation plot of TDC and ADC of the calorimeter. Left: the plot w/o slewing correction. Right: the plot with slewing correction.

injected with the energy upto 250 MeV, which is the maximum energy keeping the linearity. Figure 9 shows the comparison of the energy resolution obtained by the experimental data and the simulation, in which abscissa is injected beam energies. The resolution obtained by experimental data is a little larger than the simulated one. In the simulation, there are effects we have't considered, such as the light attenuation. However, we can say they are consistent and show the same behavior with respect to the beam energy.

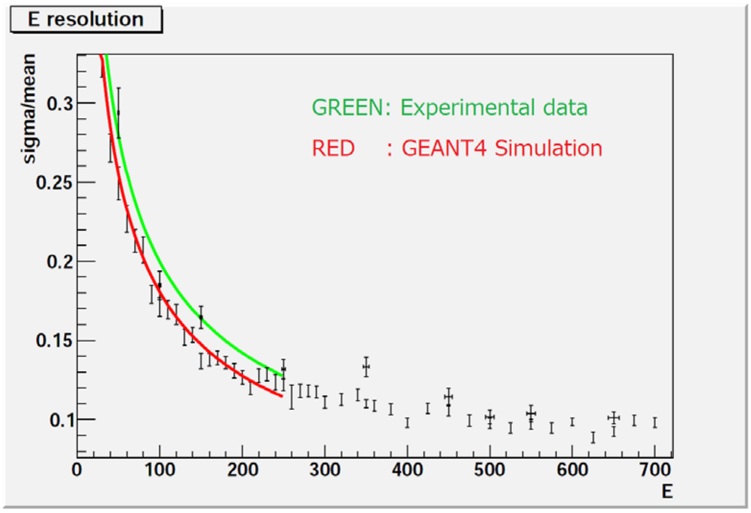

Fig.9. Comparison of Energy resolution between experimental data and simulation. Data points with only error bars are simulated results. Green line is the fitting results of the experimental data with a/$\sqrt{E}$. Red line is the fitting results of the simulation with a/$\sqrt{E}$.

For the more details of the above discussion, see ref. [5] [6].

§4. Summary

We performed a test experiment to investigate the performance of the sampling calorimeter (Barrel-γ) for the SPring-8/LEPS2 experiment. The positron beam at the energy ranging from 50 to 650 MeV was exposed to three calorimeters which are composed of the same materials as Barrel-γ . The energy resolution and time reolution of the calorimeter were found to be 13% at 250 MeV and 300 ps, respectively. The results were compared with the Monte-Carlo simulation, and they are almost consistet with each other.

Acknowledgment

We would like to express our gratitude to staff of the Research Center for Electron Photon Science for the accelerator operation and the fruitful discussion during the experiment. Part of this work was supported by JSPS KAKENHI(No. 15H00839).

References

[1] N. Muramatsu *et al.*: Few Body Syst.**54** (2013)7
[2] M.S. Atiya *et al.*: Nucl.Inst.Meth. **321** (1992) 129.
[3] T. Hyodo and D. Jido: Prog.Part.Nucl.Phys.**67** (2012) 55.
[4] K. Maruyama *et al.*: Nucl.Inst.Meth.**A376** (1996) 335.

[5] H. Goto: Master theis in RCNP (2016).

[6] Y. Yanai *et al.*: JPS Meeting at Sendai, Japan (2015 Mar.).

Longitudinal uniformity of the manufactured BGO crystals for the BGOegg calorimeter

R. Yamazaki[1], T. Ishikawa[1], D.N. Grigoriev[2,3,4], R. Hashimoto[1], Q. He[1],
Y. Honda[1], G.N. Kuznetsov[5], S. Masumoto[6], M. Miyabe[1], N. Muramatsu[1],
M. Nakamura[1], Y. Taniguchi[1], Y. Tsuchikawa[1], H. Shimizu[1], Ya.V. Vasiliev[5],
and H. Yamazaki[1]

[1]*Research Center for Electron Photon Science (ELPH), Tohoku University, Sendai 982-0826, Japan*
[2]*Budker Institute for Nuclear Physics, Siberian Branch of Russian Academy of Sciences, Novosibirsk 630090, Russia*
[3]*Novosibirsk State Technical University, Novosibirsk 630092, Russia*
[4]*Novosibirsk State University, Novosibirsk 630090, Russia*
[5]*Nikolaev Institute of Inorganic Chemistry, Siberian Branch of Russian Academy of Sciences, Novosibirsk 630090, Russia*
[6]*Department of Physics, University of Tokyo, Tokyo 113-0033, Japan*

An electromagnetic calorimeter, called BGOegg, consisting of 1,320 BGO crystals has been constructed at ELPH. All the crystals have been manufactured at the Nikolaev Institute of Inorganic Chemistry (NIIC) in Novosibirsk, Russia. Each crystal for the calorimeter takes a tapered shape, and surface roughness of the lateral sides is adjusted so as to achieve uniform light output as a function of the distance from the window of the photomultiplier tube. The relative light output and longitudinal uniformity measured at NIIC for each manufactured crystal with a wrapping material of Al foil are presented. The relative light output and longitudinal uniformity of the first crystal for each polar angle are also measured at ELPH with three wrapping materials — Vikuity Enhanced Speculator Reflector (ESR) from 3M company, DuPoint Tyvek 1082D, and Al foil. An excellent light output and longitudinal uniformity has been obtained for the crystals wrapped with ESR.

§1. Introduction

An electromagnetic (EM) calorimeter, called BGOegg, has been constructed at the Research Center for Electron Photon Science (ELPH), Tohoku University to study the structure of hadrons via the photo-induced reactions [1]. Meson photoproduction experiments [2–4] have been conducted with an EM calorimeter, FOREST [5], for baryon spectroscopy at ELPH [5]. Here, neutral mesons decaying into photons are mainly detected. We plan to extend meson photoproduction experiments for baryon spectroscopy using a laser Compton scattering photon beam with E_γ = 1.3–2.9 GeV [6] at LEPS2 [7]. We also plan to search for η' mesic nuclei [8], which are good probes for revealing the properties of the η' meson at finite density [9], by looking at the missing mass spectra for the $A(\gamma, p)$ reaction. The detection of daughter particles from the η'-mesic nucleus decay is necessary to reduce the huge background originating form the quasi-free single- and multi-meson production processes. We plan to detect an η meson and a nucleon N from the $\eta' N \rightarrow \eta N$ conversion in a nucleus.

The energy of photons to be detected ranges from several ten MeV to a few GeV in these experiments. The high energy resolution is required for the photon measurements, and a large solid angle is desired for detecting photons and other particles. We have constructed the BGOegg calorimeter consisting of 1,320 BGO crystals for the experiments at SPring-8/LEPS2. The details of the design for the calorimeter are described elsewhere [10, 11]. Since a crystal for the calorimeter takes a tapered shape, significant longitudinal non-uniformity of light output is observed due to the focusing effect when all the surfaces are polished. To achieve uniform light output as a function of the distance from the window of the photomultiplier tube (PMT), surface roughness of the lateral sides is adjusted. A test for the prototype BGO crystals with two different surface conditions (polished and etched) is described elsewhere [11].

§2. Measurement at NIIC

All the crystals have been manufactured at the Nikolaev Institute of Inorganic Chemistry (NIIC) in Novosibirsk, Russia. Surface roughness of the lateral sides is adjusted by chemical etching so as to achieve uniform light output as a function of the distance from the PMT window. The relative light output and longitudinal uniformity are measured at NIIC for each manufactured crystal. The crystal type numbers 12F–00F, and 00B–08B in Ref. [10] are converted into 01–13, and 14–22, respectively, to give the increasing crystal numbers according to the polar angles. The relative light output and longitudinal uniformity were measured for all the manufactured crystals by using γ rays from a radioactive source, ^{137}Cs (662 keV) or ^{22}Na (511 keV). A crystal was wrapped with Al foil, and was connected to a 3-inch PMT, Hamamatsu Photonics R1307. The distances from PMT were set to 10, 60, 110, 160, and 210 mm using a lead aperture for the source. The light output was given by the centroid of the peak corresponding to the photoelectric effect with a room temperature correction to 23°C ($-1.5\%/^\circ$C). The light output for each crystal was estimated by averaging five distance data. Fig. 1 shows the average light output for all the polar angle numbers of the crystals (01–22). The average light output for each polar angle number ranges from 1500 to 2000. The average light output for the backward crystals (14–22) is stable, being approximately 2000. The decrease of the average light output was observed for small crystals (01–03 and 20-22).

The relative light output was also determined among the same polar angle number. Here, the relative light output was normalized so that the average of all the 60 crystals in a polar angle should be 1. Fig. 2 shows the relative light output as a function of the crystal number at each polar angle. The polar angles are specified in the crystal types (12F–00F, and 00B–08B). Some crystal types (12F, 11F, 04B, and 03B) show a large gap between the different shipping dates. Although the shipping date was the same, a large gap exists in 04F and 03F, suggesting the dates of the manufacture or measurement were different between them. The relative light outputs range from 0.9 to 1.1, especially those are approximately 1 for

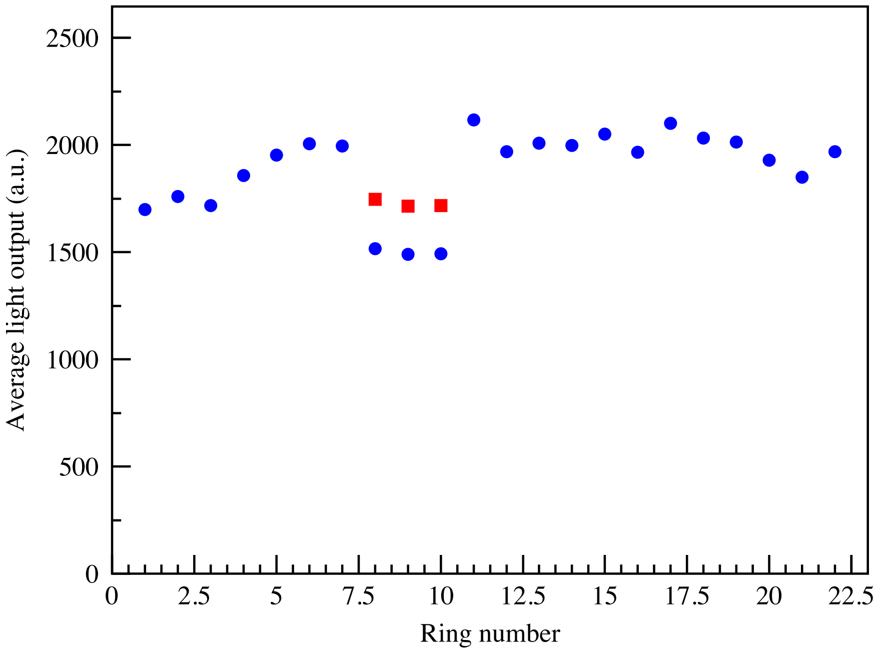

Fig.1. Average light output for all the polar angle numbers of the crystals (measured at NIIC). The average light output is given for averaging all the 60 crystals in the same polar angle. The 08–10 (05F–03F) crystals are measured by irradiating the 511 keV γ rays from the ^{22}Na radioactive source, and those of the others are measured by irradiating the 662 keV γ rays from the ^{137}Cs. The red boxes shows the corresponding light output for the ^{137}Cs irradiation.

the 01F –01B crystals.

The longitudinal uniformity U was also investigated. Here U is defined as

$$U_i = \frac{L_i - \overline{L}}{\overline{L}}, \tag{1}$$

and determined for each distance for each crystal. The L_i denotes the light output for each measurement, and $\overline{L}$ denotes the average of the five measurement of each crystal for different distances from the PMT window. Fig. 3 shows the uniformity U as a function of the distance from the PMT window. The U is well controlled within $\pm 5\%$, giving the high energy resolution (1.36% at 1 GeV) for a prototype BGO calorimeter consisting of 25 crystals arranged in 5×5 matrix [10, 11]. The further small values of U can be obtained by wrapping a crystal with a film, Vikuity Enhanced Speculator Reflector (ESR) from 3M company, as discussed below.

§3. Measurement at ELPH

The light output and longitudinal uniformity for one out of the 60 crystals were measured also at ELPH. Each crystal was wrapped with three materials, Vikuity Enhanced Speculator Reflector from 3M company, DuPoint Tyvek 1082D, and Al foil. The measurement of the 00B crystal was omitted since the shape of the 00B crystal is identical to the 00F crystal. The crystal was connected to a PMT, Hamamatsu Photonics H6410 through optical grease, OKEN6262A. A series of the measurements were made from December 20, 2011 to June 2, 2012. The supplied high voltage was -2000 V during the series

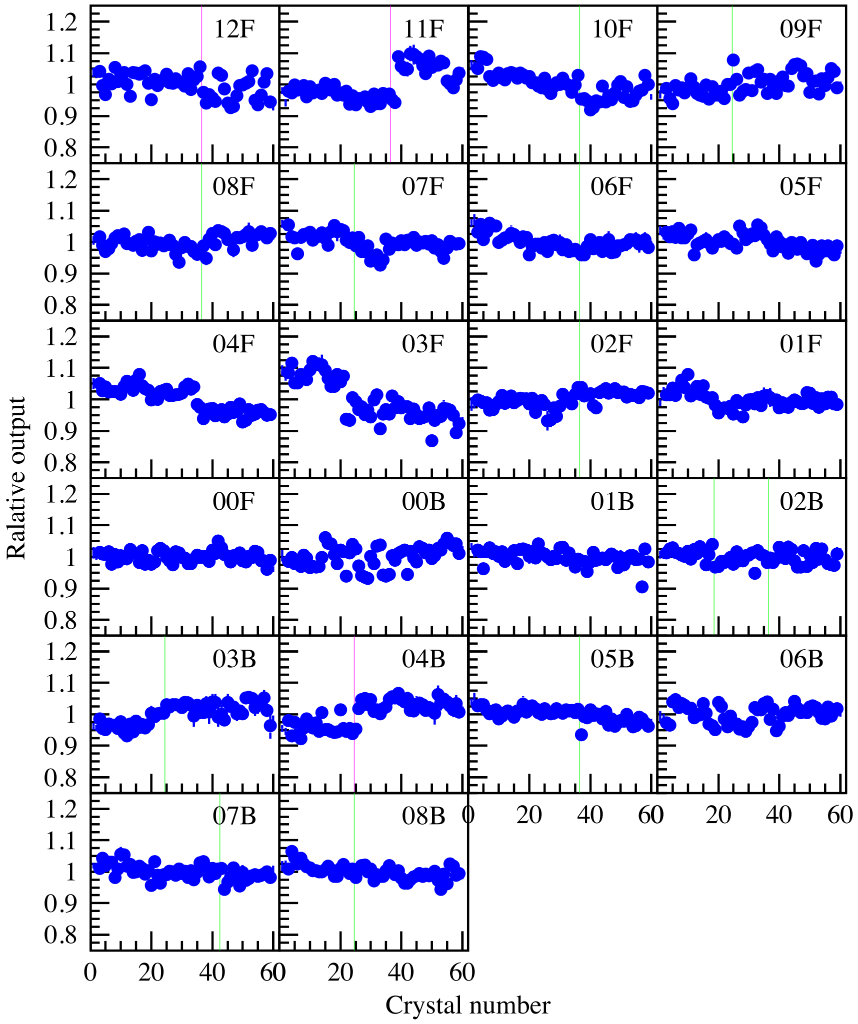

Fig.2. Relative light output as a function of the crystal number at each polar angle (measured at NIIC). The vertical magenta and green lines show the boundary giving the different shipping dates. The magenta lines show the shipping dates are different by more than three months.

of measurements. The high voltage was turned off during changing crystals or wrapping materials. To reduce the time for changing crystals or wrapping materials, two layers of a black box were used. Fig. 4 shows the experimental setup for the measurement of the light output and longitudinal uniformity Lead blocks with nine apertures with a diameter of 3 mm are placed to determine the distance of the 137Cs source irradiation from the PMT window.

We measured the energy spectra of the output signals from the BGO crystals in response to γ rays with a CAMAC-based data taking system. The anode signal from the PMT was split into two signals. One was distributed to a charge-integration ADC module, Technoland C-QV715, and its gate width was set to 2 μs. The other was used to form a trigger for the data acquisition system and to generate the gate for the ADC module. The decay time of BGO scintillator is rather long, and the output signal does not form a single pulse in response to a single γ ray from ^{137}Cs. Thus, the width of the signal for the trigger was set to 2 μs. The energy was given by a raw ADC and pedestal values, where the pedestal in

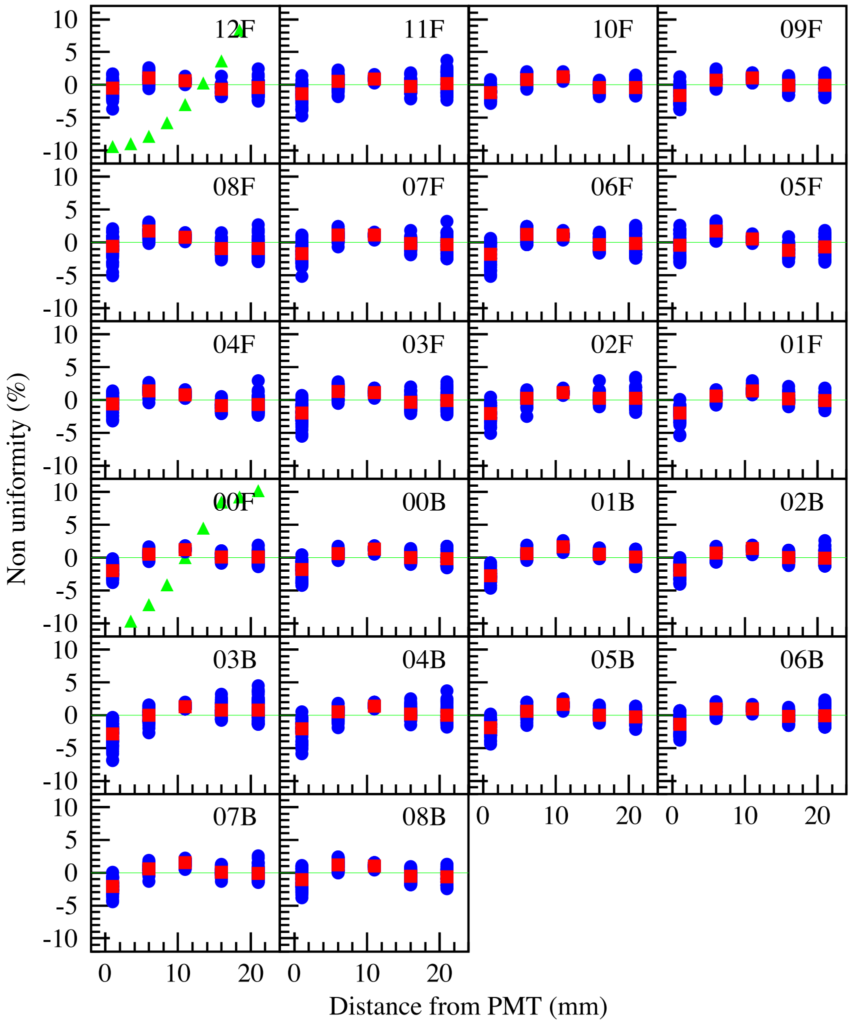

Fig.3. Uniformity U as a function of the distance from the PMT window (measured at NIIC). The Us for 60 crystals are plotted in each panel corresponding to the polar angle number. The red boxes show the average of the 60 crystals. The green triangles show U for the prototype polished crystals scaled by 1/3 [10] (namely actual U ranges from -30% to $+30\%$ fro 12F and 00F prototype polished crystals).

each energy spectrum was measured with a 1-kHz clock trigger. Background events were also measured without the ^{137}Cs source to enable background subtraction. The energy spectrum in response to the γ rays from the ^{137}Cs source was deduced by subtracting the measured spectrum without the source from that with the source. Fig. 5 shows the typical energy spectra in response to the rays from ^{137}Cs. The decrease of light output was observed for the polished 00F crystal for short distances from the PMT window when the crystals were wrapped with Al foil.

The light output varies according to the temperature in the black box due to the change of the light output of BGO scintillator (-0.9%/K) [12] and due to the change of the quantum efficiency of the bialkali surface of the PMT used (-0.4%/K) [13]. The decrease of the light output -1.3%/K was expected for this measurement. Thus the measured light output L_T was corrected using the temperature T as

$$L = L_T\,\{1 - 0.013\,(20^\circ\mathrm{C} - T)\} \tag{2}$$

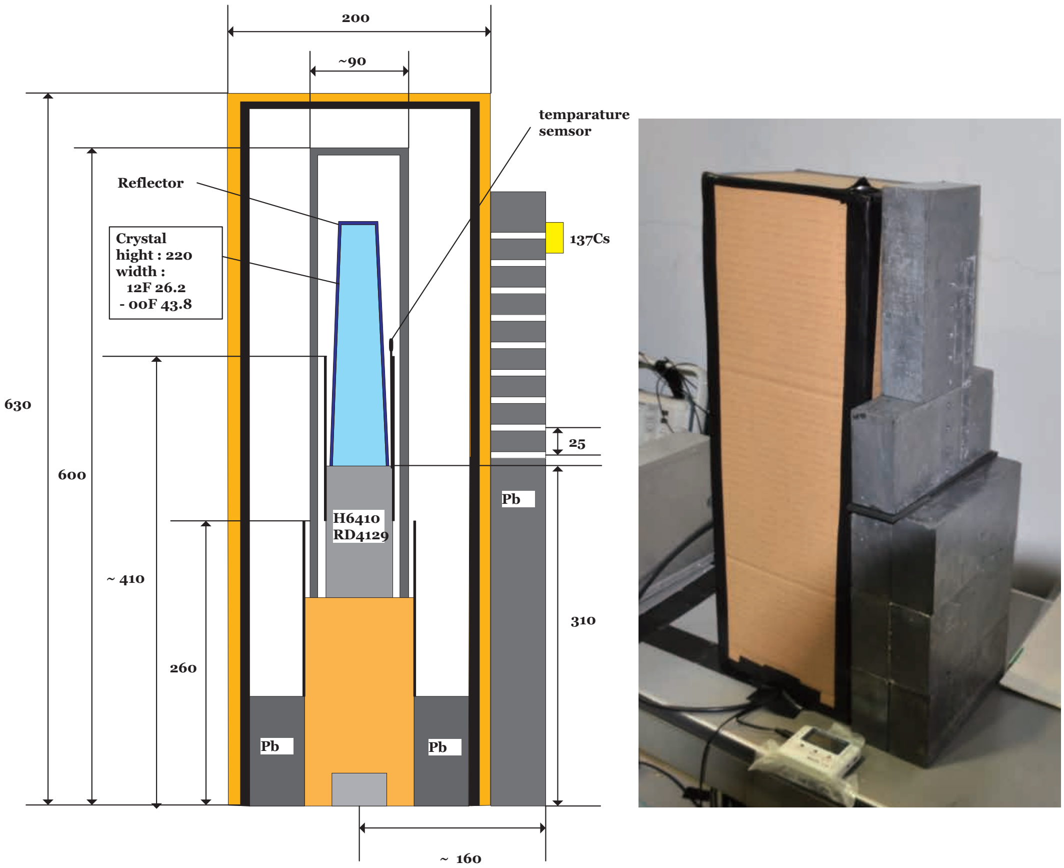

Fig.4. Experimental setup for the measurement of the light output and longitudinal uniformity. The left panel shows the schematic view of the setup, and the right panels shows the photograph. Lead blocks with nine apertures with a diameter of 3 mm are placed to determine the distance of the 137Cs source irradiation from the PMT window.

so that L stands for the light output at 20°C. Fig. 6 shows the light outputs for the different crystals with different wrapping materials.

The centroid μ corresponding to the photoelectric peak was obtained by fitting a Gaussian function to the peak. The fitting process was repeated several times in the region $[\mu - 0.8\sigma, \mu + 2\sigma)$, where σ denotes the width of the peak. Fig. 7 shows the light output as a function of the source distance from the PMT window. The light output depends on the distance when the crystals are wrapped with Al foil. When the crystals are wrapped with a ESR sheet, the light output is almost constant for all the crystals. The $|U|$ value reaches 13.0% for the crystals wrapped with Al foil. In the case of wrapping the crystals with ESR and Tyvek, the maximum Us are 5.3% and 7.1%, respectively. The standard deviations of Us are 1.5%, 2.2%, and 3.9% for ESR, Tyvek paper, and Al foil sheets, respectively.

The stability of the gain according to the environment was checked by measuring the light output for the prototype 00F crystal wrapped with a ESR sheet for every series of the measurements. The variation of the light output for the prototype 00F crystal with ESR is 3.1% for the peak-to-peak difference. The details of the analysis are described elsewhere [14].

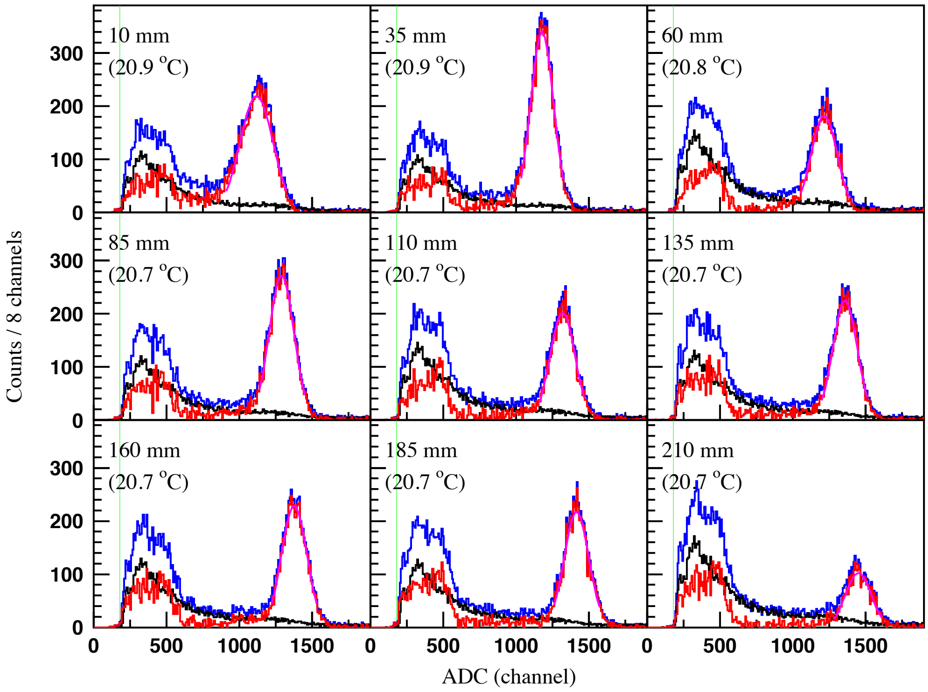

Fig.5. Typical energy spectra of the prototype etched 00F BGO crystal (Al foil) for different source distances from the PMT window (measured at ELPH). The source distance is described in each panel together with a temperature in the black box. Each energy spectrum (red) is deduced by subtracting the measured spectrum without ^{137}Cs (black) from that with ^{137}Cs (blue). The solid curves show the fitted Gaussian function for peaks corresponding to the photoelectric effect. The vertical green lines represent the pedestal position corresponding to an energy of 0.

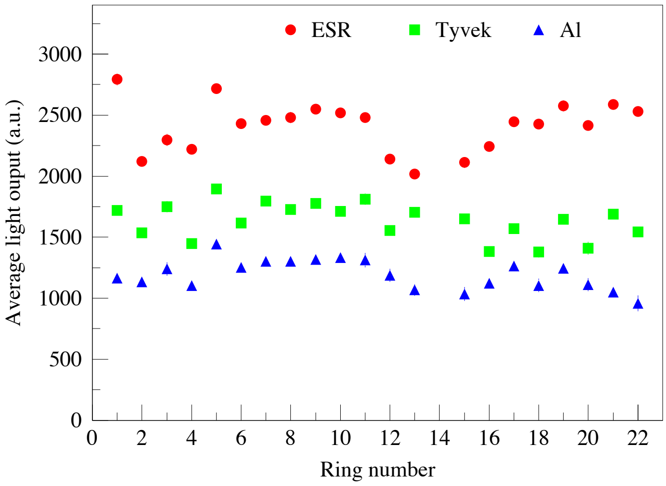

Fig.6. Light outputs for the different crystals with different wrapping materials (measured at ELPH). The red circles, green boxes, and blue triangles show the light output for the wrapping materials of ESR, Tyvek, and Al foil. The measurements for the 00B (14) crystal is omitted since the shape of the 00F (13) crystal is the same as that of the 00B (14) crystal.

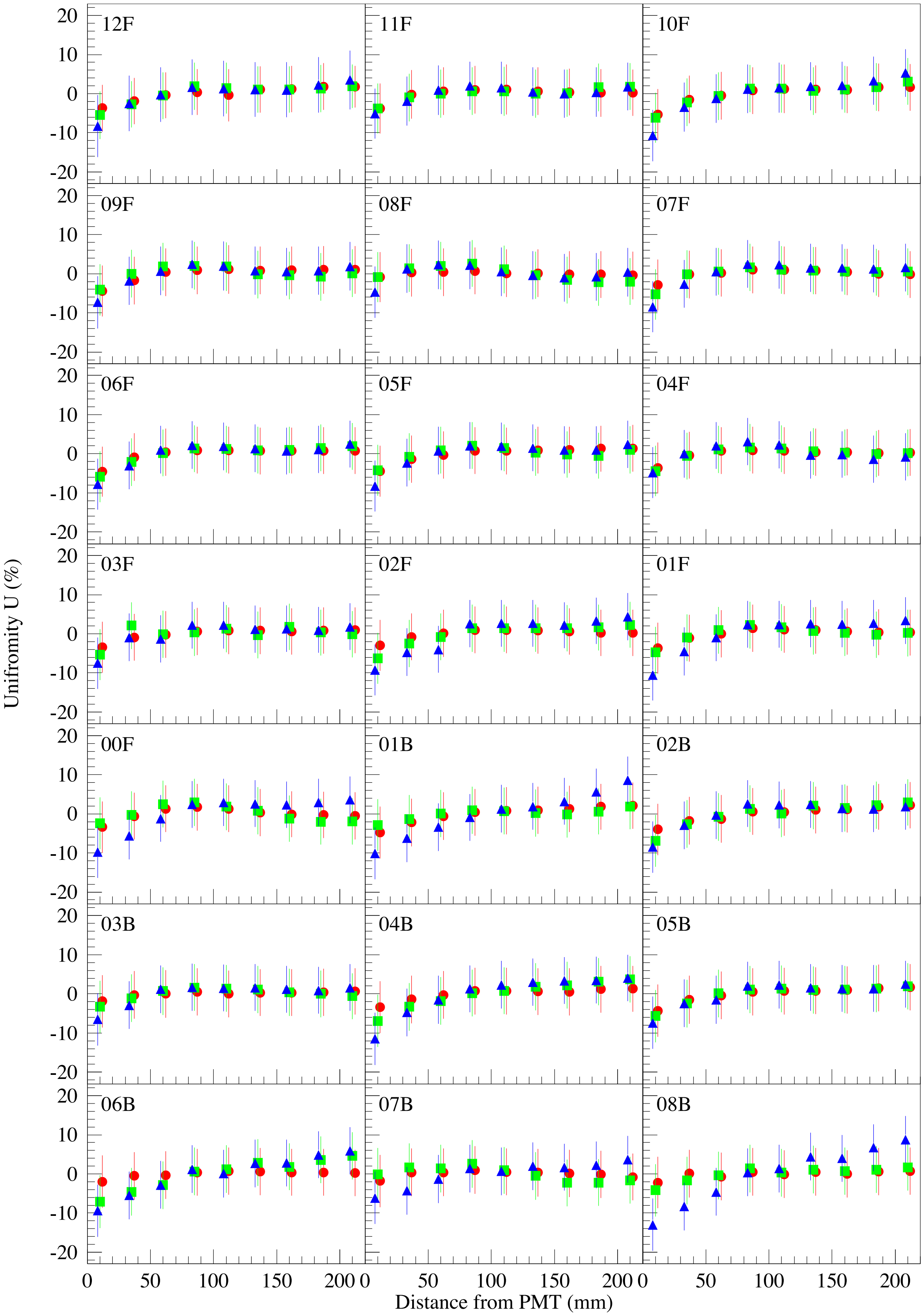

Fig.7. Light output as a function of the source distance from the PMT window. The crystal number is described in each panel (measured at ELPH). The red circles, green boxes, and blue triangles show the light output for the wrapping materials of ESR, Tyvek, and Al foil. The errors represent the widths of the peaks corresponding to the photoelectric effect.

§4. Summary

An electromagnetic calorimeter, called BGOegg, consisting of 1,320 BGO crystals was constructed at ELPH. All the crystals were manufactured at the Nikolaev Institute of Inorganic Chemistry (NIIC) in Novosibirsk, Russia. The relative light output and longitudinal uniformity for the BGO crystals were measured at ELPH for three wrapping materials, Vikuity Enhanced Speculator Reflector from 3M company, DuPoint Tyvek 1082D paper, and Al foil. An excellent light output and longitudinal uniformity has been obtained for the crystals wrapped with ESR.

Acknowledgments

This work was supported in part by Grants-in-Aid for Specially Promoted Research (19002003), for Scientific Research (A) (24244022), and for Scientific Research (C) (26400287).

References

[1] T. Ishikawa *et al.*: Proceedings of the 10th International Workshop on the Physics of Excited Nucleons (NSTAR2015), JPS Conference Proceedings 10 (2016) 031001;
T. Ishikawa: Proceedings of the XV International Conference on Hadron Spectroscopy-Hadron 2013, PoS (Hadron 2013) 095;
T. Ishikawa *et al.*: Proceedings of the 20th International IUPAP Conference on Few-Body Problems in Physics, Few Body Systems 54 (2013) 1047.

[2] T. Ishikawa *et al.*: Nuclear Instruments and Methods in Physics Research Section A **622**, 1(2010).

[3] T. Ishikawa *et al.*: Nuclear Instruments and Methods in Physics Research Section A **811**, 124 (2016).

[4] F. Hinode *et al.*: Proceedings of 2005 Particle Accelerator Conference (2005) 2458.

[5] T. Ishikawa *et al.*: Nuclear Instruments and Methods in Physics Research Section A (2016), `http://dx.doi.org/10.1016/j.nima.2016.06.054`.

[6] N. Muramatsu *et al.*: Nuclear Instruments and Methods in Physics Research Section A **737**, 184 (2014).

[7] LEPS website: ⟨http://www.rcnp.osaka-u.ac.jp/Divisions/np1-b/⟩.

[8] H. Nagahiro, S. Hirenzaki: Physical Review Letters **94** 232503 (2005);
H. Nagahiro *et al.*: Physical Review C **87**, 045201 (2013).

[9] D. Jido *et al.*: Nuclear Physics A **914**, 354 (2013); and references therein.

[10] T. Ishikawa *et al.*: ELPH Annual Report **1**, 61 (2012).

[11] T. Ishikawa *et al.*: Testing a prototype BGO calorimeter by using 100-800 MeV positron beams, submitted to Nuclear Instruments and Methods in Physics Research Section A.

[12] J. Beringer *et al.* (Particle Data Group): Physical Review D **86**, 010001 (2012).

[13] Hamamatsu Photonics, Photomultiplier Tube, 3rd Ed., 2005.

[14] R. Yamazaki and T. Ishikawa: Internal GeV-γ analysis note HD No. **405**$\mathcal{B}$ (2016);
R. Yamazaki and T. Ishikawa: Internal GeV-γ analysis note HD No. **406**$\mathcal{B}$ (2016).

The status of SPring-8 LEPS2/BGOegg experiments

Norihito Muramatsu[1], Jung Keun Ahn[13], Wen-Chen Chang[4], Jia-Ye Chen[5],
Schin Daté[3], Toshiyuki Gogami[2], Hiroya Goto[2], Hirotomo Hamano[2],
Toshikazu Hashimoto[6], Qing Hua He[1], Kenneth Hicks[7], Toshihiko Hiraiwa[2],
Yuki Honda[1], Tomoaki Hotta[2], Hiroyuki Ikuno[2], Yosuke Inoue[1],
Takatsugu Ishikawa[1], Igal Jaegle[8], Yuuto Kasamatsu[2],
Hitoshi Katsuragawa[2], Satoshi Kido[1], Hideki Kohri[2], Yukiyoshi Kon[2],
Shinichi Masumoto[9], Yuji Matsumura[1], Katsumasa Miki[12], Manabu Miyabe[1],
Keigo Mizutani[6], Taiki Nakamura[12], Takashi Nakano[2], Masayuki Niiyama[6],
Yuki Nozawa[6], Yuji Ohashi[3], Haruo Ohkuma[3], Hiroaki Ohnishi[10,2],
Takeshi Ohta[2], Masaya Oka[2], Kyoichiro Ozawa[11], Mizuki Sasagawa[1],
Takuya Shibukawa[9], Hajime Shimizu[1], Ken'ichiro Shiraishi[1],
Yorihito Sugaya[2], Mizuki Sumihama[12], Shinsuke Suzuki[3], Shintaro Tanaka[2],
Atsushi Tokiyasu[2], Natsuki Tomida[6], Nam Tran[2], Yusuke Tsuchikawa[1],
Hirohito Yamazaki[1], Ryuji Yamazaki[1], Yuka Yanai[2], Tetsuhiko Yorita[2],
and Masaru Yosoi[2]

[1]*Research Center for Electron Photon Science, Tohoku University, Sendai, Miyagi 982-0826, Japan*
[2]*Research Center for Nuclear Physics, Osaka University, Ibaraki, Osaka 567-0047, Japan*
[3]*Japan Synchrotron Radiation Research Institute (SPring-8), Sayo, Hyogo 679-5198, Japan*
[4]*Institute of Physics, Academia Sinica, Taipei 11529, Taiwan*
[5]*National Synchrotron Radiation Research Center, Hsinchu 30076, Taiwan*
[6]*Department of Physics, Kyoto University, Kyoto 606-8502, Japan*
[7]*Department of Physics and Astronomy, Ohio University, Athens, OH 45701, USA*
[8]*University of Hawaii at Manoa, Honolulu, HI 96822, USA*
[9]*Department of Physics, University of Tokyo, Tokyo 113-0033, Japan*
[10]*RIKEN Nishina Center, Wako, Saitama 351-0198, Japan*
[11]*Institute of Particle and Nuclear Studies, High Energy Accelerator Research Organization (KEK), Tsukuba, Ibaraki 305-0801, Japan*
[12]*Department of Education, Gifu University, Gifu 501-1193, Japan*
[13]*Department of Physics, Korea University, Seoul 02841, Republic of Korea*

§1. Introduction

The physics data-taking at the BGOegg experiments has started from 2014 April at the SPring-8 LEPS2 beamline (BL31LEP). As one of the main goals, we search for the η' meson-bound nuclei, which is expected as a result of the mass reduction at the nuclear density. The theories based on the Nambu-Jona-Lasinio (NJL) model [1] and the linear sigma model [2] predict the 80–150 MeV mass

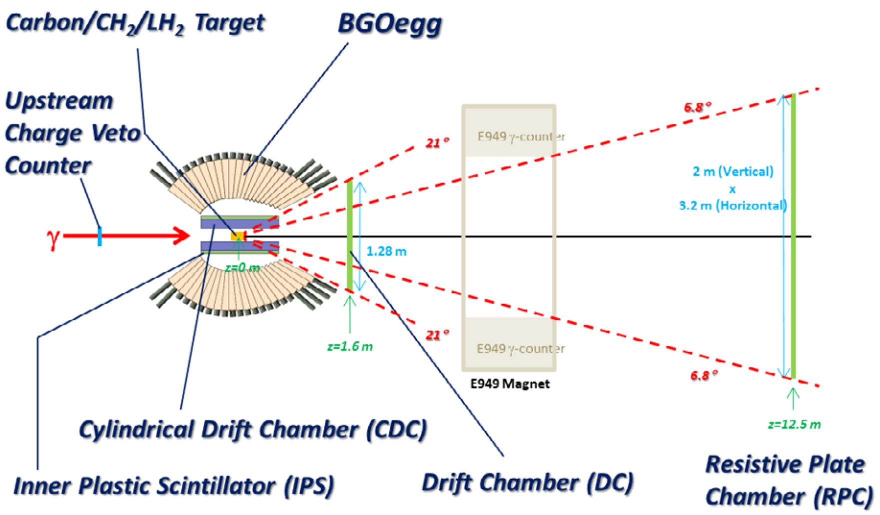

Fig.1. Setup of the BGOegg experiments. The size of the RPC wall has been decided based on the bore diameter of E949 solenoid magnet, which will be used at other experiments.

reduction due to the partial restoration of the chiral symmetry breaking and the U$_A$(1) anomaly. The BGOegg experiment is an ideal setup to improve the very small signal-to-noise ratio in the missing mass spectrum of the $A(\gamma, p)$ reaction significantly. We aim to understand the origin of mass.

We also investigate the hadron pictures through the resonances of meson(s)-baryon and meson-meson systems. For example, the excited baryon resonances are under studies in the s-channel of single or double meson (η, η', ω, $\pi^0\pi^0$, $\pi^0\eta$, etc) photoproduction from a proton target. The coupling strengths to the individual final states depend on the resonance properties like quantum numbers, internal quark flavors, a specific hadron structure, and so on. We measure not only the production cross sections but also the photon beam asymmetry by using the high linear polarization available at the LEPS2 beamline, to study the helicity amplitudes including the interferences between resonances.

At the LEPS2 beamline, a 1.3–2.4 GeV tagged photon beam is produced by the backward Compton scattering of 355 nm ultraviolet laser light from the 7.975 GeV electron beam [3]. The tagged beam intensity was 1.4–2.1 MHz with the simultaneous injection from three or four lasers (8/16/24 W “Paladin” by Coherent Inc.). The produced photon beam is delivered to the 135 m-downstream experimental building with the final beam spread of about 6.5 mm in σ [4]. Here the nuclear and liquid hydrogen targets have been exposed to the high intensity photon beam.

Figure 1 shows the setup of the BGOegg experiments. The “egg”-shaped electromagnetic calorimeter surrounds the target in the polar angle range from 24° to 144°. 1320 $Bi_4Ge_3O_{12}$ (BGO) crystals of 20 radiation lengths are assembled in the 60 azimuthal sectors and 22 polar angle layers without dead spaces. The energy resolution is 1.3% at 1 GeV [5], providing one of the world’s highest performances. The BGOegg calorimeter is essential to identify neutral mesons decayig to γs with a good invariant mass resolution and to detect the nuclear absorption signals of the η'-bound state.

Charged particles are recognized in the wide acceptance range by several detectors. The charge of a BGOegg calorimeter hit is identified by the inner plastic scintillators (IPS) and the cylindrical drift chamber (CDC). The energy loss at IPS is usable for the separation of proton and pion bands in the correlation plot with the kinetic energy measured at the BGOegg calorimeter. The forward acceptance hole of the calorimeter is mostly covered by the planar drift chamber (DC) in the polar angle region less than 21°. The charged particle direction and kinetic energy are useful to reject the backgrounds with extra particles at a kinematic fit.

A forward proton momentum can be measured by the resistive plate chambers (RPC) [6], whose wall covers the polar angle region less than 7° at the 12.5 m downstream of the target for the time-of-flight (TOF) measurement. The measured momentum is the key information to calculate the missing mass spectrum in the meson-bound nuclei search and to perform the photon beam energy calibration using the meson photoproduction from a proton target.

§2. Collected data

Table 2 summarizes the collected physics data in 2014–2015. In the first half of 2014 (2014A), a 20 mm-thick polyethylene (CH_2) or carbon (ρ=1.73 g/cm^3) block was alternatively placed as a fixed target for the initial calibration purpose and the test analysis of the η'-bound nuclei search. Since the readiness of RPC was not enough, only ~30% was usable to calculated the missing mass in the carbon data, which corresponds to 4.3×10^{12} tagged photon counts. Therefore, the carbon target data was collected again in the first half of 2015 (2015A). If we assume the cross section based on the NJL model [1], the nuclear absorption signals of the η'-bound nuclei may be expected at a hundred event level in the 2015A data, although such an estimation highly depends on the event selection conditions.

In parallel with the 2014A data-taking, the liquid target system was developed with a 40 mm-thick cell made of polyimide films [7]. The liquid hydrogen (LH_2) target became ready during the latter half of 2014 (2014B), and the physics data corresponding to 4.2×10^{12} tagged photon counts were collected after several tests. We took roughly equivalent amouts of two data sets with the vertical and horizontal polarization beams. The linear polarization vector was controled by the wave plates on lasers in order to check the possible geometrical effects in the photon beam asymmetry measurement. In the latter half of 2015 (2015B), we further accumulated the LH_2 target data up to the 1.4 times of the 2014B data especially for the η' and double meson photoproduction.

Table 1. Statistics of the data collected at the BGOegg experiments. The integrated number of tagged photons is evaluated by correcting the tagging detector counts by the trigger dead time. The numbers in parentheses at 2014A indicate the statistics for the data with RPC. In 2015A, most of the data was collected with vertical polarization.

Period	Target	Integrated number of tagged photons
2014A (Apr.–July)	Carbon/CH_2 (20 mm-thick)	C: 4.29×10^{12} (1.31×10^{12}) CH_2: 2.56×10^{12} (1.58×10^{12})
2014B (Nov.–Feb.)	LH_2 (40 mm-thick)	Hori: 2.24×10^{12} Vert: 2.01×10^{12}
2015A (Apr.–July)	Carbon (20 mm-thick)	9.77×10^{12} (Vert: 8.97×10^{12})
2015B (Sep.–Dec.)	LH_2 (40 mm-thick)	Hori: 2.87×10^{13} Vert: 2.92×10^{13}

§3. Data calibration

There has been large progress in the data calibrations and the development of event reconstruction codes. The energy scale calibration of 1,320 BGO crystals has been iterated to adjust the 2γ invariant mass peak of π^0 at the nominal value [8]. This calibration was then refined by taking into account several corrections about the realistic geometry of crystal and target positions, the energy leak to the outside of the sensitive volume, and the momentum dependence of π^0 and η masses. As a result, the mass resolutions of π^0 and η mesons are 7.7 and 21.1 MeV/c^2, respectively, for the 40 mm-thick LH_2 target data. The correctness of the energy scale calibrations is ensured by the 2γ invariant mass spectrum for the η' meson, providing the peak within 0.4% of the nominal mass, as shown in Fig. 2(a). The use of a kinematic fit must reduce the background level further. The η' meson has been reconstructed also in the $\pi^0\pi^0\eta$ decay mode, as shown in Fig. 2(b). Since the π^0 and η masses are forced to the nominal values, the invariant mass resolution becomes 8.6 MeV/c^2.

The TOF from the target to RPC is measured relative to the reference time decided by the accelerator radio-frequency (RF) signal with 508.58 MHz. The true electron bunch where the Compton scattering happens is solved by taking a coincidence with a tagging detector signal. The RPC time resolutions, measured from the $e^{\pm}$ TOF distributions with the flight length correction depending on the hit position, have been obtained to be 70–80 psec strip by strip. The TOF value is transformed to β and then a momentum by assuming the proton mass with an energy loss correction during the flight. The momentum resolution is about 1% at 2 GeV/c, providing the resolution comparable with the magnetic spectrometer. Figure 3(a) shows the measured β versus the missing energy when π^0 or η is identified at the BGOegg calorimeter. A clear proton band, corresponding to the reaction $\gamma p \to \pi^0 p/\eta p$, is seen. In the case that a slow particle is detected at RPC, the missing mass spectrum with the assumption of a proton indicates clear meson peaks, as shown in Fig. 3(b), after requiring the transverse momentum balance with the two photons detected at the BGOegg calorimeter.

Figure 4(a) shows the photon beam energy calibration for the tagging detector. The tagging de-

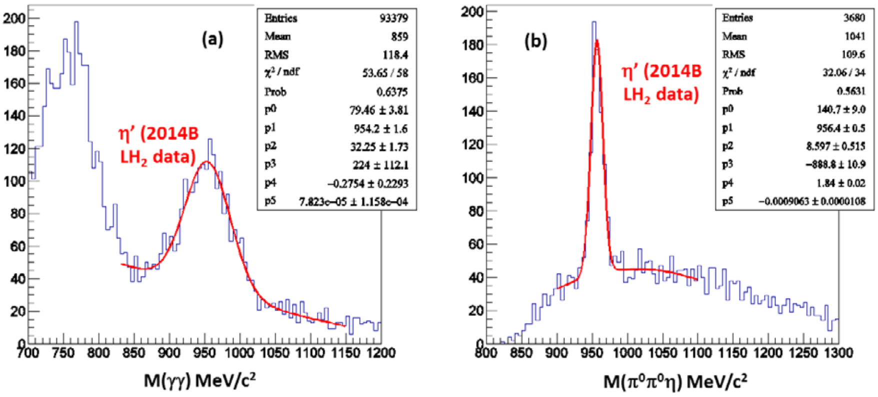

Fig.2. The η' invariant mass spectra for (a) 2γ and (b) $\pi^0\pi^0\eta$ decay modes. The 2014B data is analyzed by requiring the missing mass to be the proton mass and by confirming the angle consistency between the missing momentum and the detected charged particle.

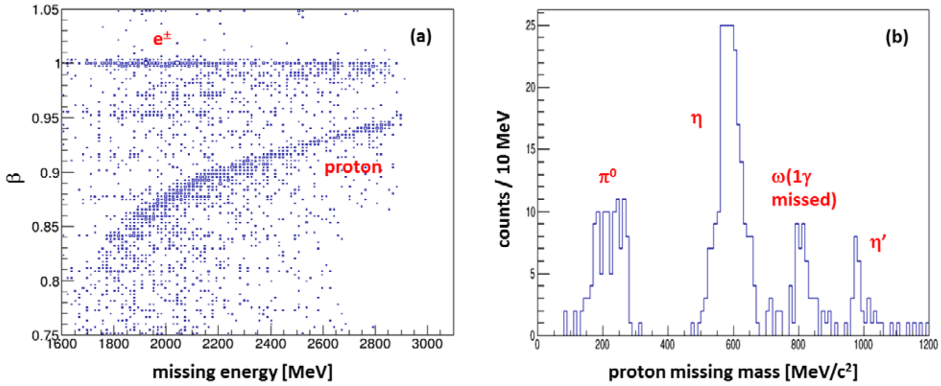

Fig.3. (a) Scatter plot of the β measured at RPC versus the missing energy obtained from meson detection at the BGOegg calorimeter. (b) Missing mass distribution for the proton whose β was measreud at RPC.

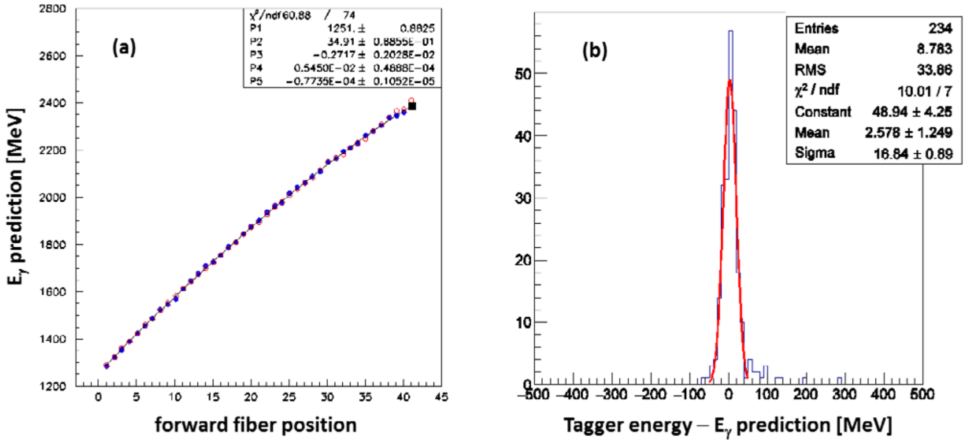

Fig.4. (a) Photon energy predictions as a function of the tagger hit position. The open circles, the filled circles, and the filled squares indicate the predictions based on BGOegg, RPC, and Compton edge, respectively. (b) The distribution of the photon energy measured at the tagging detector, relative to the prediction from a kinematic fit of the $\gamma p \to \pi^0 \eta p$ events in the 2014B LH$_2$ data.

tector hit position was related with the photon energy predictions by three independent methods: (1) a kinematic fit to the $\gamma p \to \pi^0 \pi^0 p$ events, detected at the BGOegg calorimeter, (2) an inverse calculation to force the missing mass to the nominal meson masses by detecting a forward proton at RPC in the $\gamma p \to \pi^0 p$ or ηp events, and (3) the adjustment of the Compton edge to the value expected from the laser wavelength and the electron beam energy. These methods return the tagger energy functions consistent with each other, after the careful calibrations mentioned above. The final energy function has been determined by taking a weighted mean of them. Figure 4(b) shows the measurement of a photon energy resolution by a kinematic fit to $\gamma p \to \pi^0 \eta p$ events, where the beam energy is treated as a unmeasured variable. By subtracting the contribution from the BGOegg energy resolution quadratically, the photon beam energy resolution was estimated to be 12.05±0.74 MeV. This is consistent with the expectation from the electron beam emittance.

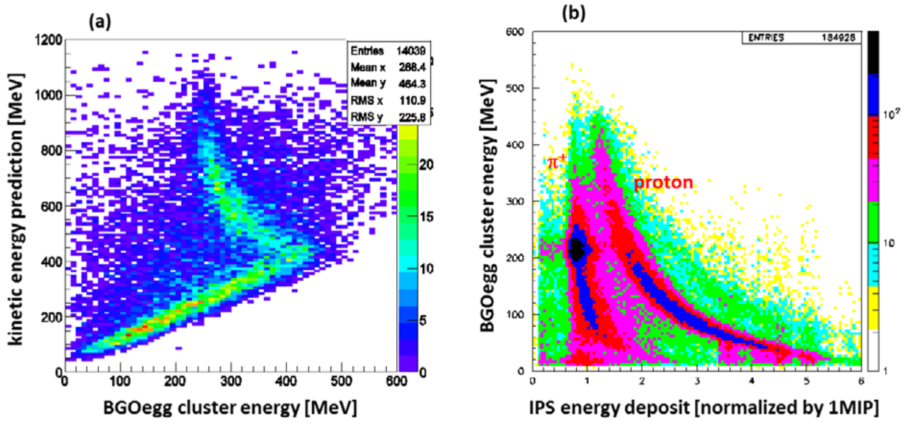

Fig.5. (a) The kinetic energy prediction as a function of the measured BGOegg cluster energy. The predicted energies are obtained from a kinematic fit to $\gamma p \to \omega p$ events in the 2014B LH_2 data. The proton from a 1-nucleon absorption is expected to possess a low kinetic energy around 100 MeV. (b) The BGOegg cluster energy as a function of the energy deposit at IPS. Events with the BGOegg hit at layer 7 are plotted here. The polar angle dependence of the IPS energy has been actually calibrated.

§4. Preliminary analyses

As described in Section 2, we have analyzed the 2014A carbon data with RPC information as a test sample of the η'-bound nuclei search in the reaction of $C(\gamma,p)^{11}_{\eta'}B$. First of all, we studied the event selection conditions for the 1-nucleon absorption signal, where the $\eta' N \to \eta N$ conversion is expected to be dominant [9]. The produced η meson was tagged at the BGOegg calorimeter in the 2γ and $3\pi^0$ decay modes for the background reduction more than two order of magnitude instead of the signal acceptance of ~0.1. The missing mass spectrum of a forward proton at RPC ($MM_{C(\gamma,p)}$) was examined in both the η-tag and sideband regions with masking the signal region of the missing mass. It turns out that the combinatorial background due to the multiple pion production is not significant in the sideband sample, but that the η-related backgrounds ($\eta\pi$ production, etc) largely remain only if the η is tagged. Therefore, we will obtain extra reduction factors by tagging the opposite proton from the ηN conversion. This proton can be identified from the kinetic energy measurement at the BGOegg calorimeter and the energy deposit at IPS, as shown in Fig. 5. We will also explore the tagging condition of 2-nucleon absorption signals, where nearly back-to-back nucleons are expected at the BGOegg calorimeter and IPS.

The analyses using the LH_2 target data are also in progress. The $\pi^0\gamma$ decay mode in the ω photoproduction and the 2γ decay mode in the η and η' photoproduction have been focussed especially to measure the photon beam asymmetries. While those mesons are measured at the BGOegg calorimeter, an additional charged track is detected at either of the DC or BGOegg calorimeter to restrict its direction. Figure 6(a) shows the $\pi^0\gamma$ invariant mass distribution after the kinematic fit with the proton direction. A clear ω peak is seen with a relatively low background level. In the 2014B data, about 33K, 44K, and 1,200 events are counted for the ω, η, and η' events, respectively. These statistics will be increased by the tagger and IPS analysis upgrades, the use of different decay modes, and the further

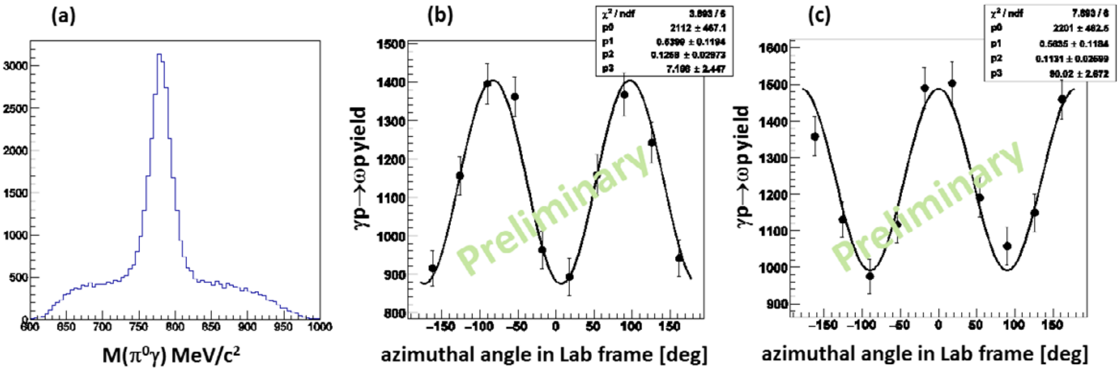

Fig.6. (a) The $\pi^0\gamma$ invariant mass distribution in the 2014B LH$_2$ data. (b) Azimuthal asymmetry patterns of the ω photoproduction yield for the vertical polarization beam. (c) Same as (b) but for the horizontally polarized photon beam.

analysis of the 2015B data. Figure 6(b) and (c) show the azimuthal asymmetry pattern of the ω photoproduction yield, without binning the energy and polar angle ranges and taking into account the beam polarization degree. In both the vertical and horizontal polarization data, the asymmetry patterns are well observed with a $\sim 90^\circ$ phase difference. Such asymmetry patterns have been seen also in the η and η' photoproduction.

§5. Summary and prospect

The LEPS2/BGOegg collaboration has started the physics data-taking from 2014 April by using carbon, polyethylene, and liquid hydrogen targets with the 1.3–2.4 GeV photon beam. We have mostly finised the preparation of the event reconstruction programs and the precise calibrations with good understandings of the detector performance. Good resolutions in the BGOegg energy measurement, the RPC TOF measurement, and the tagger beam energy measurement will satisfy our physics goals mentioned above.

On the η'-bound nuclei search, we have started the background reduction studies by tagging the 1-nucleon absorption signal of the bound state. Further improvements of the signal-to-noise ratio will be achieved in both 1-nucleon and 2-nucleon absorption modes. We already have 7 times higher statistics in the 2015A carbon target data, which will enable to examine the existence of the η'-bound nuclei for the models with deep binding energies. In 2016A, we are also accumulating more statistics with the carbon target.

For the 2014B LH$_2$ target data, we are first measuring the photon beam asymmetries in the ω, η, and η' photoproduction. The differential cross sections will be then measured with the systematic understanding of acceptance and normalization. Additional 2015B data with the 1.4 times statistics is also available, enabling the analyses for multiple meson photoproduction, K^0_S photoproduction, etc.

References

[1] H. Nagahiro *et al.*, Phys. Rev. C **74**, 045203 (2006).

[2] S. Sakai and D. Jido, Phys. Rev. C **88**, 064906 (2013).

[3] N. Muramatsu *et al.*, Nucl. Instr. Meth. **A737**, 184 (2014).

[4] N. Muramatsu, ELPH Report 2044-13 (2013) or arXiv:1307.6411.

[5] T. Ishikawa *et al.*, ELPH Annual Report Vol.1, 61 (2012).

[6] N. Tomida *et al.*, Nucl. Instr. Meth. **A766** 283, (2014).

[7] N. Muramatsu *et al.*, ELPH Annual Report Vol.5, 106 (2015).

[8] K.A. Olive *et al.* (Particle Data Group), Chin. Phys. C **38**, 090001 (2014).

[9] E. Oset *et al.*, Phys. Lett. **B 704**, 334 (2011).

Commissioning of the SCRIT electron scattering facility with ^{132}Xe target

K. Tsukada[1], K. Adachi[3], A. Enokizono[3], T. Fujita[3], M. Hara[2], M. Hori[3],
T. Hori[2], S. Ichikawa[2], K. Kurita[3], T. Ohnishi[2], T. Suda[1], T. Tamae[1],
M. Togasaki[3], T. Tsuru[1], K. Yamada[3], M. Wakasugi[2], and M. Watanabe[2]

[1]*Research Center for Electron Photon Science, Tohoku University, Sendai, 982-0826*
[2]*RIKEN Nishina Center for Accelerator-Based Science, Wako, 351-0198*
[3]*Department of Physics, Rokkyo University, Tokyo, 171-8501*

SCRIT electron scattering facility has been constructed to realize electron scattering experiments off unstable nuclei. From January 2016, a series of commissioning experiments with ^{132}Xe target has been carried out for the electron beam energies of 150, 200, and 300 MeV. By the comparison with the angular distributions and calculations, an information of nuclear shape are extracted . The present status of analysis are reported here.

§1. Introduction

Charge density distribution of atomic nuclei is one of the most important information for the nuclear structure investigation. Actually, many stable nuclei have been investigated and our understanding of nuclear structures have been established by electron scattering experiments in the latter half of the 20th century. This method, however, could be applied almost only stable nuclei because of the difficulty to prepare the target material for short-lived unstable nuclei. Recently, it has been revealed that some of nuclei far from the stability valley have exotic structures such as halo, skin, new magic numbers, and magicity loss, and so on. Many scientific efforts for understanding unstable nuclear structures are being made over the world. Because of the great advantages of electron scattering for the nuclear structure studies, actualization of electron scattering off unstable nuclei has been awaited.

We proposed a completely new target-forming technique, namely SCRIT (Self-Confining Radioactive isotope Ion Target) which made electron scattering off unstable nuclei possible [1]. After the success of the feasibility study of the SCRIT system [2, 3], we have developed the SCRIT electron scattering facility at RIKEN RI Beam Factory, Japan.

In 2015 and 2016, a series of the commissioning of whole facility with using ^{132}Xe target have been performed. In this report, the first measurement of charge density distribution of a nucleus with the SCRIT electron scattering facility is reported.

§2. Experimental apparatus

2.1 overview of the facility

The facility consists of a 150-MeV racetrack microtron (RTM), an electron storage ring (SR2) equipped with the SCRIT, an electron-beam driven RI separator for SCRIT (ERIS), a cooler buncher system based on a linear radio-frequency quadruple trap, and a window-frame spectrometer for electron scattering (WiSES). Figure1 shows an overview of the SCRIT electron scattering facility. Details of the electron accelerators and ERIS can be found elsewhere [4, 5].

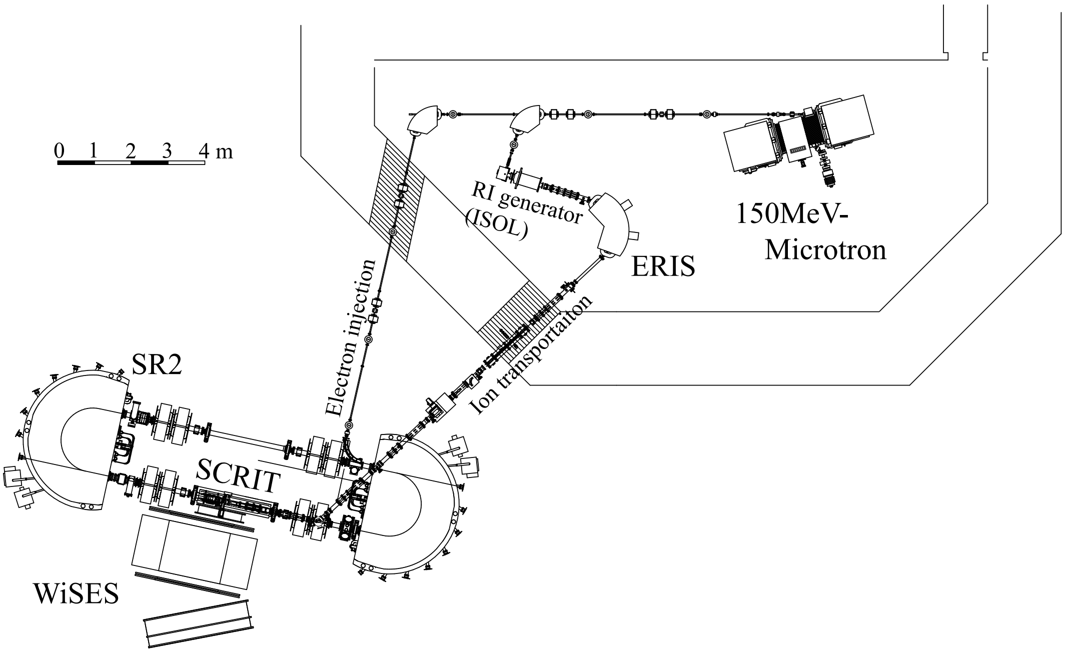

Fig.1. Overview of the SCRIT electron scattering facility.

The electron beam energy were controlled to be 150 MeV, 200 MeV and 300 MeV. The electron beam currents were typically 250 mA decreasing to 150 mA at the end of a 40-min run.

2.2 Target

For the commissioning experiment, ^{132}Xe was not provided from the ISOL system of ERIS, but extracted from the standard xenon gas which was introduced at an entrance branch of the ERIS system. After the mass separation, pure ^{132}Xe ions were bunched and delivered into the SCRIT.

The target ions were stored in the SCRIT for a few hundred ms and ejected to refresh the target quality because the amount of the residual gases also increased due to the ionization and trap by the electron beam. The SCRIT operation with and without target ions (IonIN/IonOUT) were alternated for the comparative measurement and the background subtraction. The trapping times were usually set to be 240 ms which was decided to maximize the ratio between the number of target ions and residual gases. The interval among the trapping times was fixed to be 10 ms.

2.3 Electron spectrometer (WiSES)

Details of the electron spectrometer were explained in the previous report [6]. After the previous report, we changed the gas for the drift chambers from He+CH_4 (50:50) to He+C_2H_6 (80:20) in order to improve the time resolution and keep the multiple scattering effect low at the same time.

§3. Run summary

Table 1 shows a run summary for the series of the commissioning with ^{132}Xe target until April 2016. The meaning of each term are explained in the caption. Achieved averaged-luminosities are also listed in the table. Because we started parameter tuning for the accelerator and the ion transportation system with ^{132}Xe ions from January 2016, the luminosity had been continuously increased and exceeded 1×10^{27} [/cm^2/s] at February 2016.

Table 1. Run Summary Table. The irradiation times are corresponding to the total time of IonIN conditions. The duty is defined as, $duty = T_{IonIN}/(T_{IonIN} + T_{IonOut} + 2 * T_{Interval})$. The luminosities are averaged values evaluated by WiSES assuming a nuclear charge density distribution.

Ee [MeV]	Date	Irradiation time [sec]	Trapping time [ms]	Duty [%]	Luminosity [/cm^2/s]
150	19-22/Jan	1.9×10^4	990	49.5	$8.7\times10^{26} \pm 2.0\%$
	8-10/Feb	7.8×10^3	240	48.0	$1.1\times10^{27} \pm 2.5\%$
200	6-14/Apr	1.3×10^5	240	48.0	$1.1\times10^{27} \pm 1.8\%$
300	16-18/Apr	1.3×10^4	240	48.0	$1.4\times10^{27} \pm 30\%$

§4. Data analysis

Figure 2 shows a vertex point distribution along the beam direction after the background subtraction. It is clearly shown that the target ions were trapped inside the SCRIT potential. The reason why there are two peaks is a distortion of the electric potential due to a gap of the SCRIT electrodes. Figure 3 is a reconstructed momentum distribution for Ee=200 MeV data after a 4-th Runge-Kutta analysis connecting two tracks of FDC and RDC. The background contributions are already subtracted. The analysis procedure is explained in the previous report [6]. The achieved momentum resolution of 3.5×10^{-3} is a little bit worse than the design value of 2.5×10^{-3} due to a lack of knowledge of the magnetic field. Low momentum tail below the elastic peak can be explained by a simulation as shown in Fig. 4. In the simulation, the radiative tail at the target [9] and the energy deposit at the beryllium plate which is a window of the SCRIT chamber and 2 mm thick are taken into account.

Figure 5 shows obtained angular distributions for Ee=150, 200, and 300 MeV. The systematic error are considered to be 5%, which is still a rough estimation. The differential cross sections are calculated by DREPHA code [8] assuming the two-parameters Fermi distribution as a nuclear charge density distribution,

$$\rho(r) = \frac{\rho_0}{1 + \exp(\frac{r-C}{a})}$$

$$a = \frac{t}{4\ln 3}.$$

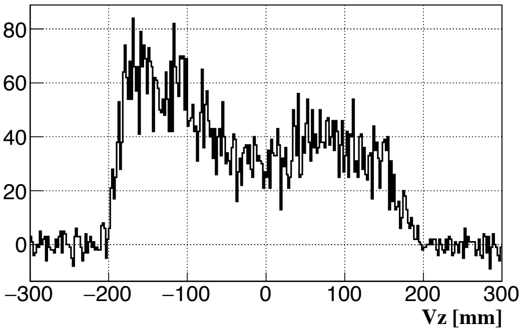

Fig.2. Reconstructed vertex point distribution for Ee=200 MeV after background subtraction (IonIN - IonOUT).

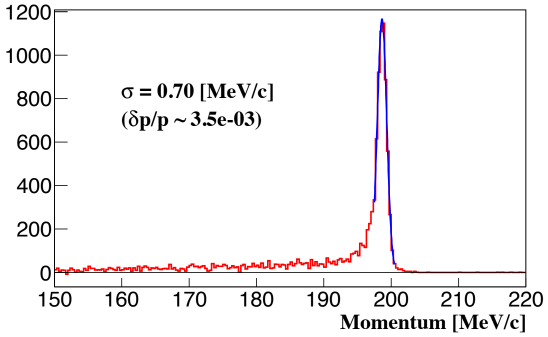

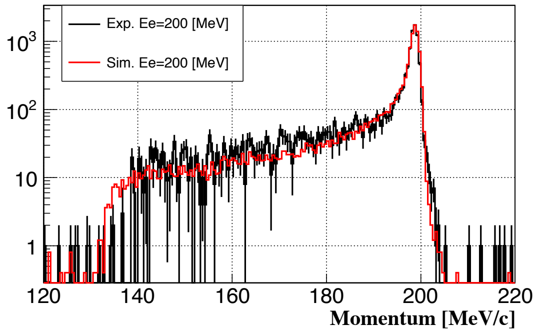

Fig.3. Reconstructed momentum distribution for Ee=200 MeV after background subtraction (IonIN - IonOUT).

Fig.4. Comparison of the low momentum tails between our data and simulation.

The luminosities are decided by fitting experimental data assuming a nuclear shape to be C=5.646 fm and t=2.3 fm which are derived from the muonic X-Ray experiment [10]. The calculation seems to well reproduce the data although the statistics for Ee=300 MeV is poor.

Figure 6 is a contour plot of χ^2 distribution for fitting the angular distributions of Ee=150 MeV and 200 MeV data at the same time by changing parameters, C and t. Here, luminosities of both data are used as free parameters. That is, we analyze only the shape of the angular distributions. From Fig. 6, the most probable point of C and t is derived with error (1σ) which are listed in Table 2 with values of the muonic X-Ray. It is found that $< r^2 >^{1/2}$ and C are consistent each other. Although the error of t is too large for a precise discussion, note that the muonic X-Ray measurement is insensitive to the parameter t. So, our result is the first data of ^{132}Xe charge density distribution.

In order to improve the accuracy of both parameters C and t, the absolute value of the luminosity is necessary. Analysis of the luminosity monitoring system is also being developed and will be used to decide the luminosity with high accuracy soon.

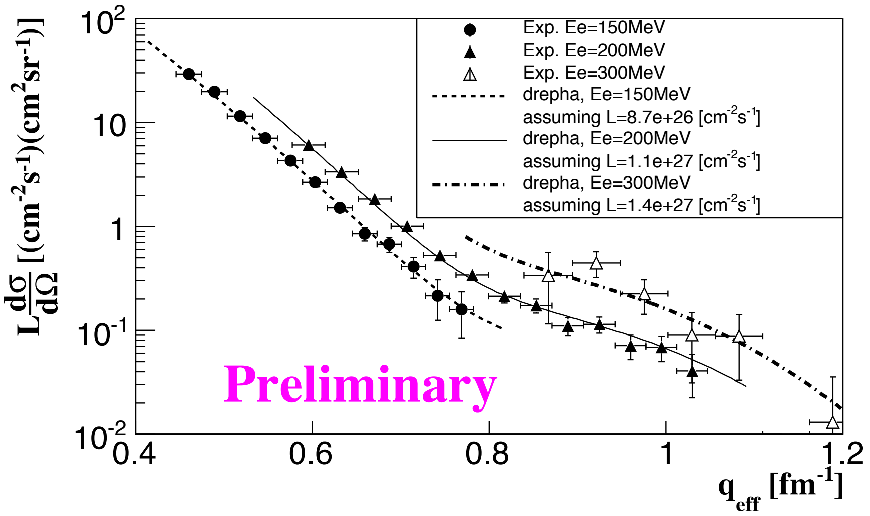

Fig.5. Obtained angular distributions for Ee=150, 200, and 300 MeV. Lines are calculation of a DWBA code assuming the two-parameters fermi distribution as a nuclear shape (C=5.646 fm, t=2.3 fm [10]).

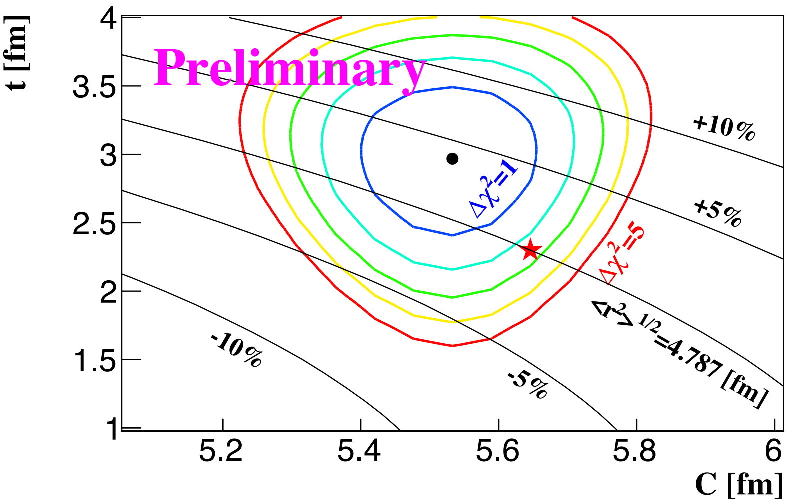

Fig.6. χ^2 distribution for fitting the angular distributions (150 and 200 MeV) by changing the nuclear shape parameters, C and t. Contour levels represent $\Delta\chi^2 = 1 \sim 5$. A black circle is a minimum χ^2 point. A red star is a position decided by the muonic X-Ray experiment. Black solid lines are contour levels of $< r^2 >^{1/2} = const.$.

§5. Conclusions and future prospects

The SCRIT electron facility has been constructed to realize electron scattering off unstable nuclei for the first time. The primary goal of this facility is to determine their charge density distributions by elastic electron scattering. The elastically scattered electrons were successfully identified, and the

Table 2. Comparison the nuclear shape parameters between muonic X-Ray and our data (preliminary).

	$< r^2 >^{1/2}$ [fm]	C [fm]	t [fm]
muonic X-Ray [10]	4.787	5.6460	2.30 (assumed)
this exp.	$4.97^{+0.25}_{-0.24}$	$5.53^{+0.12}_{-0.13}$	$2.97^{+0.52}_{-0.56}$

momentum distributions can be roughly explained by the simulation taking into account the radiative tail. The angular distributions for Ee=150, 200, and 300 MeV are well reproduced with calculations assuming a two-parameters Fermi as a nuclear charge density distribution. By changing parameters, C and t, of the two-parameters Fermi, the charge radius and diffuseness can be extracted independently.

Following this successful experiments, the electron scattering experiment with series of the Xe isotopes and ^{132}Sn trapped by the SCRIT system will be performed this year.

Acknowledgment

This work is supported by Grants-in-Aid for Scientific Research (S) (Grands No. 22224004) from JSPS.

References

[1] M. Wakasugi *et al.*: Nucl. Instr. and Meth. A 532 (2004) 216.

[2] M. Wakasugi *et al.*: Phys. Rev. Lett. 100 (2008) 164801.

[3] T. Suda *et al.*: Phys. Rev. Lett. 102 (2009) 102501.

[4] T. Suda *et al.*: ELPH Annual Report 2011-2013 Vol. 2, Tohoku University, 201 (2013).

[5] T. Ohnishi *et al.*: Nucl. Instr. and Meth. B 317 (2013) 357.

[6] K. Tsukada *et al.*: ELPH Annual Report 2014 Vol. 5, Tohoku University, 125 (2014).

[7] T. Tamae *et al.*: ELPH Annual Report 2011-2013 Vol. 2, Tohoku University, 1 (2013).

[8] B. Drepher, DREPHA: a phase-shift calculation code for elastic electron scattering, communicated by J. Friedrich.

[9] J. Friedrich: Nucl. Instr. Meth. 129 (1975) 505.

[10] H. de Vries, W. de Jager, and C. de Vries: Atomic Data and Nuclear Data Tables 36 (495-536) 1987

(ELPH Experiment : #2778)

Production of K-42,43 radioactive tracer

H. Kikunaga[1], K. Tsukada[1], and T. Suda[1]

[1]*Research Center for Electron Photon Science, Tohoku University, Sendai, 980-8578*

Photonuclear reaction yields of ^{nat}Ca(γ,X)^{43}K have been measured by comparing with ^{nat}Ni(γ,xn)^{57}Ni reaction yield. The separation method to isolate carrier-free ^{43}K isotopes from the Ca target material by using precipitation method and extraction chromatography has been described.

§1. Introduction

Potassium is an essential element for all animal and plant growth. Understanding the behavior of potassium in biosphere is important on the various fields such as biological sciences. The radioactive tracer technique has been widely recognized as a powerful tool for behavior analysis of elements. The isotopes ^{42}K ($T_{1/2}$= 12.4 h) and^{43}K ($T_{1/2}$= 22.2 h) have a potential as radioactive tracers because of their suitable half-lives. In this work, these potassium isotopes were produced in the photonuclear reaction ^{nat}Ca(γ,X)^{42,43}K and were prepared as a carrier-free tracer.

§2. Experimental

A target stack containing about a 200 mg of CaO pellet and a Ni monitor foil with thickness of 10 μm was enclosed in a quartz tube for irradiation with bremsstrahlung. The irradiation was carried out with the electron linear accelerator at Tohoku University. The accelerator was operated at an electron energy from 20, 30, 40, and 50 MeV with a mean current around 0.1 mA. The enclosed target was placed in the back of a platinum converter and cooled with running tap water during the 10 min irradiation for the yield measurements and 1 hour irradiation for the tracer production. The separation procedure for carrier-free ^{43}K tracer is shown in Fig. 1. About 20 mL of H_2O was added to the irradiated CaO, and then 0.5 M (mol/dm^3) oxalic acid was added dropwise until the pH value was close to 7. The resulting precipitation, CaC_2O_2, was aged under heating for 20 min. After centrifugation, the supernatant was dried up on a glass beaker. To the residue was added a mixture of 13 M HNO_3 and 35% H_2O_2, and the solution was heated on a hot-plate to decompose the oxalic acid and oxalates. The potassium isotopes was adjusted to an 0.001 M HNO_3 solution and passed through an extraction chromatographic resin column (Eichrom, Ln resin, 1 mL) to adsorb completely the calcium isotopes. The irradiated targets and the ^{43}K solutions after the chemical separation were subject to γ-spectrometry to determine the photonuclear reaction yields and the chemical yields, respectively.

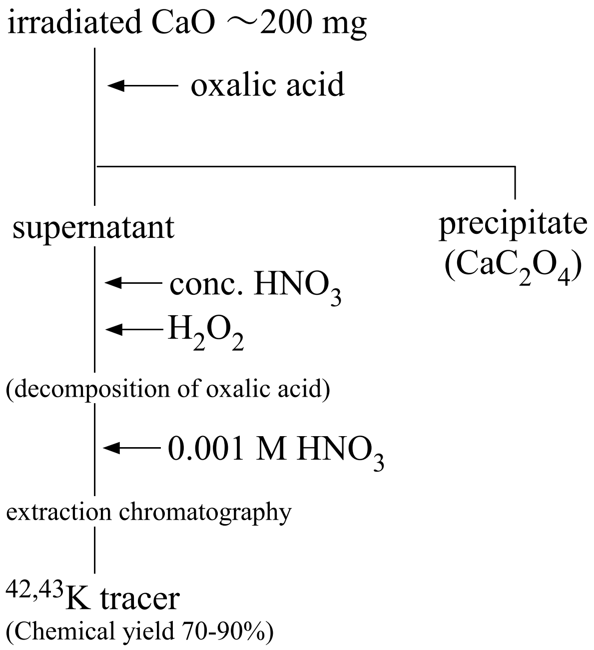

Fig.1. Chemical procedure for the preparation of carrier-free ^{43}K tracer

§3. Results

The obtained ^{nat}Ca(γ,X)^{43}K yields are shown in Fig. 2. These photonuclear reaction yields were determined by comparing with ^{nat}Ni(γ,xn)^{57}Ni reaction yield reported in the ELPH annual report (2014) [1], $1.97(6) \times 10^3$ Bq/mg/μA/h for 50 MeV, $1.23(4) \times 10^3$ Bq/mg/μA/h for 40 MeV, $6.00(17) \times 10^2$ Bq/mg/μA/h for 30 MeV, and $1.04(3) \times 10^2$ Bq/mg/μA/h for 20 MeV. Based on the reaction yields, 1 MBq of ^{43}K isotope was produced in a 200 mg of a ^{nat}KCaO target irradiated for 1 hour at the ELPH linear accelerator. A typical γ-ray spectrum for the ^{42,43}K tracer after the chemical purification is shown in the Fig. 3. Only the γ-peaks of K isotopes are observed in Fig. 3 although those of ^{47}Ca were clearly seen in the spectrum before the chemical separation. The chemical yields were in the range of 70% to 90%. A ^{43}K tracer will be distributed through a KAKENHI research project, the Grant-in-Aid for Scientific Research on Innovative Areas-Platforms for Advanced Technologies and Research Resources forms a resource and technical support platform for research “Supply Platform of Short-lived Radioisotopes for Fundamental Research”, from the latter half of 2016.

References

[1] H. Kikunaga *et al.*: ELPH Annual Report (2014) 144.

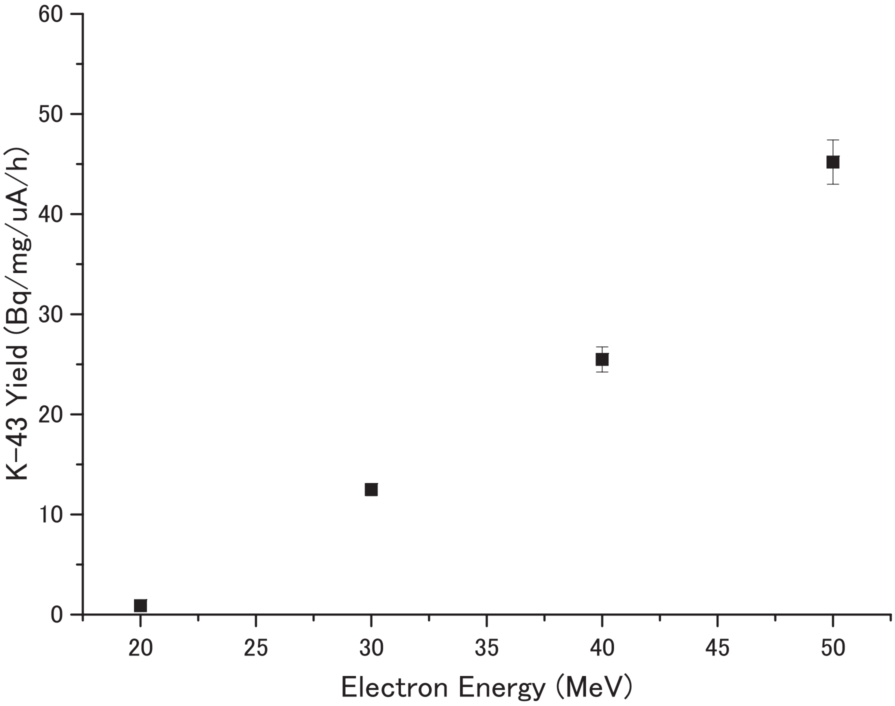

Fig.2. Photonuclear reaction yields of ^{nat}Ca(γ,X)^{43}K reaction

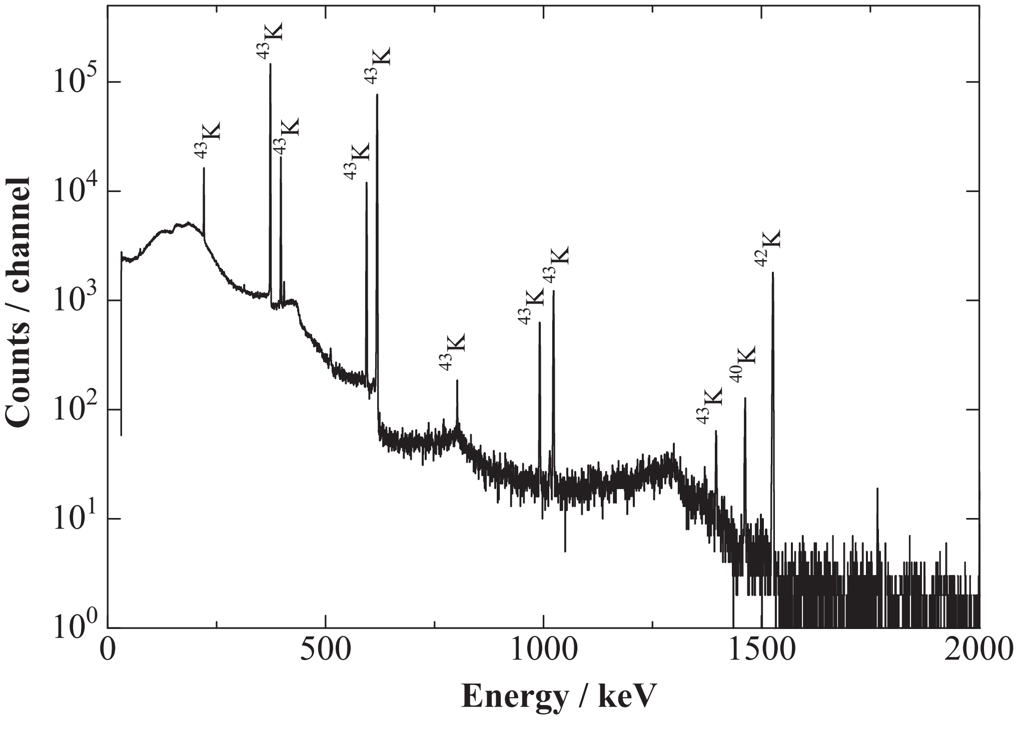

Fig.3. An example of a γ-ray spectrum of K tracer solution.

(ELPH Experiment : #2804)

土壌試料中の放射性ストロンチウムの迅速化学分離法の検討

遠藤勇[1], 大浦泰嗣[2]

[1] 首都大学東京都市教養学部理工学系化学コース （192-0397 東京都八王子市南大沢 1-1)
[2] 首都大学東京大学院理工学研究科分子物質化学専攻 （192-0397 東京都八王子市南大沢 1-1)

Rapid Chemical Separation Method of Radioactive Strontium in Soil Samples

Isamu Endo[1] and Yasuji Oura[2]

[1]*Department of Chemistry, Tokyo Metropolitan University, Hachioji, 192-0397*
[2]*Department of Chemistry, Tokyo Metropolitan University, Hachioji, 192-0397*

Chemical separation procedure for radioactive Sr in soil samples was developed using a solid extraction method. Strontium was separated quantitatively from acid leachate treating a soil by a batch procedure without any preconcentrations. Chemical yields of Sr were dependent on a volume of leachate and an amount of extraction resin, and were roughly guessed based on the distribution ratio. A processing time of chemical separation procedure for Sr in a soil was shortened rather than a traditional method.

§１． はじめに

2011 年の福島原発事故により，環境中におびただしい量の放射性物質が放出された．事故当初より，国内各地で，事故により放出された ^{131}I, ^{137}Cs など γ 線を放出する放射性核種については，様々な試料に対して，その濃度が測定されている．一方，γ 線を放出しない純 β 放射体については，その定量には化学分離操作が必須であるため，γ 線放出核種に比べて，その濃度の報告は限られている．純 β 放射体の代表的な核種である ^{90}Sr の定量には，文部科学省の「放射性ストロンチウム分析法」[1]に準拠した化学分離法が採用されることが多いが，この方法は，沈殿法やイオン交換法などを駆使した非常に煩雑で時間のかかる方法である．そのため，簡便で迅速な化学分離法が望まれている．そこで，最近，様々な分野で急速に広まっている固相抽出法を利用した簡便で迅速に ^{90}Sr を分離可能な方法を検討する．とくに，将来に同様な事故が不幸にして起こった時を想定し，緊急時の迅速な土壌からの放射性ストロンチウムの分離法を放射性トレーサを利用して検討した．

§2．実験方法

2.1 放射性トレーサ製造

ストロンチウムの化学的挙動は^{85}Sr(半減期65日)トレーサを用いて調べた．塩化ストロンチウムをAl箔で包み，直径10 mmのペレットとし，石英管に封入後，最大エネルギー50 MeVの制動放射線で，4時間照射した．これを首都大学東京RI研究施設にて水に溶解し，トレーサ溶液とした．このトレーサ溶液には，副反応により生成した^{83}Rb(半減期86日)も含まれていた．RbはCsの同族元素であるため，これを利用してRbの化学的挙動も調べ，放射性Csと分離できるかを検討した．

土壌試料には^{40}Kや，ウラン壊変系列，トリウム壊変系列の天然放射性核種が含まれているため，Srを正確に定量するには，これらの核種を十分に除去する必要がある．壊変系列の多くの核種はその半減期が短いため，たとえSrフラクションに混入しても，しばらく放置すれば十分に減衰する．しかし，^{210}Pbは半減期が22年と長いため，Srと分離する必要がある．そこで，^{203}Pb(半減期2.2日)トレーサを用いて，鉛がストロンチウムと十分分離されるか調べた．Al箔で包んだペレット状の酸化鉛と塩化ストロンチウムを最大エネルギー30 MeVの制動放射線で，30分間照射した．照射後，酸化鉛は4 mol/L HClに溶解したが，溶け残りが生じたため，上澄み液のみ利用した．そのため，トレーサ実験での鉛担体量が不明である．塩化ストロンチウムは，1 mLの8 mol/L硝酸に溶解した．^{85}Srは十分生成しなかったので，^{87m}Sr(半減期2.8時間)を利用した．

2.2 トレーサ実験

約10 gの土壌に濃硝酸あるいは8 mol/L硝酸を30 mL ～ 50 mLを加え，ホットプレート上で数時間加熱し，吸引ろ過した．このろ液を酸溶出液と呼ぶ．これまでに，酸溶出液からSrを沈殿法により予備濃縮後，固相抽出法により精製する方法を試みていたが，安定した化学収率を得ることができなかった．そこで，予備濃縮せずに，酸溶出液から直接固相抽出法によりSrを分離することを試みた．硝酸水溶液，あるいは土壌の酸溶出液に，^{85}Srトレーサ溶液を100 μL (Sr担体約1 mgを含む)と，固相抽出樹脂(Srレジン，Eichrom社)を0.5 gまたは1 gを加え，1時間攪拌した(バッチ法)．攪拌後，カラムに移し，レジンと抽出液を分離した．このSrレジンカラムに，8 mol/L硝酸を流した後，0.01 mol/L硝酸でSrを溶離した(カラム法)．適宜，溶液をGe半導体検出器で測定し，Srの挙動を追った．

§3．結果と考察

8 mol/L硝酸に調製した荒木田土の酸溶出液70 mLにSrレジンを1 g加えて約1時間攪拌したところ，52 %のSrがSrレジンに吸着し，Rbは吸着されなかった．また，参照実験として8 mol/L硝酸でも同様のバッチ実験をおこなったところ，60 %のSrが吸着し，8 mol/L硝酸での分配比は105 mL/gであった．酸溶出液から直接SrレジンにSrを吸着させることができ，その吸着率は参照実験よりもわずかに小さいだけであることがわかった．カラム法により，Srレジンに吸着したSrをほぼ100 %溶離することができたので，酸溶出液からのバッチ法よるSrの吸着にひきつづき，カラム法によるSrの溶離を行えば，Srの化学収率をバッチ法での実験条件から分配比で計算される吸着率として予測することができる．事故時の迅速な測定という状況においては，化学収率を実測する前に，おおよその定量値を得ることができることは大きな利点であるといえる．

土壌の酸溶出液は，一般に黄色から褐色をしており，鉄が多く含まれていると推察できる．これまでに，

60 g の黒土を濃硝酸 50mL 中で 3 時間加熱したところ，414 mg の鉄が溶出されたことを得た．土の種類により，溶出される鉄の量は変化すると考えられるので，鉄が Sr の吸着を妨害しないか調べた．Fe 濃度が 0.003, 0.007, 0.01, 0.03 g/mL である 8 mol/L 硝酸溶液と鉄を含まない 8 mol/L 硝酸溶液での Sr 吸着率を調べたところ，いずれも約 30 % ～ 40 %であり，吸着率は鉄濃度に依存しないことがわかった．ただし，分配比から計算される吸着率のおよそ 1/2 であり，現在のところ，その低くなった原因は不明である．また，Rb はいずれの条件でも Sr レジンに吸着しなかったため，土壌中の ^{40}K や放射性 Cs と十分分離できると考えられる．

天然放射性核種 ^{210}Pb が Sr フラクションに混入すると，Sr 定量値を過剰評価してしまう．8 mol/L 硝酸と 0.01 mol/L 硝酸での Pb の Sr レジンへの分配比はそれぞれ約 500 mL/g と約 100 mL/g であるため，Pb は Sr レジンに吸着したままで，ほとんど溶離しないと推測される．そこで，^{203}Pb トレーサを用いて，Sr フラクションへの Pb の混入率を調べた．なお，Sr は ^{87m}Sr トレーサをもちいた．25 mL の酸溶出液に 0.5 g の Sr レジンを加えて分離を行ったところ，Sr と Pb の Sr レジンへの吸着率はそれぞれ 54 %と 89 %であった．カラム法で溶離を行った Sr フラクション (0.01 mol/L 硝酸 3mL で 3 回．それぞれ第 1，第 2，第 3 サブフラクションと呼ぶ) における Sr の化学収率は 30 %で，8 %の Pb が混入していた．Sr は第 1 サブフラクションで Sr フラクションでの 94 %溶離されたが，Pb は第 3 サブフラクションでもっとも多く (Sr フラクションの 63 %) 溶離された．溶離液量を 6 mL とすることで，Pb の混入率を減少することができる．Pb が混入した Sr フラクションの Sr を鉄共沈法で精製を試みたところ，^{203}Pb/^{87m}Sr 計数率比は 0.16 %から 0.07 %以下に減少し，鉄共沈法により精製可能であることを確認した．

土壌試料は有機物を含むことが多いが，一般に，有機物があると取り扱いが難しく，また，化学分離を妨害する．放射性ストロンチウム分析法 [1]では，あらかじめ，土壌試料 100 g を 500 ℃で 5 時間加熱することにより，有機物を分解除去するように定められている．この 5 時間を短縮するために，有機物を除去していない黒土 10 g を酸溶出し，Sr レジンによる分離を試みた．Sr レジンへの Sr の吸着率は酸溶出液の有機物濃度に依存しなかったが，有機物濃度が高いほど，Sr レジンからの溶離率は低下した．また，酸溶出液は黒褐色であり，Sr レジンから溶離した Sr フラクションも着色したため，これは液体シンチレーション検出器による測定には不適切である．Sr フラクションに硝酸を加え加熱してみたが，完全に脱色することは不可能であった．また，酸溶出液に過酸化酸素水を添加して加熱したり，あるいは有機溶媒抽出による脱色を試みたが，これも不可能であった．そこで，20 g ～ 50 g の土壌試料で必要な加熱時間を土壌の色の変化で定性的に検討したところ，500 ℃で 2 時間加熱すれば，有機物を十分に分解除去できることがわかった．なお，土壌の加熱前後での質量変化率は，0.5 時間から 5 時間の間では，加熱時間に依存せず，約 47 %であった．少量の有機物が残る場合もあるが，色から判断すると，これは Sr レジンに吸着したままで，Sr フラクションには混入しないようである．

§4．まとめ

土壌試料の酸溶出液から Sr を粗分離することなく，直接，Sr レジンを用いた固相抽出法で Sr の分離を試みた．バッチ法で行うと溶出液のマトリックスに影響されず，およそ分配比で計算される吸着率で Sr が吸着した．化学収率を実測する前に，定量値を見積もることが可能である．10 g の土壌試料ならば，有機物の加熱除去をふくめて，半日あれば十分に Sr を化学分離できる．

謝　辞

制動放射線照射では，菊永英寿准教授と塚田暁助教をはじめ，電子光理学研究センタースタッフの方々に大変お世話になりました．この場を借りて深く御礼申し上げます．

参　考　文　献

[1] 文部科学省: 放射性ストロンチウム分析法 (2003) .

(ELPH Experiment : #2805)

Study on Metallofullerene Encapsulating Artificial Radio Element of Promethium

K. Akiyama and S. Miyauchi

Graduate School of Science and Engineering, Tokyo Metropolitan University, 1-1 Minami-Ohsawa, Hachioji, Tokyo 192-0397

In this study, we tried to separate trace amount of **Pm** from large amount of **Sm** for the detailed **Pm** metallofullerene study by cation exchange chromatography. The optimal condition of **Pm/Sm** separation is the conditioning by 1 **M** $\mathbf{NH_4Cl}$, 0.2 **M** HIBA with pH=3.79 as an eluent, and flow rate of 0.5 **mL/min**. The R_s value of **Pm** and **Sm** separation in this condition is found to be 1.46. This value is applicable for the actual separation of **Pm** tracer from large amount of **Sm**.

§1. Introduction

Endohedral metallofullerenes (EMFs) are known as a clathrate compound and are attracting interest of the expectation for the potential application brought from their unique physical and chemical properties. The large number of studies about the EMFs have been reported, so far. Especially for the EMFs of lanthanide, it has been studied for a variety of encapsulated elements from the dawn of metallofullerene research. However, only metallofullerene of promethium (**Pm**) has been still missing [1]. It is well known that **Pm** is one of the artificial elements belonging to lanthanide elements and do not have any naturally occurred stable isotope. The chemical property of **Pm** is considered to be almost same as those of other neighboring lanthanides, actually most stable oxidation state in water is +3 similar to neighboring element of **Nd**. In general, **Pm** is produced from processing nuclear fuel and neutron irradiation of **Nd** in High Flux Isotope Reactor. However, ^{143}**Pm** produced by these methods is not suitable for the metallofullerene research because of their small γ-ray emission rate and their long half life.

Previously, we reported the production of **Pm** metallofullerenes using ^{143}**Pm** produced by photon activation of natural samarium and their properties such as oxidation state of **Pm** in fullerene cage [2]. Though the oxidation state of **Pm** in fullerene cage and main species of **Pm** metallofullerenes were clarified, there are some problems to investigate detailed information about the properties of **Pm** metallofullerenes. One of these problems is low activity ratio of ^{143}**Pm** in irradiated **Sm** targets. In the previous work, **Pm** metallofullerenes were produced by arc discharge method using porous carbon rods including **Pm** without chemical separation from target material of **Sm** [2]. To improve the activity ratio of ^{143}**Pm**, it is necessary to separate **Pm** from the taget material.

In this study, we try to separate **Pm** from large amount of **Sm** by cation exchange method using high performance liquid chromatography (HPLC).

§2. Experimental

2.1 Production of Promethium-143

About 1.0 **g** of **Sm** oxide were wrapped by **Al** foil and sealed into quarts tubes. These targets were irradiated by 50 **MeV** photon at Research Center for Electron Photon Science in Tohoku University. Irradiated **Sm** targets were dissolved to conc. **HCl** and then evaporated to dryness to make **Sm** and **Pm** to chloride form. Chlorinated target materials were dissolved to 3 **mL** of 2 **M HCl**. Accurate 10 μ**L** of 2 **M HCl** solution was added to 9.990 **mL** of $\mathbf{H_2O}$ for dilution.

2.2 HPLC Separation of ^{143}Pm from Sm by Cation Exchange

Figure 1 shows the schematic diagram of cation exchange chromatography apparatus used in this work. Diluted **Pm/Sm** solution was loaded into cation exchange column (Inertsil CX, GL Science co ltd., size: 4.6 ϕ**mm**×250**mm**) with 0.5 **mL/min** of the flow rate. Alpha-hydroxyisobutylic acid (α-HIBA) solution was used for an eluent. As a post column reagent, 0.2 **mM** of 4-(2-pyridylazo) resorcinol (PAR) was employed. Eluted components were monitored by UV detector at wavelength of 530 **nm**. Column temperature was kept at 50 ^{o}**C** during the experiments. Eluate were collected for every two minutes. γ ray emitted from these fractions were measured by germanium detector.

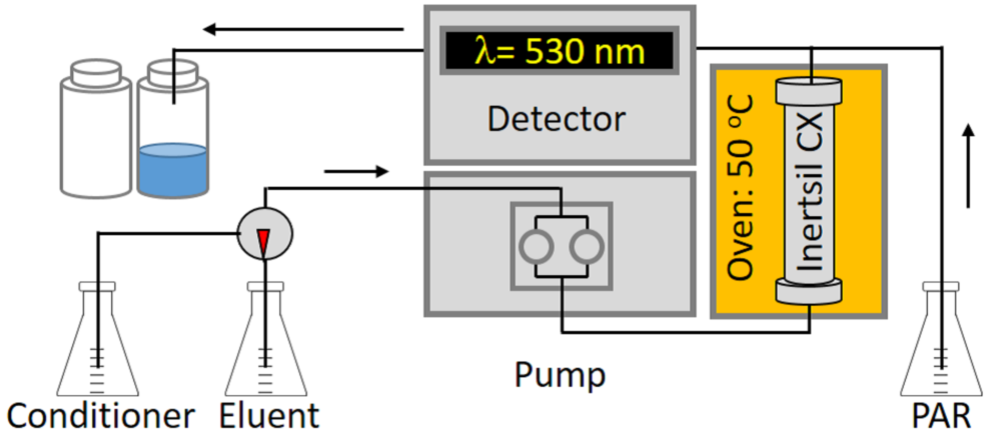

Fig.1. Schematic diagram of cation exchange chromatography apparatus used in this work.

§3. Results and Discussion

The separation conditions, such as the form of a resin, concentration of an eluent, and **pH** of a solution, were severely affect to the separation of neighboring lanthanide elements. Before **Pm/Sm** separation, we tried to check the peak resolution (Rs) on this column by cold experiment using Nd and Sm. The peak resolution is simply defined as follows:

$$R_s = 2(T_{R2} - T_{R1})/(W_1 + W_2)$$

Here, T_{R1}, T_{R2}, W_1, and W_2 indicate chromatographic retention time and peak width (3 sigma) of peak1 and 2, respectively. According to the chromatography theory, the R_s between **Pm** and **Sm** must be greater than 1.0 for the separation of **Pm** from **Sm** because more than about 99.9% of **Sm** can be removed at this R_s value [3]. To achieve R_s of **Sm** and **Pm** beyond 1.0, R_s between **Nd** and **Sm** is required to be over 2.0. Table 1 shows the R_s value for each cation exchange condition tested in this work.

Table 1. R_s value of **Sm** and **Pm** for cation exchange conditions.

No.	Conditioning	Sample	Eluent	Flow Rate **mL/min**	R_s
1	1 **M NH$_4$Cl**	10 **mg** (**Sm/Nd**=1/1) **pH**=4.00	0.3 **M** HIBA **pH**=3.87	0.5	0.86
2	1 **M NH$_4$Cl**	0.5 **mg** (**Sm/Nd**=1/1) **pH**=4.00	0.3 **M** HIBA **pH**=3.87	0.5	2.65
3	1 **M NH$_4$Cl**	0.5 **mg** (**Sm/Nd**=4/1) 0.3 **M** HIBA **pH**=3.69	0.3 **M** HIBA **pH**=3.69	1.0	1.01
4	1 **M NH$_4$Cl**	0.1 **mg** (**Sm/Nd**=4/1) 0.3 **M** HIBA **pH**=3.69	0.3 **M** HIBA **pH**=3.69	1.0	0.95
5	1 **M NH$_4$Cl**	0.1 **mg** (**Sm/Nd**=4/1) 0.3 **M** HIBA **pH**=3.69	0.3 **M** HIBA **pH**=3.69	1.0	1.30
6	1 **M NH$_4$Cl**	0.2 **mg** (**Sm/Nd**=3/1) dil. **HCl**	0.2 **M** HIBA **pH**=3.79	0.5	4.16

From these tested results, we decided to employ the cation exchange condition of batch No. 6 for the separation of **Sm** and **Pm**.

Figure 2 shows a HPLC chromatogram of **Pm/Sm** separation with above mentioned condition. Solid circles and open circles indicate radioactivity of ^{143}**Pm** and ^{145}**Sm** observed in the fractionated samples. Observed radioactivity in this figure is normalized to the radioactivity observed in the injection sample. Solid lines together with circles were results of peak fitting of the data. For comparison, HPLC chromatogram of No. 6 were also shown in this figure.

The R_s value of this result is estimated to be 1.46. For the **Pm** separation, if the peak fractions from 23 to 26 min. are collected in this chromatogram, the residual **Sm** amount would be estimated to be about 0.1%. This residual amount would be enough radioactivity ratio of **Pm** for the detailed study of **Pm** metallofullerenes.

Conclusion

In conclusion, we could find optimal condition of the separation of **Pm** and **Sm** and successfully separated **Pm** from large amount of **Sm** by cation exchange chromatography. Estimated residual amount of **Sm** is found to be about 0.1%.

Acknowledgment

We deeply thank to the facility staffs of research center for electron photon science at Tohoku University for supplying the high-quality electron beam. And also we thank to Professor Hidetoshi Kikunaga and Doctor Kyo Tsukada for helping us in the sample irradiation.

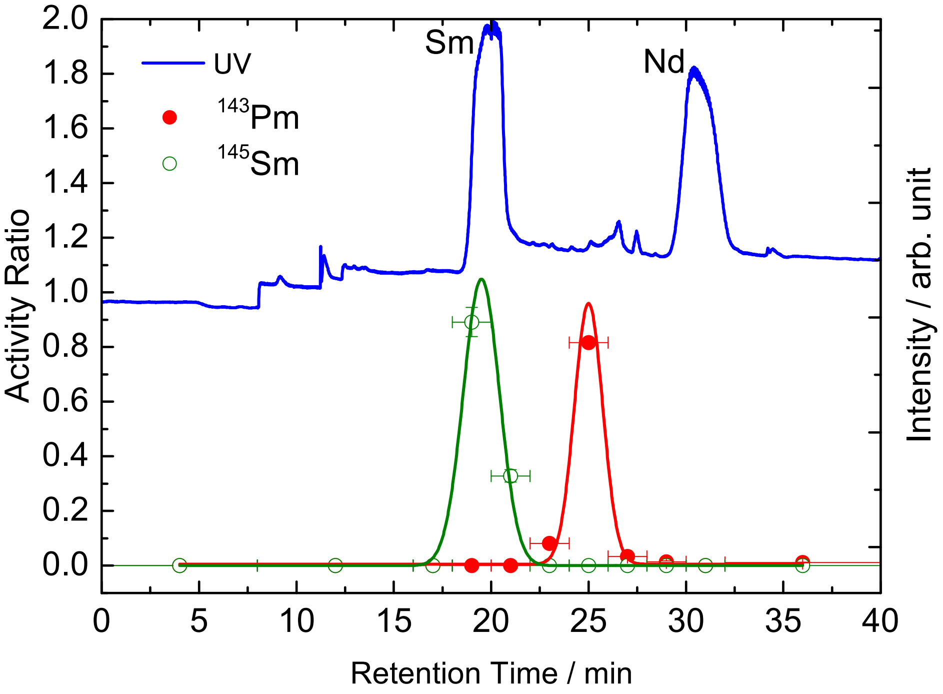

Fig.2. HPLC chromatogram of **Pm/Sm** separation under the condition No.6. Solid circles and open circles indicate radioactivity of ^{143}**Pm** and ^{145}**Sm** observed in the fractionated samples. Observed radioactivity in this figure is normalized to the radioactivity observed in the injection sample.

References

[1] H. Shinohara: Rep. Prog. Phys. **63** (2000) 843.

[2] K. Akiyama *et al.*: ELPH Annual Report **5**, Tohoku University, 135 (2014).

[3] J. Cazes and R. P. W. Scott: Chromatography Theory, Marcel Dekker Inc., New York (2002).

(ELPH Experiment : #2814)

Study of W converter's thickness of ^{100}Mo(γ,n)^{99}Mo process

Jiaolong Li[1], Mingzhang Lin[2], Liusi Sheng[2], Yuzhi Guo[1], Toshitaka Oka[3],
and Hidetoshi Kikunaga[4]

[1]*Beijing ZHIBO Bio-Medical Technology Co.,Ltd*
[2]*The University of Science and Technology of China*
[3]*Institute for Excellence in Higher Education, Tohoku University, Sendai, 980-8576*
[4]*Research Center for Electron Photon Science, Tohoku University, Sendai, 982-0826*

We carried out experiments to investigate how the thickness of bremsstrahlung converter target, tungsten (W) here, affects the yield of ^{99}Mo from ^{100}Mo(γ,n)^{99}Mo process. The photons were generated through bremsstrahlung when the high energy, 50 MeV, electron beam irradiated the W converters. The yields of ^{99}Mo were obtained by measuring the activities of ^{99}Mo of natural molybdenum targets, which placed behind the W converters along the direction of electron beam, using a high purity Ge detector and a standard radioisotopes source. The thickness of W converters were 3.5, 4.0, 4.5, 5.0, and 5.5 mm, respectively. The current analysis outcome was presented here.

§1. Introduction

^{99m}Tc having half-life of 6 hours that decays to the much longer lived ^{99g}Tc by emitting a 141 keV γ-ray and it plays a critical role in the nuclear medicine, see Fig. 1 [1]. It can be bound into a variety of special molecules that target specific parts of the body when ingested or injected. By detecting the 141 KeV γ-rays its location within the body can be pinpointed, which is known as the SPECT (single photon emission computed tomography) imaging [2]. It is used primarily to locate tumors in the body, monitor cardiac function following heart attacks, map blood flow in the brain and guide surgery. The information from these studies is used by many medical specialists including radiologists, cardiologists,

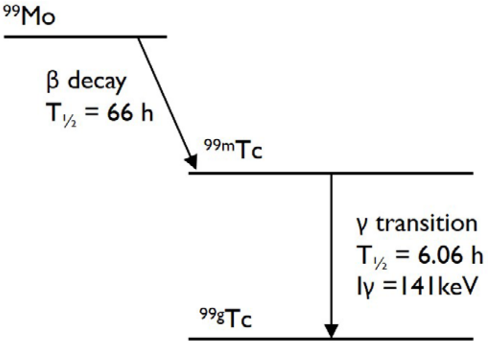

Fig.1. Decay of ^{99}Mo and ^{99m}Tc [1].

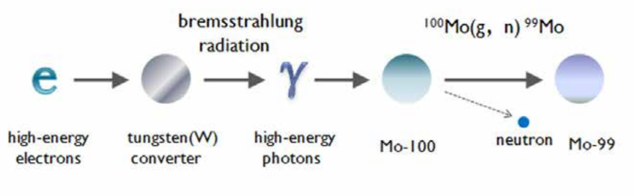

Fig.2. Schematic diagram of ^{100}Mo(γ,n)^{99}Mo.

nephrologists and oncologists to better diagnose and treat patients. It is also used for brain, cerebral perfusion, liver, bone and bone marrow, blood pool, and pulmonary perfusion imaging etc. [3].

Currently, almost all of the ^{99m}Tc used for radio-pharmacy is produced by milking out from the ^{99}Mo/^{99m}Tc generator where the ^{99}Mo is held by an alumina chromatographic column. The half-life of ^{99}Mo, 66 hours, is longer than ^{99m}Tc, see Fig. 1. That is better for shipping to radio-pharmacies and hospitals. The dominant produce route for ^{99}Mo is the fission of high enriched uranium-235 (HEU), which is of weapons grade, from several aging reactors [2]. The desirable nuclide, ^{99}Mo, only occupies 6 % among the fission products [4]. That's to say, it produces lots of reactive waste. Moreover, the HEU is expensive and restricted by IAEA avoiding the nuclear proliferation.

The planned and unplanned shutdowns of some of the aging reactors have resulted in the supply interruptions of ^{99}Mo [5]. And the construction of reactor would be much tough in terms of the cost, safety, licensing, time and complications. That prompted international organizations and several government agencies to step up efforts to find both short and long term alternative solutions to supply shortages. Recently, the ^{100}Mo(γ,n)^{99}Mo process has arisen growing interesting as an promising method since it provides an alternative, simple, ecological and safe production for produce ^{99}Mo: On the one hand, with the development of accelerator technology, the performance and reliability of electron linacs have been improved. On the other hand, there are many advantages of produce ^{99}Mo using electron accelerators, for example less construction cost, much more easily for getting licenses and operating, safer, without U-235, the less radio waste and so on. It is also provides a possibility for producing other medical radio-nuclides such as ^{22}Na, ^{58}Co, ^{47}Ca supplied from reactors.

In the process of ^{100}Mo(γ,n), a high-powered electron accelerator would be used to irradiate a bremsstrahlung radiation converter. Then the molybdenum target behind the converter along the direction of electron beam was irradiated by the bremsstrahlung photons, and the major reaction ^{100}Mo(γ,n)^{99}Mo happened, see Fig. 2. The thickness of converter target is a key factor to the yield of ^{99}Mo. In the experiment we had measured the yield of ^{99}Mo from the irradiated molybdenum targets. And observed how the thickness of W converter affected on the yield of ^{99}Mo.

§2. Experimental and current status of analysis

In the experiment we investigated how the thickness of bremsstrahlung converter target, tungsten (W) here, affected the yield of ^{99}Mo from ^{100}Mo(γ,n)^{99}Mo process. The yields of ^{99}Mo were obtained by measuring the activities of ^{99}Mo of natural molybdenum targets using a high purity Ge detector (Ortec

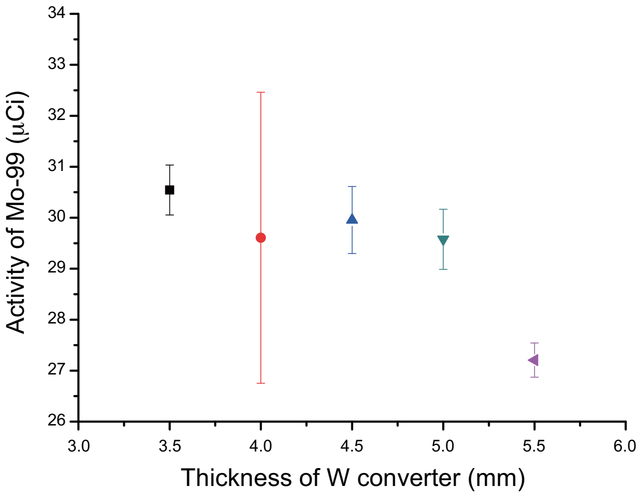

Fig.3. Measured activity of ^{99}Mo dependence on the thickness of W converter.

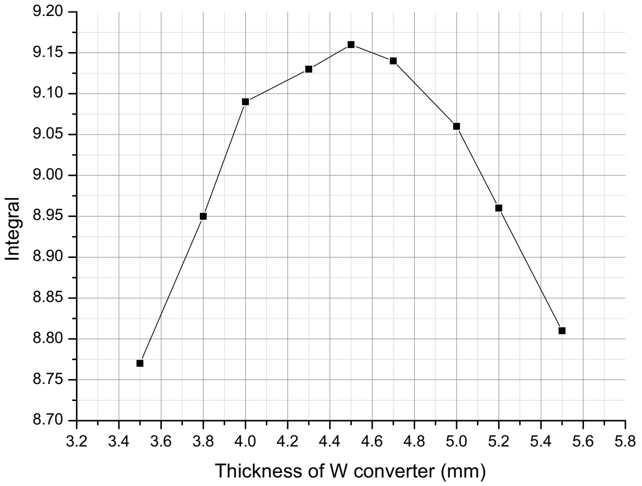

Fig.4. Simulation outcome of how W converter thickness affects the yield of ^{99}Mo.

GEM 55P4-83) and a standard radio-isotopes source (No. 1743-70). The thickness of W converters were 3.5, 4.0, 4.5, 5.0, and 5.5 mm, respectively. The current and energy of the irradiated electron beam was 11 μA and 50 MeV, respectively.

The measured activities of ^{99}Mo dependence on different W converters were shown in Fig. 3. The simulation outcome was also presented in Fig. 4. The integral in Fig. 4 resulted from the follow formula.

$$\text{Integral} = \int_{E_{\text{th}}}^{E_{\max}} \phi(E)\sigma(E)dE,$$

where E is the energy of bremsstrahlung photon. E_{th} is the threshold energy for ^{100}Mo(γ,n)^{99}Mo. $E_{\max}$ is the maximum energy of the bremsstrahlung photons, namely the energy of incident electron. $\phi(E)$ is the bremsstrahlung photon flux which is a continuous distribution up to the energy of incident electron beam. $\sigma(E)$ is the cross-section of the ^{100}Mo(γ,n)^{99}Mo.

As seen from Fig. 3, it seems that the yield of ^{99}Mo decreases when the W converter thickness increased from 3.5 mm to 5.5 mm. However, the computed outcome, see Fig. 4, indicated that the optimized thickness of W converter is 4.5 mm at 50 MeV. We are presently designing new experiment and trying to improve the analysis method.

Acknowledgment

The authors would like to thank to the accelerator group providing the stable beam, and all the facility staffs in the LNS-tohoku for their kind supports.

References

[1] R. Avakian *et al.*, Arm. J. Phys. **6** (2013) 35.

[2] H. Naik *et al.*, J. Radioanal. Nucl. Chem. **295** (2013) 807.

[3] R. Crasta *et al.*, J. Radioanal. Nucl. Chem. 290 (2011) 367.

[4] Medical Isotopes: Report of the Task Force on Alternatives for Medical-Isotope Production, A. Fong, T. I. Meyer, K. Zala (Eds.), TRIUMF, 2008.

[5] Non-HEU Production Technologies for Molybdenum-99 and Technetium-99m, IAEA Nuclear Energy Series, NF-T-5.4, 2013.

II. Status Report

Status of Accelerator Facilities in FY2015

Accelerator group

Research Center for Electron Photon Science, Tohoku University, Sendai, 982-0826

The electron accelerator complex (high intensity 60 MeV linac, 90 MeV injector linac, 1.3 GeV booster-storage ring and 50 MeV linac as a test accelerator for coherent THz source) have been well operated without any significant trouble in FY2015. In this report, machine status and some improvements are presented.

§1. Low Energy Linac for RI Production

1.1 Overview of machine operation

A 60 MeV high-power electron linac has been operated and beam-on time was for 176 hours in FY2015. A major usage for this linac is a mass production of radioactive isotopes (RI), and accelerator parameters and an irradiation system are optimized for the RI production (Fig.1). Furthermore, beam damage test for a material physics experiment have also performed using this linac in this year. For RI productions, linac had operated with beam energy from 20 to 50 MeV. The average current was up to 120 μA with beam repetition of 300 pps. The maximum energy of this linac is 60 MeV. A beam damage test experiment required as lower average current as possible. Since we have no operation experience with lowering average current, a timing system was modified for a single pulse beam injecting per a second. The experiment has done at 50 MeV with the average current of 0.3 μA for 1, 10, and 30 sec. of irradiation time (Fig.2).

Fig.1. Beam profiles for RI production. Electron beam extracted to air (left), and electron beam on ϕ40 mm screen at a converter position prior to the experiment (right).

Fig.2. Target scintillator placed at beam axis for beam damaged testing of a material physics experiment.

1.2 Beam Monitor Replacement

That stable operation of 60 MeV linac with the average current of 120 μA is possible by many years of assiduous effort. However, the current beam transport optics is not well known yet since there is only few specification datasheet for quadrupole magnets of beam transport line. The quantification of beam transport optics is our current objective. We have employed thinner screen and gated digital cameras to achieve a beam base diagnostics in this year (Fig.3). By employing Quadrupole-Scanning method, the beam emittance of 60 MeV linac was measured as about 80π mm·mrad. As the result of this measurement, we found an uncertainty in vertical Twiss parameters across the dispersion section which is inconsistent with ideal optics, and it will be investigated in next year.

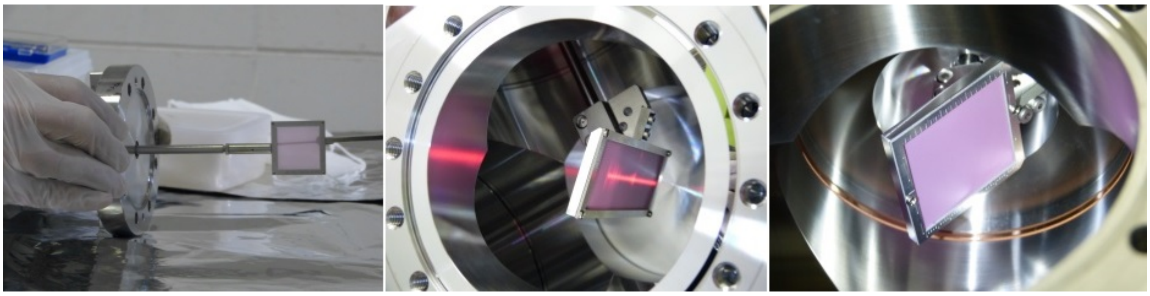

Fig.3. A screen of 50 μm thickness for an emittance measurement (Left), one of 200 μm thickness for monitoring energy spread at the dispersion section (center), and one of 200 μm thickness for monitoring beam position at downstream of the dispersion section (right).

1.3 Ion Pump Replacement

Current major concern of 60 MeV Linac is an instability of beamline vacuum condition. An operation is sometime suspended by sudden increase of vacuum pressure. In this year, a few ion pumps in a beam transport have been replaced (Fig.4). We are planning to refurbish the detached ones in 2016 by replacing the pumping elements, and an automation of ion pump baking procedure is under development. Routinization of ion pump refurbishment is our current objective.

1.4 Interlock Module Replacement

Two 25 MW klystrons feed RF power to eight accelerating structures in 60 MeV linac. As it run several decades, some function is omitted and replaced at each maintenance time or each troubleshooting. Since components goes out of production, the interlock module for klystron No.1 has replaced in this year (Fig.5). Replaced module functions as same as the original. Minor change is an employment of threshold setting to the overcurrent detector. As additional change, it is mounted on a rail to improve the accessibility for maintenance. Since many control modules goes out of date for the olds with no schematic left, redesigning module is required to operate accelerator in good shape and to run cost effectively.

Fig.4. Work for ion pumps replacement.

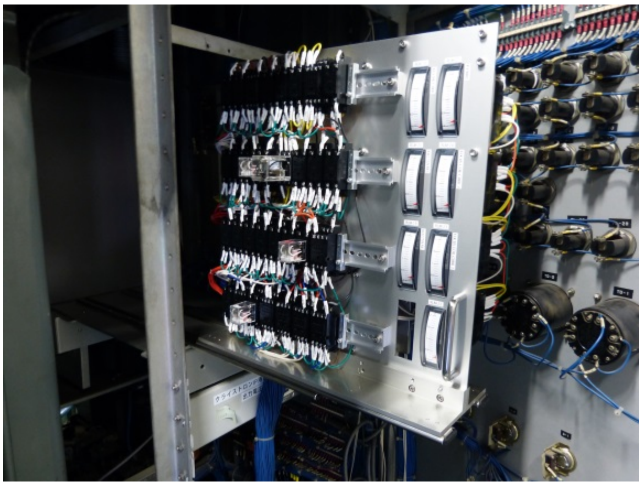

Fig.5. Replaced interlock module for Klystron No.1.

§2. 90 MeV Injector Linac for the 1.3 GeV Booster-storage ring

The injector linac had been stably operated and regularly supplied electron beam for the booster-storage ring. In the end of FY2015, however, there was a trouble on the thermionic rf gun in the injector linac. A discharge in a cathode cell of the gun cavity was frequently observed, so that the beam current extracted from the gun was very unstable. Since we have an experience that a carbon-like material deposited between the cathode and cavity wall for the CeB_6 cathode, which caused the discharge in the cathode cell, we finally decided to replace the cathode to new one. Figure 6 shows a schematic view for the cathode assembly of rf gun. The operated time of this cathode was about 13 month and a decrease of emission current had not been observed for this period. Figure 7 shows the detached cathode from the rf gun. As we expected, the deposition on the cathode was clearly observed. Although more investigation is required to make a definite strategy avoiding this cathode deposition, insufficient vacuum pressure might be considered as the reason of the deposition. Therefore an additional ion pump was installed to improve the vacuum pressure around the cathode.

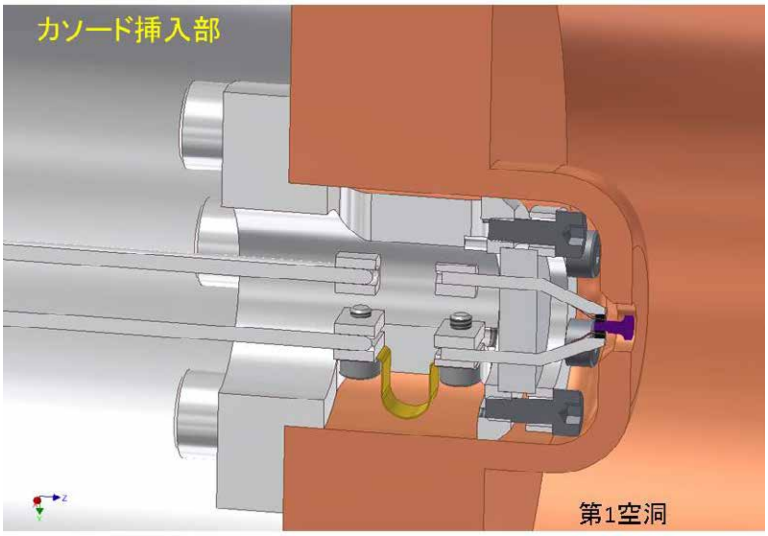

Fig.6. Schematic view for cathode assembly of thermionic rf gun

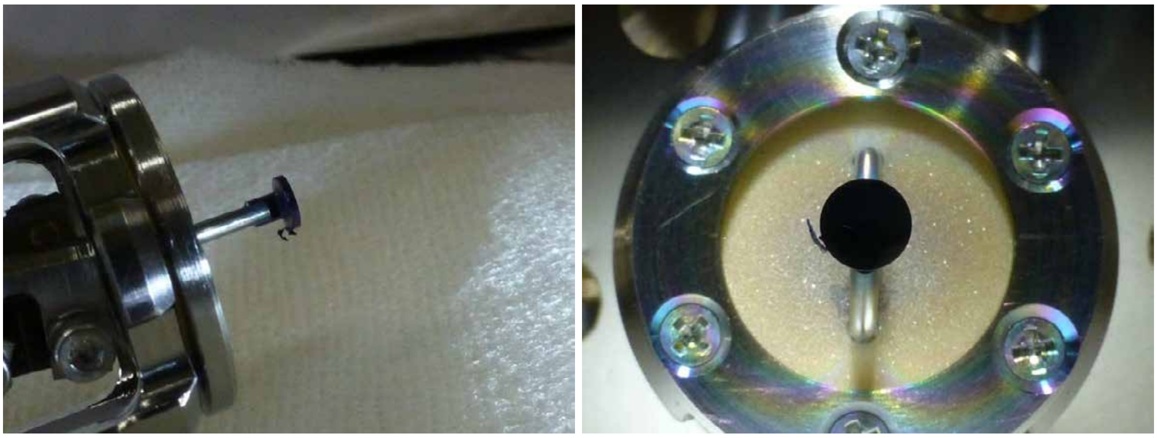

Fig.7. Detached CeB_6 cathode. It was confirmed that the carbon-like material was deposited on the cathode.

§3. 1.3 GeV Booster-storage ring (BST ring)

3.1 Improvement of control system for steering magnets

In order to suppress dynamical COD change in ramping process, it is required to control output current for steering magnet dynamically. Power supply for the steering magnets originally used in BST ring is equipped with a pattern memory and can be operated with a sequence mode that controls the output current as synchronizing with the ramping pattern. However time response for the output current in this mode is quite slow and limited only to 50 ms. Recently we have introduced a dynamical control mode for the steering magnet by applying an analog signal to the power supplies. In this system, power supplies are operated as amplifiers (namely power booster mode) and much faster time response can be realized. Figure 8 shows a configuration of control system for the steering magnet. Analog output module consists of FPGA and DAC, which are installed in CompactRIO (National Instruments Co.). A specified pattern data is converted to sequential data and stored in FPGA (Spartan-6 LX45). The stored data, then, are transferred to DAC (NI9263, 10 V, 16 bit) with each 20 μs clock timing and converted to analog data synchronized with an external trigger. The originally used power supply (KIKUSUI PBX20-5) for steering magnet has also power booster mode as well as the sequence mode that can be adopted to our new system, thus whole system was tested under the actual condition.

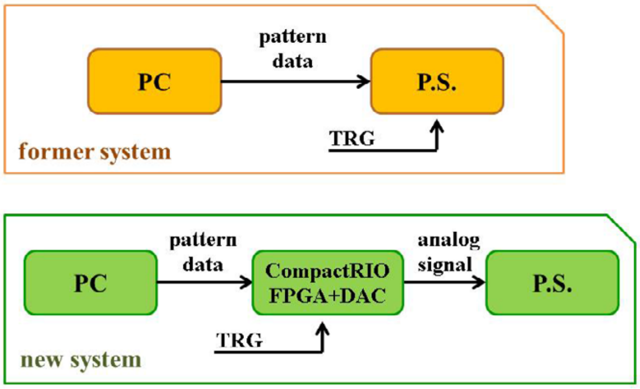

Fig.8. Configuration of former and new control system for steering magnet.

Prior to the beam operation, we confirmed the improvement of the response time of output current. The power supply was tested under a set value with the much steeper slope of 1 A/ms than nominal value in specification sheet. Figure 9 shows the comparison of the time response of output current for the former and new control system, in which it is found that the delay time from the trigger signal is drastically improved. Furthermore the ramping slope is also improved and almost approaching to a limit of 50 A/s defined by power supply and coil impedance. As the result of this upgrade, the tracking capability for ramping pattern was much improved and thus beam loss in the acceleration period has been also reduced.

In order to suppress the COD change in ramping process due to eddy current in the vacuum chamber wall, the dynamical control for the steering magnet was introduced by employing the power booster operation with CompactRIO system. Combining with effort of realignment work for the whole ring, this improved the injection-acceleration efficiency to over 50 %, and the beam current more than 30 mA are obtained at the top energy by only one macropulse injection with peak current of 40 mA. The ramping

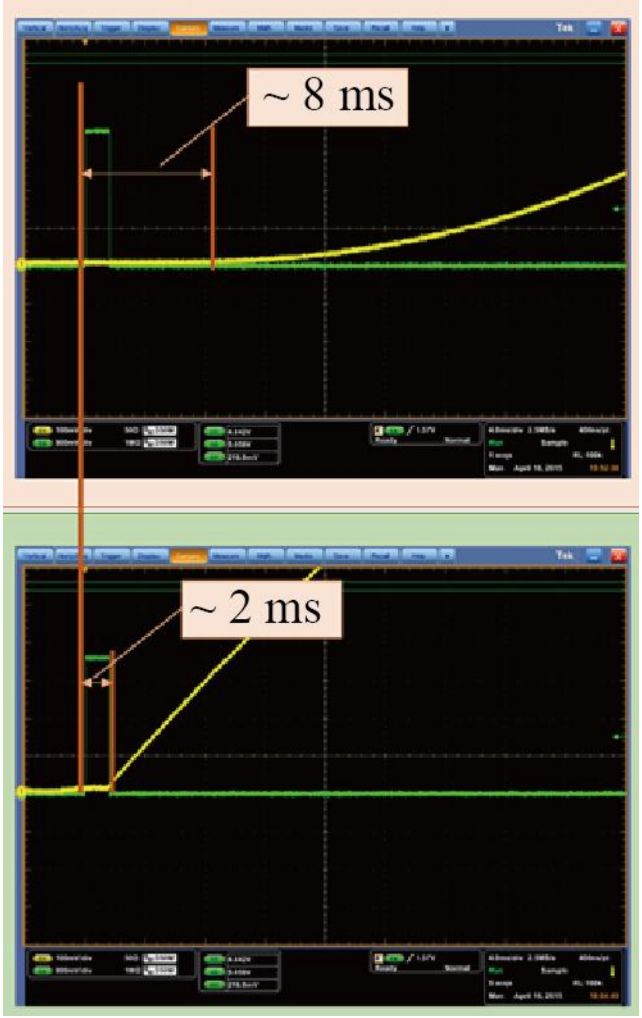

Fig.9. Comparison of output response for former (upper) and new (lower) control system. (Scales: 100 mA/div, 4 ms/div)

slope of $\sim$ 600 A/s for dipole magnets in the current operation is still 60 % for the maximum slope defined by power source, so that it should be possible to increase the slope to improve the duty factor for the pattern operation. However there is still a problem in power supply for steering magnet which prevents the increase in ramping slope. It was found that this power supply has a ringing behaviour for the larger slope of about 10 A/s and which is actually wiggling the beam. Concerning this issue, very recently we have been trying to replace these to more stable power supplies, and found that, at least, model BWS60-5 (Takasago Ltd.) is available for the slope more than 100 A/s without the ringing response. Now we are preparing to replace all power supplies to this model, and then optimization of the orbit control in the ramping process will be performed to improve the duty factor and also further reduce the beam loss.

§4. Summary and prospect

In FY2015 the approved beam time have been well consumed as scheduled. The total time of 176 and 1509 hours were operated in this year for high-power linac and BST ring, respectively. Some maintenance work were also performed, i.e. improvement of monitor system, installation of additional ion pump for rf gun, etc., which brought more reliable and stable operation for user. As the current problem for both the high-power linac and BST ring, the improvement of vacuum pressure is quite important which limits the machine performance. Reinforcement of vacuum system will be conducted in the coming years.

User Support Office Report in FY2015

M. Miyabe on behalfof the user support office[1]

[1]*Research Center for Electron Photon Science, Tohoku University, Sendai, 982-0826, Japan*

The User Support Office coordinate across the users and our facility for management of the beamtime. In 2015 financial year, we had provided the electron, photon and positron beam without big problems.

§1. Introduction

ELPH has three accelerators for Joint Research. Our facility could provide several beams with following three beam lines,

- 70 MeV electron linear accelerator (linac) at the first irradiation lab (For Radiochemistry)
- Tagged photon beam from 1.3 GeV electron synchrotron called BST ring with 93 MeV injector at the second irradiation lab (For Hadron Physics)
- Tagged photon beam at the GeV-γ irradiation room (For Hadron Physics)

In addition, positron/electron beam line for testing detectors is located at the GeV-γ irradiation room. The 70 MeV electron linear accelerator was utilized for the Radiochemistry experiments. It could produce radio active source with its high intensity. Both tagged photon beam line was used for Hadron physics experiments. NKS2 and FOREST experiment have bean held in recent years.

§2. Beamtime operated

The total radiation time was 176 hours for the RI linac operation and 1509 hours for the BST operation, and it was 1686 hours in total. The beam provided time (user beamtime) was 126 and 1474 hours for the RI linac and BST operations, and it was 1600 hours in total. Table 1 summarizes the radiation times, and user beam times in fiscal year 2015.

Many experiments for testing detectors were made by positron beam line. Positron beam was produced by bremsstrahlung photon beams from the synchrotron. Total 50 shift experiments are performed using this positron beam in this financial year.

A Next generation FOREST experiments is planned by GeV-γ group in ELPH. New bending magnet will be installed on the downstream of FOREST detectors and it covers the most forward angle. These new experimental setup enable the zero degree proton detection for the $\gamma d \rightarrow p\eta n$ reaction at $E_\gamma \sim 0.9$ GeV. This reaction gives the zero relative momentum between the η and n. This situation will enable to determine the ηn scattering length. In this financial year, All detectors of FOREST recovered from the earth quake disaster at 2011 and Tagged photon energy was newly calibrated using the TAGX magnet and η photo-production threshold measurement (#2761 T. Ishikawa, ELPH, Tohoku University).

Both the two photon beam line (NKS2 and GeV-γ) cannot be stably produced in the lower storage current and lower electron energy, because of a degree of poor vacuum in BST ring. The machine study was stil continued to improve this situation during this year.

Two experiments were proposed, and carried out for the undergraduate students. The first one (#2794: T. Ishikawa, ELPH, Tohoku University) is for the third school for giving an opportunity using an accelerator to young undergraduate students (Y. Sakemi) [1], which was supported by High Energy Accelerator Research Organization (KEK) for the corporations between Tohoku University and KEK (H. Tamura). The second one (#2796: M. Miyabe, ELPH, Tohoku University) is for the education of the undergraduate students in ELPH.

Table 1. Radiation times, and user beamtimes in financial year 2015. They are given by the sum of the times that the beam is coming to the beamtime, and that the beam is provided to the users.

	RI Linuac		BST Ring	
Month	radiation (h)	user (h)	radiation (h)	user (h)
April	0	0	79	0
May	9	9	328	346
Jun	26	22	274	266
July	15	5	8	6
August	0	0	0	0
September	1	0	0	0
October	32	26	92	103
November	26	22	129	156
December	12	10	134	133
January	25	16	15	10
February	12	11	177	177
March	17	8	275	275
Sum	176	126	1509	1474

§3. ELPH workshops and ELPH seminars

In this fiscal year, ELPH supported two ELPH workshops. The first one is hadron physics (C013: H. Fujioka, Kyoto University), the second is on an application of the high intense low energy electrons (C014: K. Watabe, CYRIC Tohoku University). Seven ELPH seminars were held in this fiscal year. Seminars title and talker are listed below.

- M. Ito, CYRIC Tohoku University, "^{12}C hoyle state and alpha cluster condensation"
- I. Nakagawa, Riken, "Study for proton spin crisis at the high energy polarized proton collider experiment"
- Steven Karataglidis, Univ. of Johannesburg, "Mapping the Densities of Exotic Nuclei"
- H. Kawai, Chiba University, "0.1 mm position resolution gamma ray detector"
- T. Nakamura, H. Kashima, Hitachi Zosen Corporation, "Development of radiation measurement device"

- T. Sanuki, Tohoku University, ”Towards the realization of ILC”
- T. Mibe, KEK, ”Precise measurement of g-2/EDM with ultra cold muon beam”

References

[1] Y. Sakemi, Web site < http://cycgw1.cyric.tohoku.ac.jp/˜sakemi/cyric2015.html >

放射線安全管理室報告

放射線安全管理室

Radiation Safety Report 2015

Radiation Safety Office

2015 年度（平成 27 年 4 月～平成 28 年 3 月）

§１．変更申請

2015 年度の変更承認申請はない。

§２．個人管理

2.1 放射線業務従事者登録

156 人（東北大 72 人、学外 73 人、研究者以外 11 人）

2.2 個人被ばく管理

1 年間の個人被ばく線量 5 mSv 以下 156 人

2.3 教育訓練

定期講習

平成 27 年 6 月 5 日　新規教育 16 人、　再教育 80 人

特別講演の内容：高エネルギー加速器研究機構
特別教授　桝本 和義氏
「核理研で学んだこと　－加速器利用と放射線安全管理－」

不定期の講習

32 回　　78 人

§３．自主点検

年 2 回実施　　平成 27 年 9 月 28 日、平成 28 年 3 月 17 日

§4．製造核種と数量

2015年度に本加速器施設で製造され、共同研究に使用された放射性同位元素は次のとおり。

核種	数量 (kBq)
Au-196	70
Cd-109	5
Ce-139	520
Co-57	1,180
Cr-51	2,000
Cs-132	50
Cu-64	300
Cu-67	200
Dy-159	500
Er-169	500
Ga-68	1,000
Gd-159	301
In-114m	20
K-42	200
K-43	1,000
Mo-99	1,000
Na-22	10
Nd-147	2,000
Ni-57	10,000
Pb-203	30
Pm-143	450
Pt-197	200
Ru-103	300
Sc-44m	500
Sc-47	3,000
Sn-119m	205
Sr-85	1,453
Ta-182	10
Tl-202	10
W-185	200
Yb-175	500
Zn-65	201
Zr-89	500
全33核種	計 28,415 kBq

III. List of Publication

List of Publication (論文リスト) (2015)

Papers Published in Refereed Journals

東北放射光（SLiT-J）計画が目指す光源性能

濱　広幸

表面科学，第 36 巻第 6 号，pp291-296

Positron capture simulation for the ILC electron-driven positron source

Yuji Seimiya, Masao Kuriki, Tohru Takahashi, Tsunehiko Omori, Toshiyuki Okugi, Masanori Satoh, Jyunji Urakawa and Shigeru Kashiwagi

Progress of Theoretical and Experimental Physics 2015, 103G01

Grid pulser for an electron gun with a thermionic cathode for the high-power operation of a terahertz free-electron laser

Shoji Suemine, Keigo Kawase, Naoya Sugimoto, Shigeru Kashiwagi, Kazuya Furukawa, Ryukou Kato, Akinori Irizawa, Masaki Fujimoto, Hiroki Ohsumi, Masaki Yaguchi, Sousuke Funakoshi, Ryouta Tsutsumi, Kumiko Kubo, Akira Tokuchi, Goro Isoyama

Nuclear Instruments and Methods in Physics Research A 773 (2015) 97-103.

The SCRIT electron scattering facility project at RIKEN RI beam factory

T Ohnishi, A Enokizono, M Hara, T Hori, S Ichikawa, K Kurita, S Matsuo, T Suda, T Tamae, M Togasaki, K Tsukada, T Tsuru, S Wang, S Yoneyama and M Wakasugi

Phys. Scr. T166 (2015) 014071 (5pp).

Observation of Spin-Dependent Charge Symmetry Breaking in ΛN Interaction: Gamma-Ray Spectroscopy of ${}^{4}_{\Lambda}$He

T.O. Yamamoto et al.

Phys. Rev. Lett. 115 (2015) 222501, 1-5.

Precise determination of ${}^{12}_{\Lambda}$C level structure by γ-ray spectroscopy

Kenji Hosomi et al.

Prog. Theor. Exp. Phys. 2015 (2015) 081D01.

Hypernuclear production cross section in the reaction of ^{6}Li+^{12}C at 2 A GeV

C. Rappold et al.

Phys. Lett. B 747 (2015) 129—134.

Comparative analysis of kdp and ktr mutants reveals distinct roles of the potassium transporters in the model cyanobacteriumSynechocysis sp. PCC6803.

Nanatani, K., Shijuku,T, Takano, Y., Zulkifli, L., Yamazaki, Y., Tominaga, A., Souma, S., Onai, K., Morishita, M., Ishiura, M., Hagemann, M., Suzuki, I., Maruyama, H., Arai, F., and Uozumi, N.

J.Bacteriol. 197, 676-687 (2015).

The jasmonate-responsive GTR1 transporter is required for gibberellin-mediated stamen development in Arabidopsis

Saito, H., Oikawa, T., Hamamoto, S., Ishimaru, Y., Kanamori-Sato, M., Sasaki-Sekimoto, Y., Utsumi, T., Chen, J., Kanno, Y., Masuda, S., Kamiya, Y., Seo, M., Uozumi, N., Ueda, M., and Ohta, H.

Nature Commun. 6:6095 (2015).

HKT transporters mediate salt stress resistance in plants: from structure and function to the field

Hamamoto, S., Horie, T., Hauser, F., Deinlein, U., Schroeder J.I. and Uozumi, N.

Curr. Opin. Biotechnol. 32, 113120 (2015).

The phytosiderophore efflux transporter TOM2 is involved in metal transport in rice

Nozoye T., Nagasaka S., Kobayashi T., Sato Y., Uozumi N., Nakanishi H. and Nishizawa N.K.

J. Biol. Chem. 290, 27688-99 (2015).

Iron deficiency regulated OsOPT7 is essential for iron homeostasis in rice

Bashir, K., Ishimaru, Y., Itai, R,N,, Senoura, T,., Takahashi, M., An, G., Oikawa, T., Ueda, M., Sato, A., Uozumi, N., Nakanishi H., Nishizawa, N.K.

Plant Mol. Biol. 88, 165-76 (2015).

Decontamination Effects of Bark Washing with a High-pressure Washer on Peach [Prunus persica (L.) Batsch] and Japanese Persimmon (Diospyros kaki Thunb.) Contaminated with Radiocaesium during Dormancy

Sato, M., Abe, K., Kikunaga, H., Takata, D., Tanoi, K., Ohtsuki, T., Muramatsu, Y.

The Horticulture Journal 84 (2015) 295-304.

Software development for estimating the concentration of radioactive cesium in the skeletal muscles of cattle from blood samples

T. Fukuda, M. Hiji, Y. Kino, Y. Abe, H. Amashiro, J. Kabayashi, Y. Shimizu, A. Takahashi, T. Suzuki, M. Chiba, K. Inoue, Y. Kuwahara, M. Morimoto, M. Katayama, K. Donai, H. Shinoda, T. Sekine, M. Fukumoto, E. Isogai

Animal Science Journal, published online: 30 SEP 2015 (DOI: 10.1111/asj.12490).

A comprehensive dose evaluation project concerning animals affected by the Fukushima Daiichi Nuclear Power Plant accident: its set-up and progress

Shintaro Takahashi, Kazuya Inoue, Masatoshi Suzuki, Yusuke Urushihara, Yoshikazu Kuwahara, Gohei Hayashi, Yashushi Kino, Tsutomu Sekine, Yasuyuki Abe, Tomokazu Fukuda, Emiko Isogai, Hideaki Yamashiro, Manabu Fukumoto

Journal of Radiation Research, 56 (2015) i36-i41.

Electron probe X-ray microanalysis of boar and inobuta testes after the Fukushima accident

H. Yamashiro, Y. Abe, G. Hayashi, Y. Urushihara,Y. Kuwahara,M. Suzuki, J. Kobayashi,Y. Kino, T. Fukuda, B. Tong, S. Takino, Y. Sugano, R. Iwashima, T. Yamada, E. Isogai, M. Fukumoto

Journal of Radiation Research, 56 (2015) i42-i47.

Cesium radioactivity in peripheral blood is linearly correlated to that in skeletal muscle: Analyses of cattle within the evacuation zone of the Fukushima Daiichi Nuclear Power Plant

Tomokazu Fukuda, Yasushi Kino, Yasuyuki Abe, Hideaki Yamashiro, Jin Kobayashi, Yoshinaka Shimizu, Atsushi Takahashi, Toshihiko Suzuki, Mirei Chiba, Shintaro Takahashi, Kazuya Inoue, Yoshikazu Kuwahara, Motoko Morimoto, Hisashi Shinoda, Masahiro Hiji, Tsutomu Sekine, Manabu Fukumoto, Emiko Isogai

Animal Science Journal, 86 (2015) 120-124.

Decay dynamics of the unbound ^{25}O and ^{26}O nuclei

K. Hagino and H. Sagawa

Phys. Rev. C93 (2016) 034330/1-12.

Are there good probes for the di-neutron correlation in light neutron-rich nuclei?

K. Hagino and H. Sagawa

Few-Body Systems 57 (2016) 185-193.

Generator coordinate method for hypernuclear spectroscopy with a covariant density functional

H. Mei, K. Hagino and J.M. Yao

Phys. Rev. C93 (2016) 011301(R)/1-5.

Enhancement factor for two-neutron transfer reactions with a schematic coupled-channels model

K. Hagino and G. Scamps

Phys. Rev. C92 (2015) 064602/1-4.

Coupled-channels description of multi-nucleon transfer and fusion reactions at energies around and far below the Coulomb barrier

G. Scamps and K. Hagino

Phys. Rev. C92 (2015) 054614/1-10.

Influence of vibrational excitation on surface diffuseness of the internuclear potential: Study through heavy-ion quasi-elastic scattering at deep-subbarrier energies

G. Kaur, B.R. Behera, A. Jhingan, P. Sugathan, and K. Hagino

Phys. Rev. C92 (2015) 044609/1-7.

Quasi-elastic barrier distributions for ^{20}Ne+^{58,60,61}Ni systems: Influence of weak channels

A. Trzcinska, E. Piasecki, K. Hagino, W. Czarnacki, P. Decowski, N. Keleey, M. Kisielinski, P. Koczon, A. Kordyasz, E. Koshchiy, M. Kowalczyk, B. Lommel, M. Palacz, A. Stolarz, I. Strojek, and K. Zerva

Phys. Rev. C92 (2015) 034619/1-6.

Theoretical models for exotic nuclei

H. Sagawa and K. Hagino

Euro. Phys. J. A51 (2015) 102/1-31.

Three-dimensional mesh calculations for covariant density functional theory

Y. Tanimura, K. Hagino, and H.Z. Liang

Prog. Theo. Exp. Phys. 2015 (2015) 073D01/1-29.

Semi-microscopic modeling of heavy-ion fusion reactions with multi-reference covariant density functional theory

K. Hagino and J.M. Yao

Phys. Rev. C91 (2015) 064606/1-11.

Microscopic study of low-lying spectra of Lambda hypernuclei based on a beyond-mean-field approach with covariant energy density functional

H. Mei, K. Hagino, J.M. Yao, and T. Motoba

Phys. Rev. C91 (2015) 064305/1-16.

Examination of fusion cross sections and fusion oscillations with a generalized Wong formula

N. Rowley and K. Hagino

Phys. Rev. C91 (2015) 044617/1-13.

Multi-dimensional fission model with a complex absorbing potential

G. Scamps and K. Hagino

Phys. Rev. C91 (2015) 044606/1-6.

High resolution spectroscopic study of ${}^{10}_{\Lambda}$Be

T. Gogami, C. Chen, D. Kawama, P. Achenbach, A. Ahmidouch, I. Albayrak, D. Androic, A. Asaturyan, R. Asaturyan, O. Ates, P. Baturin, R. Badui, W. Boeglin, J. Bono, E. Brash, P. Carter, A. Chiba, E. Christy, S. Danagoulian, R. De Leo, D. Doi, M. Elaasar, R. Ent, Y. Fujii, M. Fujita, M. Furic, M. Gabrielyan, L. Gan, F. Garibaldi, D. Gaskell, A. Gasparian, Y. Han, O. Hashimoto, T. Horn, B. Hu, Ed. V. Hungerford, M. Jones, H. Kanda, M. Kaneta, S. Kato, M. Kawai, H. Khanal, M. Kohl, A. Liyanage, W. Luo, K. Maeda, A. Margaryan, P. Markowitz, T. Maruta, A. Matsumura, V. Maxwell, A. Mkrtchyan, H. Mkrtchyan, S. Nagao, S.N. Nakamura, A. Narayan, C. Neville, G. Niculescu, M.I. Niculescu, A. Nunez, Nuruzzaman, Y. Okayasu, T. Petkovic, J. Pochodzalla, X. Qiu, J. Reinhold, V.M. Rodriguez, C. Samanta, B. Sawatzky, T. Seva, A. Shichijo, V. Tadevosyan, L. Tang, N. Taniya, K. Tsukada, M. Veilleux, W. Vulcan, F.R. Wesselmann, S.A. Wood, T. Yamamoto, L. Ya, Z. Ye, K. Yokota, L. Yuan, S. Zhamkochyan, L. Zhu

Phys.Rev. C93 (2016) no.3, 034314.

A fast profile monitor with scintillating fiber hodoscopes for high-intensity photon beams

T. Ishikawa, H. Fujimura, R. Hamano, R. Hashimoto, Y. Honda, T. Ishida, S. Kaida, H. Kanda, S. Kido, Y. Matsumura, M. Miyabe, K. Mizutani, I. Nagasawa, A. Nakamura, K. Nanbu, K. Nawa, S. Ogushi, H. Shimizu, H. Sugai, K. Suzuki, K. Takahashi, S. Takahashi, Y. Taniguchi, A.O. Tokiyasu, Y. Tsuchikawa, H. Yamazaki

Nucl. Instr. Meth. A811 (2016) 124-132.

High-Precision Three-Dimensional Field Mapping of a High Resolution Magnetic Spectrometer for Hypernuclear Spectroscopy at JLab

Yu Fujii, Osamu Hashimoto, Toshinobu Miyoshi, Satoshi N Nakamura, Atsushi Ohtani, Yuichi Okayasu, Masamichi Oyamada, Yosuke Yamamoto, Seigo Kato, Jumei Matsui, Katsuhisa Sako, Brindza Paul

Nuclear Inst. and Methods in Physics Research A 795 (2015) 351-363.

Observation of ${}^{4}_{\Lambda}$H Hyperhydrogen by Decay-Pion Spectroscopy in Electron Scattering

A. Esser, S. Nagao, F. Schulz, P. Achenbach, C. Ayerbe Gayoso, R. Bhm,O. Borodina D. Bosnar, V. Bozkurt,L. Debenjak, M. O. Distler, I. Frii, Y. Fujii, T. Gogami, O. Hashimoto, S. Hirose, H. Kanda, M. Kaneta,E. Kim, Y. Kohl,J. Kusaka, A. Margaryan, H. Merkel, M. Mihovilovi, U. Mller, S. N. Nakamura, J. Pochodzalla,C. Rappold, J. Reinhold, T. R. Saito, A. Sanchez Lorente, S. Snchez Majos, B. S. Schlimme, M. Schoth,C. Sfienti, S. irca, L. Tang, M. Thiel, K. Tsukada, A. Weber, and K. Yoshida

Physical Review Letters 114 (2015) 232501.

Backward-angle photoproduction of ω and η mesons from protons in the photon energy range from 1.5 to 3.0 GeV

Y. Morino, Y. Nakatsugawa, M. Yosoi, M. Niiyama, M. Sumihama, T. Nakano, D. S. Ahn, J. K. Ahn, S. Ajimura, W. C. Chang, J. Y. Chen, S. Dat, H. Fujimura, S. Fukui, K. Hicks, T. Hiraiwa, T. Hotta, S. H. Hwang, K. Imai, T. Ishikawa, Y. Kato, H. Kawai, M. J. Kim, H. Kohri, Y. Kon, P. J. Lin, K. Mase, Y. Maeda, M. Miyabe, N. Muramatsu, H. Noumi, Y. Ohashi, T. Ohta, M. Oka, J. D. Parker, C. Rangacharyulus, S. Y. Ryu, T. Saito, T. Sawada, H. Shimizu, E. A. Strokovsky, Y. Sugaya, K. Suzuki, K. Tanida, A. Tokiyasu1, T. Tomioka, T. Tsunemi, M. Uchida, R. Yamamura, and T. Yorita

PTEP 2015 (2015) 013D01.

Scaling properties of fractional momentum loss of high-p_T hadrons in nucleus-nucleus collisions at $\sqrt{s_{\rm NN}}$ from 62.4 GeV to 2.76 TeV

A. Adare et al. (PHENIX Collaboration)

Physical Review C 93, 024911 (2016)

Transverse energy production and charged-particle multiplicity at midrapidity in various systems from $\sqrt{s_{\rm NN}}$ =7.7 to 200 GeV

A. Adare et al. (PHENIX Collaboration)

Physical Review C 93, 024901(2016).

Measurements of Elliptic and Triangular Flow in High-Multiplicity $^3He{+}Au$ Collisions at $\sqrt{s_{\rm NN}}$ =200GeV

A. Adare et al. (PHENIX Collaboration)

Physical Review Letter 115, 142301 (2015)

Systematic study of azimuthal anisotropy in Cu + Cu and Au + Au collisions at $\sqrt{s_{\rm NN}}$ =62.4 and 200 GeV

A. Adare et al. (PHENIX Collaboration)

Physical Review C 92, 034913 (2015).

Transmutation Reactions Induced by Deuterium Permeation through Nano-structured Pd Multilayer Thin Film

Y. Iwamura, T. Itoh and S. Tsuruga

Current Science, Vol. 108, NO. 4, (2015) 628-632.

Dynamical concentration and static retention of deuterium in tungsten foil studied by low energy D(d,p)T reaction and elastic recoil detection

J.T. Zhao, Q. Wang, D.D. Liu, Z.H. Wang, T.S. Wang and J. Kasagi

Nucl. Instr. Meth. B 360 (2015) 139144.

Papers Published in International Conference Proceedings

Cherenkov Ring Camera for Direct Observation of the Longitudinal Phase Space of the Beam Extracted from RF Gun

K. Nanbu, A. Lueangaramwong, K. Takahashi, S. Kashiwagi, F. Hinode, T. Muto, H. Saito, I. Nagasawa, C. Tokoku, E. Kobayashi and H. Hama

Proc. 12th Eco-Energy and Materials Science and Engineering Symposium (EMSES2015), Krabi, Thailand, June 11-14, 2015, pp370-372.

Proof-of-Principle Experiment of Velocity Bunching for Ultra-short Electron Pulse Production

S. Kashiwagi, F. Hinode, T. Muto, H. Saito, K. Nanbu, I. Nagasawa, K. Takahashi, C. Tokoku, E. Kobayashi and H. Hama

Proc. 12th Eco-Energy and Materials Science and Engineering Symposium (EMSES2015), Krabi, Thailand, June 11-14, 2015, pp373-376.

An Optimization of ILC Positron Source for Electron-Driven Scheme

Y. Seimiya, M. Kuriki, M. Urano, S. Kashiwagi, T. Okugi, T. Omori, M. Satoh, J. Urakawa, T. Takahashi

Proceedings of IPAC2015, Richmond, VA, USA, WEPWA017, pp2529- 2531.

GaAs Photocathode Activation with CsTe Thin Film

M. Kuriki, Y. Seimiya, K. Uchida, S. Kashiwagi

Proceedings of IPAC2015, Richmond, VA, USA, TUPWA062, pp1567-1569.

FEL Enhancement by Microbuch Structure Made with Phase-Space Rotation

M. Kuriki, Y. Seimiya, S. Chen, K. Ohmi, J. Urakawa, S. Kashiwagi, R. Kato

Proceedings of IPAC2015, Richmond, VA, USA, TUPWA063, pp1570-1572.

Extremely Short Electron Bunch Generation for Producing THz Superradiance at T-ACTS, Tohoku University

S. Kashiwagi, F. Hinode, T. Muto, H. Saito, T. Abe, Y. Shibasaki, K. Nanbu, I. Nagasawa, K. Takahashi, C. Tokoku, E. Kobayashi ,H. Hama

Proceedings of 8th International Workshop on Infrared Microscopy and Spectroscopy using Accelerator Based Sources (WIRMS 2015), 2015.

Production of Z-polarized Coherent Cherenkov Light in THz Region

H. Hama, K. Nanbu , F. Hinode , S. Kashiwagi , T. Muto , H. Saito , T. Abe , Y. Shibasaki , I. Nagasawa , K. Takahashi , C. Tokoku , E. Kobayashi

Proceedings of 8th International Workshop on Infrared Microscopy and Spectroscopy using Accelerator Based Sources (WIRMS 2015), 2015.

SCRIT Electron Scattering Facility

Toshimi Suda, Akitomo Enozokizono, Masahiro Hara, Yuji Haraguchi, Sin ’ ichi Ichikawa, Kazuyoshi Kurita, Saki Matsuo, Tetsuya Ohnishi, Tadaaki Tamae, Mamoru Togasaki, Kyo Tsukada,Teruaki Tsuru, Shuo Wang, Shunpei Yoneyama and Masanori Wakasugi

JPS Conf. Proc. Volume 6 (2015) 030100.

Study of ΛN Interaction via the γ-ray Spectroscopy of $^{4}\Lambda$He and $^{19}\Lambda$F (E13-1st)

T.O. Yamamoto et al.

JPS Conf. Proc. 8 (2015) 021017, 1-6.

Measurement of the Λ Spin-flip B(M1) Value in Hypernuclei

Y. Sasaki et al.

JPS Conf. Proc. 8 (2015) 0210173, 1-4.

J-PARC E19 Experiment: Pentaquark Θ^{+} Search in Hadronic Reaction at J-PARC

Tomonori .N. Takahashi et al.

JPS Conf. Proc. 8 (2015) 022011, 1-6.

J-PARC E27 Experiment to Search for a $K^{-}pp$ Bound State

Yudai Ichikawa et al.

JPS Conf. Proc. 8 (2015) 021020, 1-7.

Three-body calculation of exotic molecules with negatively charged massive particle

Yasushi Kino

Journal of Physics: Conference Series, 635 (2015) 072089.

Ps slowing down process below the Ps break-up energy in Ar gas

Yosuke Sano, Yasushi Kino, Toshitaka Oka, Tsutomu Sekine

Journal of Physics: Conference Series, 635 (2015) 052088.

Relativistic effects in positronic alkali atoms

Takuma Yamashita, Yasushi Kino

Journal of Physics: Conference Series, 635 (2015) 052086.

Kinetic energy of Ps formed by Ore mechanism in Ar gas

Yosuke Sano, Yasushi Kino, Toshitaka Oka, Tsutomu Sekine

Journal of Physics: Conference Series, 618 (2015) 012010.

High-precision calculation of loosely bound states of LiPs^{+} and NaPs^{+}

Takuma Yamashita, Yasushi Kino

Journal of Physics: Conference Series, 618 (2015) 012009.

Three-dimensional mesh calculations for covariant density functional theory

Y. Tanimura, K. Hagino, and H. Liang

AIP Conf. Proc. 1681 (2015) 03008/1-4.

Pairing interaction and reaction mechanism for one- and two-particle transfer reactions: A simple model in one dimension

A. Vitturi, L. Moschini, K. Hagino, and A. Moro

AIP Conf. Proc. 1681 (2015) 060001/1-6.

Neutrinoless double-beta decay in covariant density functional theory

P. Ring, J.M. Yao, L.S. Song, K. Hagino, and J. Meng

AIP Conf. Proc. 1681 (2015) 050008/1-4.

Nuclear Transmutation of long-lived nucleides with laser comption scattering: quantitative analysis by theoretical approach

S. Takai and K. Hagino

in ”Nuclear Back-end and Transmutation Technology for Waste Disposal” edited by K. Nakajima (Springer Open, 2014), p. 3-11.

Two-nucleon Correlations in the Decay of Unbound Nuclei beyond the Drip Lines

K. Hagino and H. Sagawa

JPS Conf. Proc. 6 (2015) 020001/1-020001/6.

Subbarrier fusion of carbon isotopes: from resonance structure to fusion oscillations

K. Hagino and N. Rowley

J. of Phys. Conf. Series 590 (2015) 012020/1-6.

Experimental investigations of the hypernucleus $^{4}_{\Lambda}$H

P. Achenbach , F. Schulz, S. Aulenbacher, J. Berii, S. Bleser, R. Bhm, D. Bosnar, L. Correa, M.O. Distler, A. Esser, H. Fonvieille, I. Frii, Y. Fujii, M. Fujita, T. Gogami, H. Kanda, M. Kaneta, S. Kegel, Y. Kohl, W. Kusaka, A. Margaryan, H. Merkel, M. Mihovilovi, U. Mller, S. Nagao, S.N. Nakamura, J. Pochodzalla, A. Sanchez Lorente, B.S. Schlimme, M. Schoth, C. Sfienti, S. irca, M. Steinen, Y. Takahashi, L. Tang, M. Thiel, K. Tsukada, A. Tyukin, A. Weber

EPJ Web Conf. 113 (2016) 07001

The SCRIT electron scattering facility project at RIKEN RI beam factory

T. Ohnishi, A. Enokizono, M. Hara, T. Hori, S. Ichikawa, K. Kurita, S. Matsuo, T. Suda, T. Tamae, M. Togasaki, K. Tsukada, T. Tsuru, S. Wang, S. Yoneyama, M. Wakasugi

Phys.Scripta T166 (2015) 014071.

High Resolution Λ Hypernuclear Spectroscopy with Electron Beams

T. Gogami, P. Achenbach, A. Ahmidouch, I. Albayrak, D. Androic, A. Asaturyan, R. Asaturyan, O. Ates, P. Baturin, R. Badui, W. Boeglin, J. Bono, E. Brash, P. Carter, C. Chen, A. Chiba, E. Christy, S. Danagoulian, R. De Leo, D. Doi, M. Elaasar, R. Ent, Y. Fujii, M. Fujita, M. Furic, M. Gabrielyan, L. Gan, F. Garibaldi, D. Gaskell, A. Gasparian, O. Hashimoto, T. Horn, B. Hu, Ed. V. Hungerford, M. Jones, H. Kanda, M. Kaneta, S. Kato, M. Kawai, D. Kawama, H. Khanal, M. Kohl, A. Liyanage, W. Luo, K. Maeda, A. Margaryan, P. Markowitz, T. Maruta, A. Matsumura, V. Maxwell, A. Mkrtchyan, H. Mkrtchyan, S. Nagao, S. N. Nakamura, A. Narayan, C. Neville, G. Niculescu, M. I. Niculescu, A. Nunez, Nuruzzaman, Y. Okayasu, T. Petkovic, J. Pochodzalla, X. Qiu, J. Reinhold, V. M. Rodriguez, C. Samanta, B. Sawatzky, T. Seva, A. Shichijo, V. Tadevosyan, L. Tang, N. Taniya, K. Tsukada, M. Veilleux, W. Vulcan, F. R. Wesselmann, S. A. Wood, T. Yamamoto, L. Ya, Z. Ye, K. Yokota, L. Yuan, S. Zhamkochyan, and L. Zhu

JPS Conf. Proc. 8, 0200 (205).

Photoproduction of $\mathrm{K}^+\Lambda$ and $\mathrm{K}^0\Lambda$ on Deuteron

Takao Fujii, Brian Beckford, Yu Fujii, Osamu Hashimoto, Takatsugu Ishikawa, Hiroki Kanda,*, Masashi Kaneta, Chigusa Kimura, Takeshi Koike, Kazushige Maeda, Koji Miwa, Satoshi N. Nakamura, Hirokazu Tamura, Fumiya Yamamoto, and Hirohito Yamazaki for the NKS2 collaboration

JPS Conf. Proc. 8, 021003 (2015).

Double neutral pion photoproduction off the proton with FOREST at ELPH

Q. He, H. Fujimura, H. Fukasawa, R. Hashimoto, Y. Honda, T. Ishikawa, T. Iwata, S. Kaida, J. Kasagi, A. Kawano, S. Kuwasaki, K. Maeda, S. Masumoto, M. Miyabe, F. Miyahara, K. Mochizuki, N. Muramatsu, A. Nakamura, K. Nawa, S. Ogushi, Y. Okada, Y. Onodera, K. Ozawa, Y. Sakamoto, M. Sato, H. Shimizu, H. Sugai, K. Suzuki, Y. Tajima, S. Takahashi, Y. Taniguchi, Y. Tsuchikawa, H. Yamazaki, R. Yamazaki, H.Y. Yoshida

EPJ Web of Conferences 109 (2016) 04004 (Proceedings of OMEG 2015).

High Resolution Λ Hypernuclear Spectroscopy with Electron Beams

T. Gogami, P. Achenbach, A. Ahmidouch, I. Albayrak, D. Androic, A. Asaturyan, R. Asaturyan, O. Ates, P. Baturin, R. Badui, W. Boeglin, J. Bono, E. Brash, P. Carter, C. Chen, A. Chiba, E. Christy, S. Danagoulian, R. De Leo, D. Doi, M. Elaasar, R. Ent, Y. Fujii, M. Fujita, M. Furic, M. Gabrielyan, L. Gan, F. Garibaldi, D. Gaskell, A. Gasparian, O. Hashimoto, T. Horn, B. Hu, Ed. V. Hungerford, M. Jones, H. Kanda, M. Kaneta, S. Kato, M. Kawai, D. Kawama, H. Khanal, M. Kohl, A. Liyanage, W. Luo, K. Maeda, A. Margaryan, P. Markowitz, T. Maruta, A. Matsumura, V. Maxwell, A. Mkrtchyan, H. Mkrtchyan, S. Nagao, S. N. Nakamura, A. Narayan, C. Neville, G. Niculescu, M. I. Niculescu, A. Nunez, Nuruzzaman, Y. Okayasu, T. Petkovic, J. Pochodzalla, X. Qiu, J. Reinhold, V. M. Rodriguez, C. Samanta, B. Sawatzky, T. Seva, A. Shichijo, V. Tadevosyan, L. Tang, N. Taniya, K. Tsukada, M. Veilleux, W. Vulcan, F. R. Wesselmann, S. A. Wood, T. Yamamoto, L. Ya, Z. Ye, K. Yokota, L. Yuan, S. Zhamkochyan, and L. Zhu

JPS Conference Proceedings 8 (2015) 021010.

Progress of the Hypernuclear Decay Pion Spectroscopy Program at MAMI-C

Sho Nagao, Patrick Achenbach, Naoki Arai, Carlos Ayerbe Gayoso, Ralph Bohm, Olga Borodina, Damir Bosnar, Vakkas Bozsurt, Luka Devenjak, Michael O. Distler, Anselm Esser, Manami Fujita, Ivica Frisic, Yuu Fujii, Toshiyuki Gogami, Mar Gmez Rodrguez, Satoshi Hirose, Hiroki Kanda, Masashi Kaneta, Eunhee Kim, Junichiro Kusaka, Amur Margaryan, Harald Merkel, Ulrich Mller, Satoshi N. Nakamura, Josef Pochodzalla, Christophe Rappold, Joerg Reinhold, Takehiko R. Saito, Alicia Sanchez Lorente, Salvador Snchez Majos, Bjrn Sren Schlimme, Matthias Schoth, Florian Schulz, Concettina Sfienti, Simon Sirca, Yuta Takahashi, Liguang Tang, Michaela Thiel, Kyo Tsukada, Daisuke Uchiyama, and A1 hypernuclear collaboration

JPS Conference Proceedings 8 (2015) 021012.

Experimental investigations of the hypernucleus ${}^{4}_{\Lambda}\mathrm{He}$

P. Achenbach, F. Shulz, S. Aulenbacher, J. Berii, S. Bleser, R. Bhm, D. Bosnar, L. Correa, M. O. Distler, A. Esser, H. Fonvieille, I. Frii, Y. Fujii, M. Fujita, T. Gogami, H. Kanda, M. Kaneta, S. Kegel, Y. Kohl, W. Kusaka, A. Margaryan, H. Merkel, M. Mihovilovi, U. Mller, S. Nagao, S.N. Nakamura, J. Pochodzalla, A. Sanchez Lorente, B.S. Schlimme, M. Schoth, C. Sfienti, S. irca, M. Steinen, Y. Takahashi, L. Tang, M. Thiel, K. Tsukada, A. Tyukin, A. Weber

EPJ Web of Conferences 113 (2016) 07001,

The Launch of a New Plan on Condensed Matter Nuclear Science at Tohoku University

Y. Iwamura, J. Kasagi, H. Kikunaga, H. Yoshino, T. Itoh, M. Hattori, T. Mizuno

Proceeding of the 19th International Conference on Condensed Matter Nuclear Science, to be published.

Invited Talk and Oral Presentations at International Conferences

Conceptual design of variable polarized THz source based on crossed-undulator superradiant (Oral presentation)

H. Hama

The 6th Asian Forum for Accelerators and Detectors, Hsinchu, Taiwan, Jan. 26-27, 2015.

Expected performance of a high brilliant 3 GeV light source project, SLiT-J (Oral presentation)

H. Hama

The German-Japanese University Consortium “HeKKSaGOn” meeting on Mechanobiology, Tohoku University, Sendai, Apr. 16, 2015.

Cherenkov Ring Camera for Direct Observation of the Longitudinal Phase Space of the Beam Extracted from RF Gun (Oral presentation)

H. Hama

The 12th Eco-Energy and Materials Science and Engineering Symposium (EMSES2015), Krabi, Thailand, June 11-14, 2015.

SLiT-J, a high brilliant compact 3GeV light source project in Japan, at a glance (Invited oral)

H. Hama

MAX-IV Laboratory, Lund University, Lund, Sweden, Dec. 14, 2015.

Proof-of-Principle Experiment of Velocity Bunching for Ultra-short Electron Pulse Production (Oral presentation)

S. Kashiwagi, F. Hinode, T. Muto, H. Saito, K. Nanbu, I. Nagasawa, K. Takahashi, C. Tokoku, E. Kobayashi and H. Hama

The 12th Eco-Energy and Materials Science and Engineering Symposium (EMSES2015), Krabi, Thailand, June 11-14, 2015.

Extremely Short Electron Bunch Generation for Producing THz Superradiance at T-ACTS, Tohoku University (Oral presentation)

S. Kashiwagi, F. Hinode, T. Muto, H. Saito, T. Abe, Y. Shibasaki, K. Nanbu, I. Nagasawa, K. Takahashi, C. Tokoku, E. Kobayashi and H. Hama

The 8th International Workshop on Infrared Microscopy and Spectroscopy using Accelerator Based Sources (WIRMS 2015), Riverhead, NY, Oct. 11-15, 2015.

Probing the relative momentum of two-nucleon system in ^{6}He and ^{6}Li (Invited oral)

T. Suda, N. Khai, A. Yoshida and I. Tanihata

High-Resolution Spectroscopy and Tensor Interaction 2015, Osaka、2015年 Nov. 16-19, 2015.

Recent Achievements at J-PARC and Future Prospects of Hypernuclear Study (Invited oral)

H. Tamura

Hypernuclear Workshop 2016 Jefferson Laboratory, Newport News, VA, USA, March 14-15, 2016.

Present Status and Future Prospects of Hypernuclear Physics at J-PARC (Invited oral)

H. Tamura

Workshop on Hypernuclei studies and Strangeness production, CEA Saclay , France, January 19-21, 2016.

Hypernuclear physics at J-PARC (Invited oral)

H. Tamura

Frontiers in hadron and nuclear physics with strangeness and charm. ECT* Trento, Italy, October 19-23, 2015.

Gamma-ray spectroscopy of hypernuclei - recent results and prospect at J-PARC (Invited oral)

H. Tamura

12th International Conference on Hypernuclear and Strange Particle Physics (HYP2015), Tohoku University, Sendai, September 7-12, 2015.

Overview on hypernuclei –What are exciting now? (Invited oral)

H. Tamura

EMMI Workshop on anti-matter, hyper-matter and exotica production at the LHC, CERN, Geneva, Switzerland, July 20-22, 2015.

Energy levels and structures of exotic molecules with negatively charged particles (Oral presentation)

Y. Kino

12th International conference on low energy antiproton physics, Kanazawa, Japan, March 6-11, 2016.

Di-neutron correlations in the two-particle decay of unbound nuclei (Invited oral)

K. Hagino

Weakly Bound Exotic Nuclei, Natal, Brazil, May 24 May 30, 2015.

Present status of coupled-channels calculations for heavy-ion fusion reactions (Invited oral)

K. Hagino

Nucleus-nucleus 2015, Catania, Italy, June 21-June 26, 2015.

Beyond-mean-field approach to low-lying spectra of Λ hypernuclei (Oral presentation)

K. Hagino

The 12th International Conference on Hypernuclear and Strange Particle Physics, Sendai, Japan, September 7-12, 2015.

Two-neutron decay of the ^{26}O nucleus (Invited oral)

K. Hagino

Long-term workshop on Computational Advances in Nuclear and Hadron Physics, Kyoto, Japan, Sep. 21-Oct. 30, 2015.

Recent developments in heavy-ion fusion reactions around the Coulomb barrier (Oral presentation)

K. Hagino

The 5th international workshop on compound-nuclear reactions and related topics (CNR*15), Tokyo, Japan, Oct. 19-23, 2015.

Reactions with heavy nuclei (Invited oral)

K. Hagino

FRIB-theory alliance inaugural meeting, East Lansing, USA, March 31-April 1, 2016.

Study of Lambda hypernuclei with electron beams (Invited oral)

S. N. Nakamura

Nuclear Structure and Reactions: Weak, Strange and Exotic (Hirschegg2015) Kleinwalsertal, Austria, Jan. 11-17, 2015.

Hypernuclear spectroscopy via (e,e ’ K^+) reaction (Invited oral)

S. N. Nakamura

12th International Conference on Hypernuclear and Strange Particle Physics (HYP2015) , Sendai, Japan, Sep. 7-12, 2015.

Spectroscopy of Lambda hypernuclei with electron beams (Invited oral)

S. N. Nakamura

Fifth International Conference on Nuclear Fragmentation (NUFRA2015) , Kemer, Turkey, Oct. 4-12, 2015.

High-Resolution Reaction Spectroscopy of Lambda-Hypernuclei (Invited oral)

S. N. Nakamura

International workshop on physics at the extended hadron experimental facility of J-PARC Tokai, Japan, March 5-6, 2016.

Opening and Highlights of Hypernuclear Study at JLab (Oral presentation)

S. N. Nakamura

The 2nd JLab Hypernuclear Workshop, Newport News, USA, 14-15 March 2016.

Spectroscopic Study of Medium Heavy Hypernuclei (Invited oral)

S. N. Nakamura

The 2nd JLab Hypernuclear Workshop, Newport News, USA, 14-15 March 2016.

Meson photoproduction experiments at ELPH, Tohoku University (Invited oral)

T. Ishikawa

The 10th International Workshop on the Physics of Excited Nucleons (NSTAR2015), Suita, Japan, May 25-28, 2015.

Recent results and future prospects of LEPS and LEPS2 (Oral presentation)

M. Miyabe

ELPH Workshop C013, Sendai Japan, Jul. 13, 2015.

Study of $\Sigma\pi$ invariant mass spectrum in the d (γ, K^+) X reaction (Oral presentation)

A. O. Tokiyasu

HYP2015, Sendai in Japan, September 7-15, 2015.

The recent results of strangeness photoproduction in the threshold region at ELPH-Tohoku (Oral presentation)

H. Kanda

HYP2015: International Conference on Hypernuclear and Strange Particle Physics, Sendai, Japan, Sep. 7-12, 2015.

Double pion photoproduction on a deuteron for the search of two-baryonic resonances at ELPH (Invited oral)

H. Kanda

ELPH Workshop C013: Meson Production and Meson Baryon Interaction (MPMBI2015), Sendai, Japan, Sep. 13—15, 2015.

Study of Λ-n interaction via FSI in γ+d reaction (Oral presentation)

M. Kaneta

HYP2015: 12th International Conference on Hypernuclear and Strange Particle Physics, Sendai, Japan, Sep 7-11, 2015.

The Launch of a New Plan on Condensed Matter Nuclear Science at Tohoku University (Oral presentation)

Y. Iwamura

19th International Conference on Condensed Matter Nuclear Science, Padua, Italy, April 13-17, 2015.

Screening energy of the D+D reaction in an electron plasma deduced from cooperating colliding reaction (Oral presentation)

J. Kasagi

The 19th International Conference on Condensed Matter Nuclear Science ICCF19, Padua, Italy, April 13-17, 2015.

Near threshold $K^0\Lambda$ photoproduction on the neutron studied with an electromagnetic calorimeter, FOREST (Oral presentation)

Y. Tsuchikawa

The 10th International Workshop on the Physics of Excited Nucleons (NSTAR2015), Osaka, May 25-28, 2015.

The performance study of an electro-magnetic calorimeter for the LEPS2/BGOegg experiment (Oral presentation)

Y. Matsumura

The 10th International Workshop on the Physics of Excited Nucleons (NSTAR2015), Osaka, May 25-28, 2015.

$K^0\Lambda$ photoproduction studied with an electromagnetic calorimeter, FOREST (Oral presentation)

Y. Tsuchikawa

The 12th International Conference on Hypernuclear and Strange Particle Physics (HYP2015) Sendai, Sep.7-12, 2015.

学位論文 (電子光理学研究センター所属)

博士論文「Near-threshold $K^0\Lambda$ photoproduction on the neutron」

土川 雄介，平成 27 年，東北大学

修士論文 「メソン光生成反応実験のための GeV 光子ビームプロファイルモニターの開発」

木戸 聡, 平成 27 年, 東北大学

修士論文 「速度集群法を用いた極短パルス電子ビームの生成」

齊藤　寛峻, 平成 27 年, 東北大学

学位論文 (他機関所属)

修士論文「ミューオン-電子転換過程探索実験に用いるストローチューブ飛跡検出器の開発」

田中 聡一，　平成 27 年度，九州大学

学士論文「シングルコンパレータ法による光量子放射化分析 岩石試料への応用」

寺岬 均，　平成 27 年度，首都大学東京

IV. Members of Committees

Steering Committee

2015

Hiroyuki HAMA*	ELPH
Hajime SHIMIZU	ELPH
Toshimi SUDA	ELPH
Fujio HINODE	ELPH
Shigeru KASHIWAGI	ELPH
Norihito MURAMATSU	ELPH
Hidetoshi KIKUNAGA	ELPH
Hirokazu TAMURA	Graduate School of Science
Satoshi NAKAMURA	Graduate School of Science
Kazushige MAEDA	Graduate School of Science
Kouichi HAGINO	Graduate School of Science
Fuminori MISAIZU	Graduate School of Science
Yasushi KINO	Graduate School of Science
Nobuyuki Uozumi	Graduate School of Engineering
Atsuki TERAKAWA	Graduate School of of Engineering
Masaki FUJITA	Institute for Materials Research
Yuji TAKAKUWA	Institute of Multidisciplinary Research for Advanced Materials
Takeo EJIMA	Institute of Multidisciplinary Research for Advanced Materials
Keiichi EDAMATSU	Research Institute of Electrical Communication
Yasuhiro SAKEMI	Cyclotron and Radioisotope Center
Tetsuo TANIUCHI	Center for Interdisciplinary Research

* Chairperson

General Advisory Committee

2015

Hiroyuki HAMA*	ELPH
Hajime SHIMIZU	ELPH
Toshimi SUDA	ELPH
Hidetoshi KIKUNAGA	ELPH
Hirokazu TAMURA	Graduate School of Science
Yasushi KINO	Graduate School of Science
Yasuhiro SAKEMI	CYRIC
Tetsuo TANIUCHI	CIR
Takahiro IWATA	Yamagata University
Daisuke JIDO	Tokyo Metropolitan University
Takashi NAKANO	RCNP, Osaka University
Tomohumi NAGAE	Kyoto University
Hideaki OHGAKI	IAE, Kyoto University
Shigemi SASAKI	HSRC, Hiroshima University
Akihiko YOKOYAMA	Kanazawa University
Yasuji OURA	Tokyo Metropolitan University

* Chairperson

Program Advisory Committee

2015

Hajime SHIMIZU	ELPH
Toshimi SUDA	ELPH
Satoshi N. Nakamura	Graduate School of Science
Shigeru KASHIWAGI	ELPH
Hidetoshi KIKUNAGA	ELPH
Asao YAMAMURA	Institute for Materials Research
Yasuhisa TAJIMA	Yamagata University
Hiroaki OHNISHI	RIKEN
Toshiyuki TAKAHASHI *	IPNS, KEK
Yoshihiko SHOJI	LASTI, University of Hyogo
Yasuji OURA	Tokyo Metropolitan University
Koichi TAKAMIYA	Research Reactor Institute, Kyoto University

* Chairperson

V. Approved Experiments

平成27年度前期採択課題一覧

課題番号	課　　題　　名	申込責任者
2805	光量子放射化法によるプロメチウム（Pm）内包金属フラーレンの合成を目的とした RI 製造	秋山 和彦
2807	ガスジェット搬送物としての Be-7 の半減期測定	笠松 良崇
2808	高分解能飛行時間測定と光子標識化装置の時間分解能の向上	石川 貴嗣
2809	コンパクト BPM の開発	石川 貴嗣
2810	位置測定可能な電磁カロリメータモジュールの開発	石川 貴嗣
2811	E16 実験 GEM 飛跡検出器の磁場内での性能評価	小沢 恭一郎
2812	BM4 用 光子標識化装置の性能評価	神田 浩樹
2813	FOREST 実験の為の光子標識化装置 Tagger2s ワイヤーチェンバーの性能評価	田島 靖久

平成27年度後期採択課題一覧

課題番号	課題名	申込責任者
2814	^{100}Mo (γ,n) ^{99}Mo反応におけるWコンバーターの厚さ依存性	岡 壽崇
2815	BSTリングの電子ビームサイズの測定	秋山 和彦
2816	検出器テスト用電子ビームラインの再整備II	石川 貴嗣
2817	電子の速度と運動量[学生実験]	石川 貴嗣
2818	STB-Tagger IIの高時間分解能化	石川 貴嗣
2819	放射性バナジウムV-48を用いたバナジウム・レドックスフロー電池の隔膜の研究	白崎 謙次
2820	HFCを希釈剤として用いた溶媒抽出法によるSrの分離の検討	山村 朝雄
2821	LEPS2ソレノイド実験用トリガー検出器の性能評価	時安 敦史
2822	J-PARC E14実験CsI検出器両読み時の性能評価	外川　学
2823	J-PARC E42実験用タイムプロジェクションチェンバー(HypTPC)の性能評価	杉村 仁志
2824	新素材のシンチレータを用いたサンドイッチカロリメータの開発	田島 靖久
2825	ビームを用いた検出器テスト（4年生学生実験）	須田 利美
2826	シンチレータの電子線ないしはガンマ線に対する放射線耐性実験	黒澤 俊介
2827	シロイヌナズナのカリウム輸送挙動解明のためのトレーサー製造（II）	魚住 信之
2828	FOREST実験の為の光子標識化装置Taggersワイヤーチェンバーの性能評価	田島 靖久
2829	J-PARC・E21実験(COMET実験)のためのストローチューブトラッカーの開発	西口 創
2830	次世代長期線ニュートリノ振動実験に向けた検出器のテスト実験	南野 彰宏
2831	NKS2用 標識化光子ビームのコミッショニング	神田 浩樹
2832	線フラットパネルセンサーの陽電子に対する応答の測定	神田 浩樹
2833	COMET実験用電磁カロリメータの開発	東城 順治
随時申込		
2834	NKS2用 標識化装置のコミッショニング	神田 浩樹
2835	BSTリングの電子ビームサイズの測定	時安 敦史

ELPH ANNUAL REPORT 2015

December 2016

Research Center for Electron Photon Science, Tohoku University
1-2-1, Mikamine, Taihaku, Sendai 982-0826, Japan

印刷所　株式会社　東北プリント
仙台市青葉区立町24番24号
TEL　022（263）1166㈹

ELPH ANNUAL REPORT 2015

TOHOKU UNIVERSITY